Manuel Augusto Vieira

MSc in Electronic and Computer Engineering

Three Transducers for One Photodetector: essays for optical communications

Dissertation presented to obtain the PhD degree in

Electrical and Computer Engineering - Electronics

Supervisor: Paula Maria Garcia Louro Antunes, Professora Adjunta, ISEL

Co-Supervisor: Adolfo Sanches Steiger Garção, Professor Catedrático, FCT-UNL

Evaluation committee:

President:	Prof. Doutor Paulo da Costa Luis da Fonseca Pinto
Examiners:	Prof. Doutor Carlos Alberto Caridade Monteiro e Couto
	Prof. Doutor Jorge Manuel Torres Pereira
Vogal:	Prof. Doutor Manuel Martins Barata
	Prof. Doutor Alessandro Fantoni
	Prof. Doutor Ricardo Luis Rosa Jardim Gonçalves

FACULDADE DE CIÊNCIAS E TECNOLOGIA
UNIVERSIDADE NOVA DE LISBOA

October, 2012

À Maria

Ao Pedro

À Manela

Aos meus pais

Acknowledges

My work would not have been possible without a number of key people. First of all, I would like to thank my Doctorate co-supervisor Steiger Garção and my Doctorate supervisor Paula Louro. I am fortunate to have found their perfect mix for my background and interests.

I am happy to have such a supportive co-supervisor. I enjoyed his interest in my research as well as the fruitful talks. I learned a lot during this time and I am convinced that this knowledge will help me in the future. My Doctorate supervisor Paula Louro has been so very supportive throughout the life of this project. Her ideas and tremendous support had a major influence on this thesis. She allowed me to initiate this joint photonics–control project and encouraged me at every turn. She spent a lot of time helping me, as well as all the other people in our lab.

My colleagues of ISEL/UNINOVA I&D research team made valuable contributions to the refinement of my thesis through their questions and comments. To Miguel Fernandes, Alessandro Fantoni and João Costa many thanks for their contributions which helped me to push my work further on, mainly in simulation programs PSpice Orcad/Capture, ASCA-2D, Runge-Kutta method and Matlab decoding algorithm. Moreover, I would like to thank Dr. Nunes de Carvalho and Dr. Guilherme Lavareda for the manufacture of the p-i-n-p-i-n devices.

To Manuela Vieira, who offered her dedication, support, understanding, and commitment to hit deadlines. She worked long hours into the night, and occasionally became consumed by experimental results, simulations, papers, and reports. She provided an excellent appraisal of this dissertation and offered an excellent inside view on my work. Moreover, she made valuable contributions to the thesis refinement through their questions and comments.

In loving memory of my parents João and Celeste which have always been spiritually supportive in everything I have done.

To Pedro and Patrícia, who factored into my life during this time…thank you.

To Manela, my wife and my granddaughter Maria do Mar —you are the present and, I believe, the building vision of the pages that follow...

Manuel Vieira

Abstract

Optical processing devices based on a- SiC:H multilayer architectures are expected to become reconfigurable to perform WDM optoelectronic logic functions and provide as well complex photonic functions such as signal amplification and switching. This thesis, entitled *"Three Transducers for One Photodetector: essays for optical communications*", reports the main work areas to design, control, validate and evaluate the research of a voltage-controllable wavelength selective optical switching based on shifting between positive and negative electrically bias and a photodetector, which enables the filtering function with the detector itself and has the potential to be rapidly optically biasing tuned:

System Architecture – In this work area it is defined the basic requirements of the device: light-to-dark sensitivity, colour recognition, selective optical and electrical output response, amplification and opto-electronic conversion to transmit, receive, and/or process intelligence(data).The output multiplexed signals should have a strong nonlinear dependence on the light absorption profile, i.e., on the incident light wavelength, bit rate and intensity under unbalanced light generation of carriers.

Experimental Design – This test activities work area allows the evaluation of the results. Multiple monochromatic pulsed communication channels were transmitted together, each one with a specific bit sequence. The combined optical signal was analyzed by reading out, under different applied voltages and optical bias, the generated photocurrent across the device. Depending on the wavelength of the external background and irradiation side, it acts either as a short- or a long- pass band filter or as a band-stop filter

Optoelectronic Algorithm Interface – To help improve our understanding of the output multiplexed signal, computer models of monolithic photodetectors are developed. Following control theoretic methods we derive state-space representation and an equivalent circuit optoelectronic simulator. We validate each model and calibrate the spectral gain model by background–probe experiments and truth tables lookup that perform 8-to-1 multiplexer (MUX) and 1-to-8 demultiplexer (DEMUX) functions.

Applications – The purpose of this work area is to present a new optical logic architecture that offers considerable improvements in reconfigurability. Tunable WDM converters based on amorphous SiC multilayer photonic active filters are used to build blocks to perform standard digital system operations. The transducers combine the simultaneous demultiplexing operation with the photodetection and self amplification. They are optimized for provide the high-sensitivity needed for low-light applications, such as medicine, lighting, sensing and measurement, and manufacturing.

The migration to next generation packet based networks can be much easier and smoother than previously thought, using the emerging a-Si solutions and its integration with plastic optical fiber. It will push the limits of functionality, cost/performance and integration level.

Keywords: Photonic active filters, tunable WDM photodetecteur, reconfigurability, opto-electronic conversion.

Resumo

Neste trabalho, foi utilizado um dispositivo em camadas baseadas em siliceto de carbono amorfo hidrogenado. A sua arquitetura é elétrica e opticamente reconfigurável, funcionando como filtro ótico ativo na zona visível. Pretende-se utilizar este dispositivo para realizar a multiplexagem/demultiplexagem de funções lógicas com tecnologia WDM, proporcionando em simultâneo a amplificação, a comutação e o reconhecimento do sinal transmitido em cada canal.

A tese intitulada *"Três transdutores num fotodetector: ensaios no âmbito das comunicações ópticas*" compreende três áreas de trabalho:

Arquitetura do Sistema - Definição dos requisitos básicos do dispositivo: sensibilidade ao claro-escuro, caracterização optoelectrónica na banda visível. Esta caracterização tem como objetivo a sua aplicação em sistemas de foto-deteção, amplificação e conversão optoelectrónica capaz de transmitir, receber e/ou processar inteligência (dados).

Planificação Experimental– Avaliação dos resultados. A capacidade de desmultiplexagem é testada com sinais de diferentes comprimentos de onda cobrindo a região do visível. A recuperação do sinal enviado em cada canal é analisada através da sua dependência com a tensão aplicada, com a polarização óptica e com a frequência de transmissão. Os resultados obtidos permitiram aferir sobre a influência da presença e localização da radiação de fundo.

Interface Algorítmica com lógica optoelectrónica -Para melhorar a compreensão do sinal multiplexado, é desenvolvido um modelo optoelectrónico. O requisito básico é a reconfiguração do dispositivo. Na sua parametrização teve-se em conta o controlo da sensibilidade através da aplicação de polarizações elétricas ou óticas que permitem ajustar a seletividade espectral na receção. A partir da representação do espaço de estados foram desenvolvidos algoritmos relacionais, utilizados na validação do modelo. Comparando sinais multiplexados experimentais e teóricos, procedeu-se ao reconhecimento da informação de cada canal com base na aplicação e localização de radiação de fundo.

Aplicações - Os transdutores são otimizados para fornecer a alta sensibilidade necessária às aplicações de muito baixa luminosidade de sinais fluorescentes, combinando a utilização simultânea na multiplexagem/demultiplexagem, foto-deteção, amplificação e conversão opto-electrónica,. A migração para redes de nova geração, integrando soluções emergentes de a-Si proporcionar ganhos de custo e melhoria nos níveis de desempenho, configurabilidade e funcionalidade nas comunicações a curta distância.

Palavras-chave: Filtros ópticos activos, multiplexagem/demultiplexagem, amplificação, conversores WDM sintonizáveis, técnicas de reconfigurabilidade, conversão opto-electrónica

Table of contents

Chapter I

Chapter II

Chapter III

Chapter IV

Chapter V

Chapter VI

Table of Figures

Table of Tables

Table of abbreviations

A	Area of the diode
AC	Alternate current
APD	Avalanche Photo Diode
ASCA-2D	Device simulation program
a-SiC	Amorphous Silicon Carbide
a-SiC:H	Hidrogenated Amorphous Silicon Carbide
a-Si:H	Hidrogenated Amorphous Silicon
AWG	Arrayed Waveguide Grating
ADSL	Asymmetric Digital Subscriber Line
ATM	Asynchronous Transfer Mode
B	Blue
C	Carbon
CCD	Charge Coupled Device
CFP	Cyan Fluorescent Protein
YFP	Yellow Fluorescent Protein
Chap.	Chapter
CID	Charge injecting devices
CWDM	Coarse Wavelength Division Multiplexing
CMOS	Complementary metal oxide semiconductor
CN	Core network
C-V	Current-voltage measurements
C-V	Capacitance-voltage
DC	Direct current
DEMUX	Demultiplexer
DWDM	Dense Wavelength Division Multiplexing
DSLAM	Digital Subscriber Line Access Multiplexer
EDFA	Erbium Doped Fiber Amplifier
EoPOF	Ethernet over Plastic Optical Fiber
FET	Field effect transistor
FBG	Fiber Bragg Grating
FRET	Fluorescence Resonance Energy Transfer
FTTB	Fibre To The Building
FTTC	Fibre To The Curb
FTTCab	Fibre To The Cabinet

FTTD	Fibre To The Desk
FTTH	Fibre To The Home
FTTN	Fibre To The Node
FTTx	Fibre To The x
G	Green
GPS	Global Positioning System
GSM	Global System for Mobile Communications
ICP – ANACOM	Portuguese telecommunication regulators authority
IMS	IP-based Multimedia Services
IP	Internet Protocol
Iph	Photocurrent
IP-TV	Internet Protocol Television
ITO	Indium Tin Oxide
In	Indium
IR	Infra-red
I_S	Saturation current
I-V	Current-voltage
J-V	Density current-voltage
LASER	Light Amplification by Stimulated Emission of Radiation
LCD	liquid crystal display
LED	Light Emitting Diode
LSP	Laser Scanned Photodiode
NGN	Next Generation Networks
MUX	Multiplexer
OADM	Optical Add-Drop Multiplexer
OXCs	optical cross connects
PECVD	Plasma Enhanced Chemical Vapour Deposition
PIN	Positive-Intrinsic-Negative
POF	Plastic Optical Fiber ou Polymeric Optical Fiber
q	Electronic charge
R	Red
RF	Radio frequency
RGB	Red, Green, and Blue
SDH	Synchronous Digital Hierarchy
SiH_4	Silane
S/N	Signal to noise ratio
s_λ	Spectral responsivity
TCO	Transparent condutive oxide

TFT	Thin-film transistors
UMTS	Universal Mobile Telecommunication System
V_{bi}	Built-in voltage
VIS	Visible
V_{oc}	Open circuit voltage
W	Width of space charge region
WDM	Wavelength-Division Multiplexing
V_T	Thermal voltage
Φ_I	Incident radiant power
η	Ideality factor of the diode

Table of symbols

Symbol	Units	Description
A	cm^2	Area of the junction
α	$cm-^1$	Absorption coefficient
Dp	cm^2s^{-1}	Diffusion coefficient for holes
Dn	cm^2s^{-1}	Diffusion coefficient for electrons
ε_s	Fcm^{-1}	Dielectric constant of the semiconductor
E_{op}	eV	Optical gap
E_g	eV	Energy gap
φ	$cm^{-3}s^{-1}$	Light flux
G_{op}	$cm^{-3}s^{-1}$	Optical generation
h	Js	Planck's constant
I_{ph}	A	Photocurrent
I_0	A	Dark current
ν	s^{-1}	Frequency
η	%	Quantum efficiency
λ	nm	Wavelength
N_D	cm^{-3}	Density of ionized defect states
N_a	cm^{-3}	Doping concentration of the p-layer.
N_d	cm^{-3}	Doping concentration of the n-layer
P_{opt}	W	Optical power
q	C	Electron charge
R	%	Reflection coefficient
ℜ	A/W	Responsivity
Vbi	V	Built-in potential
V	V	Applied voltage
T	K	Absolute temperature
τ_p	s^{-1}	Lifetime of holes
τ_n	s^{-1}	Lifetime of electrons
W	m	Depletion region width
E_F	eV	Energy of the Fermi level
E_V	eV	Top edge of the valence band
E_C	eV	Bottom edge of the conduction band
k	$eV\ K^{-1}$	Boltzmann constant
μ_n	$cm^2V^{-1}\ s^{-1}$	Electron drift mobility
μ_p	$cm^2V^{-1}\ s^{-1}$	Hole drift mobility
σ_{ph}	$\Omega^{-1}cm^{-1}$	Photoconductivity
σ_D	$\Omega^{-1}cm^{-1}$	Dark conductivity
σ_L	$\Omega^{-1}cm^{-1}$	Conductivity under illumination
E	eV	Energy
B	$cm^{-1}eV^{-1}$	Tauc's constant

Preface

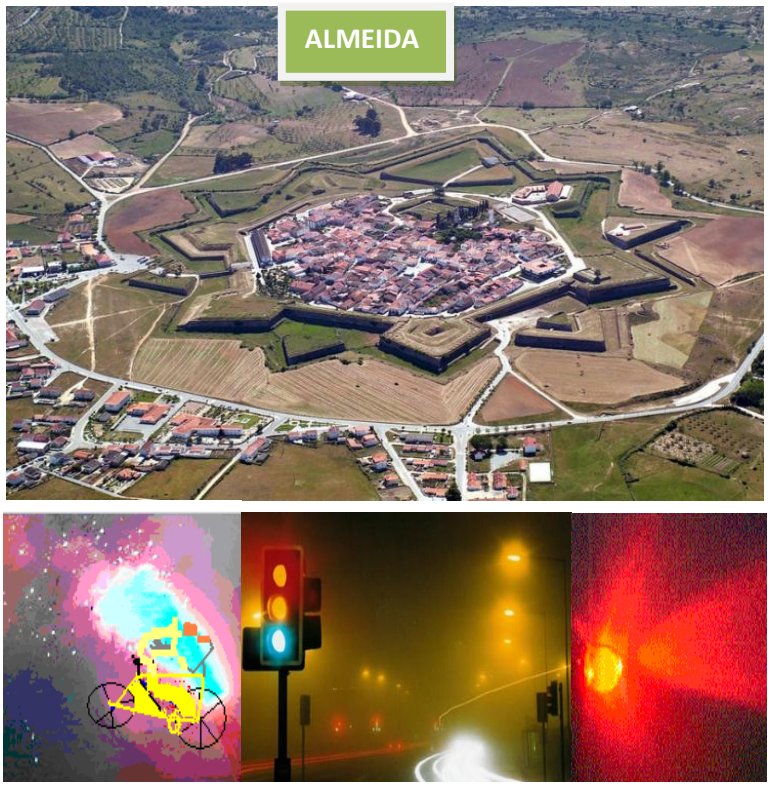

Three Real-time Visible Light Memories…

I suppose the first time I really appreciated the combination of light and control was as an adolescent watching my neighbour "Miguel Fogueteiro" with his exciting fireworks: It was demanding attendance the traditional cyclist, with special effects changing colour every minute and in "perfect synchronization" with the pyrosounds and animated magic illusion displays. I had never seen anything like it, and I was amazed by the visual impact caused by the Almeida´s pyrotechnical shows.

Urban traffic control systems are remarkable systems to combat city centre congestion, a key element in the efficiency of urban mobility and sustainable development policy. Faced with the growth in vehicle traffic, it ensures higher fluidity, thereby reducing fuel consumption, traffic jams and resulting nuisances (noise and CO_2 pollution). In the Lisbon case, for example, the urban traffic control management has produced in the near past a 50% reduction in journey time, savings of 35% in fuel, and a 70% decrease in vehicle pollution.

My fascination with the traffic lights began later on, when I became a traffic engineer in Lisbon´s municipality: the state of all local traffic lights could be changed every second!

During the last years I have been fascinated by WDM control: the visible light that pulses as a millisecond signal transmitter and the appropriate controlled device acting as a receiving component to process intelligence.

Summary and layout of Thesis

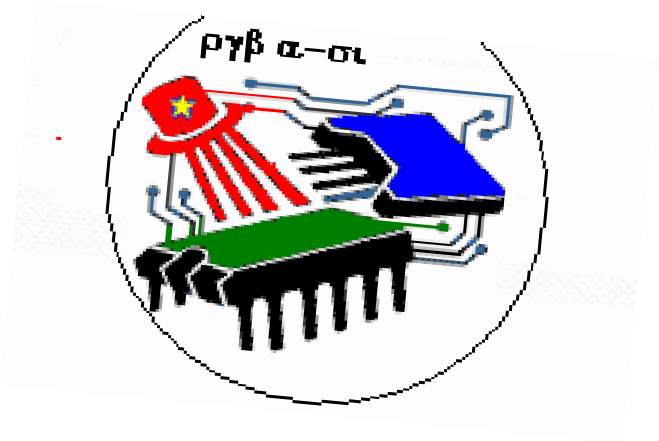

Problem introduction

"The development of an integrated device, at low cost, able to be used as a multiplex/demultipex device in the visible range for short range communication".

The increased use of electronics in automobiles has seen the installation of multiple networks in modern cars, and the expansion of these systems has quickly accelerated. It is now believed that the amount of information that will need to be transmitted in the field of automobile technology will increase rapidly in the near future, in information (in-car navigation, DVD´s), in control and safety systems and in body systems (switches, actuators). Since 1998 Europeans car makers have adopted optical fibers networks. The emergence of WDM is one of the most recent and important phenomena in the development of fiber optic transmission technology. So an increase in network data rates is urgently required.

Visible light sources are being used in the field of in-vehicle optical networks, bringing advantages in both visibility and workability. The LED/POF solution is, still now, sufficient. Key devices are visible light sources, polymer optical fibers, optical circuits and transceivers. We believe that, the use in the visible range, of a wavelength division multiplexing (WDM) device based on the a-SiC technology, is promising for realizing further advances in high-speed communications and can compete with metal-wired systems in the automobile industry. So, advanced features and reduced cost for optical fiber systems, in the visible range, are still needed.

Research question

Writing the research question is an iterative process and such concerns need to be carefully considered in our optoelectronic research design. An example of research question could be:

"Which kind of amorphous Si/SiC transducers, with low cost and appropriated transmission rates should be developed to allow the recovery, or routing of specific wavelengths for the transmission over WDM networks, in the visible spectrum, that could compete with conventional detection electronic devices in optical communications industry?"

This research question defines the thesis proposal and guides our arguments and study. It demands innovative approaches to the exploration of problems, involves a new methodology, a new conceptual approach and clearly demonstrates their relevance to society, contributing to the goals of sustainable development.

Hypothesis and approach

It is known that in order to enhance the transmission capacity and the application flexibility of optical communication and sensor systems different tasks have to be considered, namely:

-The use of Wavelength Division Multiplexing (WDM) devices when different optical signals are encoded in the same optical transmission path.

-The design of active filter circuits by combining the properties of high-pass and low-pass into a band-pass filter.

There has been much research on semiconductor devices as elements for optical communication when a band or frequency needs to be filtered from a wider range of mixed signals. Amorphous silicon carbon tandem structures, through an adequate engineering design of the multiple layers' thickness, absorption coefficients and dark conductivities can accomplish this function. The advantages of this approach are the feasibility of large area, the deposition on different substrate materials (glass, polymer, etc.), the simplicity of the device design and associated electronics, the high resolution, uniformity and the cost/simplicity of the detector. It can also be integrated vertically on top of a read-out electronics, which enables low cost large area detection systems where the signal processing can be performed by an ASIC chip underneath.

So an example of hypothesis in this optoelectronic area of research could be:

"In the visible range, integrated Wavelength-Division Multiplexing /Demultiplexing devices can be achieved at low cost and competitive transmission rates if multilayered p-i'-n-p-i-n heterostructures, produced by PECVD, are used as electrically programmable optical active filters with light triggering and light biasing control".

Topics covered in the Thesis

The topics covered in this thesis are organised in chapters as follows.

The *opening chapter* introduces many of the basic principles of the emerging technologies of photonic switching and optical signal processing. We have tried to make some kind of review and acquisition of knowledge on photo-sensing devices using a-SiC based learning materials. We hope first, to provide an overview of amorphous silicon material properties from the early groups, on the optoelectronic characterization, light-to-dark sensitivity, optical amplification, laser scanned photodiode (LSP) technique and ending with the dilemmas of self- field induced depletion layers for light detection in color and image transducer.

Second chapter deals with voltage controlled devices, in different multilayered a-SiC:H pin architectures, are compared and optimized to be used as multiplexing and demultiplexing devices in the visible range. A double pi'n/pin a-SiC:H heterostructure with two optical gate connections for light triggering in different spectral regions is presented. Multiple monochromatic pulsed communication channels, in the visible range, are transmitted together, each one with a specific bit sequence. The combined optical signal was analyzed by reading out the generated photocurrent across the device, under positive and negative applied voltages. The transducers are also optimized to provide the high-sensitivity needed for low-light applications such as fluorescence.

In third chapter, a pi'n/pin a-SiC:H voltage and optical bias controlled device is presented and its behaviour as image and colour sensor, optical amplifier and demux device discussed. The design and the light source properties (wavelength, intensity and frequency) are correlated with the sensor output characteristics (light-to-dark sensitivity, resolution, linearity, bit rate and S/N ratio). Different readout techniques are used. When a low power monochromatic scanner is used to readout the generated carriers by the scanner, the transducer recognize a color pattern projected on it, acting as a color and image sensor. If the photocurrent generated by different monochromatic pulsed channels is readout directly, the information is demultiplexed. Finally, when triggered by appropriated light, it can amplify or suppress the generated photocurrent working as an optical amplifier. SiC pi'npin wavelength selective channel filters optimized for a fine tuning of different wavelengths are analyzed. Optically switchable on SiC multilayer photonic structures based on a short- or a long- pass band active filter or as a band-stop active filter are analyzed.

In the forth chapter based on the experimental results and device configuration (chapters II and III), an optoelectronic model is developed and supported by an electrical simulation. A demux algorithm is implemented. The first step was to determine the *dc* biasing condition for each stage, followed by *ac* analysis using the proper equivalent circuits. The *ac* circuit representation is supported by the complete dynamical large signal Ebers-Moll model with series resistances and capacities. The Kirchhoff's laws give the linear state model. The concept of a parallel current bucket connection inflow is established to give insight on the physics of th e device. The multiplexed signal is simulated by analyzing the simplified *ac* equivalent circuit and the four order Runge-Kutta method to solve the corresponding state

equations. MATLAB was used as a programming environment and the input parameters chosen in compliance with the experimental results. The transfer characteristics effects due to changes in steady state light, *dc* control voltage or applied light pulses are presented.

The purpose of *fifth chapter* is to present a new reconfigurable logic architecture that offers considerable improvements in sensing, measurement, manufacturing and opto-electronic conversion applications. Combined tunable converters based on SiC multilayer photonics active filters are analyzed. MUX signals that perform 8-to-1 MUX function and truth tables lookup are compared. A decoding algorithm was implemented and tested.

In *sixth chapter* is given a overview about future priorities for optical technology support for innovation and knowledge. A framework, in the domain of photonic components, for developing a-SiC technology, as a product innovation in support of digital city of tomorrow is presented. The main conclusions and future research directions are summarized and outlined.

Chapter I

Background theory on a-Si/SiC photodiodes

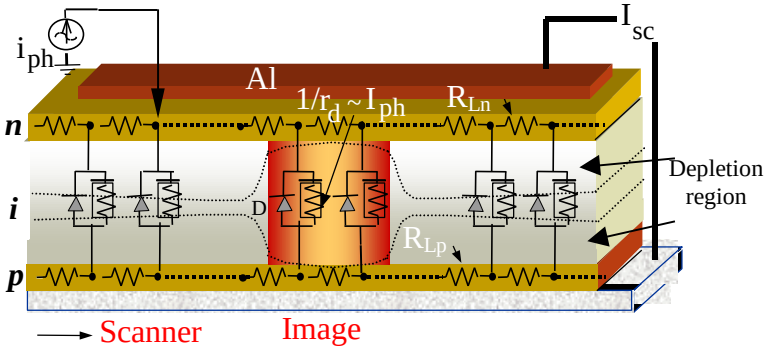

Introduction

This opening chapter introduces many of the basic principles of the emerging technologies of photonic switching and optical signal processing. Optical computing has a long and diverse history. In the future network, optical technology will play a stronger role not only for transmission but also for switching. Optical filters play important roles in communication systems. The further development of core and photonic technologies (photodetectors, optical amplifiers, transmitters and receivers, multiplexers, cross-connects, and sensors), will be fundamental in strategic applications such as medicine, communications, lighting, sensing and measurement, and manufacturing. We have seen that photonic signal processing is a key enabling technology for faster transmission, switching and control. The current trend in photonic signal processing is clearly toward integrated solutions.

We have tried to make some kind of review and acquisition of knowledge on photo-sensing devices using a-SiC based learning materials. For it, we have distilled the essence of the team knowledge, seeking to create a picture of Amorphous Si/SiC photodiodes used in different applications: Laser Scanned Photodiode black and white Image sensors, LSP image and color transducers, and Si/SiC tandem photodiodes.

We wish to do more than provide a transcription of what was done. We have set the context for the rest of this dissertation.

In order to enhance the basic requirements of the system architecture, the transmission capacity of experimental design, the simulating parameters in the optoelectronic algorithm interface and the application flexibility of optical communication and sensor systems in visible spectrum, different tasks have to be considered. We hope first, to provide an overview of amorphous silicon material properties from the early groups, on the optoelectronic characterization, light-to-dark sensitivity, optical amplification, laser scanned photodiode (LSP) technique and ending with the dilemmas of self- field induced depletion layers for light detection in color and image transducer.

1. Current state of art on Amorphous Si/SiC photodiodes.

Amorphous Si/SiC photodiodes working as photo-sensing or wavelength sensitive devices in the visible range, have been widely studied in the past for different application (solar cells, color sensors, image sensors).

The term “amorphous” is commonly applied to non-crystalline materials prepared by deposition from gases. Research into amorphous silicon began, nearly forty years ago (1960). At that time amorphous silicon was grown by evaporation or sputtering and exhibited a large defect density. In 1969 occurred

the growth of amorphous silicon from plasma of silane by Chittiwick et al [1]. An important advance occurred in 1975, with the demonstration of substitutional doping by Spear e LeComber [2].

In early studies of amorphous silicon, it was determined that plasma-deposited amorphous silicon contained a significant percentage of hydrogen atoms bonded into the amorphous silicon structure. When amorphous silicon is deposited under hydrogenation conditions the hydrogen atoms binds to dangling bond defects and removes the corresponding electronic states in the band gap, which eliminates most of the trapping and recombinations centers. This process of introducing hydrogen into silicon is usually designated as passivation of the dangling bonds. These atoms were discovered to be essential for the improvement of the electronic properties of the material. Amorphous silicon is generally known as “hydrogenated amorphous silicon”, or a-Si:H. Hydrogenated amorphous silicon (a-Si:H) has a sufficiently low amount of defects to be used within devices. However, the hydrogen is unfortunately associated with light induced degradation of the material, termed by the Staebler-Wronski Effect [3].

Amorphous alloys of silicon and carbon (also called amorphous hydrogenated silicon carbide, a-Si1-xCx:H) are an interesting variant to this material. The introduction of carbon adds extra freedom to control the properties of the material. Increasing concentrations of carbon in the alloy widen the electronic gap between conduction and valence bands (also called "optical gap" and bandgap), in order to potentially increase the light efficiency of solar cells made with amorphous silicon carbide layers. On the other hand, the electronic properties as a semiconductor (mainly electron mobility), are poorly affected by the increasing content of carbon in the alloy, due to the increased disorder in the atomic network.

While a-Si suffers from lower electronic performance compared to crystalline silicon (c-Si), it is much more flexible in its applications. It may also produce savings on silicon material cost, as a-Si layers can be made thinner than c-Si.

One advantage is that a-Si can be deposited at very low temperatures on glass. Once deposited, a-Si can be doped in a fashion similar to c-Si, to form p-type or n-type layers and ultimately to form electronic devices. Another advantage is that a-Si can be deposited over large areas by Plasma Enhanced Chemical Vapor Deposition (PECVD). The design of the PECVD system has great impact on the production cost of such panel, therefore most equipment suppliers put their focus on the design of PECVD for higher throughout, that leads to lower manufacturing cost. Besides, amorphous silicon has become the material of choice for the active layer in thin-film transistors (TFTs), which are most widely used in large-area electronics applications, mainly for liquid-crystal displays (LCDs).

2. Amorphous pin photodiodes

2.1 The physics of the p-i-n photodiode

2.1.1 Uniform illumination

As already mentioned the absorption of radiation is caused by the interaction of photons and charge carriers inside the material. The different allowed energy levels and the band structure determine the possibility of interaction and, therefore, the absorption characteristics of the semiconductor. Light is also capable of inducing conduction electrons and holes in the silicon. Photons with energy higher than the optical gap are absorbed by the material and generate conduction charge carriers (electrons and holes) by converting valence electrons to conduction electrons. Measurement of electron-hole density gives a measure of the intensity of the light falling on the semiconductor. This is commonly achieved through the use of the diode structure. Electron-hole pairs generated in the depletion region find themselves in an electrical field and are immediately collected. Those generated outside the depletion region diffuse inside the field-free semiconductor (along a concentration gradient) until they either recombine, or fall under the influence of the electric field in the depletion region. The collected carriers contribute to the photocurrent, resulting in an electrical current through the external load or without load, in an external voltage at the contact terminals, the so called open circuit voltage, V_{oc}. The equilibrium is established between the generation, the recombination of carriers, and the current flow through the load. To achieve high efficiencies, as many carriers as possible should be collected by the electrical field inside the space charge region. The width, W, of the space charge region is a function of the doping concentration and on the applied voltage. For one side abrupt junction [4]:

$$W = \sqrt{\frac{2\varepsilon_s (V_{bi} + V)}{qN_B}} \tag{1.1}$$

where V_{bi} is the built-in voltage, ε_s the dielectric constant of the semiconductor and q the electronic charge. The speed limiting capacitance of the diode is also a function of the space charge width and is given by:

$$C = \frac{\varepsilon_s}{W} A \tag{1.2}$$

where *A* is the area of the diode. Diodes based on p-i-n structures show a larger space charge width when compared with the p-n due to the lower doping level of the intrinsic layer.

The I-V characteristics of a non illuminated p-i-n photodiode are identical to the characteristics of a standard rectifier diode. If exposed to optical radiation a photocurrent (I_{ph}) is generated, which is

strongly proportional to the incident radiant power (Φ_i). The ratio of both variables defines the spectral responsivity (s_λ). The characteristics of the irradiated photodiode are then given by:

$$I_D = I_S\left[\exp\left(\frac{V_D}{\eta V_T}\right)-1\right]-I_{ph} \tag{1.3}$$

with I_S the saturation current, η the ideality factor of the diode, and V_T the thermal voltage.

For large signal or *dc* mode, the photodiode can be described as a non-linear current source, I_D, feeding into an ideal diode, and its internal characteristics are better modeled by the introduction of a shunt resistor, a shunt capacitor and a series resistor [5]. Under small-signal conditions or *ac* mode, the photodiode behaves as a non-linear photocurrent-controlled resistor (r_d), which represents an incremental resistance, around the quiescent operating point, and is expressed in terms of I_{ph} as:

$$\frac{1}{r_d}=\frac{\partial I_D}{\partial V_D}\approx\frac{I_{ph}}{\eta V_T} \tag{1.4}$$

2.1.2 Non-uniform illumination

As mentioned before the uniform illumination of a p-i-n junction leads to the appearance of a *transverse* photovoltage between the two sides. If the illumination is not spatially uniform, due to the carrier gradient between irradiated and dark regions, an additional effect arises resulting in a *lateral* photovoltage parallel to the junction, $V_{ph,l}$ in addition to the transverse one, $V_{ph,t.}$. Due to the higher conductivity of the doped layers, the photogenerated minority carriers build up across the doped layers, while the majority carriers are accumulated in the illuminated region, beyond the depletion layer edge, causing a reduction in the band bending across this region. A deviation from the carrier density equilibrium occurs resulting in lateral drift and reinjection of minority carriers (holes from the p-side and electrons from the n-side) into the intrinsic layer where they are trapped instantaneously as reported in Figure 1.1.

The density of reinjected carriers depends on the resistivity of the intrinsic and doped layers and on the charge density of the i-layer [6, 7]. This anisotropic spatial distribution is responsible by an electric field modulation across the depletion region [8]. At the illuminated regions the electrical field is reduced, the depletion width shrinks (Equation1.1) and the capacitance increases (Equation 1.2). So, low local electric fields are ascribed to illuminated regions and high electric fields to dark zones.

The equivalent electric circuit able to describe the behavior of a p-i-n device under non-uniform illumination is, then, an array of dark and illuminated photodiodes interconnected through lateral resistors, that model the sheet resistance of the n- and p-doped layers, respectively [9] (see Figure 1.3a).

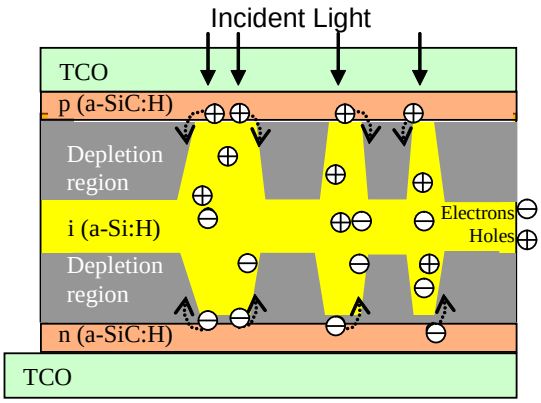

Figure 1.1 *Physical structure of a p-i-n photodiode under a light pattern illumination.*

2.2 Laser Scanned Photodiode (LSP) image sensor

2.2.1 Solid state imagers

Whether we hope to view images or count photons, we use devices that work by absorbing photons and turning them into information. Traditional optics has relied heavily on the human eye for the evaluation of light distributions, using photographic films as an intermediate storage medium, when necessary. With the advent of computers and digital image processing, electronic image sensors have become indispensable tools. Three forces directed the evolution of image sensors: Advances in technology determine what is possible, algorithms determine what is practical, and applications determine what is desirable. If we wanted to generalize about areas in which detectors and imaging technology can improve, we could talk about collecting information more quickly and efficiently, at more wavelengths, with more compact and user-friendly devices or interfaces.

Any conventional solid state imaging device consists of an array of sensing elements combined with some form of transport mechanism to deliver the sensor output signal to the periphery of the device. Sensors used in commercial devices include photodiode arrays [10, 11], charge-coupled device (CCD) [12, 13], complementary metal oxide semiconductor (CMOS) [14], charge injecting devices (CID) [15], and bipolar transistors [16]. All of these devices use essentially the same light sensing mechanism. Photons penetrating a depletion region generate electron-hole pairs. These carriers are swept away by the electric field across the depletion region and generate a small transverse photocurrent. Except under very bright conditions, it is not possible to use this photocurrent directly. Thus, in order to achieve a reasonable signal-to-noise ratio, these currents are usually integrated to produce an accumulated charge output.

It is known that a light pattern projected onto a semiconductor junction leads to a distortion of space charge regions giving rise to potential barrier modulation that depends on the spatial distribution of the

light pattern [7, 17, 18]. Low local potential barriers are ascribed to illuminated regions and high potential barriers to dark zones [19]. Based on this effect, microcrystalline [20] and amorphous [21] optical TCO/p-i-n/metal image transducers were developed. Those sensors are fundamentally different from the CCD's or from vacuum tube imager [22] systems as they are based on one single sensing element and use a modulated, low-power beam of laser light to "paint" the image directly.

2.2.2 Theory of operation and image representation

The Laser Scanned Photodiode is fundamentally different from the above described electrically scanned image systems. The main advantage is the simplicity of the structure; no special photolithography techniques for patterning or high voltage requirements and bulky design are needed. Figure 1.2 depicts the layout of image acquisition experiment.

A focused image, constituted by a steady-state light, is projected onto a fixed location in the photosensitive surface, through the transparent contact. For image acquisition, a low-power chopped laser spot scans the sensor in the raster mode.

Image retrieve starts with the front-end electronics, which receive and process signals from the sensor to a display system. The read-out of the injected carriers is achieved by measuring the *ac* component of the short circuit current, I_{sc}. The processed signal contains the information about the light intensity in each position of the sensor.

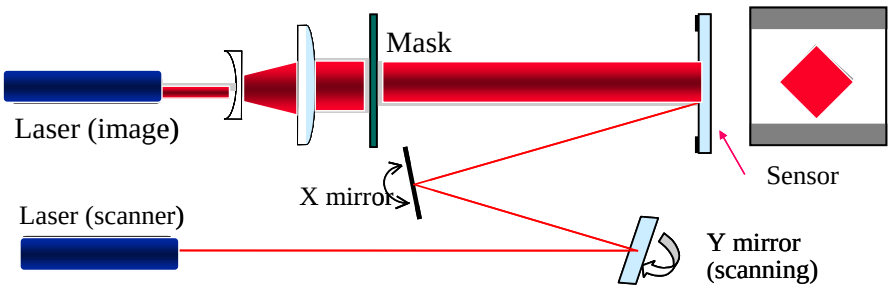

Figure 1.2 *Laser Scanned Photodiode image acquisition layout.*

It was shown that the output signal depends on the photocurrent produced by the image, I_{dc}, as much as by the one produced by the scanner, I_{ac} [23]. This component can be analytically described by the Equation 1.5 [4], where $R(\Phi_L)$ is the small signal responsivity at a given illumination Φ_L, $\Phi_S(t)$ is the average power density of the moving scanner beam and *d* its diameter.

$$i_{ac} = R(\Phi_L) \cdot \Phi_S(t) \cdot \frac{\pi d^2}{4} \qquad (1.5)$$

The signal-to-noise power ratio (S/N) depends on both components of the current ($I=i_{ac}+I_{DC}$) and is given by Equation 1.6, where Δf is the bandwidth and R_0 the sensor resistance at zero voltage bias.

$$S/N = \frac{i_{ac}^2}{(4kT/R_0 + 2q.I_{DC})\Delta f} \quad (1.6)$$

The current is amplified by a current to voltage converter with selectable gain and converted to digital format by a signal acquisition card installed on a computer. A *mxn* grid with *200μm x 250μm* spacing in *x* and *y* directions is used for image representation. All the scanning process is controlled by a microcomputer which stores the currents as a two dimensional array of discrete values, $I_{m,n}$, each one representing the photocurrent induced by the chopped light at the selected position. The data are stored as a matrix of photocurrent values which provide information about local illumination conditions on each position of the device active area. In order to get the effect of the image on the current distribution across the transducer and to outline its shape the image intensity, $X_{m,n,}$ is obtained by subtracting the input matrix $I_{m,n}$ (with image) from the background, $b_{m,n}$ (without image), $X_{m,n} = -(I_{m,n} - b_{m,n})$.

The Laser scanning methodology is explained by the junction electrical field modulation under non-uniform illumination. The optical mapping of the scene onto the sensor surface leads to a reduction of the electrical field at the illuminated regions and to a reduction in the depletion region. If, in addition, a weak light spot is scanning the device, in the dark regions the carriers generated by the probe beam are separated by the junction electric field and collected (high *ac* component of the current). Those generated inside the illuminated regions can drift in the lateral direction, due to the local lowering of the potential barrier, and recombine inside the amorphous bulk (low *ac* component of the current). So, illuminated regions are ascribed to low *ac* components of the photocurrent, and dark regions to high *ac* photocurrent values.

2.3 Electrical model and simulation

The p-i-n image sensor was modeled as an array of photodiodes interconnected through lateral resistors. In the *ac* mode, each photodiode (*D*) was replaced by its incremental resistance (r_d) and connected to its four neighbors, in a row-line matrix, by the resistors R_{Ln} and R_{Lp} that model the sheet resistance of the n- and p-doped layers, respectively. The contacts establish the points for transversal measurements (*V*) and the scanner is modeled through a sine-wave current source applied from each top node of the circuit to the *ground*.

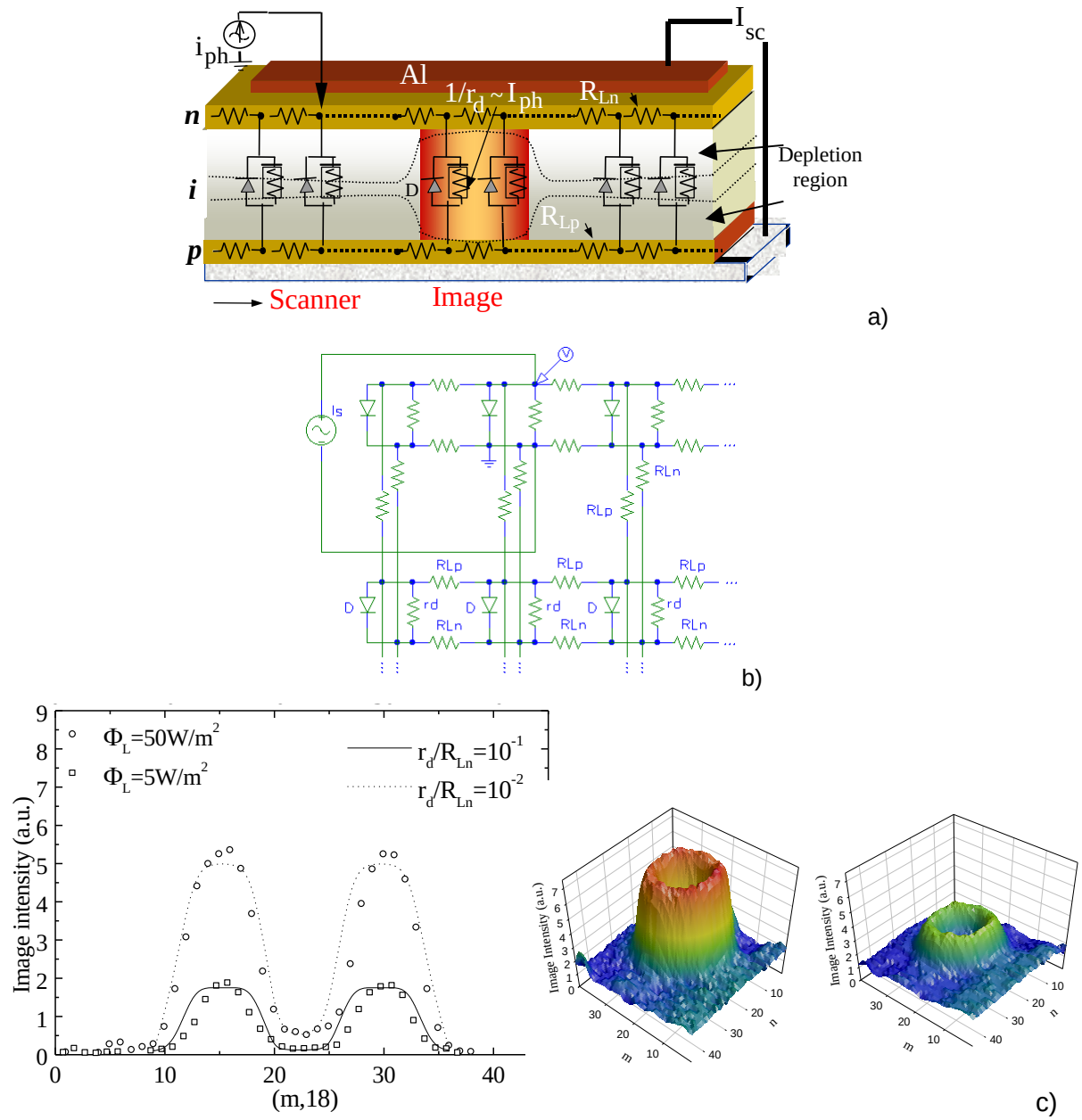

Figure 1.3 *a) LSP configuration in addition with the electrical model proposed b) A fraction of the electrical circuit used for simulation.c) Simulated and experimental image intensity, $I_{m,18}$ for a 7.5 mm donut with a 2.5 mm inner hole. Φ_L=50 W/m^2 and Φ_L=5 W/m^2.*

Those nodes are the diode anodes, i.e. the *m*×*n* points used for voltage read-out. Figure 1.3a depicts the LSP configuration in addition with the electrical model proposed. In Figure 1.3b a fraction of the electrical circuit, being part of the non-planar structure used for the electrical simulation, is presented and Figure 1.3c displays, for a 7.5 mm donut having an inner hole of 2.5 mm diameter, the image intensities at two r_d/R_{Ln} ratios, obtained along row 18 (solid and doted lines). During the simulation i_{ac}, R_{Ln} and R_{Lp} were kept constant. For comparison, the corresponding experimental results are depicted as symbols.

The simulation procedure has two main phases: the circuit construction and the simulation process. In the first phase the input parameters and the array dimension are defined in order to include the image area, the surrounding dark region and the contacts. In the second phase, a voltage distribution composed of a matrix of $m \times n$ values is obtained. Each simulation run corresponds to a different assigned node where the scanner source is applied. The stored values are the magnitudes of the sinusoidal small signals taken in each simulation process step. Several parameters such as contact geometry, layer resistivity, and image brightness can be modelled. The contact shaping is simulated by choosing the points for voltage read-out (V and the *ground*). If the contacts cover the entire surface, they change for each $m \times n$ value read-out, as it is shown in Figure 1.3. The conductivity of the doped layers is modelled by changing R_L for the whole circuit (higher conductivities correspond to lower values of R_L). The brightness of the simulated image is obtained by changing r_d on the points allocated to the image area.

2.4 Laser Scanned Photodiode Characteristics

2.2.3 Deposition

A series of large area (4 x 4 cm^2) amorphous single layers and image transducers in the assembly glass/ZnO:Al/p (Si:H)/i(Si:H) /n(Si_xC_{1-x}:H)/Al were produced. The p-i-n Si:H junction acts as a sensing element, the back and the front contacts are used as electrical interfaces.

Table 1.1 *Deposition parameters for the amorphous LSP sensors.*

Sensor code	Layers	SiH_4 (sccm)	H_2 (sccm)	PH_3 (sccm)	B_2H_6 (sccm)	CH_4 (sccm)	Thickness (Å)
	p	11.96	—	—	0.04	0	500
#M006291	i	20	10	—	—	—	5000
	n	10	—	0.02	—	0	500
	p	11.96	—	—	0.04	0	500
#M006301	i	20	10	—	—	—	5000
	n	10	—	0.02	—	20	500
	p	10	—	—	0.04	20	500
#M007192	i	20	10	—	—	—	5000
	n	10	—	0.02	—	20	500

All the layers in p-i-n transducers were deposited by Plasma Enhanced Chemical Vapor Deposition, at a 13.56 MHz radio frequency and the contacts were produced by sputtering technique [24]. The

deposition pressure was 200 mTorr, the substrate temperature was held at 150ºC and the rf- power was 4W. The deposition conditions of all p- and i-layers were kept constant while they varied in the n-layer as reported on Table 1.1.

2.2.4 Optoelectronic properties of individual layers

A preliminary electrical and optical characterization of the films was carried out by measuring the electrical conductivity in the coplanar direction and by obtaining the absorption spectra from transmission and reflection measurements. The deposited n-layers present conductivity, σ_d, in the range of $1.0x10^{-5}\ \Omega^{-1}cm^{-1}$ to $2.6x10^{-4}\ \Omega^{-1}cm^{-1}$ and optical gaps, E_{op}, between 2.1 eV and 1.8 eV, depending on the methane flux, while for the p-type film $7x10^{-5}\ \Omega^{-1}cm^{-1}$ and 1.8 eV were inferred. The i-layer has a dark conductivity of approximately $1x10^{-10}\ \Omega^{-1}cm^{-1}$ and a photosensitivity higher than 10^4 under AM1.5 (100 mW/ cm^2). The front contact ZnO:Al is a 300nm thick and has a transmission of approximately 80% from 425 nm to 700 nm and a resistivity around $9x10^{-4}\ \Omega cm$. The optoelectronic characteristics of the individual layers are displayed in Table 1.2.

Table 1.2 *Optoelectronic characteristics for the amorphous LSP sensors*

Cell code	Layers	σd ($\Omega^{-1}\cdot cm^{-1}$)	ΔE (eV)	Eop (eV)	σ_{ph}/σ_d
#M006291	p	8.2×10^{-7}	0.499	1.80	7.3
	i	7.6×10^{-11}	0.739	1.79	7.1×10^4
	n	5.7×10^{-8}	0.795	1.73	7.0
#M006301	p	8.2×10^{-7}	0.499	1.80	7.3
	i	7.6×10^{-11}	0.739	1.79	7.1×10^4
	n	1.9×10^{-12}	0.834	2.10	21
#M007192	p	2.5×10^{-9}	0.649	2.06	4.5
	i	7.6×10^{-11}	0.739	1.79	7.1×10^4
	n	1.9×10^{-12}	0.834	2.10	21

2.2.5 Device characterization

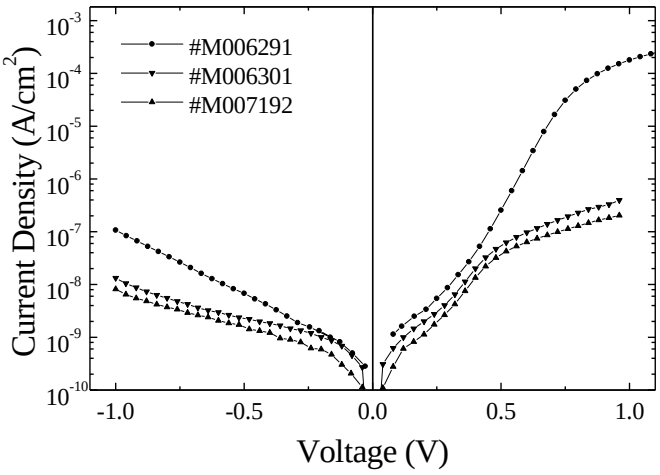

Figure 1.4 *J-V characteristics in dark and at 300K.*

The amorphous transducers were characterized by current-voltage in dark and under illumination and spectral response measurements. Density current-voltage (J-V) characteristics in dark at room temperature are displayed in Figure 1.4 and in Figure 1.5 they are displayed under AM1.5 illumination.

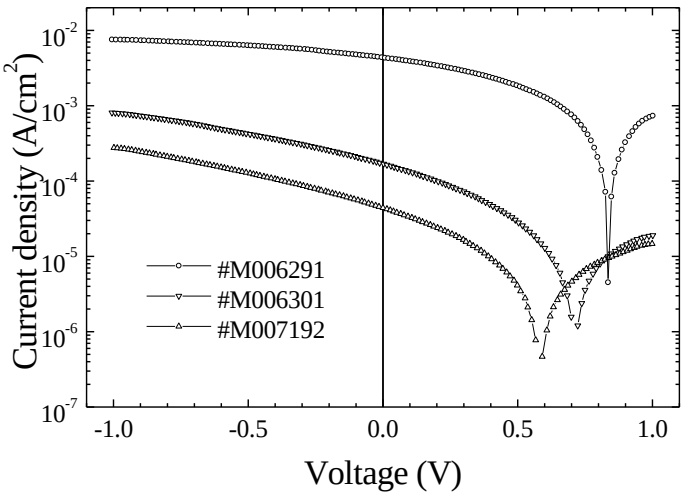

Figure 1.5 *J-V characteristics under AM1.5 irradiation and 300K.*

Open circuit voltages, V_{OC}, of the order of 0.8 V and short circuit currents, I_{SC}, of about 8 $mAcm^{-2}$ were measured for the amorphous transducers.

2.2.6 Light-to-dark sensitivity

To improve the light-to-dark sensitivity the resistivity of the doped layers and the optical gap were optimized. From short circuit spectral measurements and capacitance-voltage (C-V) behavior under different bias conditions (530 nm; $0< \Phi_L<5$ mWcm^{-2}) the light-to-dark sensitivity [$S=i_{ac}(\Phi_L)/i_{ac}(0)$] and the corresponding depletion widths, were inferred. In Figure 1.6 the sensitivity as a function of the wavelength is displayed without optical bias ($\Phi_L=0$) and under uniform illumination (524 nm, 2 mWcm^{-2}), respectively.

In Figure 1.7 it is plotted the light to dark sensitivity as a function of the applied optical bias, Φ_L**.** The depletion width dependence for sensor #M007192 is also superimposed (circles). The dash lines are exponential decay fits to the experimental data with Φ_0 the correspondent flux constant.

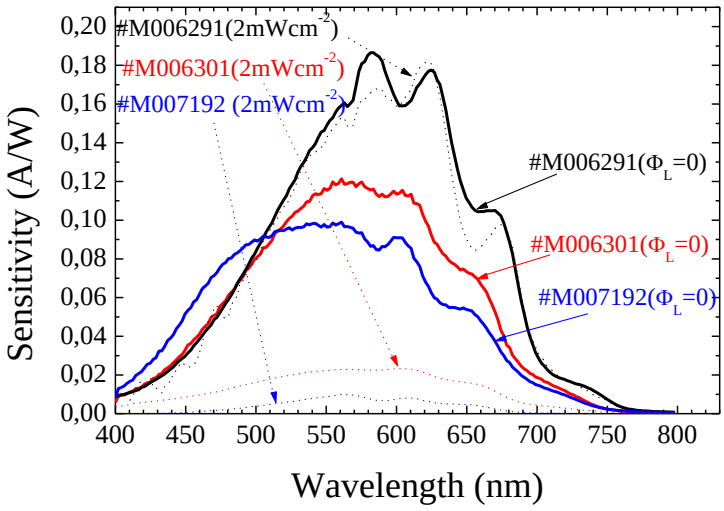

Figure 1.6 *Spectral sensitivity with (dash) and without (solid) applied optical bias.*

Data reveal that the sensitivity, when wide band gap doped layers are used, is lower and decreases significantly with the optical bias. In the heterostructures the output signal decays exponentially with Φ_L while in the homostructure no significant decrease is detected in the analyzed flux range. Φ_0 determines the flux range of the sensor and decreases with the presence of wide band gap doped layers. The heterostructures can “see” small light-to-dark variations while the homostructure remains “blind” in a large flux range.

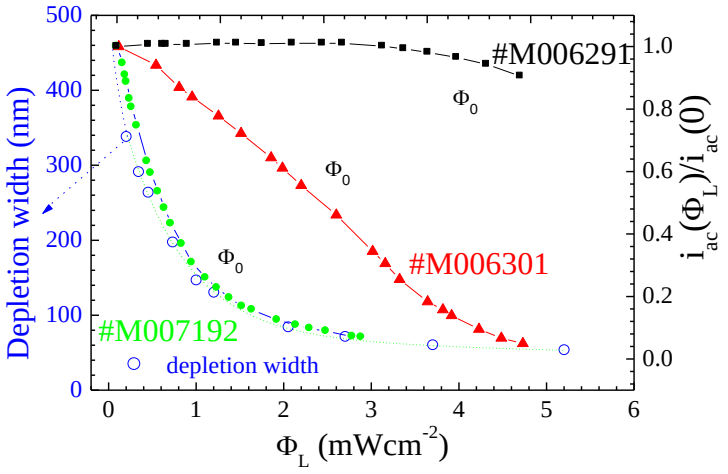

Figure 1.7 *Depletion width (open) and $i_{ac}(\Phi_L)/i_{ac}(0)$ ratio (solid) dependence with Φ_L.*

Results also show that for sensor #M007192, in dark the device is almost fully depleted (480 nm) while for Φ_L> 2 mW/cm^2 it is reduced to a minimum value (80 nm). So, under steady state irradiation the band misalignment reduces the electrical field in the bulk and increases the recombination at the interfaces decreasing the carrier collection. The light-to-dark signal ratio depends strongly on the material of the doped layers. When both layers are based on a-SiC:H material (#M007192) the signal ratio presents a steep decreases with Φ_L and reaches 50% of its dark value at Φ_0=0,4 mWcm^{-2}. If only the n-layer is based on a wide band gap material (#M006301) the signal ratio decreases slowly and only at 2.5 mW/cm^2 the same ratio is achieved. If both a-Si:H doped layers are used (#M006291) the sensor remains "blind" until 4 mW/cm^2 and after that the signal ratio slowly decreases. The higher optical gaps (2,1 eV) and the lower conductivity of the n- and p-SiC:H layers (2.5×10^{-9} Ω^{-1}cm^{-1}; 1.9×10^{-12} Ω^{-1}cm^{-1}) when compared either with the intrinsic (1.8 eV; 7.6x10^{-11} Ω^{-1}cm^{-1}) or with the a-Si:H n- and p-layers (1,8 eV; 8.2×10^{-7} Ω^{-1}cm^{-1}, 5.7×10^{-8} Ω^{-1}cm^{-1}), are responsible for the quench of the depletion region. This effect blocks the carrier collection at the illuminated interfaces decreasing the light-to-dark signal ratio. This light bias dependence enables different applications of the device depending on the readout technique.

Based on experimental results, the small signal responsivity used in Equation 1.5 can be expressed as:

$$R(\Phi_L) = R(\Phi_S)\exp\left(-\frac{\Phi_L}{\Phi_0(V_0)}\right) \tag{1.7}$$

where Φ_0, is the light to dark responsivity and V_0 the built-in voltage. As expected (Figure 1.7), at a given scanner intensity (Φ_S) and sensor configuration (Φ_0) it presents an exponential decay with Φ_L. In the heterostructures the incident power threshold for image detection is low (0.5 mWcm^{-2} and 1.5 mWcm^{-2}) while in the homostructure it is much higher (65mWcm^{-2}).

2.2.7 Optimization of the read-out parameters

In order to analyze the behavior of the sensor under different electrical and image brightness a pattern composed by dark and illuminated regions was projected on the active area of the sensor (#M007192). Figure 1.8a shows, at different image intensities, the image brightness ($\Delta=i_{ac}(0)- i_{ac}(\Phi_L)$) normalized to the maximum flux as a function of the applied electrical bias. In Figure 1.8b the image intensity as a function of the light flux under different bias voltages is depicted.

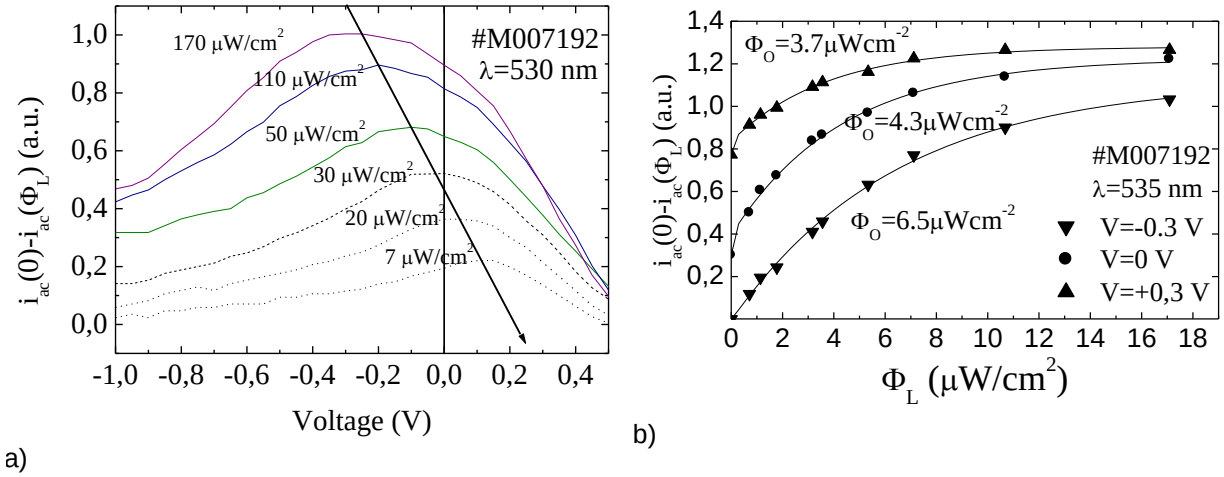

Figure 1.8 *a) $\Delta=i_{ac}(0)- i_{ac}(\Phi_L)$ as a function of the applied bias for different image intensities. b) Image intensity as a function of λ_L under reverse, forward and zero bias for. Φ_0 is the flux constant for each exponential fit (solid line).*

Results show that the signal difference between dark and illuminated regions depends on the power flux, Φ_L. $\Delta=i_{ac}(0)- i_{ac}(\Phi_L)$ is low at high reverse and forward bias and has a maximum, Δ_{max}, near open circuit conditions. Δ maximum has a linear dependence on V and shifts from reverse to forward voltages as Φ_L decreases. As Φ_L increases, the image intensity increases and saturates. A good associated stretch exponential fit (solid lines in Figure 1.8b) is achieved. As the applied bias goes from reverse to forward, Φ_0 decreases. This suggests that Φ_0 depends on the flat band condition (V_0-V) [25], as it increases with the built-in voltage and decreases with the electrical bias.

Based on equations 1.5 and 1.7 the image intensity will depend on Φ_L and V according to the equation:

$$i_{ac}(0,V)-i_{ac}(\Phi_L,V)=i_{ac,sat}\left[1-\exp\left(-\frac{\phi_L}{\phi_0}\right)\right]=R(0,V_0-V)\cdot\phi_S\cdot\frac{\pi d^2}{4}\left(1-\exp\left(-\frac{\phi_L}{\phi_0(V_0-V)}\right)\right) \quad (1.8)$$

where $i_{ac,sat}$ is the saturated image intensity, V_0 is the built-in voltage and V the applied voltage.

The shrinkage of the depletion region (Figure 1.7) and the local quench of the electrical field under illumination [26] reduce the collection of the carriers generated by the scanner at the bright zones. At

high Φ_L, the signal saturates easily due to the maximum shrinkage of the depletion region (flat band condition). So, if the sensor is biased in reverse mode, Φ_0 increases and the flux range before the saturation regime is enhanced. At low values of Φ_L it is difficult to reach the saturation regime. With a small forward bias Φ_0 is decreased and so, the collection at the illuminated region decreases, while in the dark regions it remains almost the same. In both cases Δ will be enhanced (Figure 1.8). By applying an electrical bias, a trade-off between flux range and image responsivity may be established, as the reverse bias increases the flux range while forward bias enhances the image responsivity.

a) b)

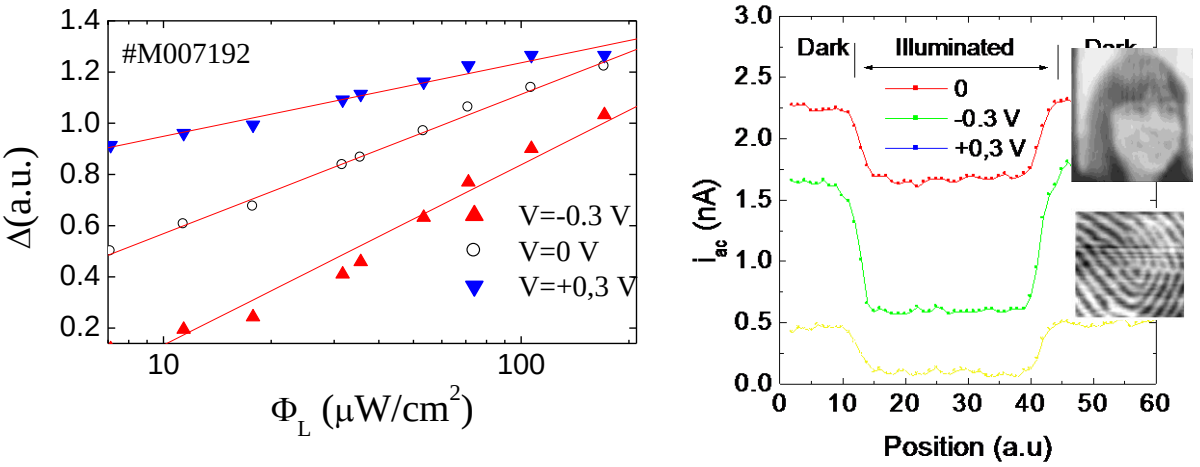

Figure 1.9 *a) Image intensity as a function of Φ_L b)The ac photocurrent for one dimension scans under forward, reverse and zero bias and a grayscale photo and fingerprint representations.*

In Figure 1.9a the image intensity as a function of Φ_L and in Figure 1.9b one line scan of the image are represented under forward, reverse and zero bias voltage. The image brightness ($2\mu Wcm^{-2}$), scanner intensity (two order of magnitude lower) and spot diameter (50 μm) were kept constant. Results show that under reverse bias the image sensitivity and the dynamic range are higher than in short circuit or forward bias. In reverse mode a dynamic rate two orders of magnitude higher with a sensitivity of 6 mA/W and a responsivity of 17 μWcm^{-2} was achieved.

As a possible application, insert shown in the figure, we also display a grayscale photo and a fingerprint representation acquired under short circuit and Φ_L=10 μWcm^{-2}. No image processing algorithms were used. This image presents a good contrast and a resolution around 30 μm showing the potential of these devices for biometric applications. Data also shows that sensor response is logarithmic, just like the human eye, independently on the applied voltage. Data reveals that the performance of an optimized sensor is enhanced by a tight control of the signal acquisition technique and read-out parameters. The output characteristics were limited by the cell configuration and by the light source flux used to map the image onto the sensor. In the heterostructures with wide band gap/low conductivity

doped layers an increase on the image signal is achieved with a dynamic range of two orders of magnitude, a sensitivity of 6 mA/W and a responsivity of 170 μWcm^{-2}.
Examples of possible applications are imaging and display devices, optical character recognition, facsimile transmitters, biometric readers and optical input point of sale terminals.

3. LSP image and color transducer

3.1 The current-voltage characteristics

Figure 1.10 shows the experimental current-voltage characteristics for monochromatic illumination at different wavelengths. Dark characteristics are superimposed. Results show that the current density and the open circuit voltage depend on the wavelength and on the intensity of the incident light.

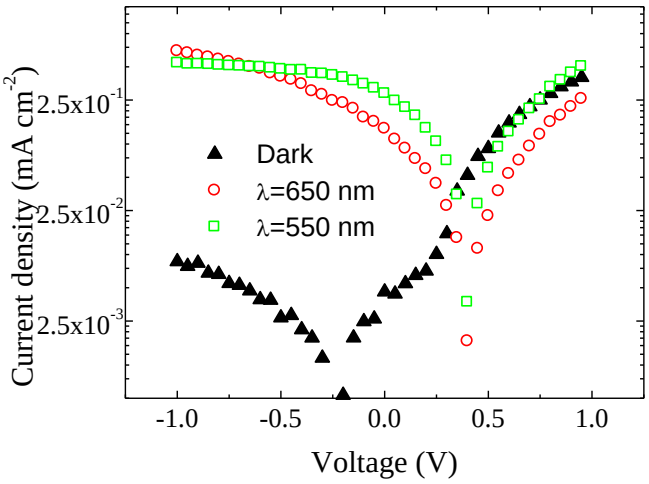

Figure 1.10 *Current density as a function of the electrical bias under dark and under different wavelengths (Φ_L=10 $\mu W/cm^2$).*

Under reverse mode and in dark, the J-V curves present a large current change. No saturation point is detected and the current is canceled at –0.2 V of applied voltage. In short circuit a carrier response is still obtained due to the motion of the carriers in the internal field of the depleted regions.

3.2 The spectral sensitivity in dark and under optical bias

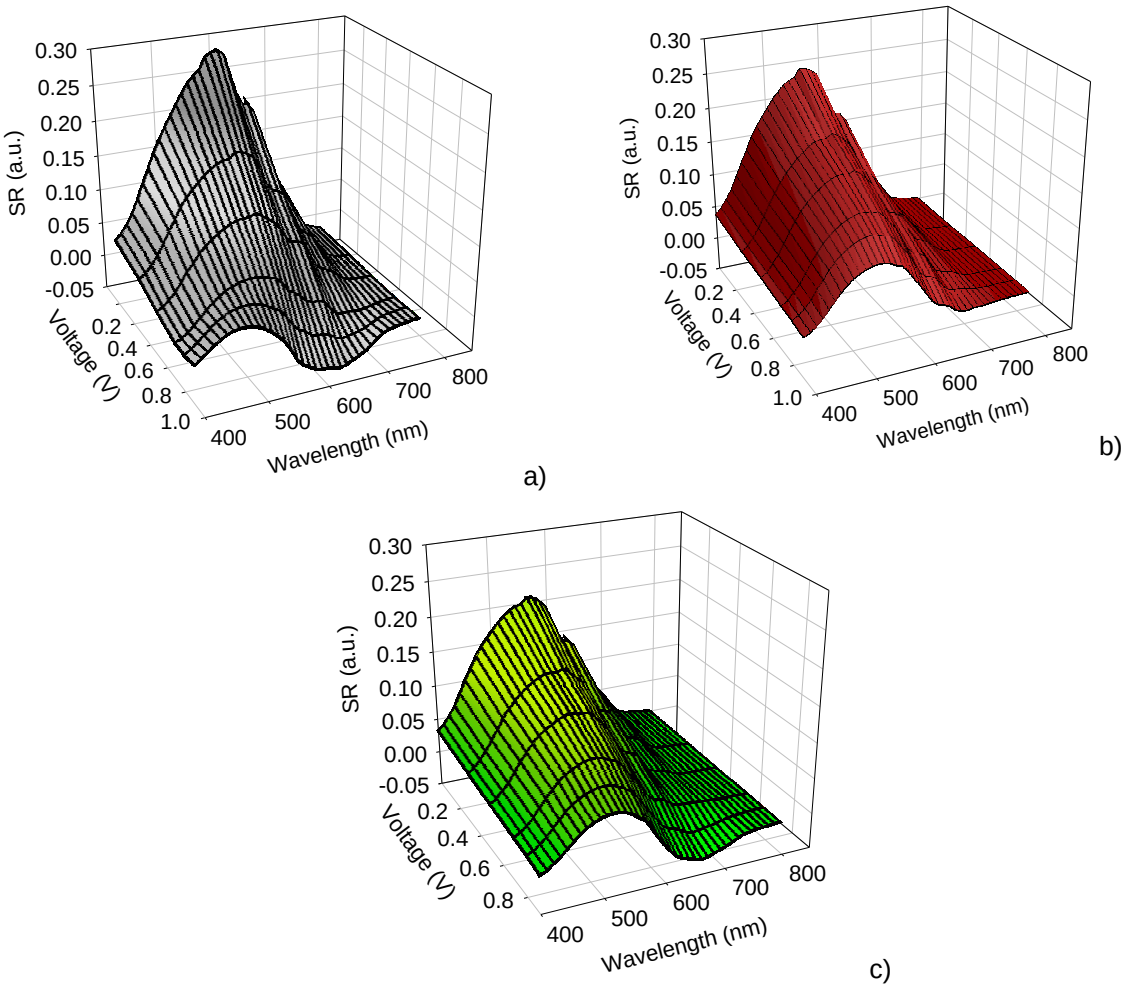

Figure 1.11 *Spectral response dependence on the applied voltage under steady state light conditions: (a) in dark,(b) red (650 nm); and (c) green (550 nm), Φ_L=10 μW/cm^2 .*

Figure 1.11 shows the spectral response as a function of the applied voltage under different steady state light conditions.

The spectral sensitivity depends strongly on both the optical and the electrical bias. As the applied voltage increases the spectral sensitivity decreases continuously with a slope that depends on the optical bias. In dark (Figure 1.11a) the spectral response becomes negative near the open circuit condition and the maximum shifts to lower wavelengths, as it is expected for a drift controlled device. Under illumination the spectral response behavior is quite different. No significant spectral shift is observed, the decay is slower and, even at bias higher than the open circuit voltage the response is positive, which reflects a diffusion-aided transport mechanism. Under green bias the spectral response is smaller than under red bias.

It decreases slowly with the increase of the forward bias and slightly reverses in sign at higher wavelengths. The earlier transition from a field aided to the diffusion regime is due to its high absorption coefficient.

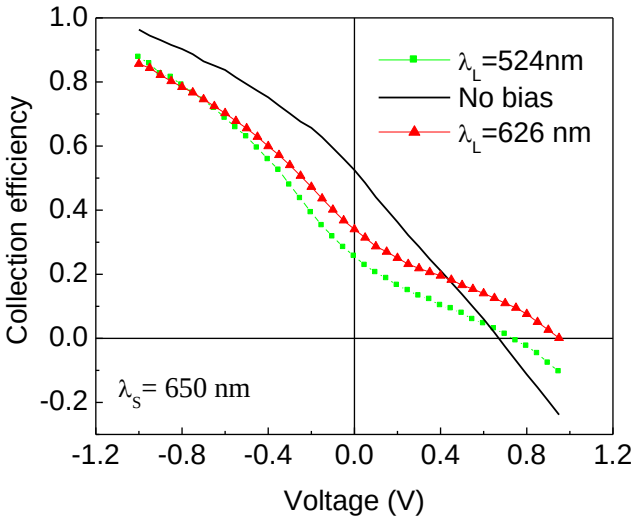

Figure 1.12 *Collection efficiency as a function of the applied voltage in dark and under steady state light conditions.*

Carriers generated under green illumination can only be collected at the p-i interface; otherwise they diffuse towards the dark region and recombine. At high forward bias, the obscured part of the device dominates the transport. So, the red response is in between the dark and the green, as can be observed in Figure 1.12 where the light sensitivity under different optical bias is normalized to its value under high reverse bias (-1.5 V) and plotted in the voltage range analyzed. Results confirm that the collection efficiency at λ_s = 650 nm, under green and red illumination are different than under no optical bias conditions (dark) clearly showing the possibility of detecting a monochrome image and also to perform color extraction.

3.3 Spectral selectivity

Color sensitivity depends mainly on the penetration depth of the light and on its influence at the induced depletion region at the p and n layer.

In Figure 1.13 the image output signal [27] defined as the difference between the *ac* component of the photocurrent in dark (Φ_L=0) and under illumination (λ_s=524 nm, 626 nm and Φ_L=10 μWcm^{-2}) is displayed as a function of the electrical bias.

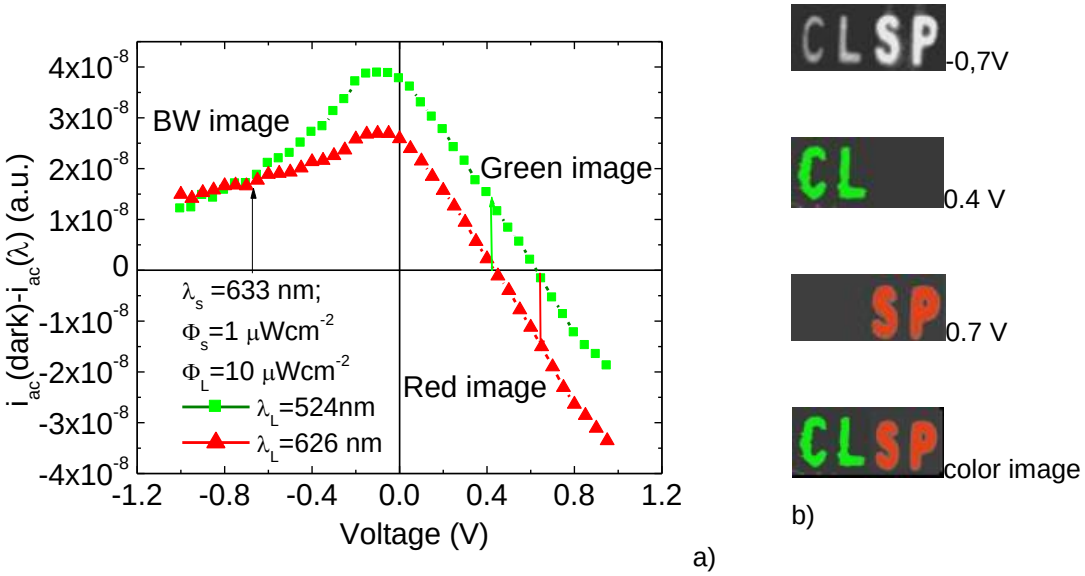

Figure 1.13 *a) Image intensity as a function of the electrical bias under different optical bias. b) A picture image of the sensor acronym CLSP with green "CL" and red "SP".*

Data show that at -0.7 V, the image intensity for the red or the green image presents the same magnitude and signal. No color information can be extracted at this voltage, which leads to a black and white image. In this mode the brightness of the image is proportional to the output signal (i_{ac}), which gives to the sensor the ability of acquiring monochrome gray level images. Color information can only be obtained under forward bias. By tuning the voltage to 0.4 V the red signal is suppressed allowing green recognition. The red information is obtained at 0.7 V, where the green signal goes down to zero. Combining the signal information at these voltages (-0.7 V; 0.4 V, 0.7 V) enables the reconstruction of the color image without the need of the usual color filters. A picture image of the sensor acronym CLSP (Color Laser Scanned Photodiode) with green "CL" and red "SP" was projected onto the sensor. The result is shown in Figure 1.13b at V=-0.7V, V=0.4 V and V=0.7 V. The full color image in was obtained by combining the information.

3.4 Summary

Heterostructures based on p-i-n a-SiC:H were analyzed under different optical and electrical bias. Considerations about modified electrical field profiles and drift-diffusion transport mechanism were used to explain the atypical shapes of the light I-V characteristics, the enhanced ratio between the spectral responsivity in dark and under optical bias conditions and the fine tune of the spectral sensitivity under high forward bias. Numerical simulation gives insight into the physical process and explains the filtering wavelength properties of those devices.

4. Amorphous Si/SiC photodiodes

4.1 Introduction

Color sensitivity in crystalline silicon video cameras is obtained by using different detection channels with three CCD arrays, or by using a mosaic of filters deposited directly onto one single solid state sensor [28, 29]. This method can also be used for large area amorphous silicon sensor arrays and requires three sensors for each pixel. Several attempts to achieve structures capable of modifying their sensitivity spectrum by simply changing the applied bias have been reported in the literature [30, 31, 32, 33]. Those approaches simplify the interconnections as only two terminals are necessary.

The conventional capturing technology in an image sensor is called mosaic capture. The way that mosaic capture works is by using just one single layer of photo detectors in a mosaic pattern to capture the red, green, and blue light, or three separate layers which can absorb different wavelengths of light at different depths with each layer capturing a different color. Using three separate layers does not need to interpolate. In contrast to color filter arrays that use light-absorbing filters, this technology converts light of all colors into useful signal information at every pixel location.

The image sensors that use the mosaic capture system have to rely on interpolation for the colors that it misses. The process is complex and demands processing power. For this reason, the more accurate the image sensor can get, the more processing power it has to use. Since guessing that many colors will probably never be 100% accurate, it obviously leads to color artifacts and loss of image detail.

Amorphous silicon-carbon (a-SiC:H) is a material that exhibits excellent photosensitive properties. This feature together with the strong dependence of the maximum spectral response with the applied bias has been intensively used for the development of color devices. Various structures and sequences have been suggested [34, 35, 36, 37, 38]. In our group efforts have been devoted towards the development of a new kind of color sensor. Large area hydrogenated amorphous silicon single and stacked p-i-n structures with low conductivity doped layers were proposed as color Laser Scanned Photodiode (LSP) image sensors [39, 40, 41]. These sensors are different from the other electrically scanned image sensors as they are based on only one sensing element with an opto-mechanical readout system. No pixel architecture is needed. The advantages of this approach are quite obvious like the feasibility of large area deposition and on different substrate materials (e.g. glass, polymer foil, etc.), the simplicity of the device and associated electronics, high resolution, uniformity of measurement along the sensor and the cost/simplicity of the detector. The design allows a continuous sensor without the need for pixel-level patterning, and so can take advantage of the amorphous silicon technology. It can also be integrated vertically, *i. e*. on top of a read-out electronic, which facilitates low cost large area detection systems where the signal processing can be performed by an ASIC chip underneath.

4.2 Device configuration and sample preparation

Voltage controlled devices, were produced by PECVD in different architectures, as displayed in Figure 1.14, and tested for a proper fine tuning of the visible spectrum.

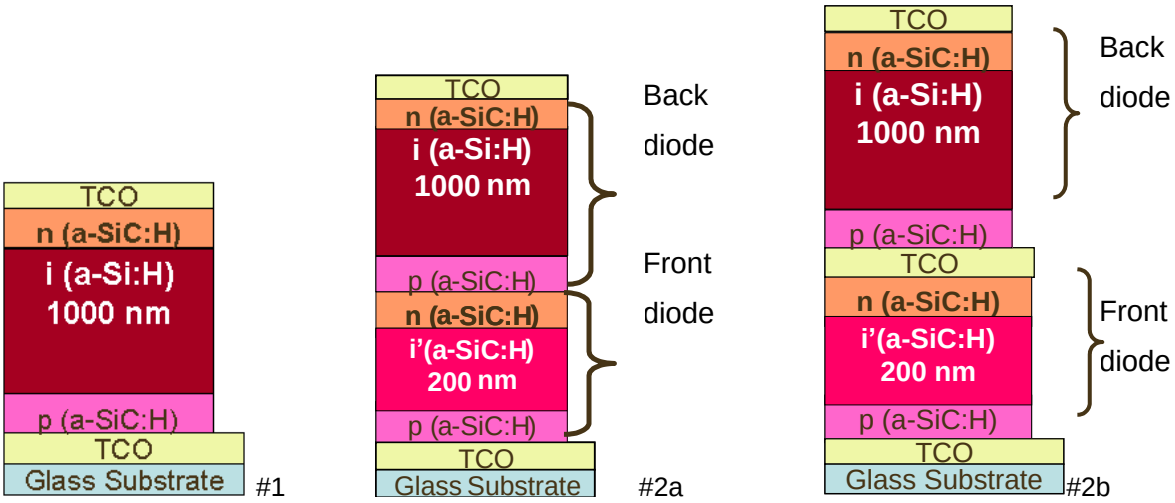

Figure 1.14 *Sensor element configuration.*

The simplest configuration is a p-i-n photodiode (#1) where the active intrinsic layer is a based on an a-Si:H thin film (similar to sensor #M7192). In the others two (#2), the active device consists of a p-i'(a-SiC:H)-n / p-i(a-Si:H)-n heterostructures (#2a, NC5 sample code). To test the efficiency of the internal n-p junction, a third transparent contact was deposited in-between (#2b). The thickness (200nm) and the optical gap (2.1 eV) of all a-SiC:H intrinsic layers (i'-) are optimized for blue collection and red transmittance. The thickness (1000 nm) of the a-Si:H i-layers was adjusted to achieve full absorption in the green and high collection in the red spectral ranges. As a result, both front and back diodes act as optical filters confining, respectively, the blue and the red optical carriers, while the green ones are absorbed across both [42].

The deposition conditions of the i- and i'- intrinsic layers were kept constant in all the devices. They present good properties with conductivities between 10^{-11} and $10^{-9}\ \Omega^{-1}\ cm^{-1}$ and photosensitivity higher than 10^{4} under AM1.5 illumination (100 mW/ cm^2). To decrease the lateral currents which are crucial for device operation [43, 44], low doping levels were used and methane was added during the deposition process. The doped layers (20 nm thick) have high resistivity (>$10^{7}\Omega$cm) and optical gaps around 2.1 eV. Transparent contacts have been deposited on front and back surfaces to allow the light to enter and leave from both sides. The back contact defines the active area of the sensor (4×4 cm^2)**.** The front and back contacts are based on ZnO:Al or ITO and have an average transmission around 80% from 425 nm to 700 nm and a resistivity around $9x10^{-4}\ \Omega$cm.

Table 1.3 *Deposition conditions of the a-Si:H and a-SiC:H films.*

Type	RF Power (W)	Pressure (mTorr)	Gas flow(sccm)			
			SiH_4	1% TMB+99% H_2	2%PH_3+98% H_2	CH_4
p (a-SiC:H)	4	600	10	25	–	15
i (a-SiC:H)	4	500	10	–	–	15
n (a-SiC:H)	4	500	10	–	5	15
i' (a-SiC:H)	2	400	20	–	–	–
p' (a-SiC:H)	2	400	20	10	–	–

Besides, the stacked devices, the simplified test a-SiC:H p-i-n and a-Si:H p-i-n structures have also been deposited during the same deposition process. The film layers were deposited using a parallel-plate PECVD reactor. Deposition conditions such as the RF power, partial pressure and gas flow rates are shown in Table 1. 3. The substrate temperature was held at 260 ºC.

4.3 I-V characteristics under illumination

The typical I-V characteristics in dark and under red, blue and red&blue irradiation are displayed in 1.15.

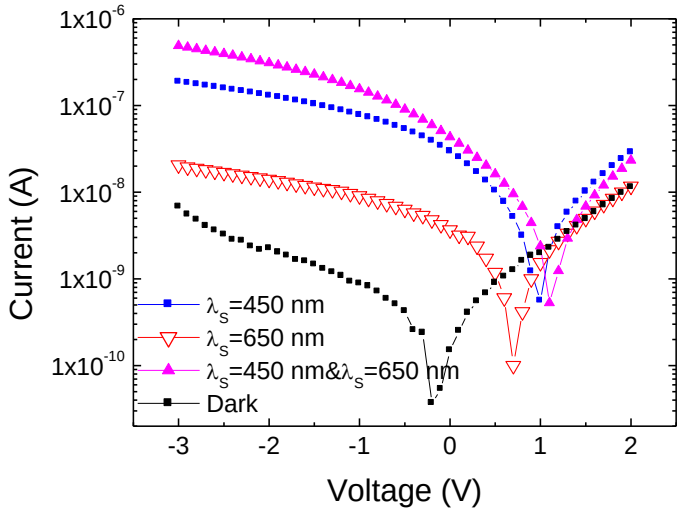

Figure 1.15 *I-V characteristics in dark and under red, blue and red&blue irradiation.*

Results show that the shape of the I-V characteristics are controlled by the background light and by the applied voltage.

4.4 A Multilayer a-SiC:H Color and Image Sensitive Sensor with Optical Readout

4.4.1 Optical read-out

The image to acquire is optically mapped onto the photosensitive surface and a low-power light spot scans the device. The photocurrent generated by the moving spot is recorded as the image signal, and its magnitude depends on the light pattern localization and intensity.

The imaging is performed in a write-read simultaneous process (Figure 1.16): the write exposure, which converts the optical image into a localized packet of charges and the optical readout which performs the charge to current conversion by detecting the photocurrent generated by a light beam scanner. During the image acquisition process no charge transfer to move the packets of charge within the sensor is needed. This allows a real-time optically addressed readout.

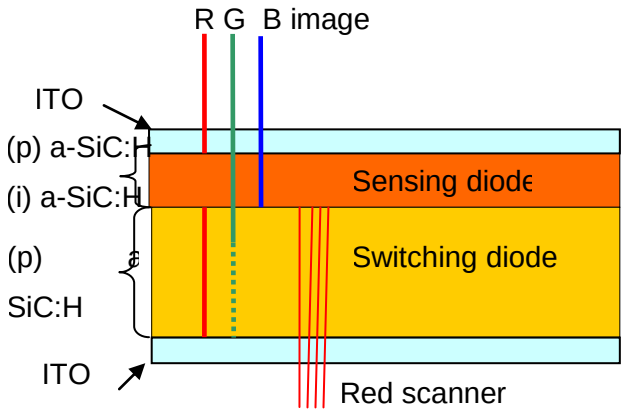

Figure 1.16 *Schematic of the optically addressed device optimized for colour recognition.*

The image and the scanner are incident on opposite sides. This approach simplifies the optical system as image and scanner have different optical paths. A low power solid state red laser ($\lambda_S = 650$ nm; Φ_S=10μW/cm^2) is used as scanner. The scanning beam position is controlled by a two axis deflection system. The line scan speed is close to 1 kHz. Two additional photodiodes provide the synchronization signals for the scanner position information needed for real time image reconstruction.

The current from the device is amplified and converted to digital format by a signal acquisition card installed in a computer. The data is stored as a matrix of photocurrent values (electronic image) which provide in real-time, the spatial information on the illumination conditions at the active area of the sensor (optical image). No image processing algorithms are used during the image reconstruction process.

4.4.2 Image and color recognition

In order to optimize the readout parameters (electrical bias) and to evaluate the sensors responsivity to different light pattern wavelengths, the photocurrent generated by the scanner was measured with a lock-in amplifier under different steady-state illumination conditions bias (Φ_L=200 μWcm^{-2}, λ_L=650 nm; 550 nm; 450nm) and displayed in Figure 1.17.

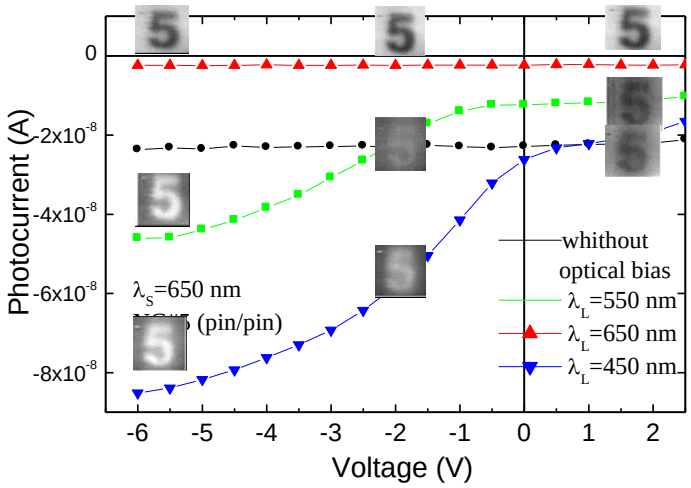

Figure 1.17 *Photocurrent as a function of the applied bias for sensors NC#4 (a) and NC#5 (b) in dark and under blue, green and red irradiation. (Φ_L=50μW/cm^2). The inserts show, at the acquired applied voltages, the images from the same RGB picture (5).*

The images, defined as the difference between the photocurrents with and without optical bias, are shown as inserts, at the acquired applied voltages. Here the same green, red and blue pictures (**5**) were projected, one by one, onto the front diode and acquired through the back one with a moving red scanner. The line scan frequency was close to 1 kHz and no algorithms were used during the image restoration process. For readout time of 1 ms the frame time, for a 50 lines image, is around 50 ms.

Results show that under red irradiation or in dark (without optical bias) the photocurrent generated by a red scanner is independent on the applied voltage. Under blue/green irradiation it decreases as the applied voltage changes from reverse to forward bias being higher under blue than under green irradiation. The main difference occurs in the green spectral range. It is interesting to notice that around -2 V the collection with or without green optical image are the same, leading to the rejection of the green image signal. Taking the signal without bias as a reference, and tuning the voltages to -2 V, the red and blue signal are high and opposite and the green signal suppressed allowing blue and red color recognitions. The green information is obtained under slight forward bias (+1 V), where the blue image signal goes down to zero and the red remains constant. Readout of 1000 lines per second was achieved allowing continuous and fast image sensing.

The combined integration of this information allows recording full range of colors at each location instead of just one color at each point of the captured image as occurs with the CCD image sensors. Readout of 1000 lines per second was achieved allowing continuous and fast image sensing, and colour recognition.

Figure 1.18 shows the digital image using as optical image a graded wavelength mask (rainbow) to simulate the visible spectrum in the range between 400 and 700 nm. For image acquisition two applied voltages were used to sample the image signal: + 1V and -6 V. The line scan frequency was close to 500 Hz. For a readout time of 2 ms the frame time for a 40 lines image takes around 80 ms. The algorithm used for image color reconstruction took into account that at -6 V the positive signals correspond to the blue/green contribution and the negative ones to the red inputs. The green information was extracted from the image signal sampled at +2 V, where the blue signal is almost suppressed (Figure 1.17) and the green and red signals are negative.

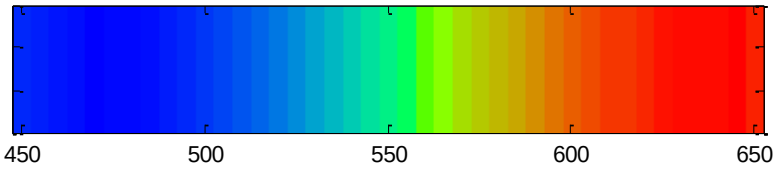

Figure 1.18 *Digital image representation of the rainbow picture acquired with device #2a.*

4.4.3 Optical bias intensity and color rejection

In order to tune correctly the applied voltage that leads to color rejection and to be sure that this value is independent on the image intensity, the photocurrent generated by the scanner (λ_S=650nm, 10 μWcm^{-2}) was measured with a lock-in amplifier under different steady-state illumination conditions (400nm<λ_L<750nm, 0<Φ_L<160 μWcm^{-2}). In these measurements the element sensor was uniformly illuminated through the switching diode with red pulsed light and the different optical bias were applied through the sensing one.

In Figure 1.19, for sensor NC#5, the scanner photocurrent dependence on the applied voltage is shown under blue (a), green (b) and red (c) optical bias and different flux irradiations (Φ_L).

Results confirm that for a wide flux range of the blue and green irradiation the amplitude of the image signal can be cancelled by tuning the applied voltage to an appropriated voltage (see arrows) allowing blue and green color rejection.

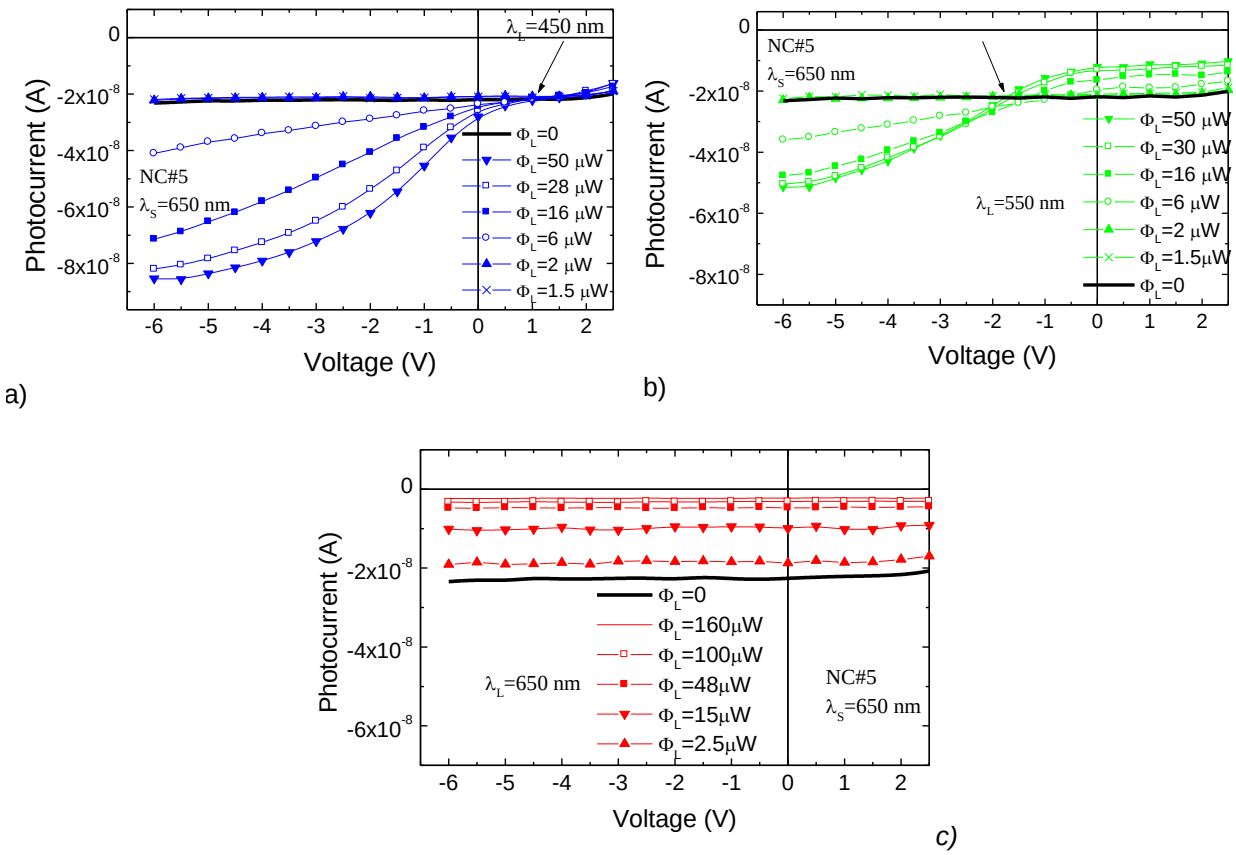

Figure 1.19 *Photocurrent as a function of the applied bias (in dark and under blue (a), green (b) and red (c) irradiation, ($0<\Phi_L<160\mu W/cm^2$).*

4.5 Summary

A wavelength-optimized optical signal and imaging device for colour and image recognition is presented. A trade-off between sensor configuration (thickness and absorption coefficient of the a-SiC:H/ a-Si:H sensing switching absorbers) and readout parameters (light pattern and scanner wavelength) was established in order to improve the resolution and the contrast of the image.

When a thin a-SiC:H sensing absorber, optimized for red transmittance and blue collection, is used the detector behaves itself as a filter giving information about the radiation wavelength and the position where it is absorbed. By sampling the absorption region with three different bias voltages it was possible to extract separately the RGB integrated information with a good rejection ratio. For both sensors readout of 1000 lines per second was achieved allowing continuous and fast image sensing, and color recognition.

5. Self bias effect in pinpin photodiodes

5.1 Numerical simulation

We used a device simulation program ASCA-2D [45] to analyze the potential profiles in the investigated structure. Typical values of band tail and gap state parameters for amorphous materials were used. The doping level was adjusted in order to obtain approximately the same conductivity of the layers as in the tested samples. In the films the optical band gaps were chosen in compliance with the obtained experimental values (Table 1.3). Band discontinuities were equally distributed over the valence and conduction band offsets ($\Delta E_v = \Delta E_c = 0.15$ eV).

5.2 Generation/recombination profiles

The photogeneration/recombination profiles used in this simulation are depicted in Figure 1.20 for a tandem p-i(a-SiC:H)-n/p-i(a-Si:H)-n -cell having, respectively, 200 nm and 1000 nm thick absorbers.

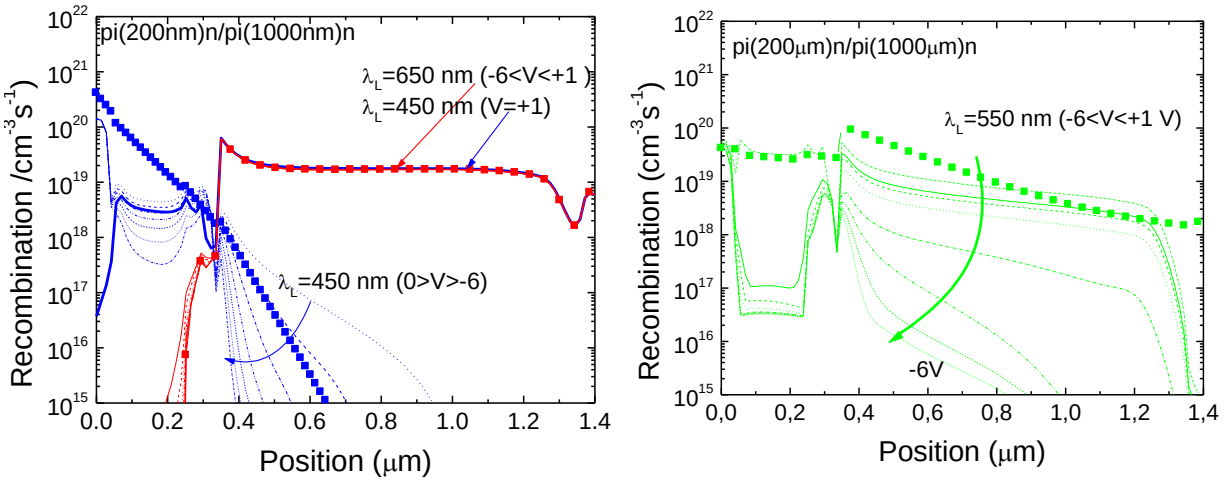

Figure 1.20 *Numerical simulation under different applied voltages and background light: generation (solid lines)/recombination (dash lines) rates.*

The thickness of the front diode and its optical gap was optimized for high conversation efficiency in the blue/green light and transparency of the red photons coming either from the image or from the scanner. In the a-SiC:H and a-Si:H absorbers an optical band gap of 2.1 eV and 1.8 eV and a thickness of 200 nm and 1000 nm were, respectively, chosen in compliance with the obtained experimental values. The

doping level was adjusted in order to obtain approximately the same conductivity of the layers as in the tested samples.

5.3 Electrical field profiles

Figure 1.21 a), b) and c) reports the simulated electric field profile within a #2-like structure under different optical bias wavelengths and for different values of the external electrical bias. In Figure 1.21d) it is displayed the electric field profile under thermo-dynamical equilibrium.

Simulated results show that the shallow penetration of the blue photons into the front diode, the deep penetration of the red photons into the back absorber or the decay of the green absorption across both, controls the internal electrical field. The balance between the electrical field adjustments due to the non uniform absorption throughout the structures depends on the generation/recombination ratio profiles at each applied voltage (Figure 1.20).

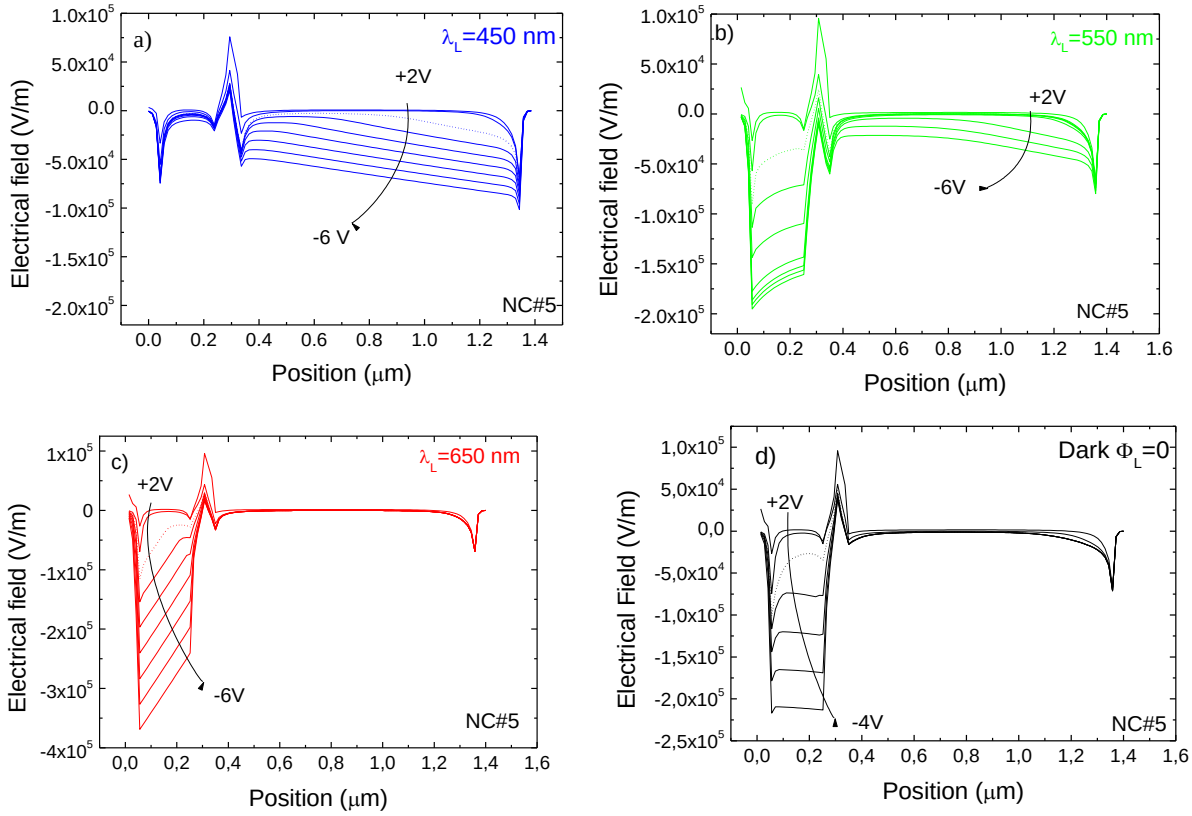

Figure 1.21 *Electric field profile within the p-i-n/p-i-n tandem structure for different values of the external electrical bias and for different wavelengths of impinging light: a) 650 nm; b) 550 nm ; c) 450 nm d) thermo-dynamical equilibrium (dark).*

When an external electrical bias (forward or reverse) is applied, it mainly influences the field distribution within the less photo excited sub-cell. When compared with the electric field profile under thermo-

dynamical equilibrium conditions, the field under illumination is lowered in the most absorbing cell, while the less absorbing one reacts by assuming a reverse bias configuration. Consequently, opposite behavior is observed under red and blue background light while under green light condition the redistribution of the field profile is balanced between the two sub-cells. If an additional intrinsic a-SiC:H layer is present in the back diode the green generation increases across the a-Si:H i'-layer reinforcing the forward self bias effect across it.

5.4 Potential profile

Figure 1.22 shows the simulated potential profiles at different applied voltages in dark (dash line) and under red (straight line), green (cross +) and blue (cross x) irradiation.

Results show that the application of an external electrical bias interferes mainly with the less absorbing cell. In the blue range as the reverse bias increases the potential drop across the non irradiated diode increases while in the front it remains almost negligible. In the red range the potential drop occurs across de front diode where no carriers are generated and remains negligible at the absorbing region. Due to the non uniform absorption across the back diode (Figure 1.21), under green irradiation, the potential drop is distributed across both diodes and balanced between the blue (in the back diode) and the red (in the front diode) behaviors.

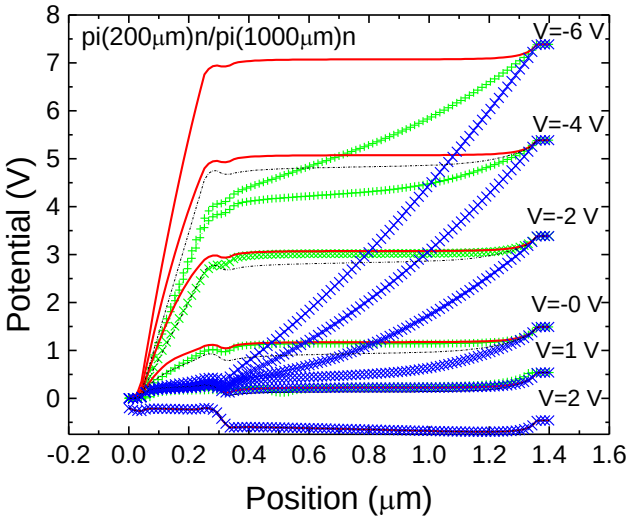

Figure 1.22 *Simulated potential profile under different applied voltages in dark and under red (λ_L, =650 nm) green and blue (λ_L, =450 nm) irradiation.*

Both the front and the back diodes are optically and electrically in series. Since light traverses through the sequence and is absorbed accordingly it wavelength (Figure 1.21) and since they are electrically in

series, the successive diodes should ensure that they each give the same current. Any diode whose current is bellow the other would have to reduce its bucking current and consequently voltage to try to catch up. This diode may even have to reverse bias itself in its efforts to get in line with the other. Consequently voltage is lost, if the diode is reverse biased, it becomes a power sink. This effect is what we call the self bias effect.

5.5 Self-bias effect in p-i-n/p-i-n structures

Taking into account the geometry of the structure, both the front and the back diodes are optically and electrically in series. The incident light traverses through the sequence and is absorbed accordingly to it wavelength. As the diodes are electrically in series, both must ensure that each supplies the same current:

$$I_1^{pin} = I_2^{pin} = I \qquad V = V_1 + V_2 \tag{1.9}$$

$$I_1^{pin} = I_{01}\left(\exp\left(\frac{V_1}{\eta V_T}\right)-1\right) - I_{ph1} \qquad I_2^{pin} = I_{02}\left(\exp\left(\frac{V_2}{\eta V_T}\right)-1\right) - I_{ph2} \tag{1.10}$$

Where V_1 and V_2 are the voltage drop across each diode and *V* the external voltage. $I_{0,1,2}$ and $I_{ph,1,2}$ are, respectively, the leakage and the photo currents, V_T the thermal voltage and η the ideality factor. Neglecting the series resistance and assuming: $I_1 = I_{01} + I_{ph1}$ and $I_2 = I_{02} + I_{ph2}$ the current across the structure will be given by:

$$I = 0.5\times\left(-(I_1+I_2)+\sqrt{(I_1-I_2)^2 + 4I_{o1}I_{02}\exp\left(\frac{V}{\eta V_T}\right)}\right) \tag{1.11}$$

$$V = \eta V_T \ln\frac{(I+I_1)(I+I_2)}{I_{01}I_{02}} \qquad V_1 = \eta V_T \ln\left(\frac{(I+I_1)}{I_{01}}\right) \qquad V_2 = V - V_1 \tag{1.12}$$

In Figure 1.23 it is displayed the trend of potential across the front (V_1) and back (V_2) diodes as a function of the applied voltage (V) and for different photocurrent values. The η, I_{01} and I_{02} parameters were obtained in compliance with the experimental I-V characteristics ($I_{01} < I_{02}$).

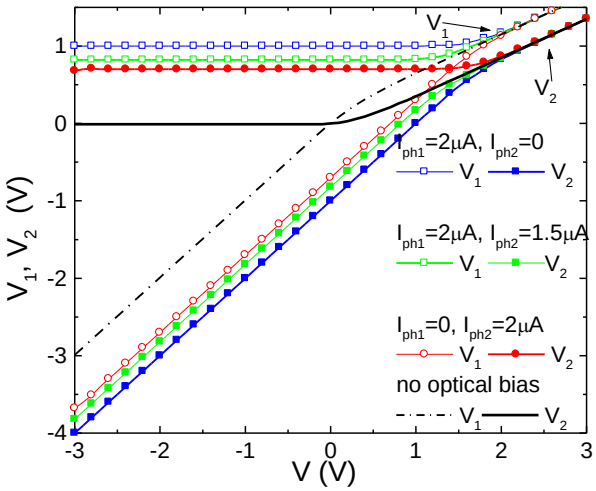

Figure 1.23 *Potential drop across front (V_1) and back (V_2) diodes as a function of the applied voltage (V) and for different photocurrent values.*

Data show that the potential across each diode depends on the level of irradiation of both front and back diodes. Opposite behaviors are observed under red (I_{ph1}=0, I_{ph2}≠0, Fig.21c) and blue (I_{ph1}≠0, I_{ph2}=0, Fig.21a) background light. Under green (I_{ph1}≠0, I_{ph2}≠0, Fig.21b) the trend depends on the I_{ph1}/I_{ph2} ratio, it approaches the blue trend if $I_{ph1}>I_{ph2}$, the red if $I_{ph1}<I_{ph2}$ and is the same as in dark if both photocurrent are balanced. Any diode whose current ($I_{1,2}^{pin}$) is below the other would have to reduce its net current (Equation 1.10) and consequently voltage (1. 12) in order to try to hold up. This diode may even have to reverse bias itself in its efforts to get in line with the other. This effect is what we call the self bias effect.

6. Conclusions

This chapter presents a photonic vision building which defines the thesis and guides our arguments and study. It demands innovative approaches to the exploration of problems and gaps to achieving the vision, involves a new methodology and a new conceptual approach. Detailed remote state of art is presented:

Single and stack pin heterojunctions based on a-SiC:H alloys were compared under different optical and electrical bias conditions and different readout techniques. Several applications are presented. A theoretical model gives insight on the physics of the device.

Results show that when a pinpin device is used as colour and image transducer it uses self- field induced depletion layers for light detection and a modulated laser beam for sequential readout. By sampling, at appropriated voltages, it is possible to extract separately the RGB integrated information

with good rejection ratio allowing continuous and fast colour recognition and image detection. Scans speeds up to 10^4 lines per second can be achieved without degradation in the resolution.

7. Reference

[1] R.C. Chittick, J.H. Alexander, H. F. Sterling, J. Electrochem. Soc. 116, 77 (1969).

[2] W. E. Spear and P. G. Le Comber, Solid State Commum. 17, 1193 (1975).

[3] D. E. Carlson and C. R. Wronski, Applied Physics Letters 33 (1976) 935.

[4] S. M. Sze, Physics of the semiconductor devices, 2nd Ed.; New York: John Wiley, (1981).

[5] J. Wilson, J. Hawkes. Optoelectronics, an Introduction. London: Prentice Hall, 1998.

[6] Inan Chen, J.Appl. Phys., 64 (1988) 2224.

[7] J. Torkel, Wallmark, Proc. IRE, 43 (1956) 474.

[8] E. Fortunato, M. Vieira, G. Lavareda, L. Ferreira, and R. Martins, J. of Non-Crystalline Solids, 164-166 (1993) 797.

[9] M. Vieira, E. Morgado, A. Maçarico, S. Koynov, R. Schwarz, Vacuum, 52 (1999) 67.

[10] J. W. Horton, R. V. Mazza, and H. Dym Proc. IEEE, 52 (1964) 1513.

[11] P. W. Fry, J. of Physics E: Scientific Instruments, 8 (1975) 337.

[12] G. S. Hobson, Proc. IEEE, 124 (1977) 925.

[13] S. Chakrabarti, O. H. W. Siegmund, and J. Hecht, Proc. SPIE 834 (1987) 222.

[14] C. Jonsson, Analog Integrated circuits and Signal Processing, 4 (1993) 37.

[15] G. J. Michon, and H. K. Burk, IEEE Solid-State Circuits Conf. Digest (New York: Lewis Winner), (1974) 26.

[16] M. A. Schuster, and G. Strull, IEEE Trans. Electron Dev. ED 13 (1966) 907.

[17] I. Chen, J. Appl. Phys. 64 (1988) 2224.

[18] M. Vieira, Appl. Phys. Lett. 70 (1997) 220.

[19] M. Vieira, A. Fantoni, S. Koynov, and R. Schwarz, Thin Solid Films, 296 (1997) 164.

[20] F. Sousa, J. Martins, M. Fernandes, A. Maçarico, R. Schwarz, and M. Vieira, J. of Non-Crystalline Solids, 266-269 (2000) 1228.

[21] M. Vieira, M. Fernandes, J. Martins, P. Louro, A. Maçarico, R. Schwarz, and M. Schubert, In Amorphous and Heterogeneous Silicon Thin Films- 2000, Mat. Res. Soc. Symp. Proc., S. Francisco (USA), 609 (2000) A14.2.

[22] L. B. Henke, J. Liesegang, and S. D. Smith, Phys. Rev., 19 (1979) 3004.

[23] M. Fernandes, M. Vieira, J. Martins, P. Louro, A. Maçarico, R. Schwarz, and M. Schubert, Thin Solid Films 383 (2001) pp. 65-68

[24] C. Koch, M. Ito, M. Schubert, and J. H. Werner, Mat. Res. Soc. Symp. Proc, 575 (1999) 749.

[25] M. Vieira, M. Fernandes, J. Martins, P. Louro, A. Maçarico, R. Schwarz, and M. Schubert, IEEE Sensors Journal, 2, August 2001.

[26] M. Vieira, M. Fernandes, P. Louro, Y. Vygranenko, R. Schwarz, and, M. Schubert, Mat. In Amorphous and Heterogeneous Silicon Thin Films- 2001, Mat. Res. Soc. Symp. Proc., (S. Francisco, April 17-20 USA), 664 (2001) A18.5.

[27] M. Vieira, P. Louro, M. Fernandes, A. Fantoni , Sensor and Actuators A 114/2-3 (2004), pp. 219-223.

[28] Digital television, Edited By C. P. Sanbdbank, John Wiley & Sons (1990)..

[29] R.F. Wolffenbuttel, IEEE electron device letters, Vol. EDL-8, No. 1 (1987) pp.13-15.

[30] K.C. Chang, Chun-Yen Chang, Y.K. Fang and S.C. Jwo, IEEE electron device letters, Vol. EDL-8,No. 2 (1987) pp.64-65.

[31] Y.K. Fang, S.B. Hwang, Y.W. Chen, and L.C. Kuo, IEEE electron device letters, Vol. EDL-8,No. 2 (1987) pp.64-65.

[32] F. Palma in “Technology and Applications of Amorphous Silicon”, Edited by R. A. Street, Spring-Verlag, Berlin Heidelberg New York (2000).

[33] M. Vieira, M. Fernandes, A. Fantoni, P. Louro, and R. Schwarz, Mat. Res. Soc. Symp. Proc., Editors: Cohen, Abelson, Matsumura, Robertson, 715 (2002) pp.695-700.

[34] H.K. Tsai, S.C. Lee, IEEE electron device letters, EDL-8, (1987) pp.365-367. .

[35] G. de Cesare, F. Irrera, F. Lemmi, F. Palma, IEEE Trans. on Electron Devices, Vol. 42, No. 5, May 1995, pp. 835-840.

[36] A. Zhu, S. Coors, B. Schneider, P. Rieve, M. Bohm, IEEE Trans. on Electron Devices, Vol. 45, No. 7, July 1998, pp. 1393-1398.

[37] M. Topic, H. Stiebig, D. Knipp, F. Smole, J. Furlan, H. Wagner, J. Non Cryst. Solids 266-269 (2000) 1178-1182.

[38] M. Mulato, F. Lemmi, J. Ho, R. Lau, J. P. Lu, R. A. Street, J. of Appl. Phys., Vol. 90, No. 3 (2001), pp. 1589-1599.

[39] M. Vieira, M. Fernandes, J. Martins, P. Louro, R. Schwarz, M. Schubert, IEEE Sensor Journal, 1, no.2 (August, 2001) pp. 158-167.

[40] M. Vieira, M. Fernandes, P. Louro, R. Schwarz, M. Schubert, J. Non Cryst. Solids 299-302 (2002) pp.1245-1249.

[41] M. Vieira, A. Fantoni, M. Fernandes, P. Louro, I. Rodrigues. Mat. Res. Soc. Symp. Proc 762@2003 A.18.13.

[42] P. Louro, M. Vieira, Yu. Vygranenko, A. Fantoni, M. Fernandes, G. Lavareda, N. Carvalho, Mat. Res. Soc. Symp. Proc., 989 (2007) A12.04.

[43] P. Louro, M. Vieira, Yu. Vygranenko, M. Fernandes, R. Schwarz, M. Schubert, Applied Surface Science 184, 144-149 (2001).

[44] M. Vieira, M. Fernandes, P. Louro, A. Fantoni, Y. Vygranenko, G. Lavareda, C.Nunes de Carvalho, Mat. Res. Soc. Symp. Proc., Vol. 862 (2005) A13.4.

[45] A. Fantoni, M. Vieira, R. Martins, Mathematics and Computers in Simulation, Vol. 49. pp. 381-401 (1999).

Chapter II

Voltage controlled amorphous Si/SiC devices as optical WDM in the visible spectrum

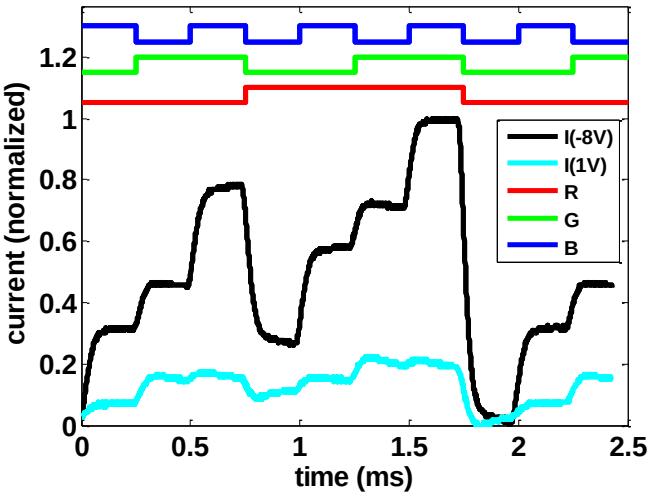

II Voltage controlled amorphous Si/SiC devices as optical WDM in the visible spectrum

1 Introduction

With increasing data traffic load in telecommunications networks, wavelength division multiplexing (WDM) is essential for network capacity and flexibility.

In a simple WDM system the information to transmit is coded into an optical signal assigned to a certain wavelength. The multiplexer, placed before the transmission medium, integrates every wavelength into the waveguide. After being transmitted through the transmission medium, the combined optical signals are received by the demultiplexer at the receiving end that splits the polychromatic light into its monochromatic components allowing therefore the recovery of the original signal. These components are well known for infrared telecom systems [1], but for a different transmission window technology must be developed completely new. [2, 3]. For WDM two key-functions are indispensable, a multiplexer mode and a demultiplexer mode.

ISEL group has developed, in the past, an optical image sensor; the Laser Scanned Photodiode [4, 5, 6, see chapter I] and is presently developing an optical WDM device [7, 8]. Several structures are possible, single and stacked, sharing the advantage of not needing special photolithography techniques for patterning or complex design as required by the active matrix approach, resulting in low cost and high reliability devices. In these devices the spectral sensitivity in the visible range is controlled by the external applied voltage. Thus, proper tuning of the device sensitivity along the visible spectrum allows the recognition of the absorbed light wavelength and intensity, and consequently the identification of the RGB components of an input signal [9, 10, 11, 12, 13, 14, 15]. As we have just seen in the overview of amorphous silicon material properties, it has been used for light detection in color and image transducer. Here, it can be reconfigured to perform those different optoelectronic logic functions. A novel SiC based tunable photodetector, which enables the filtering function with the detector itself and has the potential to be rapidly biasing tuned. It filter, store and transport the photogenerated carriers, keeping its memory (color, intensity and frequency) without the need to add any separate optical pre-amplifier or typical existing tunable filter used for wavelength selection. Tunable photodetectors that could programmably discriminate the narrowly spaced channels in such WDM system would be very useful for reconfiguring the network.

A previous proposal for voltage-controllable wavelength selective optical switching based on shifting between positive and negative electrically bias, in the visible range, is analysed, The color discrimination was achieved by ac photocurrent measurement under different externally applied bias. Experimental data on spectral response analysis and current –voltage characteristics are reported. To support the wavelength selective behaviour, a theoretical analysis and an electrical simulation procedure will be performed, and experimental and simulated results will be compared in chapter IV to

validate the use of multilayered structures based on amorphous silicon technology as a solution in WDM technique for information transmission and decoding in the visible range. Other technical issues related to the attenuation of the signal and the light-to-dark sensitivity of the optical device will also be analysed.

The transducers are also optimized for the detection of the fluorescence resonance energy transfer between Cyan Fluorescent Protein (CFP) and Yellow Fluorescent Protein (YFP). The ratio between both fluorescence pairs correlates with the distance between the fluorophores. If the peak of the fluorescence signal is in the cyan region (475-495 nm) it means the two fluorophores are far apart. On the other hand if the peak is in the yellow (560-586 nm) region it means they are within close distance (there is transfer of energy between fluorophores). The sensor was optimized to distinguish between these two situations. To simulate the FRET pairs (CFP, YFP) two modulated Cyan (470nm), and Yellow (580 nm) input monochromatic beams were used as input channels.

2 WDM based on amorphous technology

2.1 Device configuration and operation

2.1.1 Configuration

The device design attempts to optimize the most important performance attributes which are the color sensitivity, the transmission rate and the dynamic range. In this configuration full color filtering is attempted based on spatially separated absorption of different wavelengths.

The WDM device is a double heterostructure produced by PECVD (Plasma Enhanced Chemical Vapor Deposition) as depicted in Figure 1.1 and in Figure 1.14 (Chapter I, §4.2). Deposition conditions are described elsewhere ([16], and Chapter I, §4.2) The thickness and the absorption coefficient of the front photodiode are optimized for blue collection and red transmittance, and the thickness of the back one adjusted to achieve full absorption in the greenish region and high collection in the red spectral one. As a result, both front and back diodes act as optical filters confining, respectively, the blue and the red optical carriers, while the green ones are absorbed across both [17]. On the top of the figure it is displayed the recombination profiles (straight lines) under red (λ_R =650 nm) green (λ_G =550 nm) and blue (λ_B =450 nm) optical bias and different electrical bias (-6V<V<0V). The generation profiles are also shown (symbols). We used a device simulation program ASCA-2D [18] to analyze the profiles in the investigated structures (Chap. 1, §5.2).

The WDM device consists of a glass/ITO/a-SiC:H (p-i-n) photodiode which faces the incoming modulated light followed by an a-SiC:H(-p) /a-Si:H(-i')/a-SiC:H (-n')/ITO heterostructure that allows the optical readout. By reading out, under different applied bias, the total photocurrent generated by all the

incoming optical carriers the information (wavelength, modulation frequency) is multiplexed or demultiplexed and can be transmitted or recovered again [19].

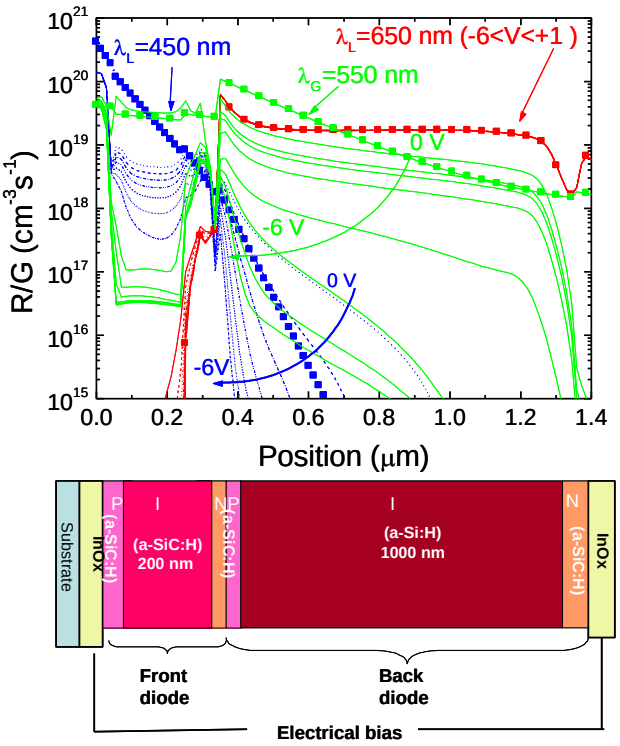

Figure 2.1 *a-SiC:H WDM device configuration. On the top the recombination profiles (straight lines) under red (λ_R =650 nm) green (λ_G =550 nm) and blue (λ_B =450 nm) optical bias and different applied voltages (-6V<V<0V). The generation profiles are also shown (symbols).*

2.1.2 WDM working principle

In Figures 2.2 and 2.3 the device configuration is depicted in both multiplexing and demultiplexing modes. Here, multiple monochromatic (Figure 2.2) or a single polychromatic (Figure 2.3) beams are directed to the device where they are absorbed, accordingly to each wavelength, giving rise to a time and wavelength dependent electrical field modulation across it [20] (Chap. I, §5.3).

In the multiplexing mode the device faces the modulated light incoming together from the fibers, each with a wavelength in a specific range (R, G, B channels). The combined effect of each input channel is then converted to an electrical signal via the WDM device (Figure 2.2) keeping the memory of the input channels (wavelength and bite rate) [21, 22].

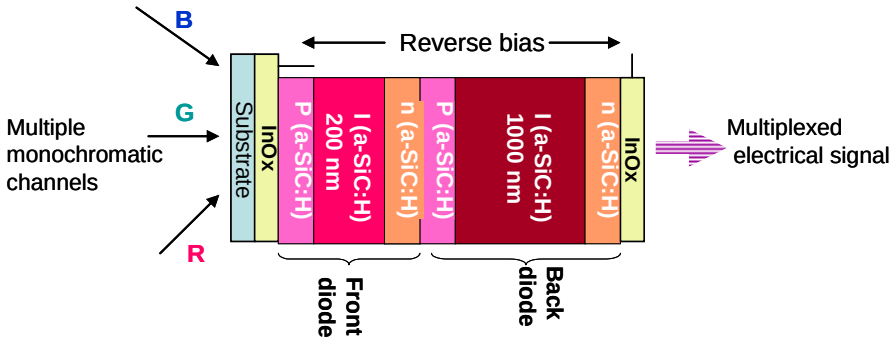

Figure 2.2 *WDM device configuration(multiplexing mode).*

In the demultiplexing mode a polychromatic light beam (mixture of different wavelength) is projected onto the device and the signal measured at appropriated applied voltages. Here, the spectral sensibility of the device is voltage controlled allowing the recognition of the RGB channels (Figure 2.3).

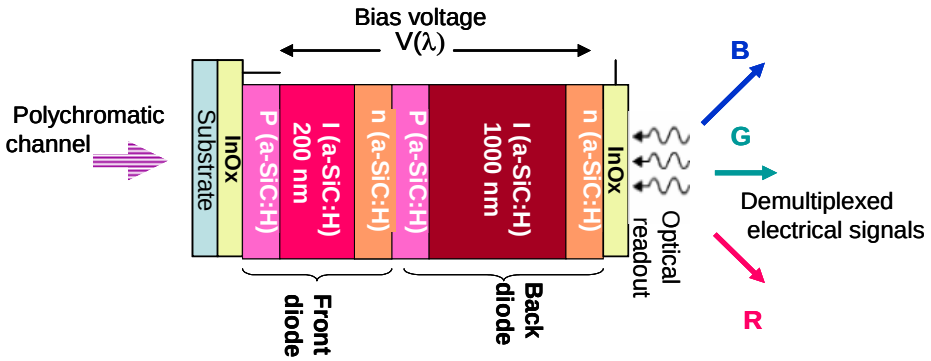

Figure 2.3 *WDM device configuration (demultiplexing mode).*

2.2 Optical characterization

2.2.1 Spectral response

The devices were characterized through spectral response measurements (400-800 nm), under different modulated light frequencies (15 Hz to 2 KHz) and electrical bias (-10V to +3V) [23, 24, 25, 26]. In Figure 2.4a it is displayed, under reverse bias, the spectral photocurrent at different frequencies and, in Figure 2.4b, the trend with the applied voltages is shown at 2 KHz.

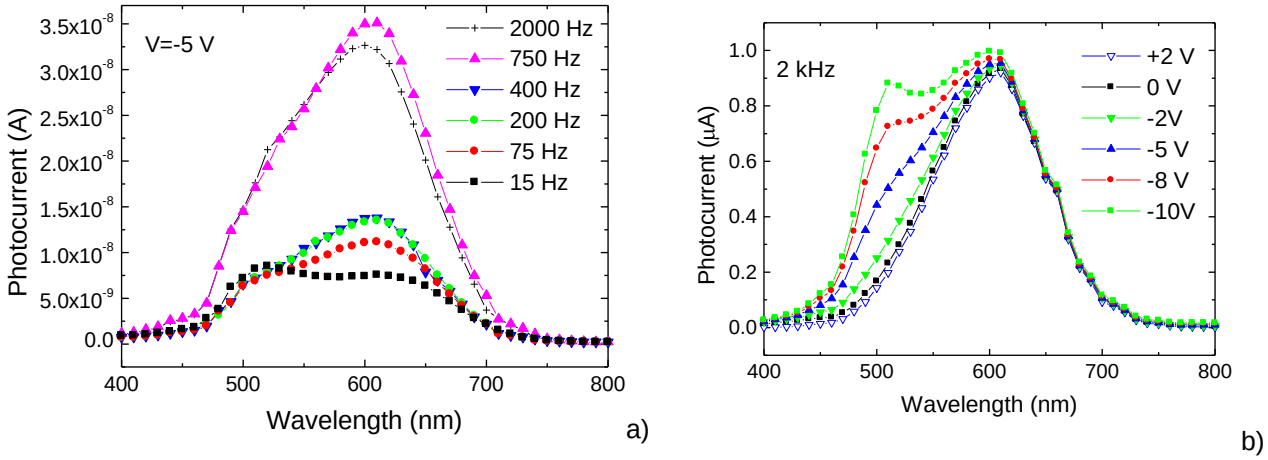

Figure 2.4 *Spectral photocurrent under: a) reverse bias (-5V) and different frequencies; b) different applied voltages and at a modulated frequency of 2000 Hz.*

Different trends with the frequency are observed. Under reverse bias and low frequencies (f<400Hz), the spectral response increases with the frequency in the reddish region while in the blue/green spectral regions the photocurrent remains constant (Figure 2.4a). For higher frequencies (f>400Hz) the spectral response does not depend on the modulated light frequency and, as the applied voltage changes from forward to reverse (Figure 2.4b), the blue/green spectral collection is enlarged while the red one remains constant.

2.2.2 Voltage controlled sensitivity

In Figure 2.5a it is displayed the measured spectral photocurrent and in Figure 2.5b the *ac* current-voltage characteristics under illumination are shown. In this last measurement three modulated monochromatic lights: R (λ_R=626 nm); G (λ_G=520 nm) and B (λ_B=470 nm), and their polychromatic combinations; R&G (Yellow); R&B (Magenta); G&B (Cyan) and R&G&B (White) illuminated separately the device and the photocurrent was measured as a function of the applied voltage. As light sources it were used ultra-bright LEDs with a 20 nm spectral bandwidth. The output optical power was adjusted for each independent wavelength at 19 μW/cm^2.

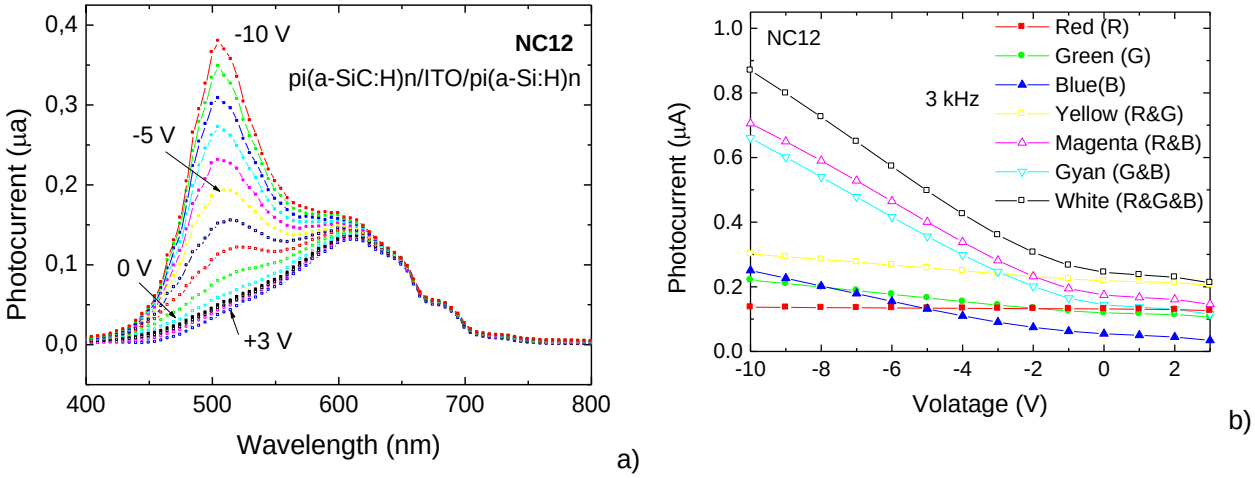

Figure 2.5 *a) Spectral response at different applied bias. b) Photocurrent voltage characteristics under different light wavelengths.*

Data from Figure 2.5 confirms that, as the applied voltage changes from forward to reverse the blue/green spectral collection is enlarged while the red one remains constant (a). The photocurrent under red modulated light (b) is independent on the applied voltage while under blue, green or combined irradiations it increases with the reverse bias. If the blue spectral component is present (B&R, B&G), a sharp increase with the reverse bias is observed.

Under positive bias the blue signal becomes negligible and the R&B, the G&B and the R&G&B multiplexed signals overlap, respectively with the R, the G and the R&G signals. This behavior illustrates, under forward bias, the low sensitivity to the blue component of the multiplexed signal. It is interesting to notice that under reverse bias the green signal has a blue-like behavior, while under forward bias its behavior is red-like confirming the green photons absorption across both front and back diodes.

In Figure 2.6 (a, c) the spectral photocurrent under different electrical bias and its trend (b, d) with the applied voltage, under specific wavelengths, are displayed separately for the front, p-i' (a-SiC:H)-n, and back p-i (a-Si:H)-n, photodiodes. Here, the internal transparent ITO contact was used to apply the voltage (See Chap. I Figure 1.14).

In Figure 2.6e the spectral photocurrent, under different electrical bias, is compared for the front (p-i' (a-SiC:H)-n) and the back photodiodes (p-i (a-Si:H)-n).

Results confirm that the front and back photodiodes act, separately, as optical filters. The front diode, based on a-SiC:H heterostructure, cuts wavelengths higher than 550 nm while the back one, based on a-Si:H, cuts the ones lower than 500 nm. Each diode, separately, presents the typical response of single p-i-n cells with intrinsic layers based on a-SiC:H or a-Si:H materials, respectively. As the current across the device has to remain the same, in the stacked configuration (2. 5a), it is clearly observed the influence of both front and back diodes modulated by its series connection through the internal n-p junction.

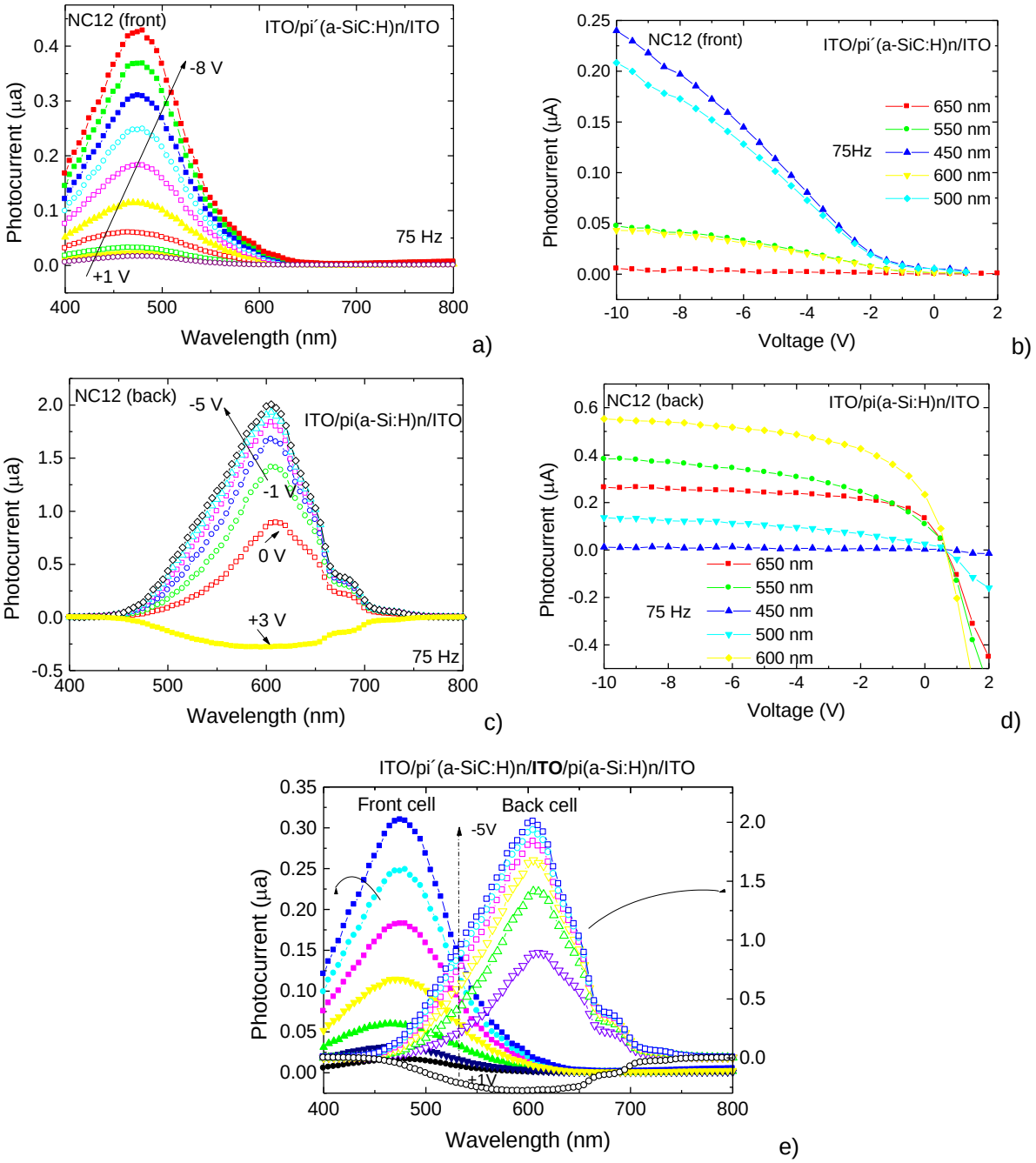

Figure 2.6 *Spectral photocurrent under different applied bias (a, c, e) and its trend with the applied voltage, at different wavelengths (b, d), for the front, p-i' (a-SiC:H)-n, and back, p-i (a-Si:H)-n.*

2.2.3 Selective wavelength discrimination

In Figure 2.7 it is displayed, the spectral photocurrent under negative (-10V) and positive (+3V) external bias and its differences (symbols), the dash lines show the multi peak curve fit of the photocurrent measured at -10V.

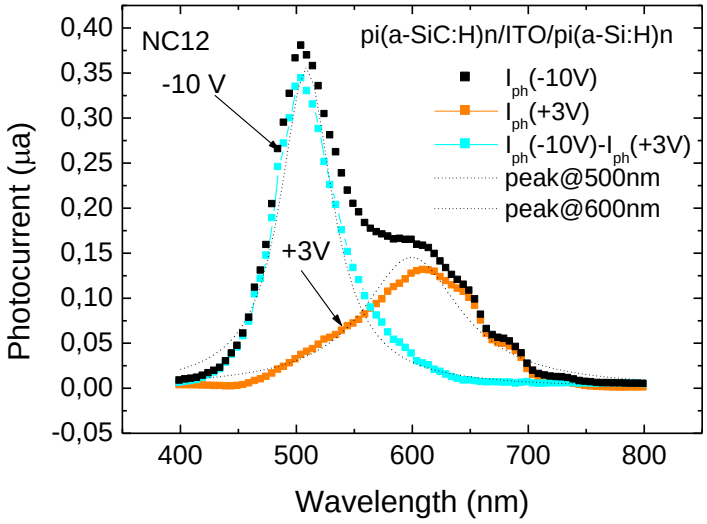

Figure 2.7 *Spectral response at under negative and positive electrical bias.*

Under negative bias the contribution of both front and back diodes (dotted lines) is clear. Two peaks centered, respectively at 500 nm and 600 nm are observed**.** Under positive bias, the response around 500 nm disappears while the one around 600 nm remains constant as expected from Figure 2.5a. So, under forward bias the device becomes sensitive to the red region and under reverse bias to the blue one working as a selective optical device in the visible range.

2.2.4 Frequency dependence

In Figure 2.8 the ac current-voltage characteristics under different wavelengths: 626 nm (R); 470 nm (B); 626 nm & 470 nm (R&B), and at the low and high frequency regimes is displayed.

Results show that in both regimes, under red modulated light, the collection efficiency remains always independent on the applied voltage being higher at high frequencies, as expected from Figure 2.4. Under blue irradiation the collection does not depend, significantly, on the frequency regime. Those effects suggest different capacitive effects in both front and back diodes as it will be analyzed in the next chapters.

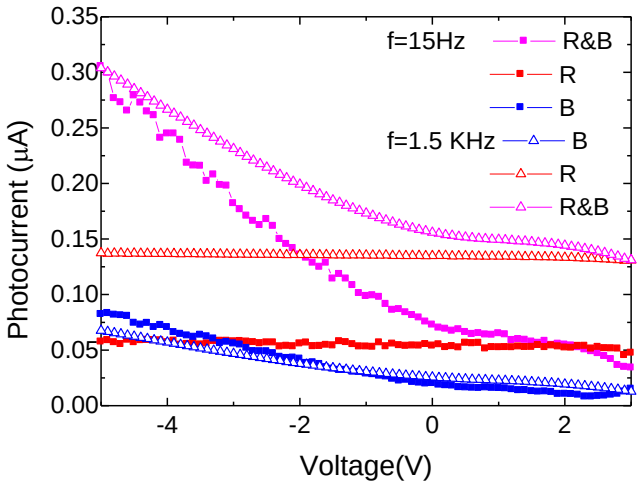

Figure 2.8 *ac IV characteristics under R (λ_L =626 nm); B(λ_L =470 nm), R(λ_L =626 nm) & B (λ_L =470 nm) modulated light and different light frequencies (15Hz;1.5KHz).*

3 Wavelength division multiplexing device

3.1 Voltage controlled device

The effect of the applied voltage on the output transient multiplexed signal is analyzed. To readout the combined spectra, the generated transient photocurrent due to the simultaneous effect of two (λ_R =626 nm, λ_B =470 nm) and three (λ_R =626 nm, λ_G =520 nm, λ_B =470 nm) pulsed monochromatic channels was measured, under different applied voltages.

The results are displayed, respectively, in Figure 2.9a and in Figure 2.9b. The input wavelength channels are superimposed in the top of the figures to guide the eyes. The reference level was assumed to be the signal when all the input channels were OFF (dark level). In Figure 2.9a the red frequency was 1.5 KHz and the blue one half of this value while in Figure 2.9b the ratios between the three frequencies were always one half.

In Figure 2.9c the dependence of each pulsed single channel with the applied voltage is also displayed. The transmission spectra of the Red, Blue and Green test signals (channels) are depicted in Figure 2. 9d.

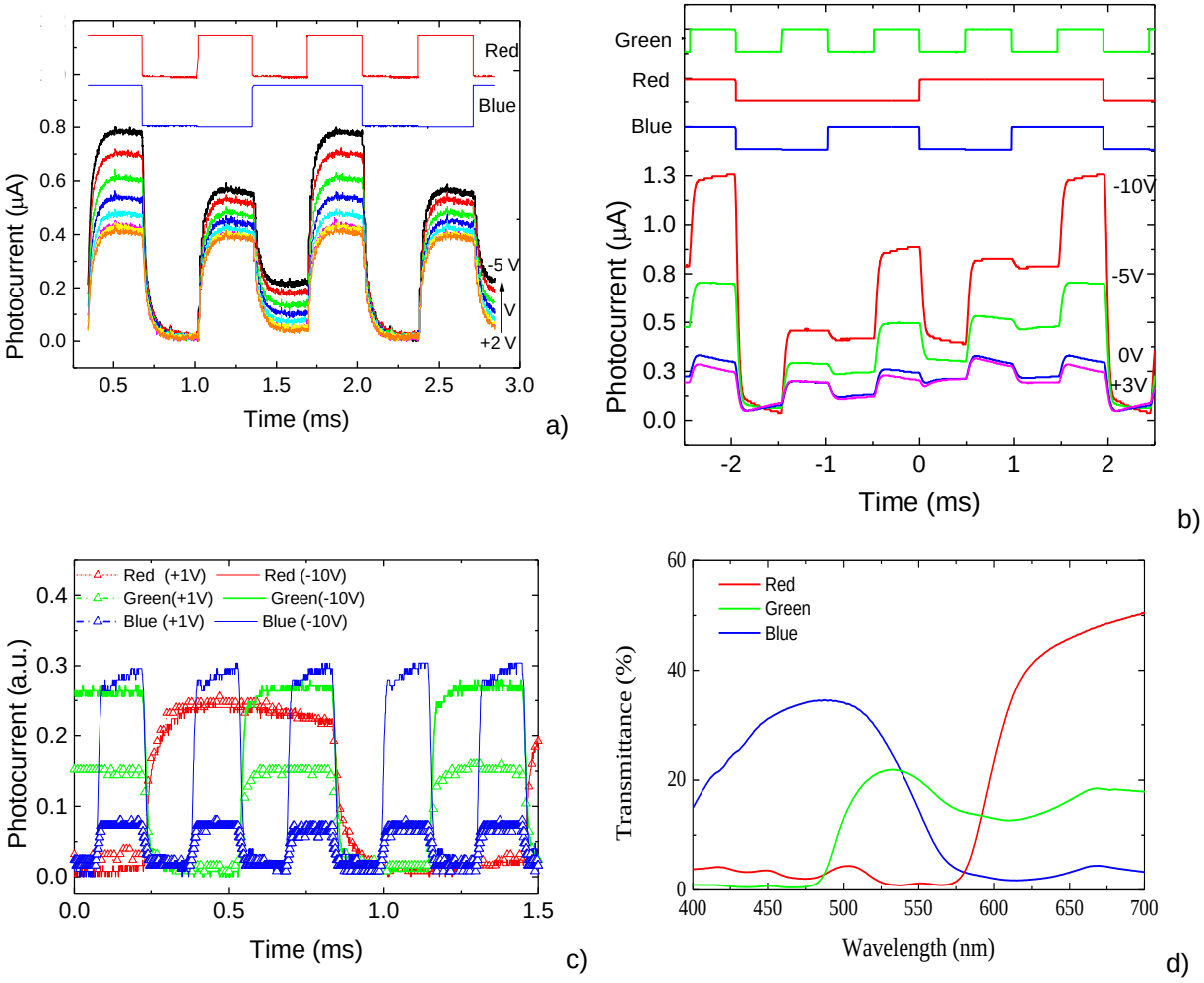

Figure 2.9 *Transient multiplexed signals at different applied voltages and input wavelengths: a) R&B ($\lambda_{R,B}$=626nm, 470 nm). The highest frequency of the input signal is 1.5 kHz. b) R&G&B ($\lambda_{R,G,B}$=626 nm, 524 nm, 470 nm). The highest frequency of the input signal is 1 kHz. c) dependence of the input colour channel with the applied voltage d) Transmission spectra of used red, green and blue signals.*

As expected from Figures 2.4 and 2.5 the red signal remains constant while the blue and the green decrease as the voltage changes from negative to positive. The lower decrease in the green channel when compared with the blue one is related with to the lower bias dependence of the back diode where a part of the green photons is absorbed.

Data show that the multiplexed signal depends on the applied voltage and on the wavelength and transmission rate of the each input channel. Under reverse bias, there are always four (Figure 2.9a) or eight (Figure 2.9b) separate levels depending on the number of input channels. The highest level appears when all the channels are ON and the lowest if they are OFF. Furthermore, the levels ascribed to the mixture of two input channels (R&B, R&G, G&B) are higher than the ones due to the presence of only one (R, G, B). The step among them depends on the applied voltage and channel wavelength. As expected from Figure 2.4 and 2. 5, as the reverse bias increases the signal exhibit a sharp increase if

the blue component is present. Under forward bias the blue signal goes down to zero, so the separated levels are reduced to one half.

In Figure 2.10a it is displayed the multiplexed signals (solid lines) due to two input channels in the low and high frequency regimes. The transient signals were acquired at different applied voltages (-5V <V<+2V). The blue ($\lambda_{L=}$470 nm; dotted line) and the red (λ_L =626 nm; dash line) input channels are superimposed to guide the eyes across the monochromatic R and B input channels. The red signal frequency was 1.5 KHz and the blue one was half of this value.

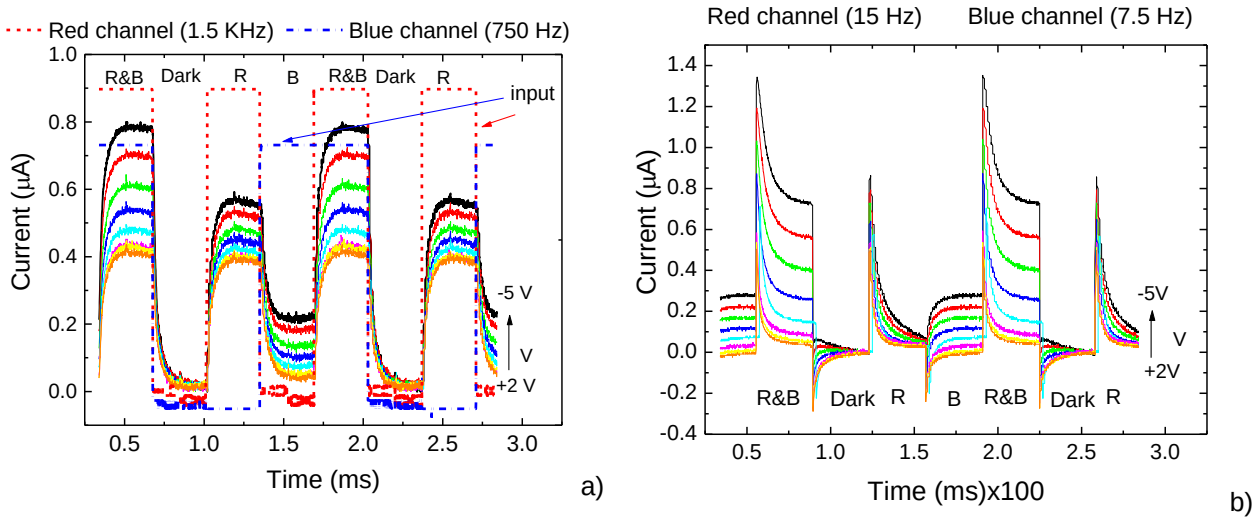

Figure 2.10 *Wavelength division multiplexing (solid lines) at different applied voltages, obtained using the WDM device: a) High frequency regime. The blue (dotted blue line) and the red (dash-dot red line) guide the eyes into the input channels; b) Low frequency regime.*

In Figure 2.10b the same output signals of Figure 2.10a are shown, but using for the input frequencies two orders of magnitude lower.

Both figures show that the multiplexed signal depends on the applied voltage and on the frequency regime of the input channels. Results show also that in the high frequency regime (Figure 2.10a) the multiplexer acts as a charge integrator device while in the low frequency regime it works as a differentiator. In the high regime, the output signals (multiplexed signals) show the potentiality of using the device for WDM applications since it integrates every wavelength to a single one retaining the input information.

3.2 Bias sensitive multiplexing technique

Figure 2.11 displays the photocurrent signal obtained with the WDM device under single and combined modulated light bias: red (R: 626 nm), green (G: 524 nm) and blue (B: 470nm) from the glass side. The generated photocurrent is measured under negative (-8V; solid arrow) and positive (+1V, dotted arrow) bias to readout the combined spectra. The light modulation frequency of each channel was chosen to

be multiple of the others to ensure a synchronous relation of ON-OFF states along each cycle. For each independent wavelength, the output optical powers were adjusted to give different signal magnitudes at -8V (solid arrows). The correspondent photocurrent signals at +1V are also displayed (dotted arrows). The reference level was assumed when all the input channels were OFF.

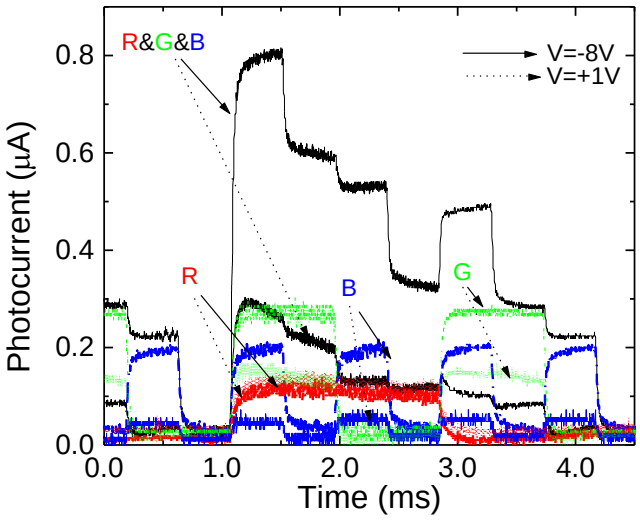

Figure 2.11 *Multiplexed signals obtained under reverse (solid arrow) and forward (dotted arrow) bias using single (R, G and B) and combined (R&G&B) optical bias of different wavelengths.*

As it was expected from Figure 2.9b, under negative bias, there are eight separate levels while under positive bias they were reduced to one half. Also, the highest level appears when all the channels are ON and the lowest if they are OFF. Under forward bias, the front photodiode becomes blind to and the blue component of the combined spectra falls into the dark level, allowing the tuning of the red and green input channels.

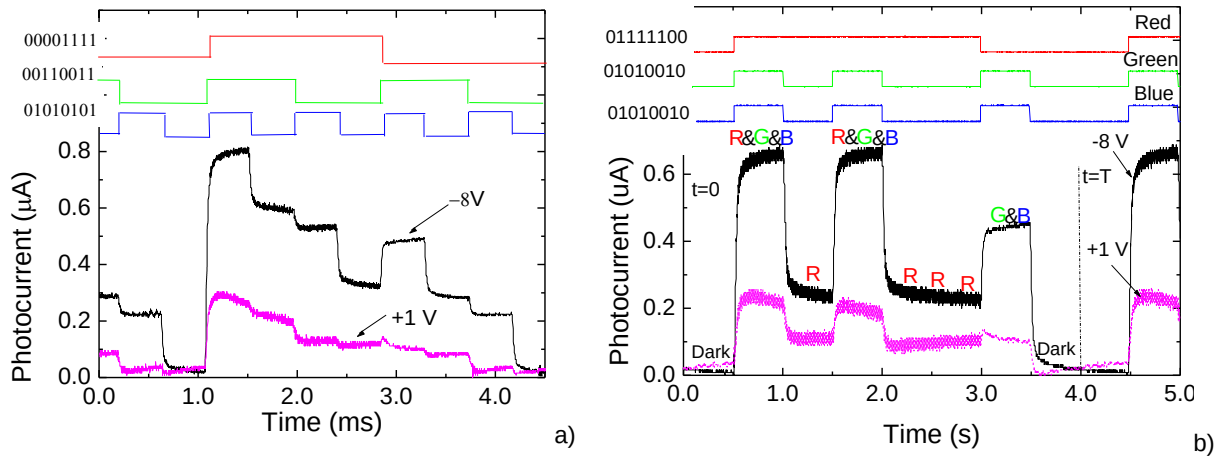

Figure 2.12 *Multiplexed signals under negative and positive bias using two different bit sequences: a) R [00111100], G [01010010], B[00110011]; b): R [01111100], G [01010010], B[01010010]. On the top, the optical signal used to transmit the information guide the eyes on the different ON-OFF states.*

In Figure 2.12 it is compared the multiplexed signals, under reverse and forward bias, obtained with two RGB bit sequences and the same bit rate (2000 bps).

In the bit sequence of Figure 2.12a there is a synchronous relation of ON-OFF states along each cycle. The photocurrent under reverse bias, exhibits the expected eight different levels that correspond each to different optical bias states. As the electrical bias goes from reverse to forward the signal amplitude decreases and the levels of the threshold photocurrent associated to each optical state become closer and less defined showing the extinction of the photocurrent caused by the short wavelength optical signals. This mechanism can be used for the identification of the input channels using the photocurrent signal obtained under forward and reverse signals and comparing the magnitude of the variation in each optical state. In the input sequence of Figure 2.15b the blue and the green channels transmit the same information, and thus the thresholds assigned to the single green or blue channel ON (G or B) and their combination with the red (R&G, R&B) do not appear in the multiplexed signal that contains only four photocurrent levels: R&G&B, G&B, R and Dark. However as under forward bias the the front photodiode becomes blind to blue component of the combined spectra falls into the dark level, allowing the tuning of the red and green input channels.

3.3 Influence of the bit rate

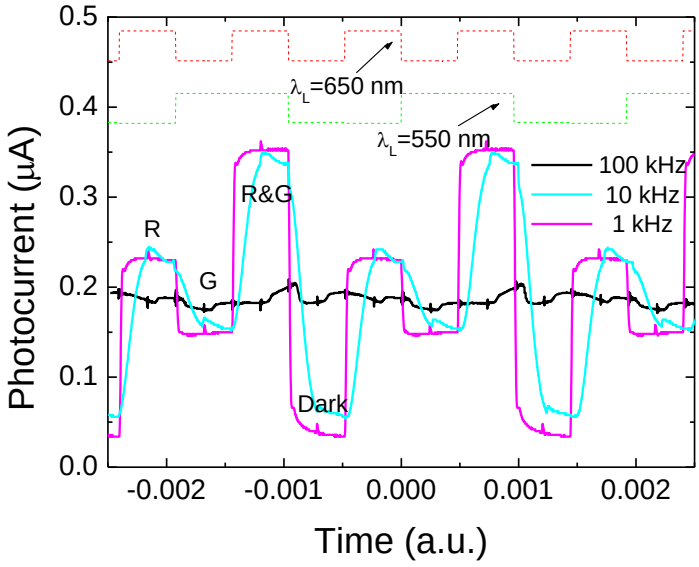

Figure 2.13 *Wavelength division multiplexing (solid lines) at – 5 V under different values of the modulation light frequency. The red and the green dashed lines guide the eyes into the input channels.*

In Figure 2.13 the acquired signals (solid lines) due to the simultaneous presence of two input channels, respectively λ_L=626 and λ_L=524 nm, under different values of the modulation light

frequencies (1k Hz, 10 kHz and 100 kHz), at –5 V are shown. The superimposed red and green dashed lines correspond to different input channels, and are displayed just to illustrate the different ON-OFF states of the light bias.

The multiplexed signal shows that in each cycle it is observed for the different frequencies, the presence of the same four levels. The highest occurs when both red and green channels are ON (R&G) and the lower when both are OFF (dark). The green level (G) appears if the red channel is OFF and is lower then the red level (R) that occurs when the green channel is OFF. This behavior is observed even for high frequencies although the measured current magnitude is reduced. So the sensitivity of the device decreases with the increase of the bit rate.

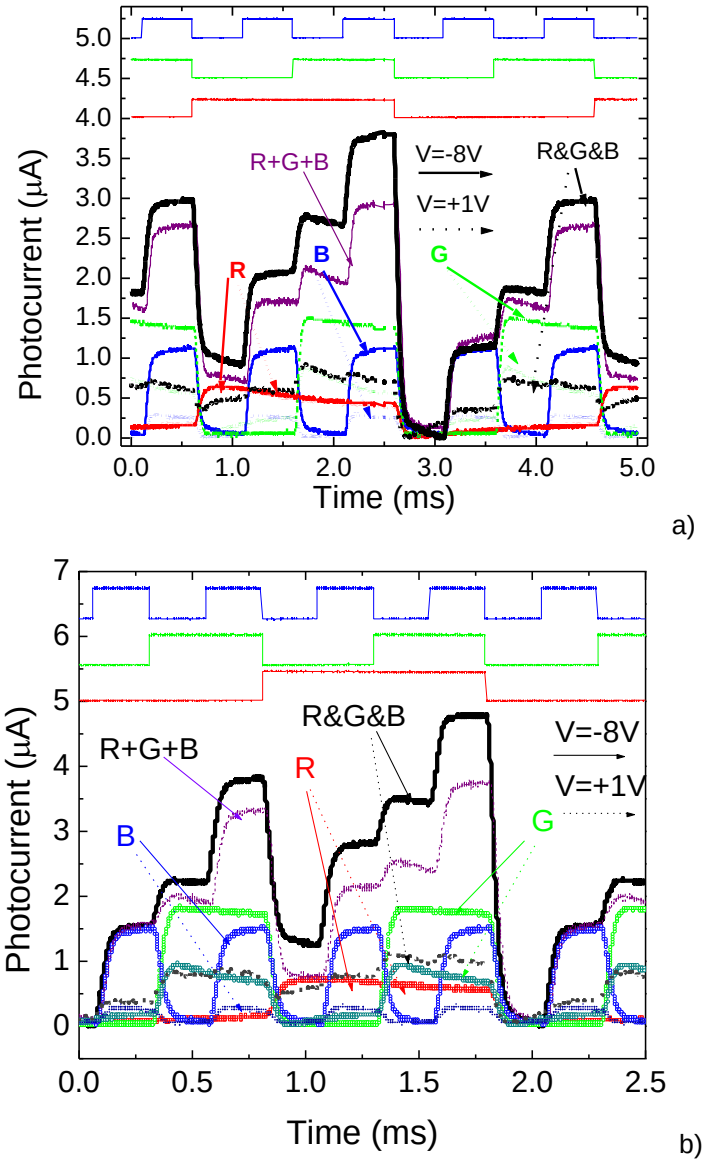

Figure 2.14 *Multiplexed signals under negative and positive bias using two different bit rates: a) 2000 bps, b)4000bps. On the top figure, the optical signal used to transmit the information guide the eyes on the different ON-OFF states.*

In Figure 2.14 the multiplexed and the single input channels are shown at different bit rates but with the same bit sequence: a) 2000bps, b) 4000bps. In the top of both figures the bit sequences are displayed to guide the eyes

Results show that in the analyzed range, the multiplexed signal is independent on the bit rate. It is interesting to notice that in both and under reverse bias, the sum of the input channels is lower than the correspondent multiplexed signals. This optical amplification, mainly on the ON-ON states, suggests capacitive charging currents due to the time-varying nature of the incident lights.

3.4 Influence of optical signal intensity

The identification of different input channels requires a previous calibration of the transmission signal in order to know the response of the WDM device to each individual channel as the signal attenuation along the transmission medium causes a reduction of the optical intensity at the reception end (WDM device). In order to analyze the influence of this effect the multiplexed signal was acquired with input signals of different optical intensities at -8V and +1V. Measurements were made with different levels of increasing optical power, up to 140 μWcm^{-2}.

In Figure 2.15 it is displayed the output photocurrent density variation with the optical bias measured for each optical channel (R: 626 nm, G: 524 nm and B: 470 nm) at -8 V and + 1V.

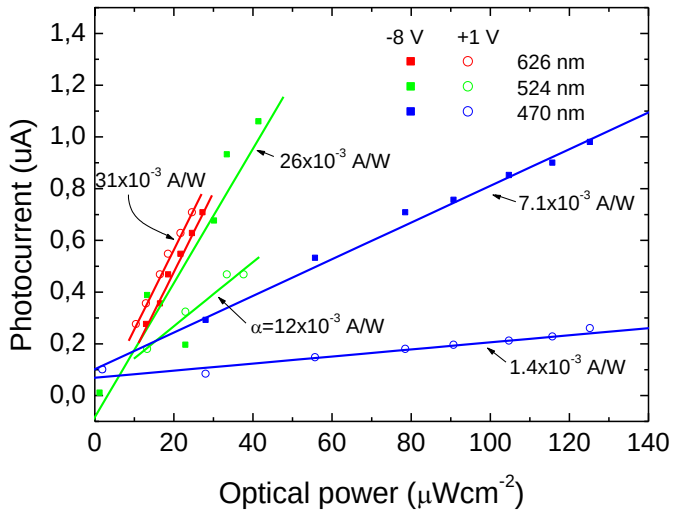

Figure 2.15 *Photocurrent density variation with the optical bias measured for each optical channel (R: 626 nm, G: 524 nm and B: 470 nm) at -8 V (solid symbols) and + 1V (open symbols). The solid lines correspond to linear fits of the experimental data. Slopes (α) of each plot are also displayed.*

Results show that under red illumination the multiplexed signal magnitude under the same intensity conditions is almost independent on the applied bias. Its magnitude increases with the optical power intensity, exhibiting a linear behavior with a growth rate around 31×10^{-3} A/W. Under green and blue light the dependence of the photocurrent magnitude is strongly dependent on the polarity of the applied

bias as already demonstrated before. It increases with the optical intensity of each channel either for reverse and forward bias and the growth rate depends on the applied voltage, being higher at reverse bias. Under blue light (470 nm) the growth rate is 5 times higher at reverse than under forward bias, while under green illumination (524 nm) this ratio is only of a factor of 2. This is due to the strong reduction of the device sensitivity to shorter wavelengths under forward bias.

4 Wavelength division demultiplexing device

4.1 Bias sensitive wavelength division demultiplexing technique

The major purpose of the WDM device is to detect the signal that is being communicated. So, different wavelengths which are jointly transmitted must be separated to regain all the information. These separators are called demultiplexers.

A chromatic time dependent wavelength combination of red and blue (Figure 2.16a) or red, green and blue (Figure 2.16b) with different transmission rates, were shining on the device. The generated photocurrent was measured under negative and positive bias to readout the combined spectra.

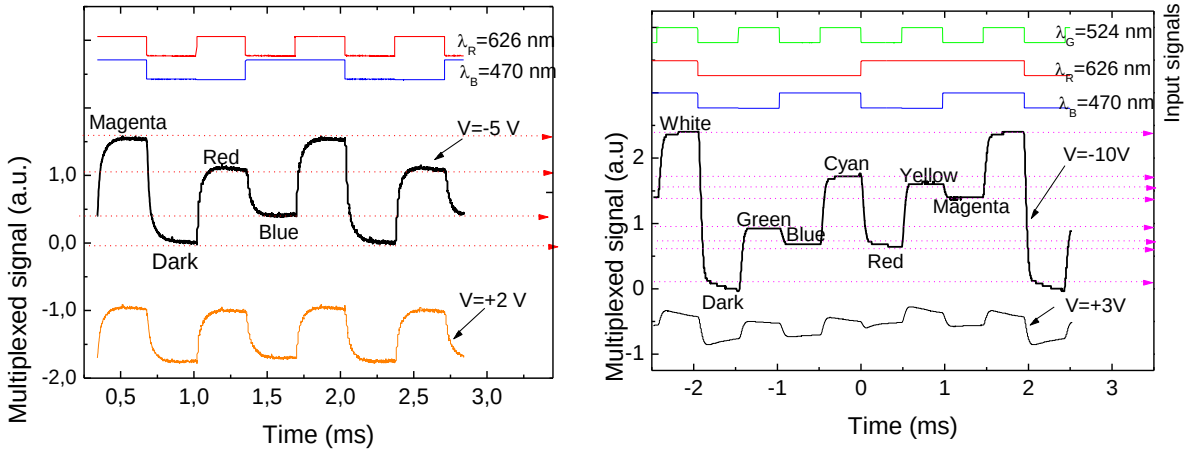

Figure 2.16 *Transient multiplexed signals under negative and positive bias. a) Polychromatic red and blue time dependent mixture. b) Polychromatic red, green and blue time dependent mixture. The digital wavelength demultiplexed signal is displayed on the top of both figures.*

If only two R and B channels are involved (four levels; Figure 2.16a), under forward bias, the blue component of the combined spectra falls into the dark level, tuning the red input channel. Thus, by switching between reverse and forward bias the red and the blue channels were recovered and the transmitted information regained. If three R, G and B input channels with different transmission rates

are being used (eight levels, Figure 2.16b), under reverse bias, the levels can be grouped into four main thresholds, ascribed respectively to the simultaneous overlap of three (R&G&B), two (R&B, R&G, B&G), one (R, G, B) and none (dark) input channels. As under forward bias, the blue component of the multiplexed signal approaches the dark level the R, the G and the R&G components are tuned. By comparing the multiplexed signals under forward and reverse bias and using a simple algorithm that takes into account the different sub-level behaviors under reverse and forward bias (2. 16b) it is possible to split the red from the green component and to decode their RGB transmitted information. The digital wavelength division demultiplex signals are displayed on the top of both figures.

In Figure 2.17, it is displayed the photocurrent generated by the combination of the red and the blue input channels in short circuit (open symbol) and under reverse bias (line). Results show that under short circuit the blue component of the combined spectra falls into the dark level, tuning the red input channel. Thus, by switching between short circuit and reverse bias the red and the blue channels were recovered.

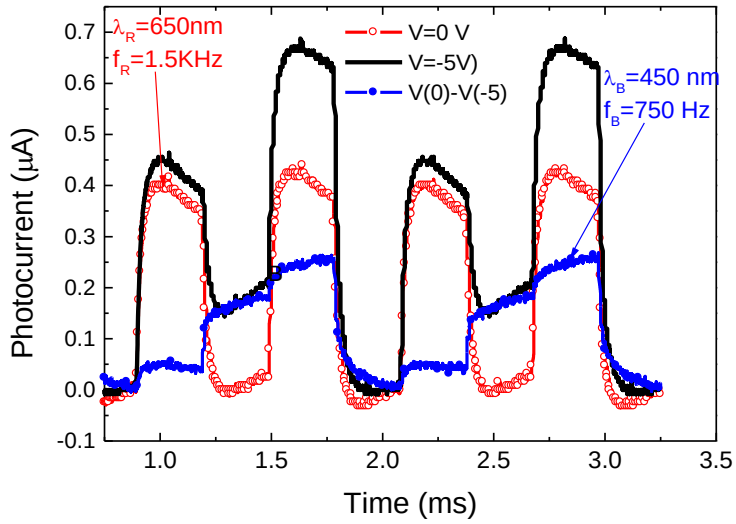

Figure 2.17 *Blue and red wavelength division demultiplexing output channels (dot lines) for the input signal (solid line)*

The device acts as a charge integrator, keeping the memory of the input channels. So, it can be used as a division wavelength multiplexing device.

4.2 Signal recovery

In the demultiplexing mode a polychromatic modulated light beam is projected onto the device and the readout performed by shifting between forward and reverse bias.

In Figure 2.18 it is displayed, under reverse and forward bias, the multiplexed signals due to the simultaneous transmission of three independent bit sequences, each one assigned to one of the RGB color channels. On the top, the optical signal used to transmit the information is displayed to guide the eyes on the different ON-OFF states. The bit sequence obtained for the demultiplexed signal is also shown for comparison.

To recover the transmitted information (8 bit per wavelength channel) the multiplexed signal, during a complete cycle (0<t<T), was divided into eight time slots, each corresponding to one bit where the independent optical signals can be ON (1) or OFF (0). As, under forward bias, the WDM device has no sensitivity to the blue channel, the red and green transmitted information can be identified from the multiplexed signal at +1V. The highest level corresponds to both channels ON (R&G: R=1, G=1), and the lowest to the OFF-OFF stage (R=0; G=0). The two levels in-between are related with the presence of only one channel ON, the red (R=1, G=0) or the green (R=0, G=1) (see horizontal labels in Figure 2.18). To distinguish between these two situations and to decode the blue channel, the correspondent sub-levels, under reverse bias, have to be analyzed. From Figures 2.9, 2.11 and 2.14 it is observed that the green channel is more sensitive to changes on the applied voltage than the red, and that the blue only appears under reverse bias. So, the highest increase at -8V corresponds to the blue channel ON (B=1), the lowest to the ON stage of the red channel (R=1) and the intermediate one to the ON stage of the green (G=1) (see colour arrows and vertical labels in Figure 2.18). Using this simple algorithm the independent red, green and blue bit sequences can be decoded as: R[00111100], G[00110011] and B[01010010].

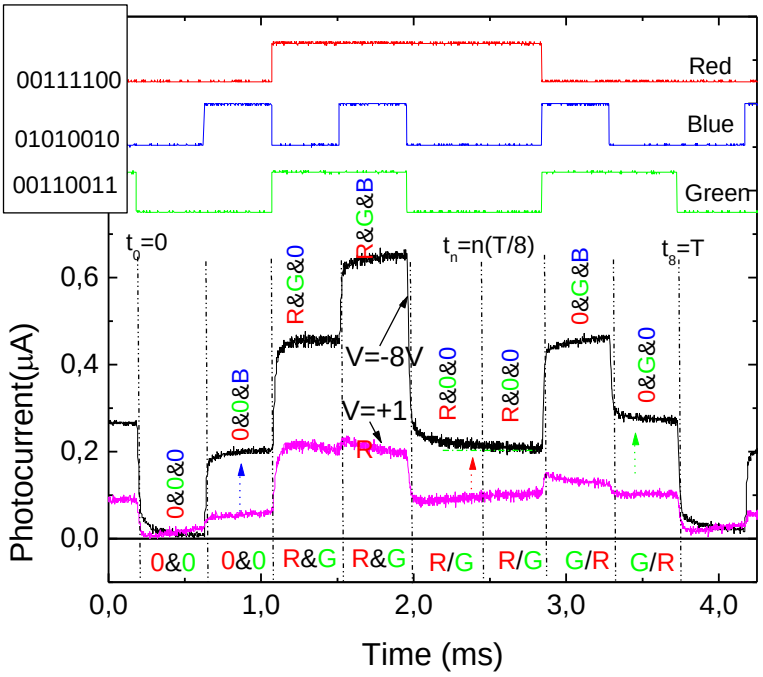

Figure 2.18 *Multiplexed signals under reverse and forward bias. On the top, the optical signal used to transmit the information guide the eyes on the different ON-OFF states. The bit sequence for the demultiplexed signal is shown for comparison.*

To validate the ability of this device to multiplex and demultiplex optical signals, the multiplexed signals, in Figure 2.11 were analyzed, in a time window between 0.7ms and 4.2ms, resulting in the bit sequences: R[11110000], G[11001100] and B[10101010] which are in agreement with the signals acquired for the independent channels.

4.3 DEMUX algorithm

A demux algorithm was implemented in Matlab that receives as input the measured photocurrent and derives the sequence of bits that originated it. The algorithm makes use of the variation of the photocurrent instead of its absolute intensity to minimise errors caused by signal attenuation.

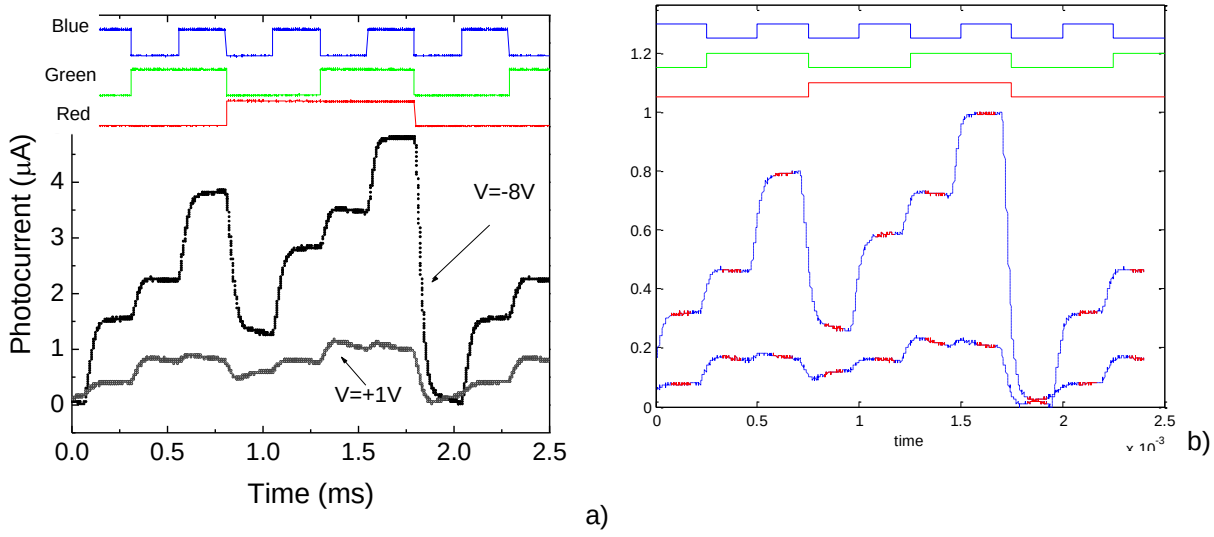

Figure 2.19 *a) Multiplexed experimental signal used for the calibration. On the top the input channels signals guide the eyes.b) A snapshot of the output from the MatLab routine used to demux the transmitted sequence of bits. The sequence of red, green and blue bits (shown at the top) was derived from the measured currents.*

A single linkage clustering method is applied to find automatically eight different clusters based on the measured current levels in both forward and reverse bias. This calibration procedure is performed for a short calibration sequence (Figure 2.19). Each cluster is naturally bound to correspond to one of the known eight possible combinations of red, green and blue bits.

Following this procedure the sequence of transmitted bits can be recovered in real time by sampling the photocurrent at the selected bit rate and finding for each sample the cluster with closest current levels.

In Figure 2.20 a multiplexed signal where the sequence of both blue and green input channels is the same was used to test the demux algorithm. A good agreement was achieved.

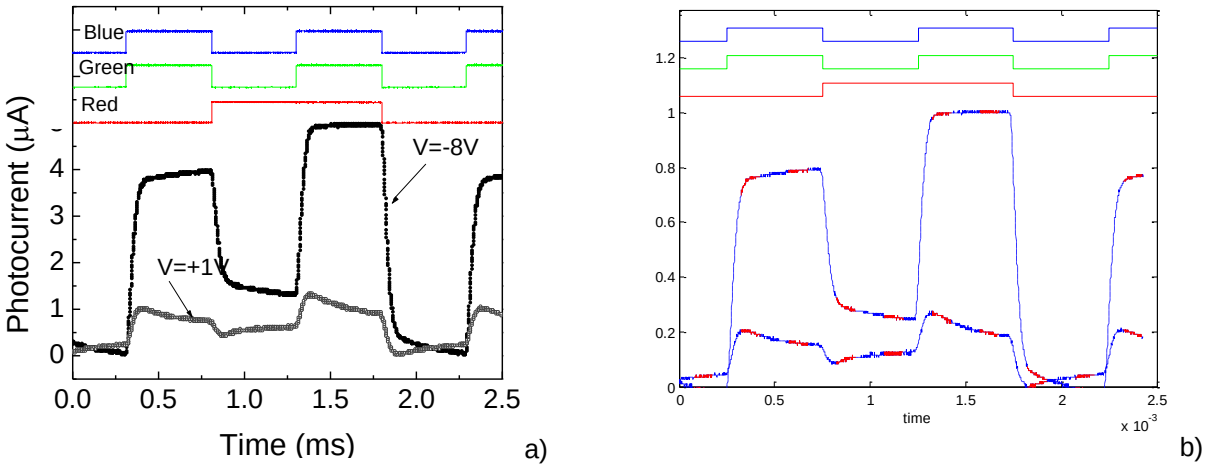

Figure 2.20 *a) Multiplexed experimental signal used for decoding. On the top the input channels signals guide the eyes.b) A snapshot of the output from the MatLab routine used to demux the transmitted sequence of bits. The sequence of red, green and blue bits (shown at the top) was derived from the measured currents.*

In Figure 2.21 we present an example of the output obtained for the two different sequences at 4000 bps.

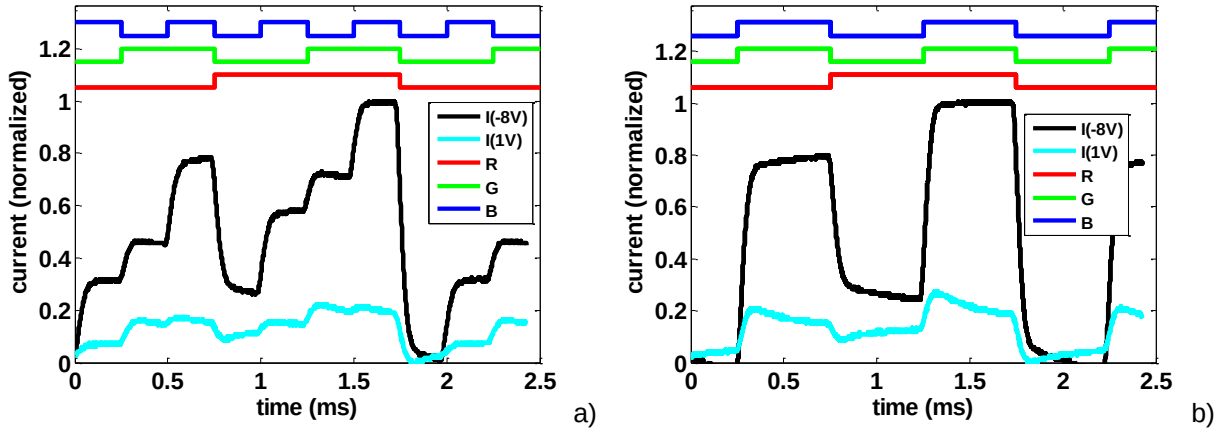

Figure 2.21 *A snapshot of the output from the MatLab routine used to demux the transmitted sequence of bits. The sequence of red, green and blue bits (shown at the top) was derived from the measured currents.*

Output data of the demux algorithm show that the derived sequences are R [00011100], G [011001100] and B [10101010] for the multiplexed signal of Figure 2.21a and R [00011100], G [011001100] and B [011001100] for Figure 2.21b. Both were found to be in exact agreement with the original sequences of bits that were transmitted (Figure 2.19 and 2.20).

Those observations indicate that is possible to improve the performance of the WDM device without adding any optical pre-amplifier or optical filter, which is an advantage when compared with the standard p-i-n cells. The impulsive response of the nano-optical filter is bias controlled and the recovery

algorithm is very simple, without the limiting factors associated with the operation of an optical complex receiver structure when using a standard p-i-n cell.

5 Signal Attenuation

The identification of the different input channels requires a previous calibration of the transmission signal in order to know the response of the WDM device to each individual channel as the signal attenuation along the transmission medium causes a reduction of the optical intensity at the reception end (WDM device). In order to analyze the influence of this effect the multiplexed signal was acquired with input signals of different optical intensities.

In Figure 2.22 the output multiplexed signal is displayed at -8V and +1V for different optical power intensities of the different input channels. Measurements were made with three levels of increasing optical power, starting with R= 11 μWcm^{-2}; G= 14 μWcm^{-2}; B= 28 μWcm^{-2} (I=1×) and then for twice (I=2×: R = 13 μWcm^{-2}; G = 28 μWcm^{-2};B = 56 μWcm^{-2}) and five times (I=5×: R= 22 μWcm^{-2}; G= 38 μWcm^{-2};B = 105 μWcm^{-2}) more current to drive the LEDs. On the top, the optical signal used to transmit the information is displayed to indicate the different ON-OFF states along the cycle (as shown by the bit sequence sent along each channel).

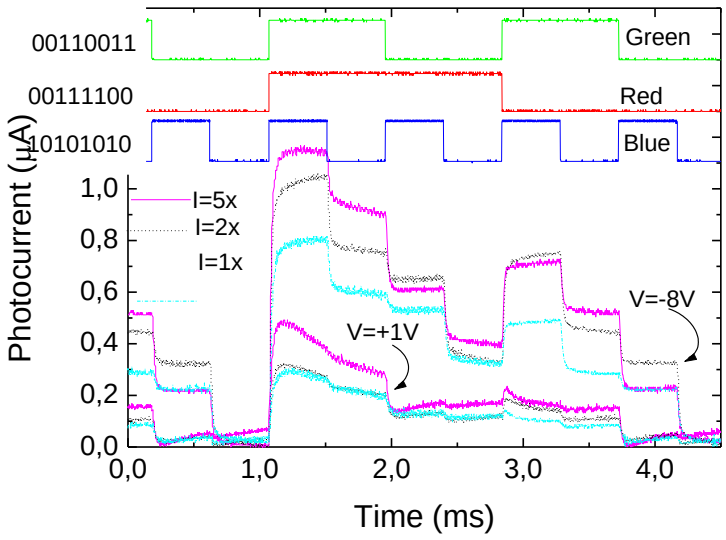

Figure 2.22 *Multiplexed signal at -8V and +1V under different optical power intensities of the RGB input channels.*

Results show that under reverse bias, as the channel intensity decreases, the multiplexed output signal also decreases. Under forward bias the signal is almost unaltered for the lowest intensities.

6 FRET approach

6.1 Introduction

There is an increasing demand of autonomous sensors capable of in situ detection and quantification of chemical and biological substances in real time [27]. For this purpose, sensors must have exceptional sensitivity and specificity. There is great interest, for example, in constructing nanoelectronic and optical devices [28, 29, 30] that can detect the concentrations of biomolecules, in real time, for use as medical diagnostics [31].

Many proteins have benefited from the process of selective evolution to become very sensitive to specific molecular species such that in their presence conformational changes and binding events take place. One possible approach to detect such events is Fluorescence Resonance Energy Transfer (FRET), a mechanism by which the fluorescence wavelength changes if two labeled molecules come close enough. This change in fluorescence can signal for example a binding event. This technique has grown in popularity due to the emergence of green fluorescent protein (GFP) mutants with blue (Cyan Fluorescent Protein, CFP) or yellow (Yellow Fluorescent Protein, YFP) shifted spectral properties. FRET analysis relies on the ability to capture and measure weak and transient fluorescent signals efficiently and rapidly from the interactions of labeled molecules in live samples [32].

The optical transducer has to accomplish the color recognition of the transient fluorescent signal coming from the different fluorescent proteins in addition to their capacity of combining them onto a single output signal without losing any specificity (color and intensity). The advantage of this type of sensor is that it does not rely on mechanical parts, it is compact and cost effective.

6.2 Spectral sensitivity

In Figure 2.23 it is displayed the spectral photocurrent of the entire device under different applied bias (+1V<V<-5V), the internal transparent contact was always floating during the measurements. The spectral emissions of both cyan and yellow fluorescent proteins are superimposed to guide the eyes.

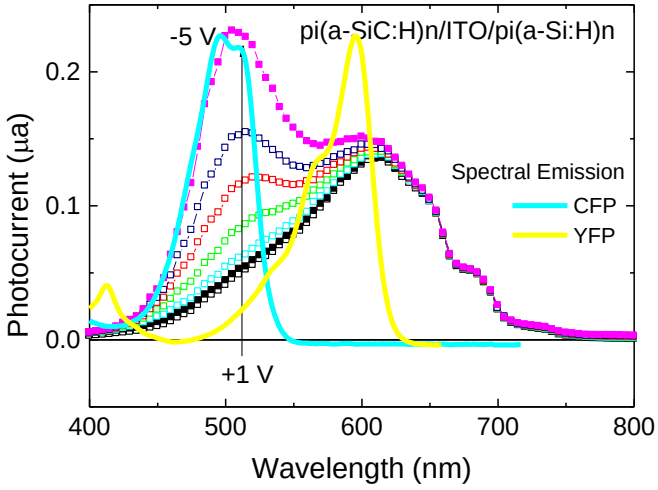

Figure 2.23 *p-i'-n-p-i-n spectral photocurrent under different the applied voltages. The spectral emission of the cyan and yellow fluorescent proteins are superimposed.*

Two modulated (3kHz) monochromatic lights: Y (λ_Y=588 nm); and C (λ_C=470 nm), and their polychromatic combinations (C&Y) illuminated separately the device and the photocurrent was measured. The *ac* photocurrent-voltage characteristics are displayed in Figure 2.24 The sum of both the monochromatic contribution (dash line) is displayed for comparison. Ultra-bright LEDs (470nm, 588nm) with a 20 nm spectral bandwidth were used as light sources.

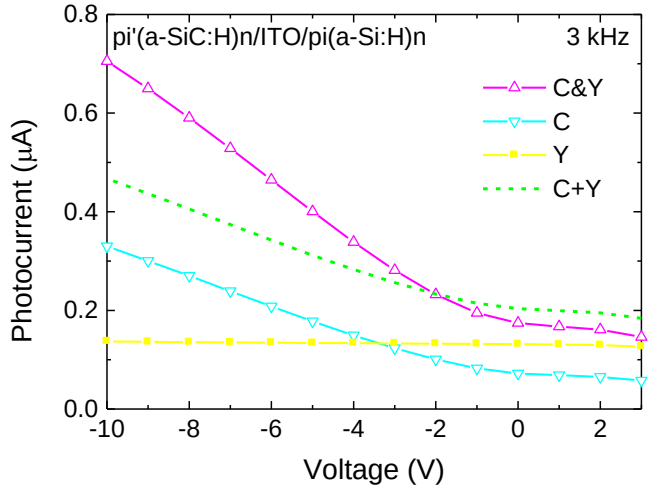

Figure 2.24 *ac photocurrent-voltage characteristics under monochromatic (C, Y) and polychromatic (C&Y) irradiation.*

6.3 Signal decoding

The photocurrent under yellow modulated light (Figure 2.24) is independent on the applied voltage while, under cyan or combined irradiations, it increases under reverse bias. If the cyan spectral component is present, a sharp increase with the reverse bias is observed. It is interesting to notice that the polychromatic mixture of cyan and yellow (C&Y) is higher than sum of the individual monochromatic contributions (C+Y) reviling an increased collection, when both front and back photodiodes are simultaneously irradiated. Under positive bias the cyan signal becomes negligible and the cyan and yellow mixtures overlap with the yellow one. This behavior illustrates, under forward bias, the low sensitivity to the cyan component of the multiplexed signal.

To simulate the FRET pairs (CFP, YFP) two modulated Cyan (470nm), and Yellow (580 nm) input monochromatic beams were used as input channels. In Figure 2.25 a chromatic time dependent wavelength combination of cyan (C) and yellow (Y) with different frequencies impinges the device from the glass side (see Figure 2.1). The generated photocurrent (symbols) is measured under negative (-8V) and positive (+1V) bias to readout the combined spectra. The light modulation frequency of one channel was chosen to be double of the other to ensure a synchronous relation of ON-OFF states along each cycle. For each independent wavelength, the output optical powers were adjusted to give approximately the same signal amplitude at -8V (lines). The reference level was assumed to be the signal when all the input channels were OFF.

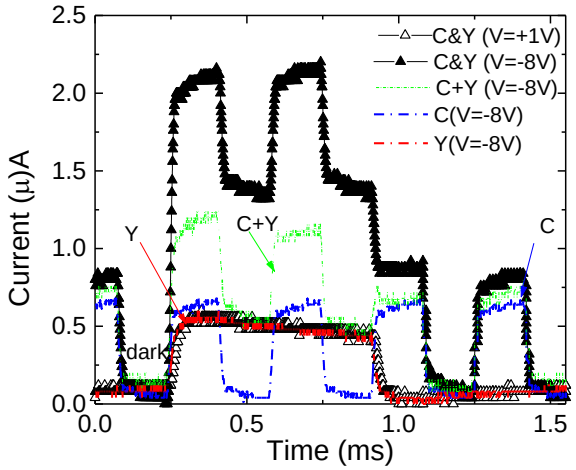

Figure 2.25 *Input channels (lines) and multiplexed signals (symbols) under negative and positive bias.*

Results show that the multiplexed signal depends on the applied voltage and on the state of each channel. Under negative bias there are four separate levels while under positive bias, they were reduced to one half due to the blindness of the sensor to the cyan component (Figure 2.24). Also, under negative bias, the sum of the input channels is lower than the correspondent multiplexed signals (see arrows in the figure). This optical amplification, mainly on the ON-ON state, suggests capacitive

charging currents due to the time-varying nature of the incident lights. Under positive bias the device becomes blind to the top photodiode (Figure 2.24) and the cyan component of the combined spectra falls into the dark level, allowing the recognition of the yellow input channel. By comparing the signals under positive and negative bias and using a simple algorithm that takes into account the different sub-level behaviors it is possible to decode the cyan and yellow components.

6.4 Influence of the optical power intensity and frequency

In Figure 2.26a the output multiplexed signal is displayed at -8V (symbols) and +1V (lines) for different optical power intensities of a cyan input channel (470 nm, 3kHz). During the measurements, the yellow channel (588 nm, 750 Hz) was always kept constant at 55μWcm^{-2}. In Figure 2.26b both input channels are modulated at the same frequency (3kHz).

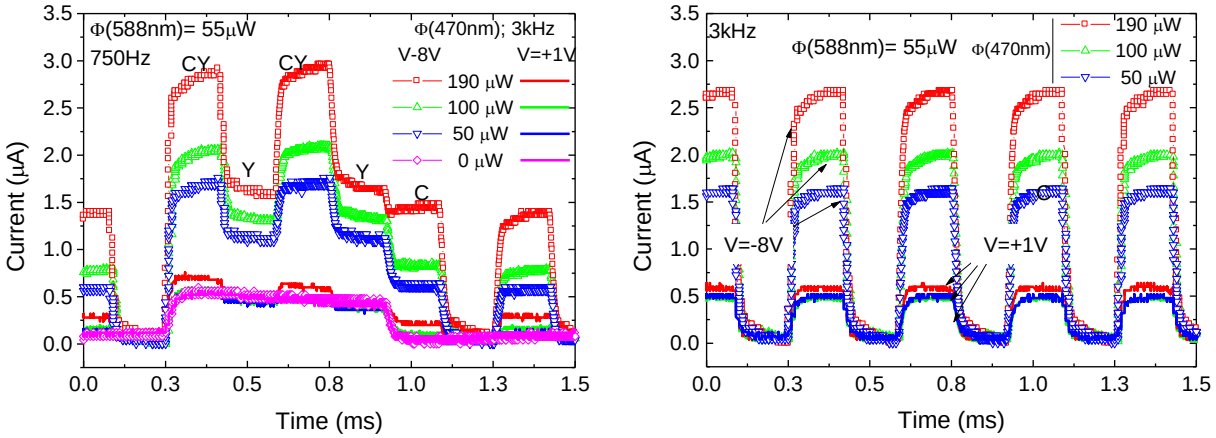

a) b)

Figure 2.26 *Multiplexed signal at -8V (symbols) and +1V (lines) under different optical power intensities of the cyan input channel and: a) different input channel frequencies. b) same input channel frequencies.*

Results show that under negative bias, as the cyan intensity decreases, the multiplexed output signal decreases. Under positive bias the signal is almost the same as the one obtained when the cyan channel was OFF due to the blindness of the transducer to the cyan channel. By comparing the ON-ON signal (CY) under negative and positive bias the ratio between both cyan and yellow intensities can be known, either if the emission occurs separately (Figure 2.26a) or at the same instant (Figure 2.26b). If this optical transducer is used in FRET analysis for the detection and analysis of cyan and yellow fluorescence pairs, the ratio between both input channels intensity can be correlated with the analyte levels and so, with the distance between the fluorophores.

7 Conclusions

In this chapter we present results on the optimization of multilayered a-SiC:H heterostructures for wavelength-division (de) multiplexing using the voltage control technique.

The non selective WDM device is a double heterostructure in a glass/ITO/a-SiC:H (p-i-n) /a-SiC:H(-p) /a-Si:H(-i) /a-SiC:H(-n)/ITO configuration. The single or the multiple modulated wavelength channels illuminated the device, and are absorbed accordingly to its wavelength, giving rise to a time dependent wavelength electrical field modulation across it. The effect of single or multiple input signals is converted into an electrical signal to regain the information (wavelength, intensity and frequency) of the incoming carriers. Here, the (de) multiplexing channels are accomplished electronically, not optically. This approach has advantages in terms of cost since several channels share the same optical components; and the electrical components are typically less expensive than optical ones. An electrical model gives insight into the device operation

Stacked structures that can be used as wavelength selective devices, in the visible range, are analysed. Two terminal heterojunctions ranging from p-ií-n to p-i-n-p-i'-n configurations are studied. Three terminals double stacked junctions with transparent contacts in-between are also considered to increase wavelength discrimination. The color discrimination was achieved by ac photocurrent measurement under different externally applied bias. Experimental data on spectral response analysis and current –voltage characteristics are reported. A theoretical analysis and an electrical simulation procedure are performed to support the wavelength selective behavior.

By switching between positive and negative voltages the input channels can be recovered or removed. So, this optical device allows adding and dropping one or several channels in a WDM optical network (OADMS) and can be used in optical communications.

Voltage controlled multiplexing devices, in multilayered a-SiC:H pin architectures, were compared. Experimental results show that the device acts as a charge transfer system. It filters, stores and transports the minority carriers generated by current pulses, keeping the memory of the input channels (color and transmission speed). In the stacked configuration, both front and back transistors act separately as wavelength selective devices, and are turned on and off sequentially by applying current pulses with speed transmissions dependent off the on-off state of all the input channels.

To enhance the bandwidth of the optical transmission system more work has to be done in order to enlarge the number of input channels and to improve the frequency response.

Results on the optimization of multilayered a-SiC:H heterostructures that can be used as an optical transducer for fluorescent proteins detection are also presented. The transfer characteristics of the transducers are studied experimentally under several wavelength illuminations corresponding to different fluorophores and tested for a proper fine tuning in the violet, cyan and yellow wavelengths. The devices were characterized through spectral response measurements under different electrical conditions and excitation frequencies. Results show that the output waveform is balanced by the wavelength and frequency of each input fluorescent signal, keeping the memory of the wavelength and

intensity of the incoming optical carriers. To selectively recover only one wavelength a specific voltage has to be applied.

8 Reference

[1] Michael Bas, Fiber Optics Handbook, Fiber, Devices and Systems for Optical Communication, Chap, 13, Mc Graw-Hill, Inc. 2002.

[2] S. Randel, A.M.J. Koonen, S.C.J. Lee, F. Breyer, M. Garcia Larrode, J. Yang, A. Ng'Oma, G.J Rijckenberg, H.P.A. Boom. “Advanced modulation techniques for polymer optical fiber transmission”. proc. ECOC 07 (Th 4.1.4). Berlin, Germany (2007) 1-4.

[3] M. Haupt, C. Reinboth and U. H. P. Fischer. “Realization of an Economical Polymer Optical Fiber Demultiplexer”, Photonics and Microsystems, 2006 International Students and Young Scientists Workshop, Wroclaw, 2006.

[4] P. Louro, Y. Vygranenko, J. Martins, M. Fernandes and M. Vieira “Colour sensitive devices based on double p-i-n-i-p stacked photodiodes” Thin Solid Films Vol. 515, Issue 19, 16 July 2007, pp 7526-7529.

[5] M. Vieira, A. Fantoni, P. Louro, M. Fernandes, R. Schwarz, G. Lavareda, C.N. Carvalho “Self-biasing effect in colour sensitive photodiodes based on double p-i-n a-SiC:H heterojunctions” Vacuum, Volume 82, Issue 12, 8 August 2008, pp 1512-1516.

[6] M. Vieira, P. Louro, M. Fernandes, M. A. Vieira, A. Fantoni and J. Costa (2011). Three Transducers Embedded into One Single SiC Photodetector: LSP Direct Image Sensor, Optical Amplifier and Demux Device, Advances in Photodiodes, Gian Franco Dalla Betta (Ed.), ISBN: 978-953-307-163-3, InTech, Chap.19, pp:403-425 (2011).

[7] P. Louro, M. Vieira, M A Vieira, M. Fernandes, A. Fantoni, C. Francisco, M. Barata “Optical multiplexer for short range application” Physica E: Low-dimentional Systems and Nanostructures , Vol. 41, Pages 1082-1085 (2009).

[8] M. Vieira, M. Fernandes, A. Fantoni, P. Louro, M. A. Vieira, “Large area a-SiC:H WDM devices for signal multiplexing and demultiplexing in the visible spectrum”, Thin Solid Films, Thin Solid Films 517 (2009), pp. 6435-6439.

[9] P. Louro, M. Vieira, A. Fantoni, M. Fernandes, C. Nunes Carvalho, G. Lavareda, “Image and color recognition using amorphous silicon p-i-n photodiodes “Sensor and Actuators A: Physical, 123-24: (2005) pp. 326-330.

[10] P Louro, M. Vieira, Y. Vygranenko, M. Fernandes, A. Garção “Optical readout in pinpi’n and pini’p imagers: a comparison” in Amorphous and Polycrystalline Thin-Film Silicon Science and

Technology—2007, edited by Virginia Chu, Seiichi Miyazaki, Arokia Nathan, Jeffrey Yang, Hsiao-Wen Zan (Mater. Res. Soc. Symp. Proc. Volume 989, Warrendale, PA, 2007), A12-04

[11] P. Louro, M. Vieira, M. A. Vieira, M. Fernandes and J. Costa (2011). Use of a-SiC:H Photodiodes in Optical Communications Applications, Advances in Photodiodes, Gian Franco Dalla Betta (Ed.), ISBN: 978-953-307-163-3, InTech, Chap.19, pp:377-402 (2011).

[12] M. Vieira, M. Fernandes, P. Louro, A. Fantoni, M. Barata, M A Vieira, "Multilayered a-SiC:H device for Wavelength-Division (de)Multiplexing applications in the visible spectrum" Symposium A: S. Francisco, USA, 24 -29 March, 2008, in Amorphous and Polycrystalline Thin-Film Silicon Science and Technology, edited by A. Flewitt, J. Hou, S. Miyazaki, A. Nathan, and J. Yang (Mater. Res. Soc. Symp. Proc. Volume 1066, Warrendale, PA, 2008), pp.225-230 A08-01

[13] M. Vieira, P. Louro, M. Fernandes, M. A. Vieira, J. Costa, "Optical transducers based on amorphous Si/SiC photodiodes", Technological Innovation for Sustainability IFIP Advances in Information and Communication Technology, 2011, Volume 349/2011, 604-611.

[14] P. Louro, M. Vieira, M. A. Vieira, M. Fernandes, A. Fantoni, G. Lavareda, C. N. Carvalho "Optical Processing Devices for Optical Communications: Multilayered a-SiC:H Architectures Amorphous and Polycrystalline Thin-Film Silicon Science and Technology — 2009, MRS Proceedings Volume 1153, A19-01.

[15] M A Vieira, M. Vieira, M. Fernandes, A. Fantoni, P. Louro, M. Barata, "Voltage Controlled Amorphous Si/SiC Phototransistors and Photodiodes as Wavelength Selective Devices: Theoretical and Electrical Approaches" Amorphous and Polycrystalline Thin-Film Silicon Science and Technology — 2009, MRS Proceedings Volume 1153, A08-03.

[16] M. Vieira, A. Fantoni, M. Fernandes, P. Louro, G. Lavareda and C.N. Carvalho, "Bias sensitive multispectral structures for imaging applications" Thin Solid Films, 515, Issue 19, 2007, 7566-7570.

[17] M. Vieira, Y. Vygranenko, M. Fernandes, P. Sanguino, A. Fantoni, P. Louro, R. Schwarz, "Preliminary results on large area X-ray a-SiC:H multilayer detectors with optically adressed readout" in Amorphous and Polycrystalline Thin-Film Silicon Science and Technology—2007, edited by Virginia Chu, Seiichi Miyazaki, Arokia Nathan, Jeffrey Yang, Hsiao-Wen Zan (Mater. Res. Soc. Symp. Proc. Volume 989, Warrendale, PA, 2007) A19-02.

[18] A. Fantoni, M. Vieira, R. Martins, "Simulation of hydrogenated amorphous and microcrystalline silicon optoelectronic devices", Mathematics and Computers in Simulation, Vol. 49. (1999) 381-401.

[19] M. Vieira, M. Fernandes, P. Louro, A. Fantoni, M. Barata, M A Vieira, "Multilayered a-SiC:H device for Wavelength-Division (de)Multiplexing applications in the visible spectrum" Symposium A: S. Francisco, USA, 24 -29 March, 2008, in Amorphous and Polycrystalline Thin-Film Silicon Science and Technology, edited by A. Flewitt, J. Hou, S. Miyazaki, A. Nathan, and

J. Yang (Mater. Res. Soc. Symp. Proc. Volume 1066, Warrendale, PA, 2008), pp.225-230 A08-01.

[20] M. Vieira, M. Fernandes, J. Martins, P. Louro, R. Schwarz, and M. Schubert "Laser Scanned p-i-n Photodiode (LSP) for image detection", IEEE Sensor Journal, 1, 2001, 158-167.

[21] M. Vieira, P. Louro, M. A. Vieira, J. Costa, M. Fernandes, "Direct Color Sensor, Optical Amplifier and Demux Device Integrated on a Single Monolithic SiC Photodetector" Eurosensors 2010 - European Conference on sensors, actuators and Microsystems, Eurosensor XXIV Conference Procedia Engineering, Volume 5, 2010,Pages 232-235..

[22] P. Louro, M. Vieira , M. Fernandes, M. Barata, A. Fantoni, J. Costa,, J Caeiro M. A. Vieira "Optical demultiplexer based a-SiC:H voltage controlled device" " Phys. Status Solidi C 7, No. 3–4, 1188– 1891 (2010)

[23] P. Louro , M. A. Vieira, M. Fernandes, A. Fantoni, M. Barata, M. Vieira, "Demultiplexer/Photodetector Integrated System Based on a-SiC:H Multilayered Structures" Symposium B: Amorphous and Polycrystalline Thin-Film Silicon Science and Technology — 2010, MRS Proceedings, Editors: Q. Wang, B. Yan, S. Higashi, C.C. Tsai, A. Flewitt Volume 1245, A18-05, DOI: 10.1557/PROC-1245-A18-05

[24] M. Vieira, P. Louro M. A. Vieira, J. Costa, M. Fernandes, and A. Fantoni, "Wavelength Selective a-SiC:H p-i-n/p-i-n Heterostructure for Fluorescent Proteins Detection", Sensor Letters, Vol. 8 (3), 413-418 (2010) ISSN 1546-198X. eISSN 1546-1971.

[25] M. Vieira, P. Louro, A. Fantoni, M. Fernandes, M. A Vieira, M.Barata "New stacked photodevices for signal multiplexing and demultiplexing applications in the visible spectrum" , 6th International Multi-Conference on Systems, Signals and Devices, MAR 23-26, 2009 Djerba, TUNISIA 2009, VOLS 1 AND 2, pp: 869-874 (2009),

[26] Paula Louro, Manuela Vieira, João Costa, M. A. Vieira, Miguel Fernandes, Alessandro Fantoni, Manuel Barata "a-SiC:H Based Devices as Optical Demultiplexers", in Silicon Carbide 2010 — Materials, Processing, and Devices, edited by S.E. Saddow, E. Sanchez, F. Zhao, M. Dudley (Mater. Res. Soc. Symp. Proc. Volume 1246, Warrendale, PA, 2010), B07-07

[27] L. Shenkman, M. Koukaki, S. Karamanou, A. Economou, Proceedings of the 29th Annual International Conference of the IEEE EMBS, 2007.

[28] D.A LaVan, Terry McGuire, Robert Langer, Nat. Biotechnol. 21 (10), 2003, 1184–1191.

[29] S .Saito, Science 278, 1997, 77–78.

[30] D. Grace, Medical Product Manufacturing News, 12, 2008, 22–23.

[31] A. Cavalcanti, B. Shirinzadeh, Jr Freitas, A.Robert, Tad Hogg, Nanotechnology, 19 (1), 015103, 2008, (15pp).

[32] Jovin, T.M. and Arndt-Jovin, D.J. FRET microscopy: Digital imaging of fluorescence resonance energy transfer. Application in cell biology. In Cell Structure and Function by

Microspectrofluometry, E. Kohen, J. G. Hirschberg and J. S. Ploem. London: Academic Press, 1989. pp. 99-117.

CHAPTER III

Light-activated amplification in Si-C tandem devices

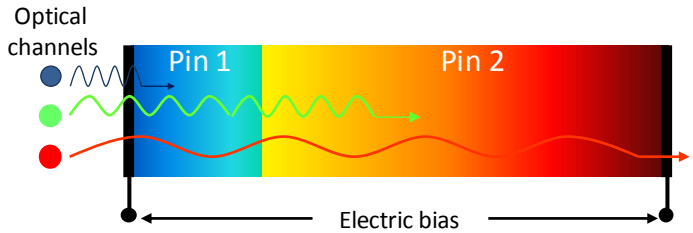

III Light-activated amplification in Si-C tandem devices: A capacitive active filter model

1 Introduction

Multilayered structure based on amorphous silicon technology is expected to become reconfigurable to perform WDM optoelectronic logic functions as we have just seen in Chapter II and provide as well complex photonic functions such as signal amplification and switching [1, [2]. It should be a solution in WDM technique for information transmission and decoding in the visible range. The basic operating principle in wavelength conversion schemes is the exploitation of the physical properties of a nonlinear element to perform a logic function. Amplification and amplitude change are two key functionality properties, depending on the background placement within a WDM link, wavelength optical bias and frequency of the optical signal [3, 4, 5].

A complete theoretical analysis and an electrical simulation procedure will be performed, and experimental and simulated results will be compared in Chapter IV.

Key subsystems that take advantage of these benefits are optical multiplexers/ demultiplexers and switching fabrics for optical circuit switching applications and optical logic gates implemented in basic building blocks for band-pass filters.

A numerical simulation support new optoelectronic logic architecture, especially for optical switches that employ different induced background photo capacitances whose resonance mode is shifted by the depletion or injection of carriers. Depending on the wavelength of the external background they act either as a short- or a long- pass band filter or as a band-stop filter.

A light-activated photonic device that combines the demultiplexing operation with the simultaneous photodetection and self amplification of an optical signal was used to simulate the FRET approach. The transfer characteristics are studied experimentally in Chapter II, under several wavelength illuminations corresponding to different fluorophores and tested for a proper fine tuning in the violet, cyan and yellow wavelengths. The devices were characterized through spectral response measurements under different electrical conditions and excitation frequencies.

2 Experimental details

2.1 Configuration

The tunable optical devices were produced by PECVD (Plasma Enhanced Chemical Vapor Deposition) and optimized for a proper fine tuning of a specific wavelength (Chapter I, §4.2).
The active device consists of a p-i'(a-SiC:H)-n/p-i(a-Si:H)-n heterostructure with low conductivity doped layers. Device configuration was described in Chapter II, §2.2 and is depicted in Figure 3.1.
The thicknesses and optical gap of the thin í'- (200 nm; 2.1 eV) and thick i- (1000 nm; 1.8 eV) layers are optimized for light absorption in the blue and red ranges, respectively [6]. As a result, both front and back pin structures act as optical filters confining, respectively, the blue and the red optical carriers (Chapter II, §2.2).

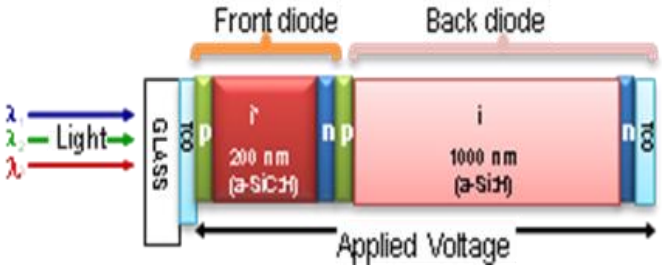

Figure 3.1 *Device configuration .*

2.2 Operation

Systems that transmit, receive, and/or process intelligence require some form of modulation, which is the deliberate distortion of a carrier to impress intelligence (data) upon it, in a manner that allows the subsequent recovery of the information. Here, as in Chapter II, the manipulation of the magnitude is achieved by changing the wavelength (color channels) of the optical signals and its frequency.
By providing a complex illumination of the device combining radiations with different and complementary penetration depths it is possible to control the spectral response of the device.
In the WDM signal transmission, three channels (red, green and blue) are demultiplexed using wavelength selective channel filters. Background light can be changed to select different wavelength channels. By superimposing background illumination to the pulsed channel the device behaves as a filter, producing signal attenuation, or as an amplifier, producing signal gain, depending on the channel/background wavelength combination. This effect is reported and fully discussed elsewhere [7] and can be described in terms of a wavelength controlled photo-capacitance that will be investigated recurring to numerical techniques.

The device operates within the visible range using as input color channels (data) the wave square modulated light (external regulation of frequency and intensity) supplied by a red (R: 626 nm; 51 μW/cm^2), a green (G: 524 nm; 73 μW/cm^2) and a blue (B: 470 nm; 115 μW/cm^2) LED. Additionally, steady state red, green and blue illumination (background) was superimposed brought in LEDS driven at a constant current value (R: 290 μW/cm^2, G: 150 μW/cm^2, B: 390 μW/cm^2). Here, light was impinging from the glass side.

3 Numerical simulation

3.1 Recombination and generation profile

In order to understand the light filtering properties of the device (Figure 3.1), under different electrical and optical bias conditions, a simulation program ASCA-2D [8] was used having as input parameters the experimental data. For the a-SiC:H and a-Si:H absorbers an optical band gap of 2.1 eV and 1.8 eV and a thickness of 200 nm and 1000 nm were chosen, respectively. The doping level was adjusted in order to obtain approximately the same conductivity of the typical thin film layers [chapter I, §4.2].

In Figure 3.2a the recombination profiles (straight lines) under red (λ_R =650 nm) and blue (λ_B =450 nm) irradiation are displayed at different electrical bias. In Figure 3.2b it is shown the same profiles but under green bias optical (λ_G =550 nm). The generation profiles are also displayed (symbols).

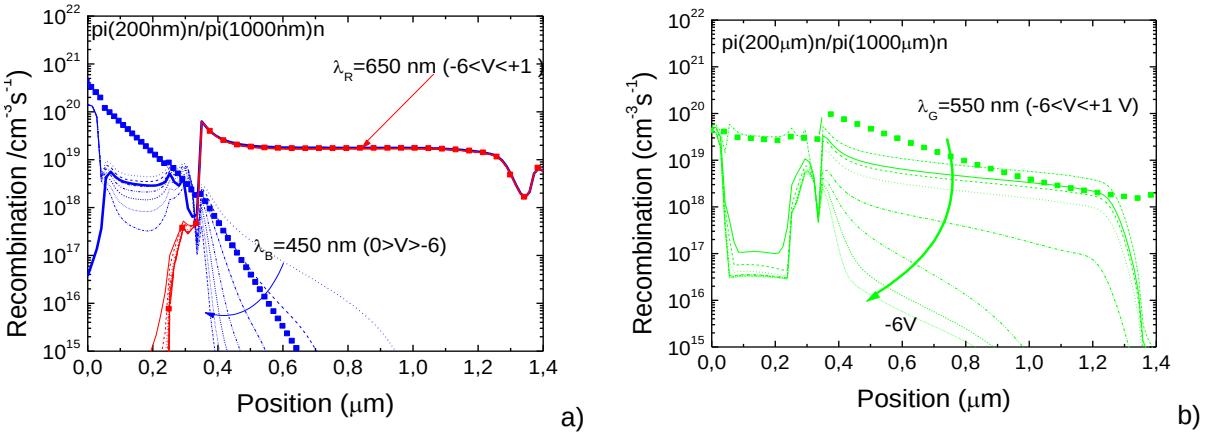

Figure 3.2 *Recombination profiles (straight lines) under: a) red (λ_R =650 nm) and blue (λ_B =450 nm) b) green (λ_G =550 nm) optical bias and different applied voltages. The generation profiles are shown (symbols).*

Simulated results show that the thickness and the absorption coefficient of the front photodiode are optimized for blue collection and red transmittance, and the thickness of the back one adjusted to achieve full absorption in the greenish region and high collection in the red spectral range. As a result, both front and back diodes act as optical filters confining, respectively, the blue and the red optical carriers, while the green ones are absorbed across both.

3.2 Electric field profile

Under negative applied voltage, in Figure 3.3a, it is reported the electric field profile under different wavelengths backgrounds of the optical bias. In Figure 3.3b, under red background, the three red, green and blue channels were added and the electrical field profile displayed.

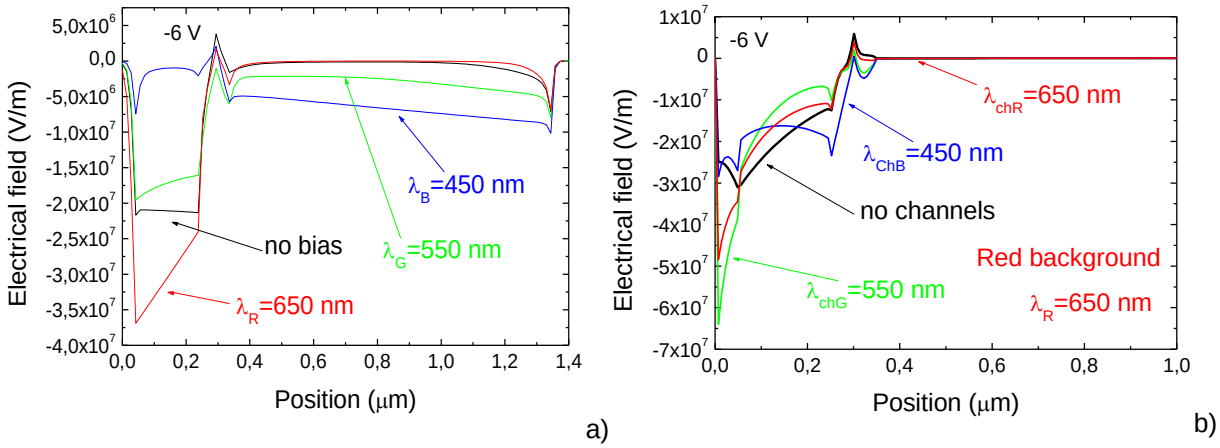

Figure 3.3 *Electric field profiles within the p-I'-n/p-i-n tandem structure. a) under different wavelengths backgrounds ($\lambda_{R,G,B}$) and without it, b) red background (λ_R) and different color channels (λ_{chR}, λ_{chG}, λ_{chB}).*

Results show that the balance between the electrical field adjustments due to the non uniform absorption throughout the structure depends on the generation/recombination ratio profiles at each background wavelength. The shallow penetration of the blue photons into the front diode, the deep penetration of the red photons exclusively into the back diode or the decay of the green absorption across both controls the sensor behavior. The external background interferes mainly with the less absorbing cell (the front under red, the back under blue and with both under green irradiations). Both the front and the back diodes are optically and electrically in series. Under steady state irradiation, to sustain the current across the device, the current at the less absorbing diode has to be adjusted through an increase of the electrical field and thus it becomes reverse biased (Figure 3.3a). The superposition of a color channel will affect locally this field. Under red background (Figure 3.3b), the blue channel increases the field intensity in the front diode and even reverses it at the internal interface increasing carrier collection. The red and the green channels change the field in an opposite way.

When an external electrical or optical bias is applied to a double pin structure, its main influence is in the field distribution within the less photo excited sub-cell: the front cell under red irradiation; the back cell under blue light, and both, under green steady state illumination. In comparison with thermodynamic equilibrium conditions (no background), the electrical field under illumination is lowered in the most absorbing cell (self forward bias effect) while the less absorbing reacts by assuming a reverse bias configuration (self reverse bias effect) [9].

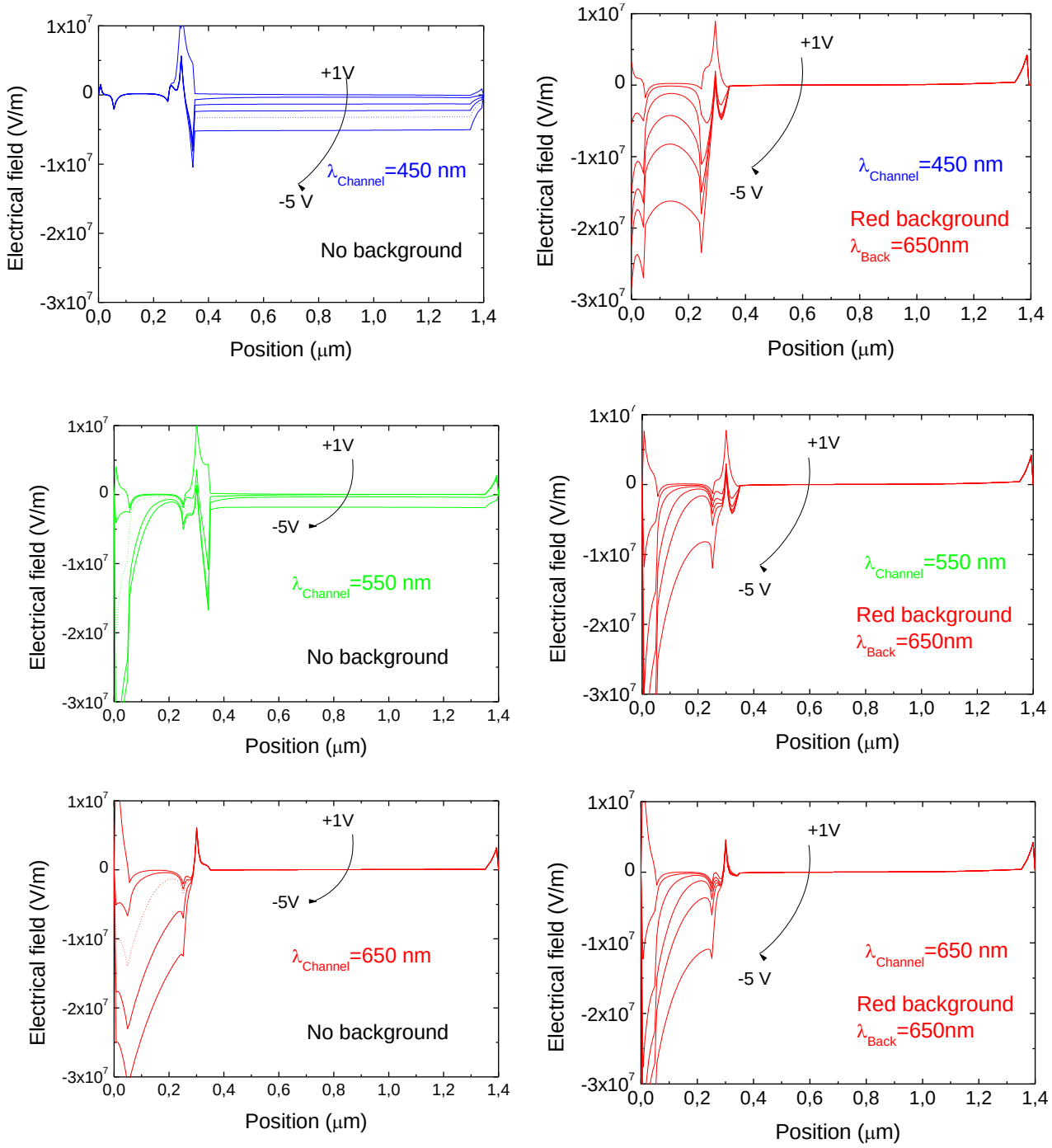

Figure 3.4 *Electric Field profile using the blue, the green, and the red channels without (left) and with (right) red optical bias.*

In Figure 3.4 (left side) it is displayed the electrical field profile, at different values of the electric bias, under the effect of the RGB channels. In Figure 3.4 (right side) a red steady state optical bias was superimposed. As expected as the voltage changes from positive to negative the electric field increases in the less absorbing cell. The addition of the red background to the blue channel quenches the field in the back diode where the red photons are absorbed (reverse bias effect) and increases it (reverse bias effect) in the front diode where the blue channel generates the optical carriers. So, the induced variation of the field brings on the blue collection, from which results the observed amplification of the signal. If the red background is superimposed to the red or to the green channels the reverse bias effect is enhanced in the front diode resulting in a decreased collection on both channels.

3.3 Potential profile

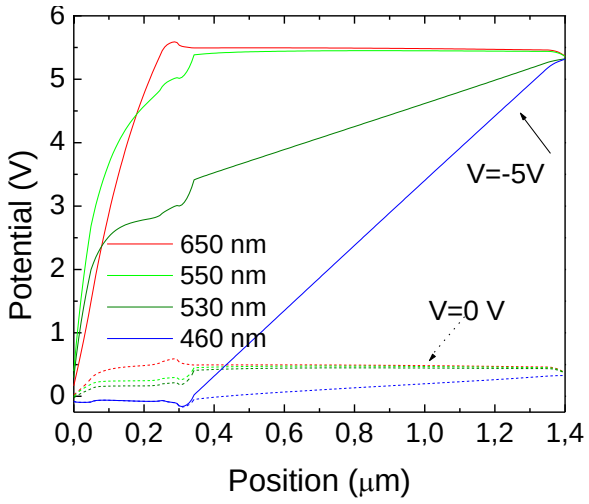

Figure 3.5 *Internal potential profile within the device under different light wavelength. Results are shown with and without external reverse bias.*

The internal potential distribution is also strongly influenced by the asymmetric photogeneration profile [10]. Figure 3.5 shows the internal potential profile within the complete device under different light wavelength. Results are shown with and without external reverse bias. When the device is illuminated by light with different wavelength, the internal electrical configuration varies according with the different light penetration profile. When photogeneration is unbalanced between the two internal diodes, the one which is less photo-excited acts under a self polarization regime. Also the externally applied bias falls mainly upon the less photo-stimulated diode.

Figure 3.6 reports the internal potential profile under different light wavelength and different background illumination. If a light background is present, when the device is illuminated by light with different wavelength, the internal electric configuration varies depending on the combination of the

channel/background wavelength. So, the device can be made selective to a certain wavelength range by adjusting the background light.

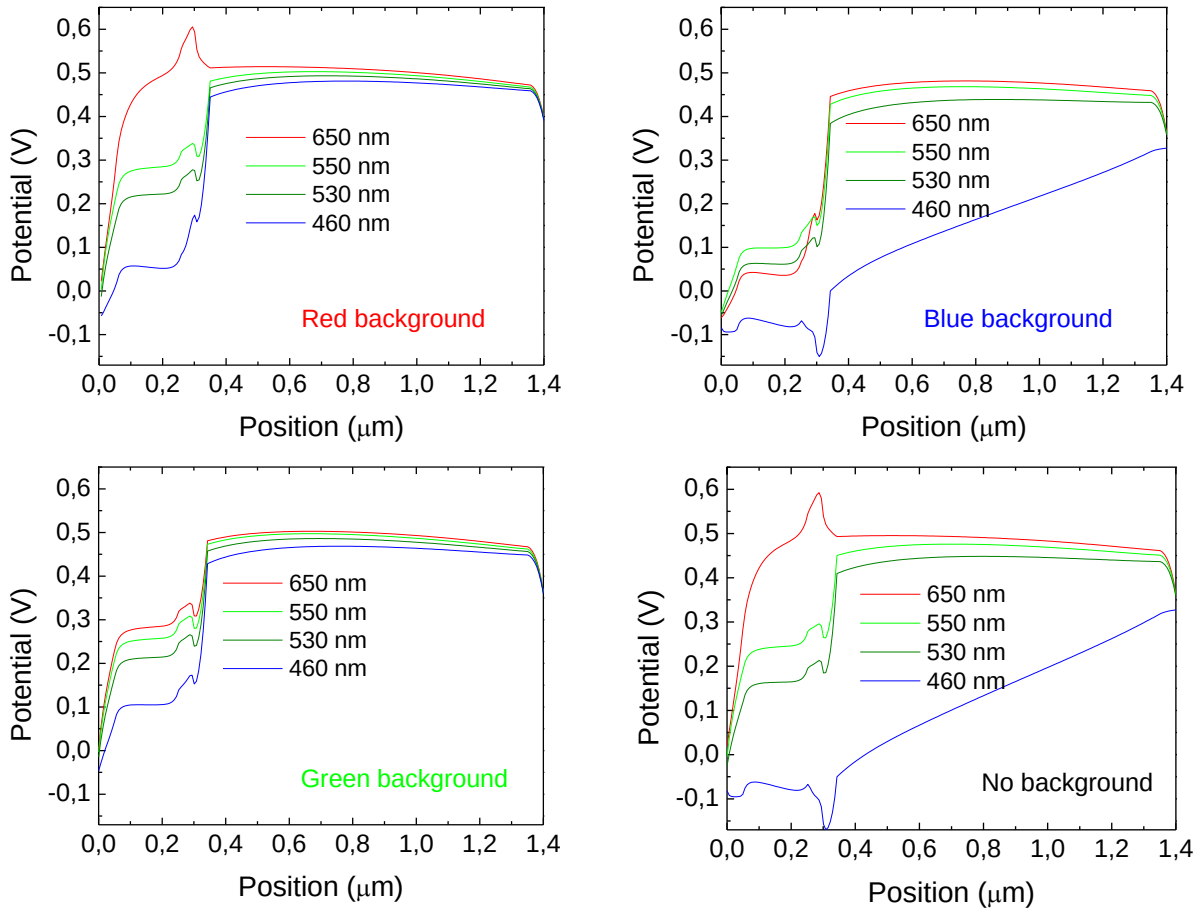

Figure 3.6 *Internal potential profile within the complete device under different light background wavelengths and without it.*

3.4 Charge accumulation profile

Frequency dependence of the device responsivity can be explained by considering the charge accumulation (free and trapped) that is created in the top diode region. Figure 3.7 shows the internal space charge profile within the pi'npin device under different light wavelength.

Depending on the imposed background the different channel wavelengths produce a different displacement of the space charge distribution. This effect produces a light dependence of the device frequency response, permitting frequency filtering, or even the definition of an oscillatory frequency resonance.

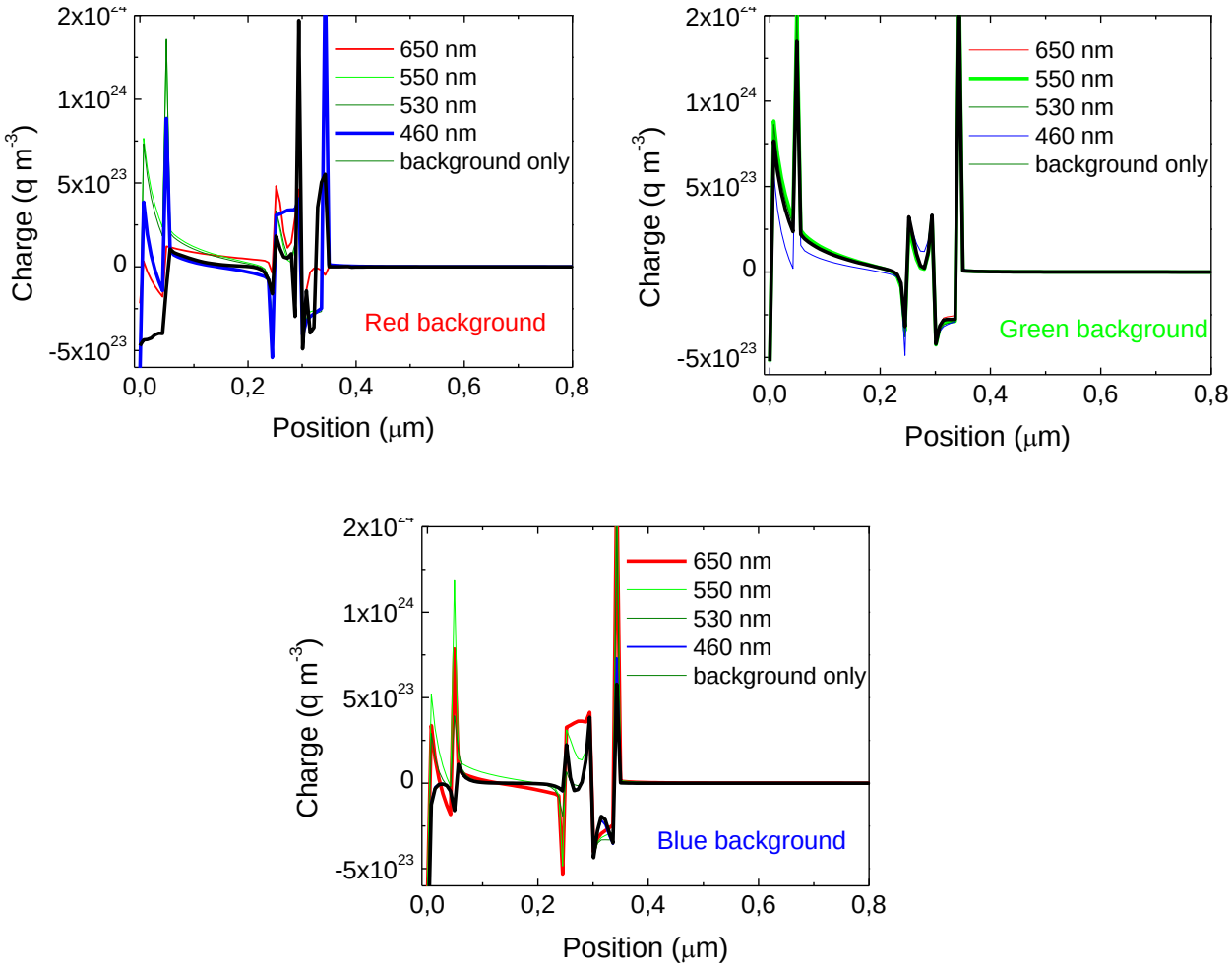

Figure 3.7 *Internal space charge profile within the complete device under different light wavelength. Results are shown under reverse bias and for different background illumination.*

Charge accumulation is mainly localized at the internal interface between the two diodes. Under blue and red background light the charge accumulation is maximized for complementary wavelengths. Under green background there is no marked difference between the space charge accumulation caused by the three signals and the background itself, suggesting so a similar frequency response for the different WDM channels. This charge accumulation corresponds to a photo capacitance behavior of the internal recombination junction. An increase of space charge within the transition regions at the i/n and at the i/p and n/i´ interface would reduce the depletion layer width in those regions and therefore, by definition of depletion capacitance, increase the photocapacitance value.

Under red background light the photogenerated charge accumulations from deep trap levels is maximized for the blue channel and corresponds to a photo capacitance behavior of the internal recombination junction (considered as a measure of the density of photogenerated carriers in the space charge region [11]. Electrons or holes trapped by deep centers in the depletion layer are emitted to the

conduction band or the valence band, and removed from the depletion layer, resulting in a change in the space charge. Under homogeneous absorption and assuming constant electric field, the photogenerated electrons move rapidly to the n contact layer, whereas the holes make up most of the photocharge that constitutes the photocapacitance signal.

Combined this photocapacitance with the series and parallel resistance of the diodes will result in the explicit definition of cut off frequencies for a frequency capacitive filters activated by the light background or an oscillatory resonance of photogenerated carriers between the two diodes.

These results address the explanation of the device functioning in the frequency domain to a wavelength tunable photocapacitance due to the accumulation of space charge localized at the internal junction.

It must be remarked that the charge accumulated is calculated by the simulator using the Shockley-Read-Hall model, which is the most suitable for simulation of amorphous semiconductors. Following this model the space charge distribution is mainly due to the charge trapped by the defects caused by the disordered structure of a-Si:H. The doped layers of the structure are explicitly deposited with the intention of obtaining a low dark conductivity value, and this is obtained by producing a semiconductor with a high density of localized states. Also the introduction of carbon leads to, again, a high density of localized states. This frequency dependence was not observed in full a-Si:H tandem solar cells with good material properties, nor experimentally neither by simulations. The results here presented show the existence of a direct relation between the experimentally observed capacitive effects of the stacked diodes and the quality of the semiconductor materials used to form the internal junction.

3.5 Spectral response

In Figure 3.8 the simulated spectral response under red, green and blue backgrounds are displayed confirming the non linear effect of the optical bias in the spectral response [12,13].

Under blue irradiation spectral response in the red range will increase when compared with it value without applied optical bias. Under red irradiation, the deep penetration of the red photons uniformly and exclusively into the back diode, and the transparency of the front diode to this wavelength push the electrical field up in the front diode (self-reverse effect) and down into the back one (self-forward effect), resulting an increased spectral sensitivity in the short wavelength range . In the green range both reverse and forward self bias effects coexist.

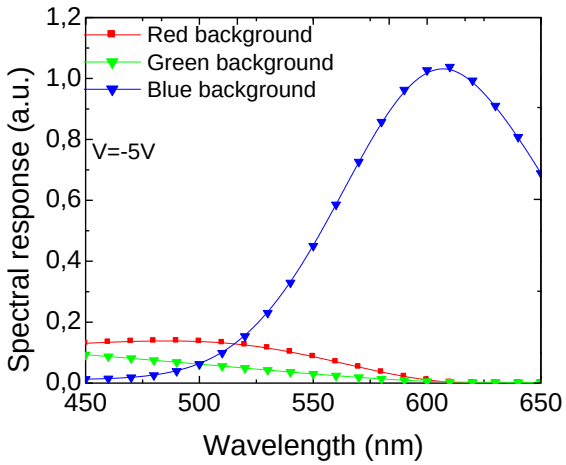

Figure 3.8 *Simulated spectral photocurrent under different background wavelengths.*

The sensor is a bias wavelength current-controlled device that makes use of changes in the wavelength of the background to control the power delivered to the load, acting as an amplifier of the optical signals. Its gain depends on the background illumination wavelength. If the electrical field increases locally (self optical amplification) the collection is enhanced and the gain is higher than one. If the field is reduced (self optical quench) the collection is reduced and the gain becomes less than one. This optical nonlinearity makes the transducer attractive for optical communications and can be used to distinguish a wavelength, to suppress a color channel or to multiplex or demultiplex an information-modulated wave.

4 Self bias amplification

4.1 Self bias amplification under uniform irradiation

In Figure 3.9, the spectral photocurrent at different applied voltages and 600Hz is displayed under red (a), green (b) and blue (c) background irradiations.

Results confirm that a self biasing effect (Chapter I, §5) occurs under unbalanced photogeneration. As the applied voltages changes from positive to negative the blue background enhances the spectral sensitivity in the long wavelength range. The red bias has an opposite behavior since the spectral sensitivity is only increased in the short wavelength range. Under green background the spectral photocurrent increases with the applied voltage everywhere.

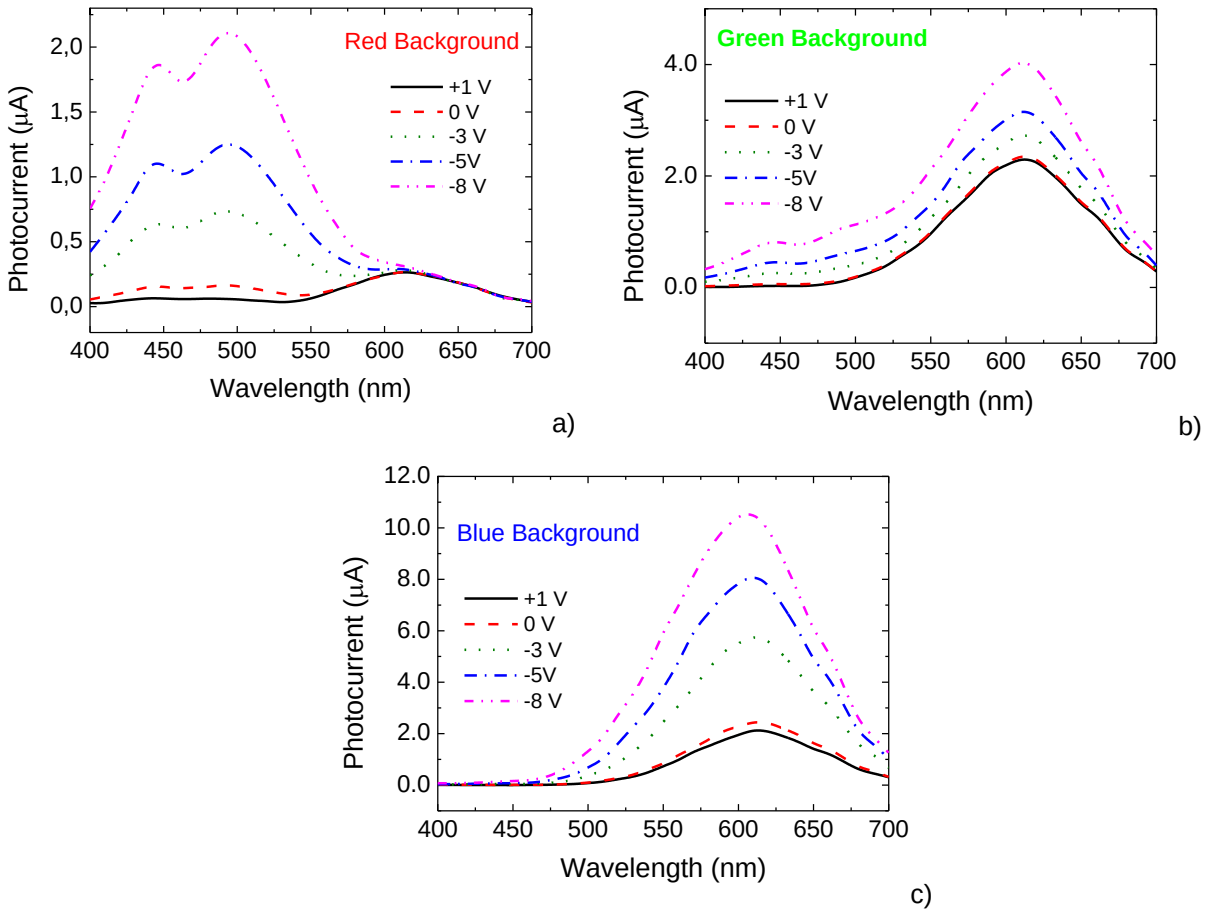

Figure 3.9 *Spectral photocurrent under reverse and forward bias measured with: a) Red, b) Green and c) Blue background illumination.*

In Figure 3.10 the spectral photocurrent is displayed at negative and positive electrical bias; without and under red (626 nm), green (524 nm) and blue (470nm) background illumination from the p side.

We have demonstrated (Chapter I, §5) that when an external bias is applied to a double pin structure, its major influence is in the field distribution within the less photo excited sub-cell. The front cell when under red irradiation, the back cell when under blue light and both when under green steady state illumination. In comparison with thermodynamic equilibrium (no background), the electric field under illumination is lowered in the most absorbing cell (self forward bias effect) while in the less absorbing cell reacts by assuming a reverse bias configuration (self reverse bias effect).

Results confirm that, under negative bias, a self biasing effect occurs under an unbalanced photogeneration. Blue optical bias enhances the spectral sensitivity in the long wavelength ranges and quenches it in the short wavelength range. The red bias has an opposite behavior: it reduces the collection in red/green wavelength ranges and amplifies in the blue range. The green optical bias only reduces the spectral photocurrent in the medium wavelength range keeping the other two almost unchangeable. Under positive bias no significant self bias effect was detected. This voltage controlled

light bias dependence gives the sensor its light-to-dark sensitivity allowing the recognition of a color image projected on it.

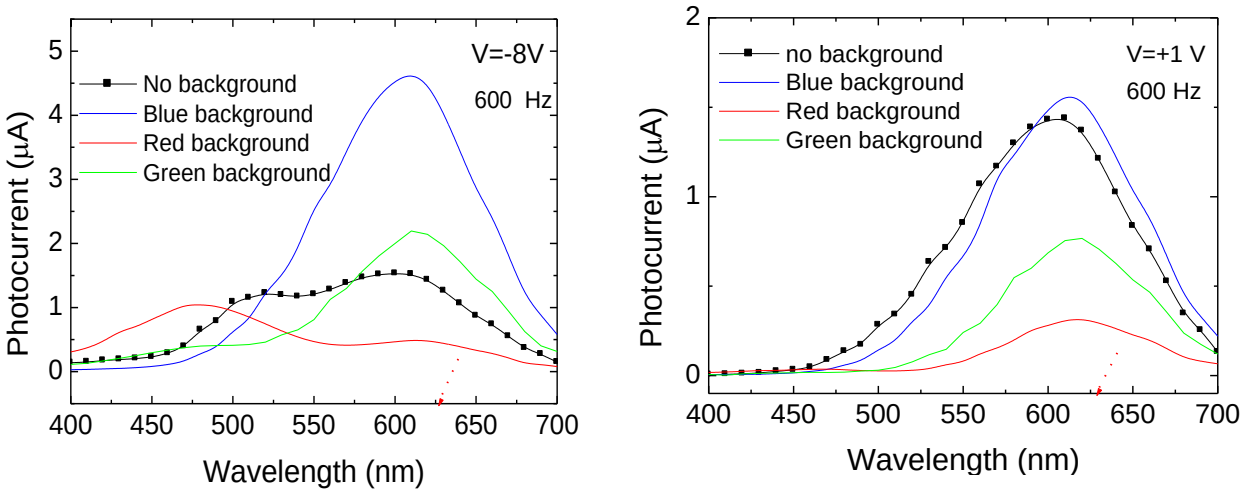

Figure 3.10 *Spectral photocurrent @ +1 V, -8 V without (dark) and under red, green and blue optical bias.*

In Figure 3.11 the ratio between the spectral photocurrents under red, green and blue steady state illumination and without it (dark) is plotted.

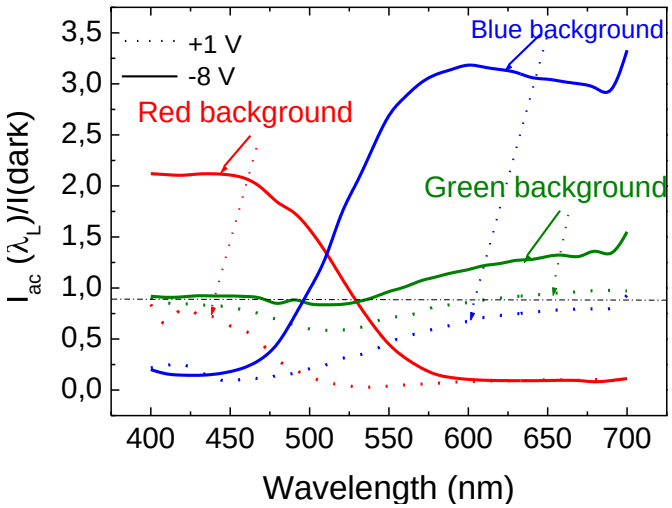

Figure 3.11 *Ratio between the photocurrents under red, green and blue steady state illumination and without it (dark).*

The sensor is a wavelength current-controlled device that makes use of changes in the optical bias wavelength to control the power delivered to a load, acting as an optical amplifier. Its gain, defined as the ratio between the photocurrent with and without a specific background depends on the background wavelength that controls the electrical field profile across the device. If the electrical field increases

locally (self optical amplification) the collection is enhanced and the gain is higher than one. If the field is reduced (self optical quench) the collection is reduced and the gain is lower than one. This optical nonlinearity makes the transducer attractive for optical communications.

4.2 Optical and voltage controlled light filtering

In order to analyze the spectral sensitivity of the device under different excitation frequencies, light bias and applied voltages, spectral response measurements without and with steady state applied optical bias and current-voltage characteristics were performed.

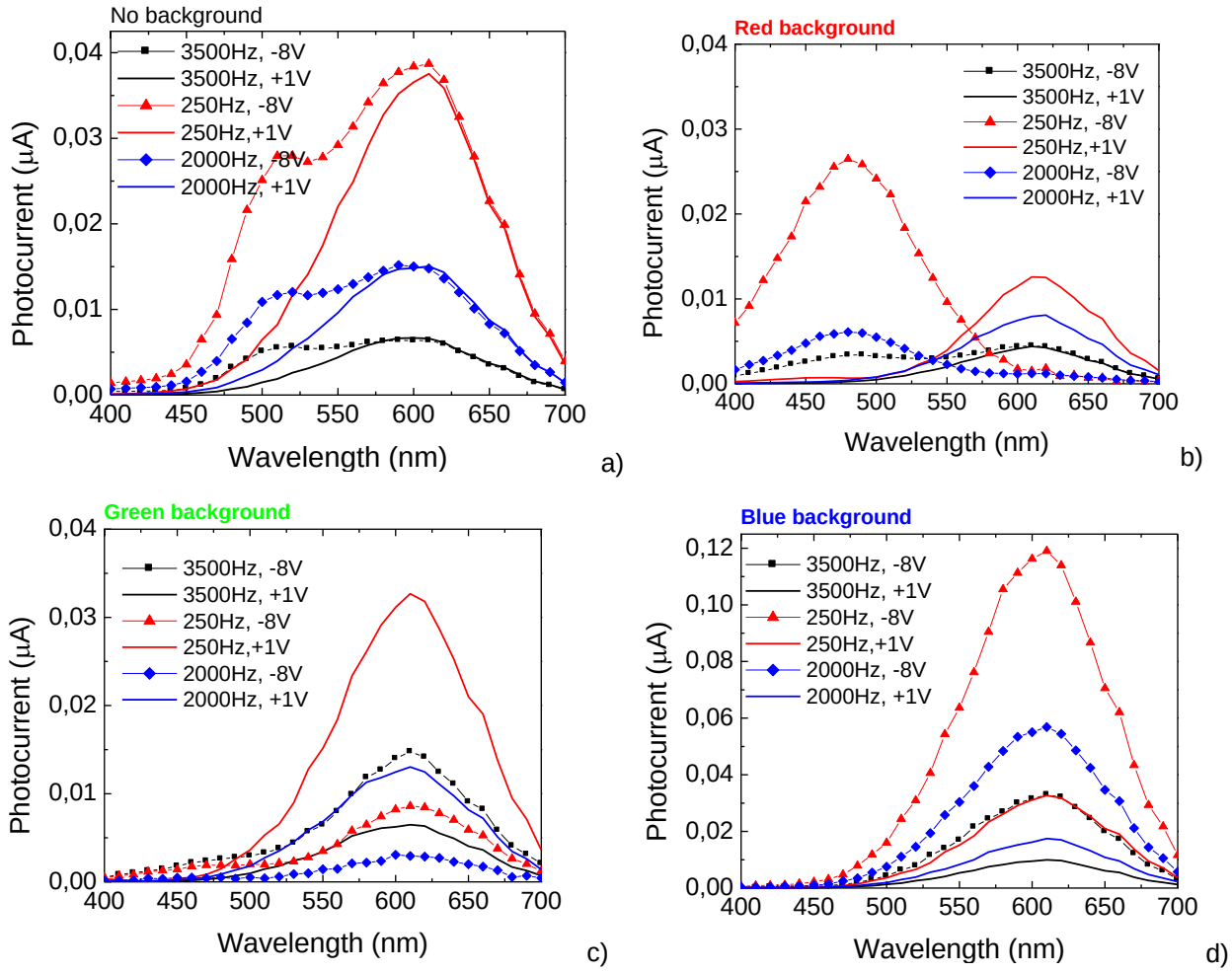

Figure 3.12 *Spectral photocurrent under positive (+1V) and negative (-8V) applied voltage and different frequencies without additional optical bias (a) or under steady state red (b), green (c) and blue (d) irradiations (background).*

In Figure 3.12 the spectral photocurrent at different frequencies is displayed under positive and negative applied voltages: a) without additional optical bias (φ=0) or under steady state irradiation: b) red (λ=624 nm); c) green (λ=526 nm) and d) blue (λ=470 nm) backgrounds.

Data show that the spectral sensitivity depends not only on the optical and electrical bias but also on the excitation frequency used. As the frequency increases the spectral photocurrent decreases suggesting unbalanced capacitive effects between both front and back diodes.

In Figure 3.13 it is displayed the measured photocurrents at 470nm, 526nm and 624 nm without (lines) and under red irradiation (symbols) as a function of the applied voltage. Results from Figure 3.12a and Figure 3.13 show that without applied optical bias, in the long wavelength range (> 600 nm), the spectral response is independent on the applied bias. An opposite behavior is found in the short wavelength range as, in this region of the spectrum, the collection increases strongly with the reverse bias. Under steady state optical bias and negative applied voltage, the blue background (Figure 3.12d) enhances the light-to-dark sensitivity in the long wavelength range and quenches it in the short wavelength range. The red bias (Figure 3.12b, Figure 3.13) has an opposite behavior; it reduces the ratio in the red/green wavelength range, mainly under reverse bias, and amplifies it in the blue one. Under green background no self amplification was detected (Figure 3.12c).

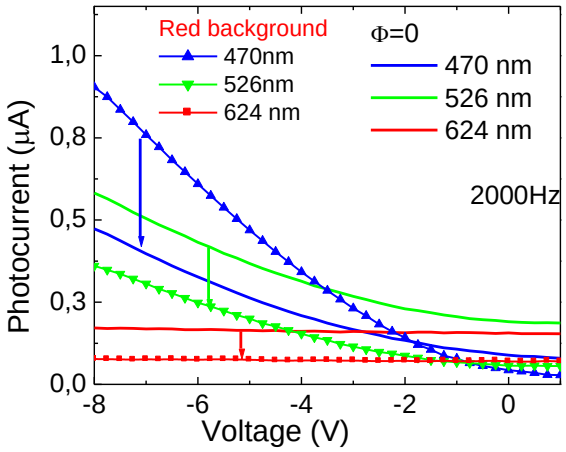

Figure 3.13 *Photocurrents at 470 nm, 526 nm and 624 nm without (lines) and under red irradiation (symbols) as a function of the applied voltage.*

4.3 Transfer function characteristics

The transfer function magnitude (or gain) at each wavelength allows us to determine the device ability to work as an optical filter and distinguish signals at different wavelengths. The spectral sensitivity was tested through spectral response measurements under different frequencies (250 Hz-3500 Hz), with and without steady state bias.

In Figure 3.14, the spectral photocurrent at 250 Hz, is displayed under red, green and blue background irradiations (color symbols) and without it (black symbols). For comparison the normalized spectral

photocurrent for the front, p-i'-n, and the back, p-i-n, photodiodes (lines) are superimposed (Chap II, §2.3).

Data show that each diode, separately, presents the typical response of single p-i-n cells with intrinsic layers based on a-SiC:H or a-Si:H materials, respectively. The front diode, based on a-SiC:H heterostructure, cuts wavelengths higher than 550 nm while the back one, based on a-Si:H, rejects the ones lower than 500 nm. The overall device presents a high spectral sensitivity in-between.

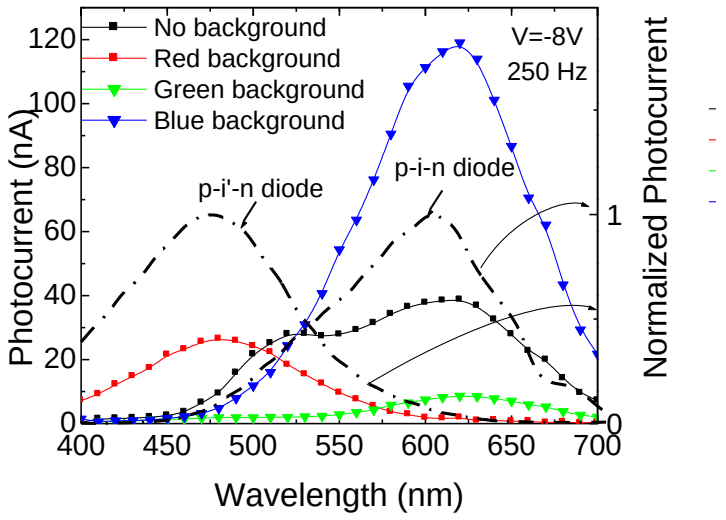

Figure 3.14 *Spectral photocurrent without and under different backgrounds (symbols).The normalized current of the front, p-i'-n, and the back p-i-n photodiodes (lines) is superimposed.*

By changing the wavelength of the background the front and back diode sensitivities can be tuned. Under red irradiation, when compared with its value without external background, the photocurrent is strongly enhanced at short wavelengths and disappears for wavelengths higher than 550 nm, acting as a short-pass filter. Under blue irradiation the devices behaves as a long-pass filter for wavelengths higher than 550 nm, blocking the shorter wavelengths.

In Figure 3.15 the spectral gain, defined as the ratio between the spectral photocurrents, under red (α^R), green (α^G) and blue (α^B) steady state illumination and without it (no background) are plotted at 250 Hz (lines) and 3500 Hz (symbols).

Results from both Figure 3.14 and Figure 3.15 confirm the wavelength controlled spectral sensitivity of the device, under steady state illumination. Under green irradiation the spectral response depends on the frequency. At 250 Hz the spectral sensitivity is strongly reduced while at 3500 Hz the device behaves as a band-stop active filter that screens out the medium wavelength range (green) enhancing only the photocurrent for wavelengths outside of that range.

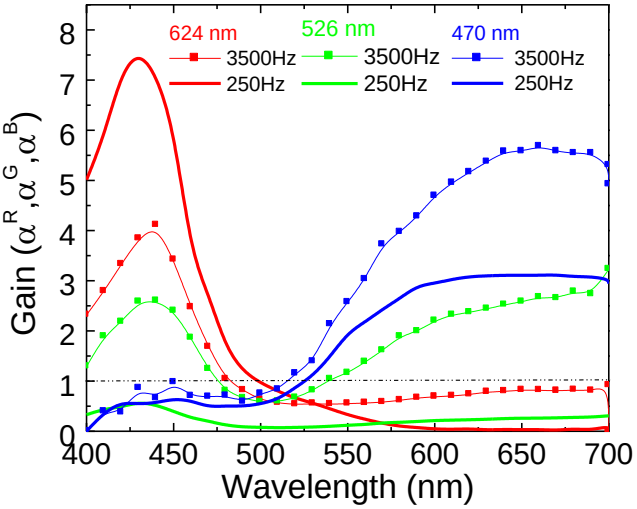

Figure 3.15 *Spectral gain under red (α^R), green (α^G), and blue (α^B), optical bias for different frequencies.*

4.4 Frequency analysis

The study of the frequency influence on the device performance was analyzed through the spectral response of the device without and with steady state optical light. Results are displayed in Figure 3.16. Figure 16a shows that without background light the curves measured under different frequencies exhibit the same trend with two peaks located at 500 nm and 600 nm. The signal is reduced with the increase of the frequency. Under blue steady state illumination (Figure 3.16 c) the spectral response exhibits a different trend with a single peak located at 600 nm. This is due to the strong attenuation of short wavelengths. The red steady state illumination (Figure 3.16 b) has the opposite effect with a single peak at 500 nm. Under green background (Figure 3.16 d) the spectral response shows two different regimes depending on the operation frequency. In the low frequency range the signal is similar to the trends obtained under red steady state light, while at higher frequencies it follows the behavior obtained with blue background.

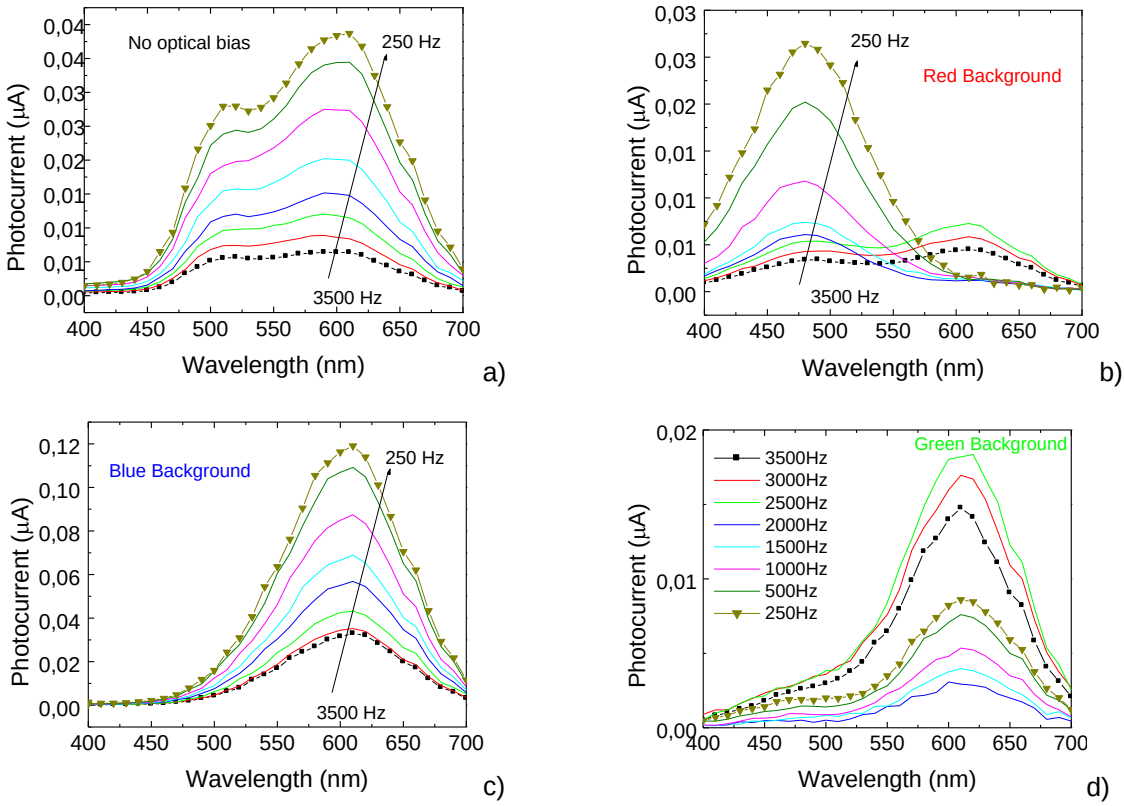

Figure 3.16 *Photocurrent variation with the wavelength for different frequencies at -8 V obtained: a) without, b) with red, c) with blue and d) with green background.*

Figure 3.17 shows the spectral gain as a function of the frequency under red (α^R), green (α^G) and blue (α^B) backgrounds at 624 nm (α_R, red channel), at 526 nm (α_G, green channel) and at 470 nm (α_B, blue channel).

Results show how the device reacts to the background wavelength and to the modulated input color channels (pulses) between 250 Hz and 3500 Hz.

Under red and green irradiations two frequency regimes can be considered. One, for frequencies lower than 2000 Hz, where either under red and green backgrounds the green and the red channel gains are very low (<<1) and the blue channel gain is strongly enhanced (>>1) under red background or reduced (<1) under green irradiations. In the other regime, for frequencies higher than 2000 Hz, the gain increases with the frequency, gradually under red and quickly under green steady state illumination. Under blue, the gain increases slowly with the frequency being higher than unity for the red and green channels and lower for the blue one.

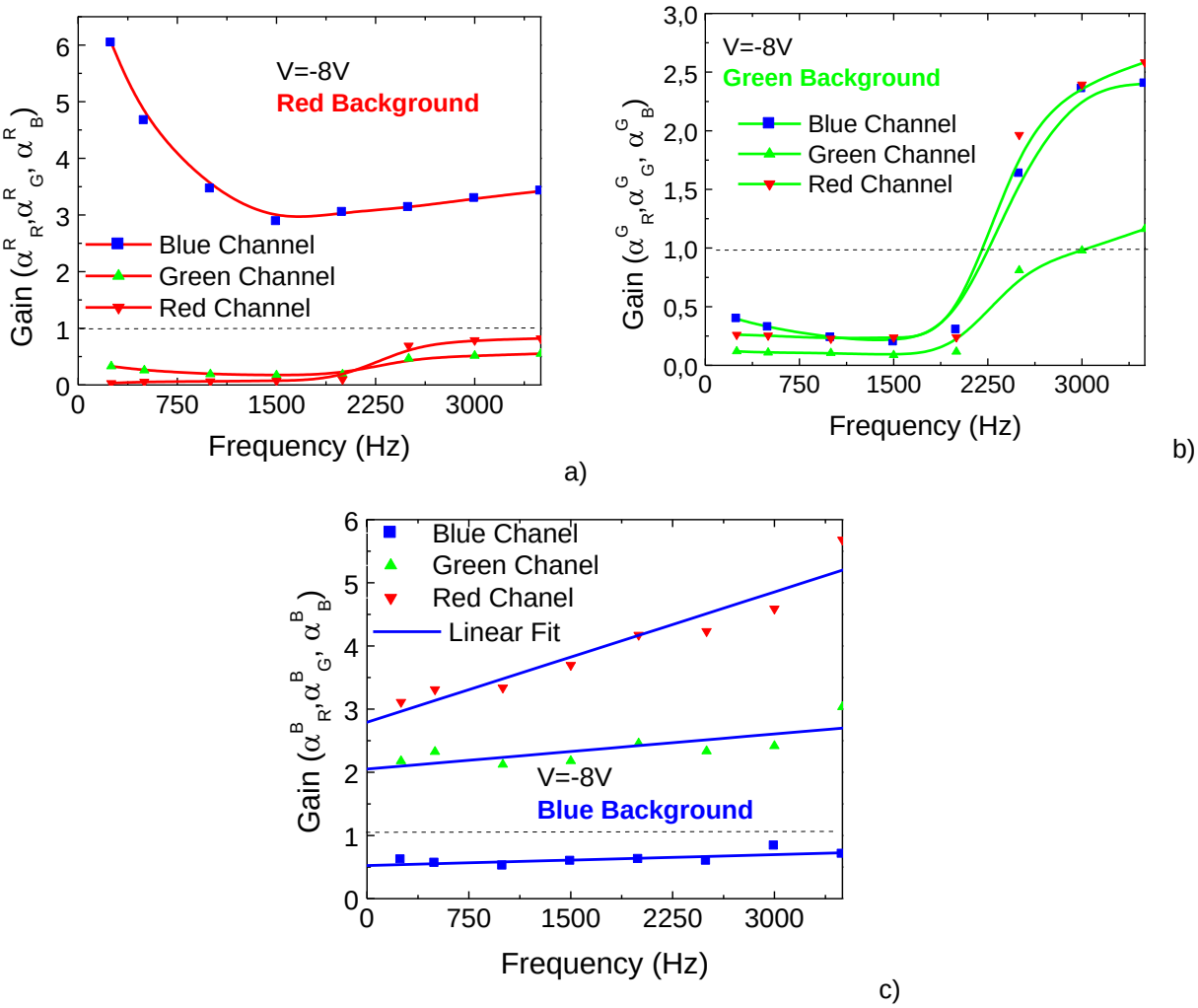

Figure 3.17 *Spectral gain as a function of the frequency at 624 nm (red channel), at 526 nm (green channel) and at 470 nm (blue channel) under red (α^R), green (α^G) and blue (α^B) backgrounds. a) short-pass filter , b) band-stop filter, c) long-pass filter.*

Consequently, under red irradiation (Figure 3.17a) the transfer function has extra gain at short wavelengths (blue channel), than at longer wavelengths acting as a short-pass filter whatever the frequency. Under green background (Figure 3.17b), the manipulation of amplitude is achieved by changing the frequency of the modulated lights. At high frequencies the device is a band-stop active filter that works to screen out wavelengths that are within a certain range (green channel), giving easy passage only all wavelengths below (blue channel) and above (red channel). In the low frequency regime all the amplitudes are quenched. Under blue steady state optical bias (Figure 3.17c) the device behaves as a long-pass active filter that transmits and enhances long wavelength ligth (red and green channels) while blocking shorter wavelengths (blue channel).

5 Transient optical bias controlled amplification

5.1 Monochromatic channels

5.1.1 Effect of the background wavelength

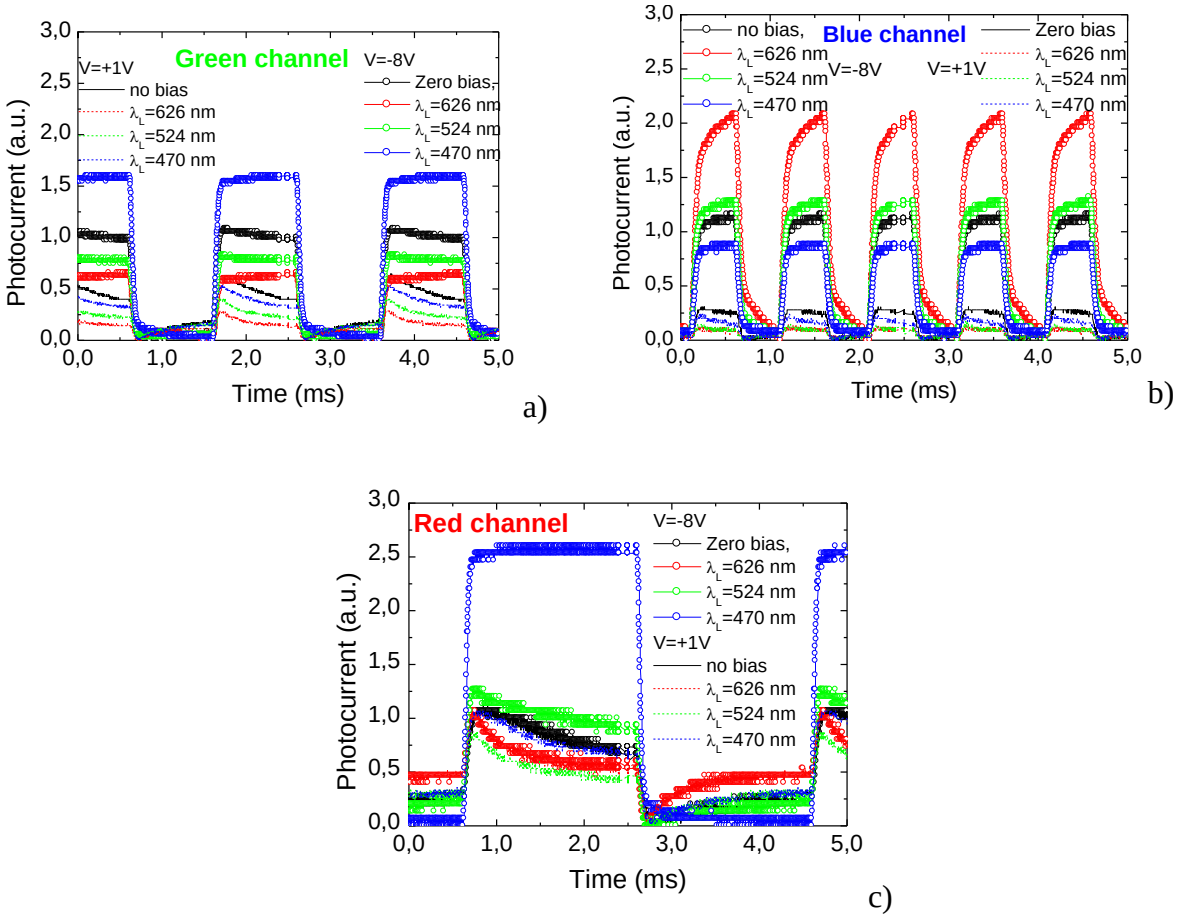

Figure 3.18 *Green (a), blue (b) and red (c) channels under negative (symbols) and positive (dot lines) voltages without (no bias) and with (λ_L) bias.*

Three monochromatic input channels: red (R: 626 nm), green (G: 524 nm) and blue (B: 470nm) illuminated separately the device. Steady state red, green and blue optical bias is superimposed separately and the photocurrent generated measured at -8V and +1 V. In Figure 3.18 the signal is displayed for each monochromatic input channels. The signal without optical bias was normalized to unity.

Results confirm that, even under transient conditions, blue steady state optical bias amplifies the red and the green channels and reduces the blue one. Red steady state optical bias has an opposite behavior while the green steady state optical bias reduces the green channel keeping the other two almost unchangeable.

5.1.2 Effect of the frequency

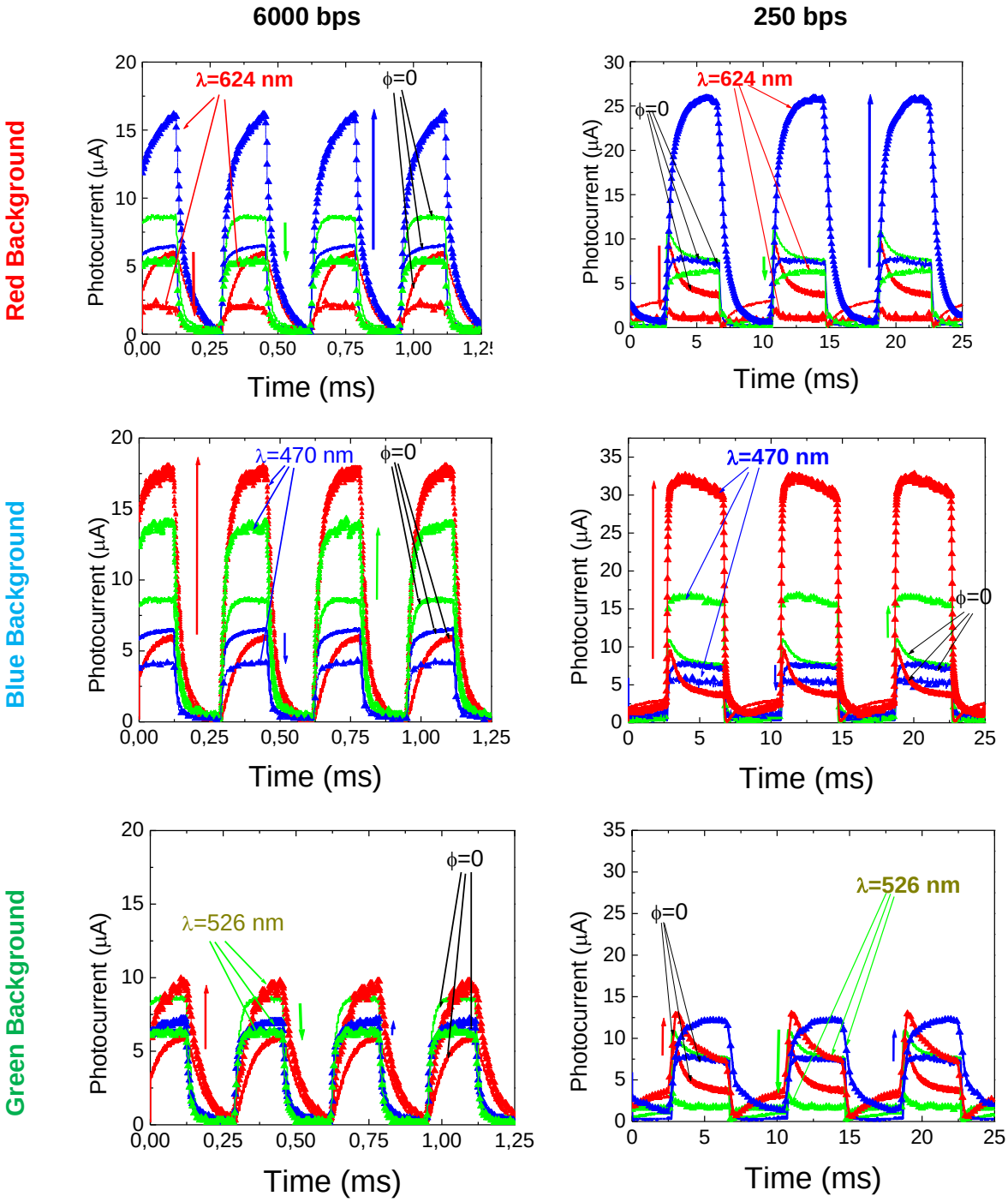

Figure 3.19 *Input red, blue and green transient signals at -8V without (φ =0) and with: red (624 nm), blue (470 nm) and green (526 nm) steady state optical bias at 6000 bps (left) and 250 bps (right).*

Three monochromatic pulsed lights (input channels): red, green and blue at 6000 bps and 250 bps illuminated separately the device. Steady state red, green and blue optical bias was superimposed

separately and the photocurrent generated measured at -8 V. In Figure 3.19 the transient photocurrent is displayed for each monochromatic input channel, at the high and low frequency regime.

Results show that, at both bit rates, the blue background enhances the light-to-dark sensitivity of the red (α^B_R>1) and green (α^B_G>1) channels and quenches the blue (α^B_B<1) as shown in Figures 3.15 and 3.16. The red bias has the opposite behavior; it reduces the ratio in the red/green wavelength range and amplifies it in the blue one. Under green irradiation the red and blue signals are enhanced and the green reduced by α factor that depends strongly on the bit rate used for the transmission (see color arrows trend in the figures).

5.2 Channel discrimination

Taking into account the input channels of Figure 3.18, in Figure 3.20 it is displayed the difference between the blue (a) and red (b) channels (λ_S) with red (λ_R), green (λ_G) and blue (λ_B) optical bias and without.

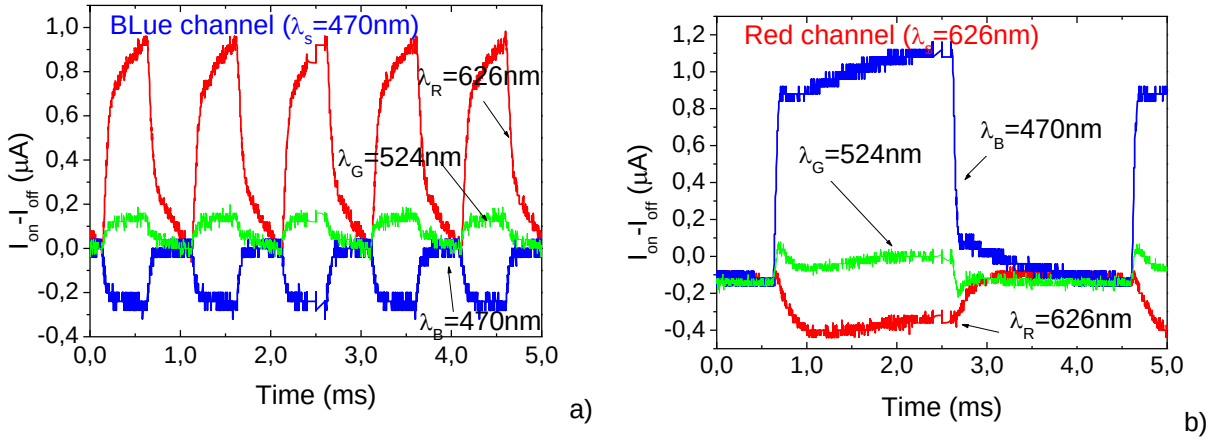

Figure 3.20 *Difference between the blue (a) and red (b) channels (λ_S) with red (λ_R) green (λ_G) and blue (λ_B) optical bias and without it.*

Results show that under appropriated homogeneous wavelength irradiation it is possible to select or to suppress a color channel by changing the wavelength of the background [14].

5.3 Optical bias controlled wavelength discrimination

For the color image sensor analyzed in Chapter I (§4.4.2), only the red channel (the scanner) is used (red channel). To simulate a color image at the XY position, using the multiplexing technique, a low

intensity moving red pulse scanner (Φ_S, λ_S), impinges in the device in dark or under different red, green and blue optical bias (color pattern, $\Phi_{L,}$ $\lambda_{RGB,L,}$ $\Phi_L>\Phi_S$). Figure 3.21 displays the experimental acquired electrical signals. The image signal is defined as the difference between the photocurrent with (light pattern) and without (dark) optical bias (arrows in Figure 3.21).

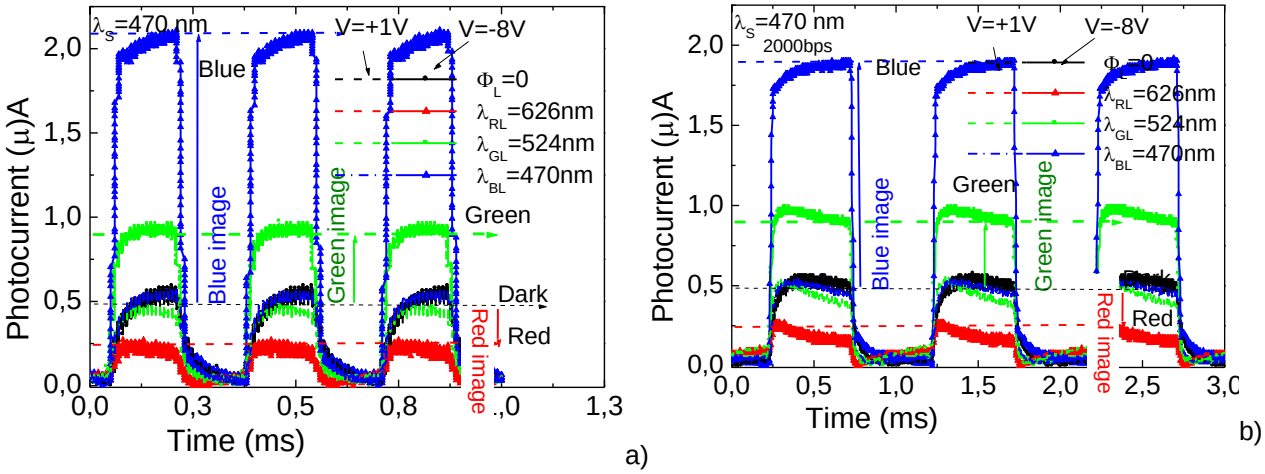

Figure 3.21 *Experimental color recognition using the WDM technique: a)6000bps. b)2000bps.*

Results from Figure 3.21 are in agreement with the data from Figure 1.17 (Chapter I, §4.4.2). At -8V the green and blue image signals are positive while the red one is negative which is in. Around +1V the signals with and without blue background are the same leading to an image signal null (color rejection). Also, as the voltage changes from negative to positive the image signal reverses in signal confirming the color rejection in between.

CCD digital image sensors are only capable of recording one color at each point. Since, under steady state illumination (optical image) each phototransistor acts as a filter this multiplexing readout technique can also be used if the stack device is embedded in silicon forming a two layer image sensor that captures full color at every point. Here, a demosaicing algorithm is needed for color reconstruction.

6 MUX/DEMUX device

6.1 WDM device

Usually the term wavelength division multiplexing, WDM, is used when channels are quite widely separated in the spectral domain. MUX channels are demultiplexed (DEMUX) using wavelength selective channel filters (Figure 3.22).

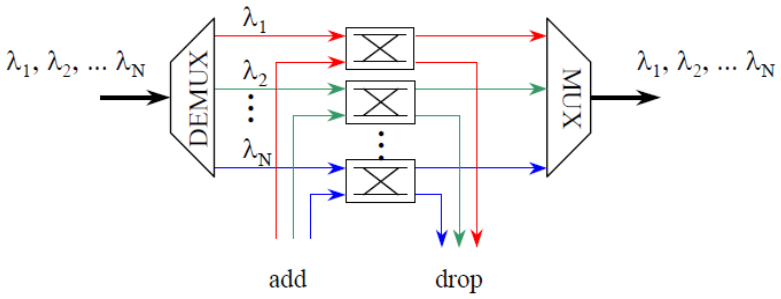

Figure 3.22 *Schematic MUX/DEMUX diagram.*

Wavelength demultiplexer performs a wavelength-to-space conversion. In the figure, a wavelength (de)multiplexer is used in each edge of the network, to accommodate the wavelength switching. This is a photonic implementation of two-by-two switches and has been the basis of many classical network architectures. The switches have two states: in the BAR state, data entering on the upper/lower input leaves on the upper/lower output and in the CROSS state, the data leaves on the lower/upper output. In the BAR states and CROSS states, signal in input channels are delivered to the output at the same wavelength (BAR) or are shifted (CROSS) to another wavelength.

The proposed DEMUX [15, 16, 17] consists of a pi´npin tunable capacitive demultiplexer whose background can be varied to select different wavelength channels. We choose this new concept for communicating in visible range in a "language" that can be understood by all components of the system.

6.2 Multiplexed signal under steady state optical bias

Three monochromatic pulsed lights (input channels): red, green and blue at 6000 bps illuminated separately the device. Steady state red, green and blue optical bias was superimposed separately and the photocurrent generated measured at -8 V.

In Figure 3.23 the input and the multiplexed channels, with and without green bias, are displayed at -8V. The sequence of bits is shown at the top of the figure to guide the eyes. Results show that the presence of the optical bias reduces significantly the amplitude of green channel while a slight increase is observed for the other two. The sum of the input channels (R+G+B; symbol) shows that when the green channel is ON no amplification occurs. This suggests that the green channel can be tuned by making the difference between the multiplexed signal with and without green irradiation (Δ, symbols).This nonlinearity is due to the transient asymmetrical light penetration of the input channels into the device and to its optical filters properties. Under green light irradiation, since the green photons are absorbed across front and back photodiodes, the electric field decreases on both sub-cells. So, some of the

carriers generated by the green channel, also in both sub-cells, recombine and the collection decreases. When the red or blue channels are ON, the generation occurs only in one sub-cell. The electrical field, in the presence of the red and blue channels, lowers, respectively, in the back and front photodiodes, while the correspondent front and back photodiodes react by assuming a reverse bias configuration compensating the effect of the green optical bias. This self bias effect explains the slight increase on the red and blue collection under green optical bias. This nonlinearity provides the possibility for selectively remove and add a particular wavelength and can be used to boost signal power after multiplexing or before demultiplexing which usually introduce optical loss into the system.

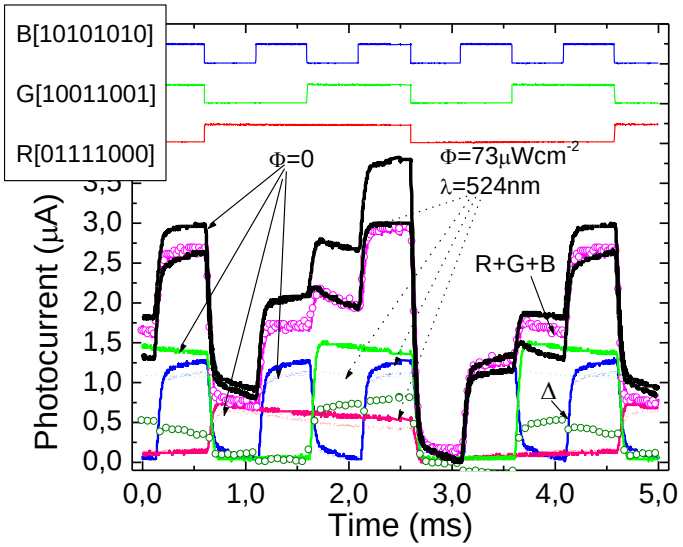

Figure 3.23 *Single and combined signals @-8V; without (solid arrows) and with (dotted arrows) green optical bias.*

In Figure 3.24, at +1 V and -8 V, the same multiplexed signal is displayed under red, green and blue optical bias wavelengths (color lines) and without it (Black lines) [18]

Results show that under reverse bias the background wavelength controls the output signal accordingly with Figure 3.18. Under negative bias the red background enhances the blue channels and quenches the red and green ones. Green irradiation reduces the green channel and the blue background reduces the blue channel contribution. Under positive bias, whatever the background wavelength, only a small reduction of the signal is observed.

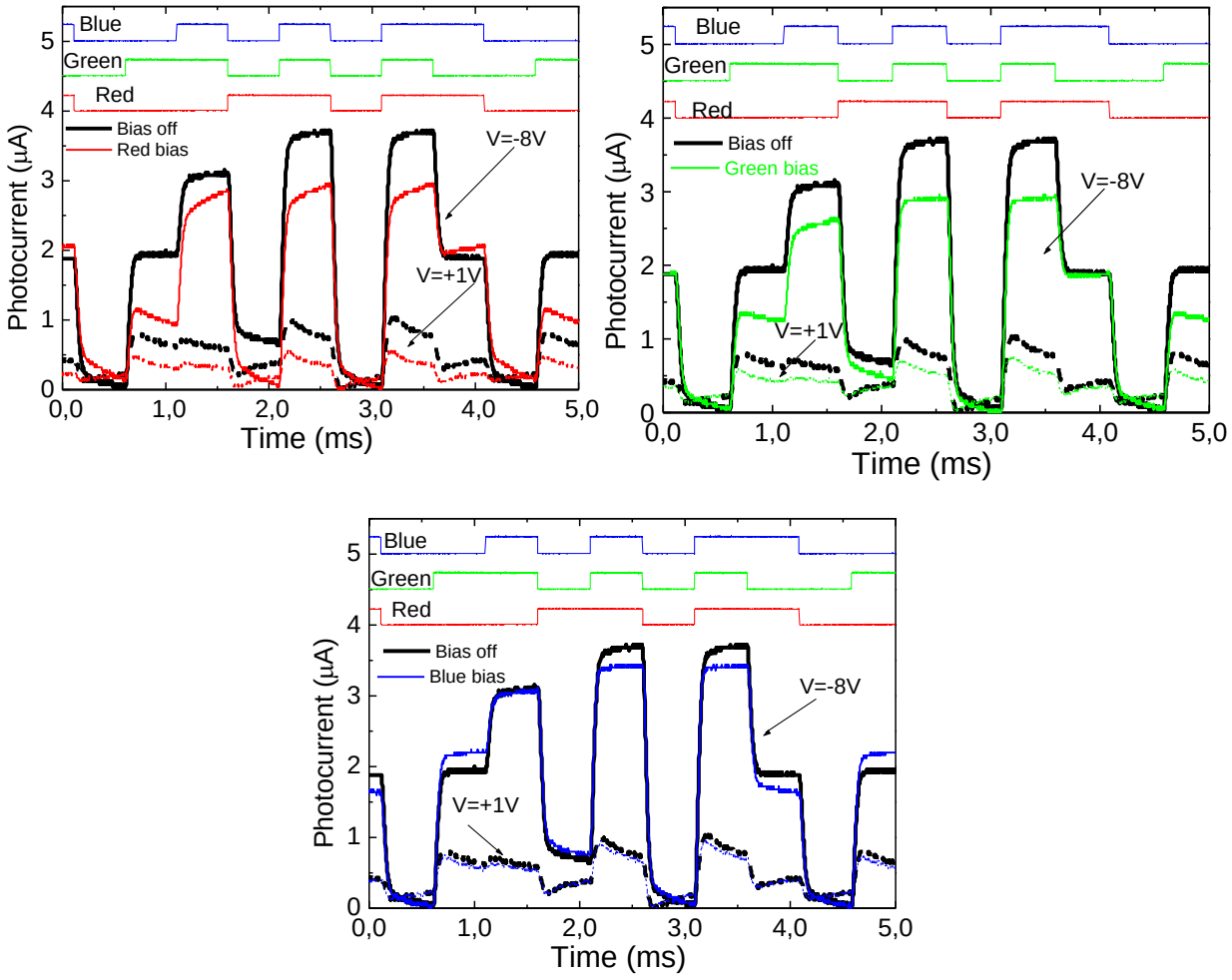

Figure 3.24 *Multiplexed signals at -8V/+1V (solid /dot lines); without (bias off) and with red, green and blue optical bias*.

6.3 Optical tuning of the input channels

One possible device application is the optical tuning of the green and blue channels using adequate steady state optical bias. In Figure 3.25 it is displayed the multiplexed signal obtained at reverse bias using the same optical signal combinations of Figure 3.23.

The output signal was acquired without steady state optical bias and with green (Figure 3.25 left) and blue (Figure 3.25 right) optical bias.

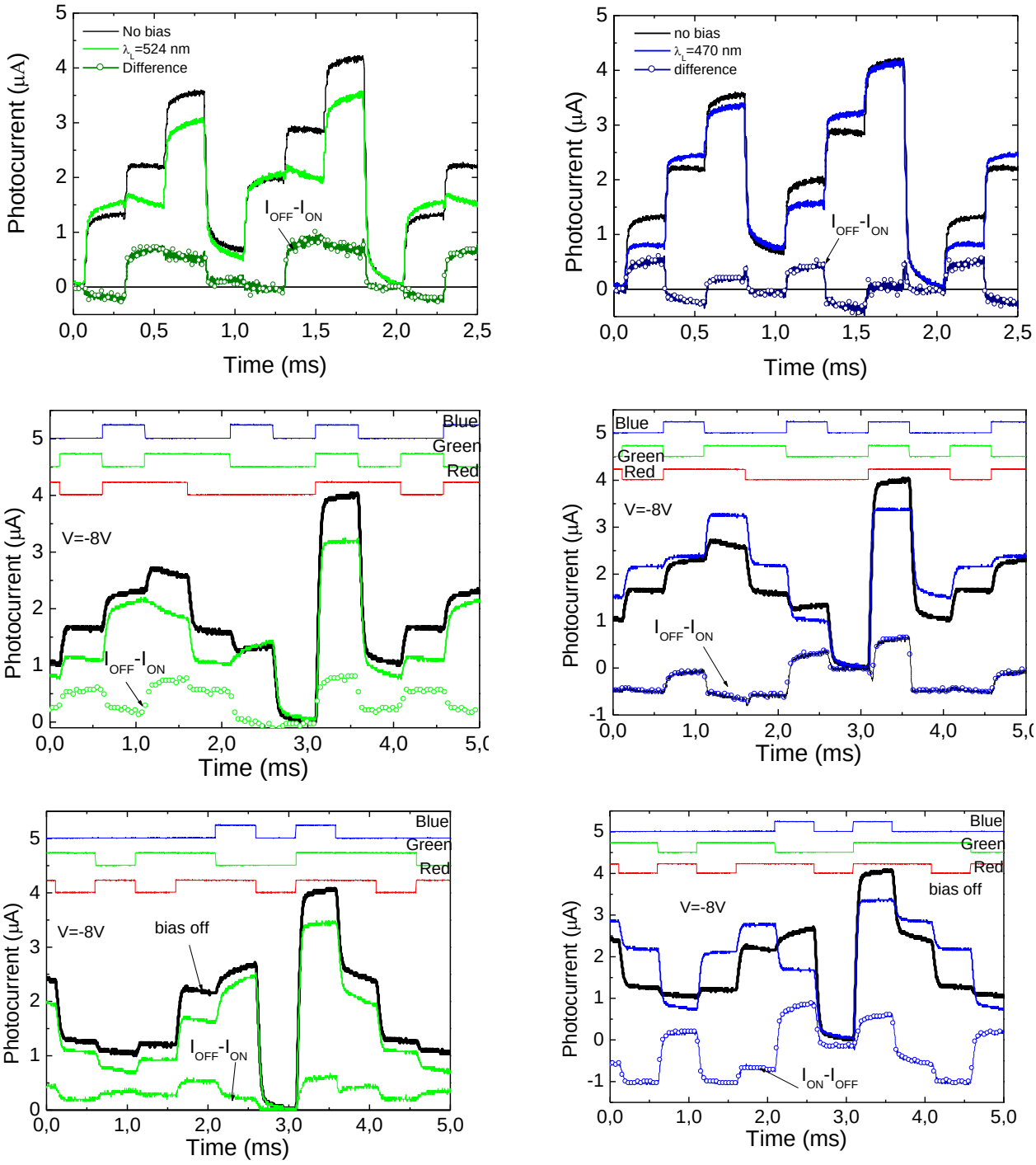

Figure 3.25 *Multiplexed signal under obtained at reverse bias without optical bias (black line) and under steady state illumination of wavelength (light colored line): Left-524 nm and Rigth-470 nm. The difference between both signals is also plotted (dark colored line).*

Results show that the presence of steady state illumination changes the output signal. Under green optical bias the multiplexed signal decreases when the green channel is ON and remains unchanged when it is OFF (Figure 3.25 left). Thus, the difference between the signals without and with green bias

indicates the presence and absence of the green channel. A similar behavior is observed under blue steady state illumination (Figure 3.25 right), and thus the difference signal represents the successive ON-OFF states of the blue channel.

It is important to remark that when the three channels are ON the signal with and without blue optical bias are identical, which results in a mismatch for the recognition of the blue channel. This mechanism can be used for the detection of the presence of the input green and blue channels, which integrated in the optical communication systems can work as an alarm or optical diagnostic, identifying any anomalous transmission of these channels.

6.4 Optical encoded data stream

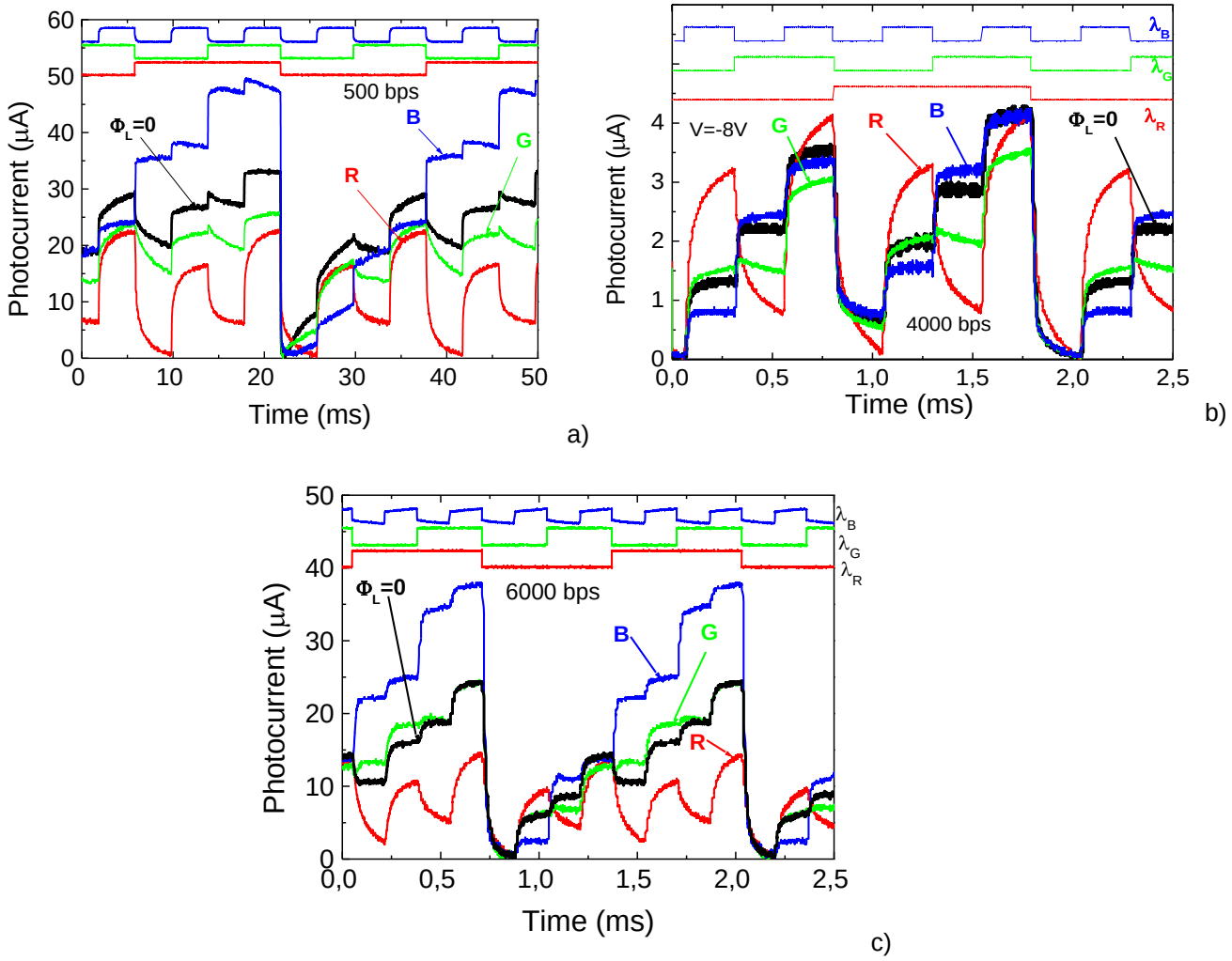

Figure 3.26 *Output waveform signal at -8V; without (φ_L=0) and with (R, G, B) optical bias. The bit sequences are shown at the top of the figures.*

In Figure 3.26 a chromatic time dependent wavelength combination of R (λ_R=624 nm), G (λ_G=526 nm) and B (λ_B=470 nm) pulsed input channels, with different bit sequences and bit rates was used to generate a multiplexed signal in the device: a) 500 bps, 250 Hz, b) 4000 bps, 2000Hz and (6000 bps, 3000Hz). The output photocurrents, under negative (-8V) voltage with (color lines) and without (black lines) background. The bit sequences are shown at the top of the figures.

Results show that, even under transient input signals, the background wavelength controls the output signal due to the asymmetrical light penetration of the input channels across the device together with the modification on the electrical field profile due to the optical bias. This high optical nonlinearity makes the optimized devices attractive for the amplification or quenching of all optical signals and enables the device to demultiplex an optical encoded data stream.

To recover the transmitted information (4000bps, 8 bit per wavelength channel) the output waveforms under red irradiation and without it were used as displayed in Figure 3.27. Both multiplexed signals, during a complete cycle (T), were divided into eight time slots (Δ=250 μs) corresponding to one bit where the independent optical signals can be ON (1) or OFF (0). In Figure 3.27 all the possible combinations of the three input channels are present. So, the waveform of the output signal, without optical bias, is an 8-level encoding (2^3) to which it corresponds 8 different photocurrent thresholds.

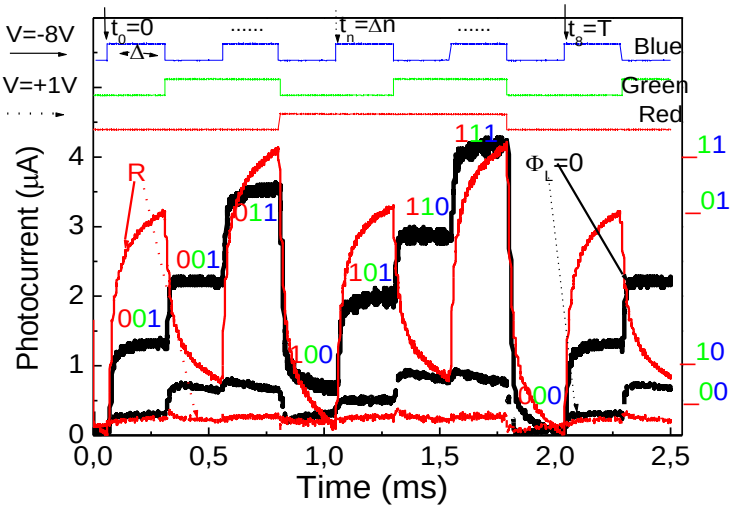

Figure 3.27 *Output waveform signal at -8V and +1 V; without (φ_L=0) and with (R) optical bias.*

Taking into account Figure 3.17, under red background the red channel is strongly quenched (α^R_R<<1) and the blue are enhanced (α^R_B>>1) for the three bit rates. So, the output waveform becomes a main 4-level encoding (2^2, right axis in Figure 3.27). Here, the higher level corresponds to both blue and green ON (_11) and the lower to the absence of both (_00). The other two intermediate levels are ascribed, the upper level to the ON state of the blue (_01) channel and the lower to the green channel ON (_10). To decode the red channel, the same time slots without and with red background have to be compared, being higher the ones when the red channel is ON. Using this simple algorithm the

independent red, green and blue bit sequences were decoded as: B [10101010], G [01100110] and R [00011110].

A demux algorithm was implemented in Matlab that receives as input the measured photocurrent and derives the sequence of bits that originated it. The independent red, green and blue bit sequences in Figure 3.26 were decoded as: a) B[10101010], G[10011001], R[01111000]; b) B[10101010], G[011001100], R[00011110]; and c) B[01010101], G[00110011], R[1111000].

6.5 Data inputs prediction

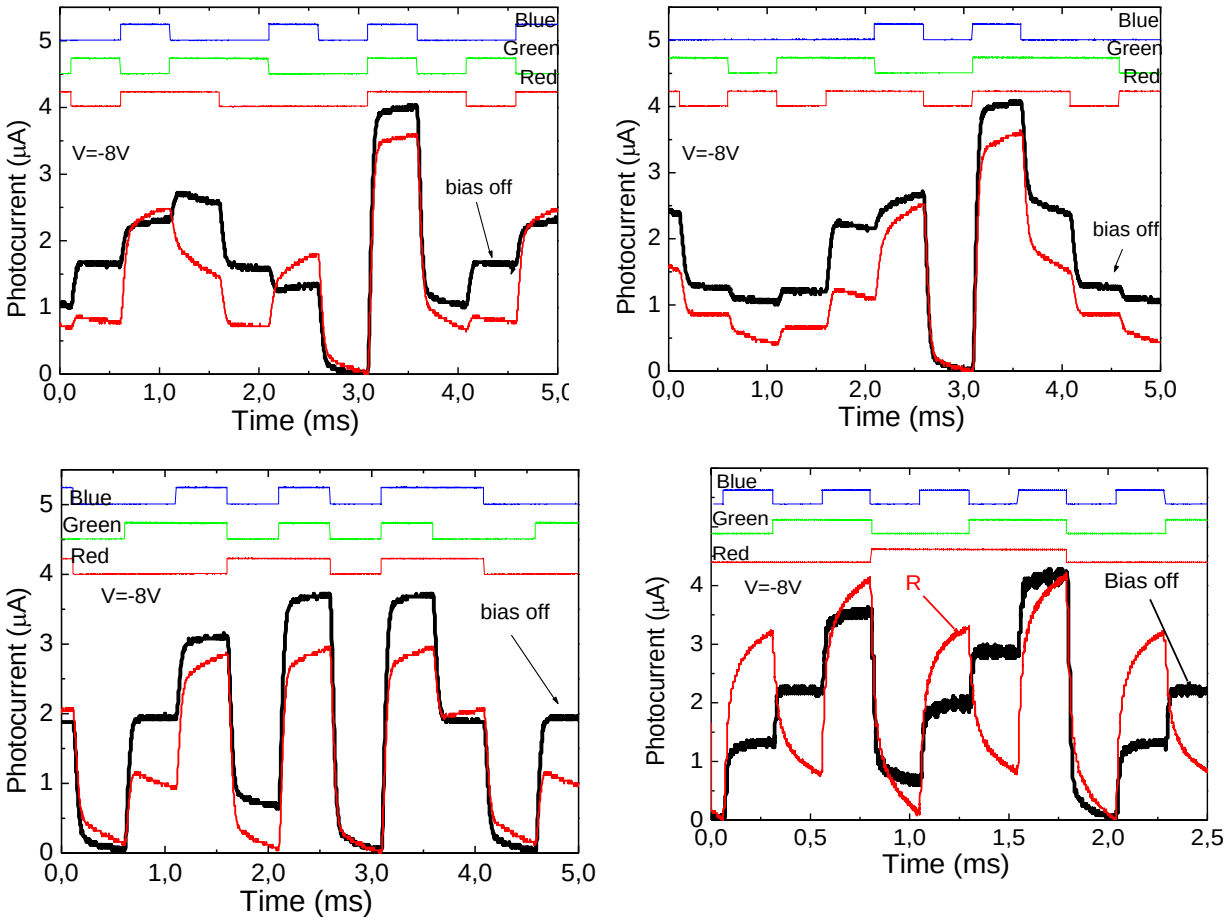

Figure 3.28 *Output waveform signal at -8V; without (bias off) and with (R) optical bias.*

The goal is to extract independent red, green and blue bit sequences. We have used the same algorithm as in Chapter II, §4.2. This algorithm uses of the variation of the photocurrent instead of its absolute intensity to minimize errors caused by signal attenuation. A single linkage clustering method is applied to find automatically eight different clusters based on the measured current levels with and

without red optical bias. This calibration procedure is performed for a short calibration sequence. Each cluster is naturally bound to correspond to one of the known eight possible combinations of red, green and blue bits. Following this procedure the sequence of transmitted bits can be recovered in real time by sampling the photocurrent at the selected bit rate and finding for each sample the cluster with closest current levels.

In Figure 3.28 different chromatic wavelength combination of R (λ_R=624 nm), G (λ_G=526 nm) and B (λ_B=470 nm) pulsed input channels with different bit sequences are displayed without and with red background. The decoded bit sequences for each color channel are displayed in the top of the figures.

The results show the good potentialities of the algorithm in predicting the transmitted sequences and in attenuating through the filtering method possible noise distortions in the relational experimental output waveforms. As a result, it can be concluded that the operation of the transmitted sequence's algorithm presents a viable option for inclusion within a demultiplexed network.

7 Optical filters

7.1 Long, short and stop band photonic filters

The deployment of Fiber to the Home (FTTH) access networks and the emergence of Passive Optical Network (PON) installations leads to a need for mass production of bi-directional optical modules that can exchange data up- and downstream through a single fiber.

There has been much research on semiconductor optical filters [3, 4, 19]. Here, a specific band or frequency need to be filtered from a wider range of mixed signals. Filters are often used to emphasize signals in a certain wavelength range and reject signals in other ranges. Optical filters have a nonlinear amplitude-dependent response to each incident light wave. This nonlinearity provides the possibility for selectively removing and adding wavelength and can be used to boost signal power after multiplexing or before desmultiplexing.

Long-pass filters are used in applications requiring the rejection of short-wavelength signals and short-pass filters are used in applications requiring the rejection of long-wavelength signals. Photodiodes with high optical isolation in the stop-band as well as high responsivity in the pass-band for a short-pass and a long-pass filter can be designed. Amorphous silicon carbon tandem structures, through an adequate engineering design of the multiple layers' thickness, absorption coefficient and dark conductivities can accomplish those functions.

Here, we propose photodiodes with integrated optical thin film filters reducing module cost by minimizing the number of discrete filters. A new method is presented for optical routing using a double pi'n/pin a-SiC:H heterostructure that presents wavelength router properties and can be used to construct photonic integrated circuits with capacitive demultiplexer, optical amplifier and photodetectors [20, 21, 22]. We demonstrate the integration of short-pass and long-pass optical thin film filters targeting

Passive Optical Network (PON) applications combined with a versatile a-SiC p-i'-n/pin photodiode device concept.

7.2 Frequency dependence

Figure 3.29 shows the time dependent photocurrent signal measured under reverse (-8V, symbols) and forward (+1V, dotted lines) bias using different input optical signals without (no bias) and with (λL) red, green and blue steady state additional optical bias, at low (top side of the figure) and high (down side of the figure) sampling frequencies. Both optical signals and steady state bias were directed onto the device by the side of the a-SiC:H thin structure. The optical signals were obtained by wave square modulation of the LED driving current and the optical power intensity of the red, green and blue channels adjusted to 51, 90, 150 μW/cm^2, respectively. The steady state light was brought in LEDS driven at a constant current value (R: 290 μW/cm^2, G: 150 μW/cm^2, B: 390 μW/cm^2).
The main difference between both sampling frequencies is related to the decay time of the photocurrent signal.

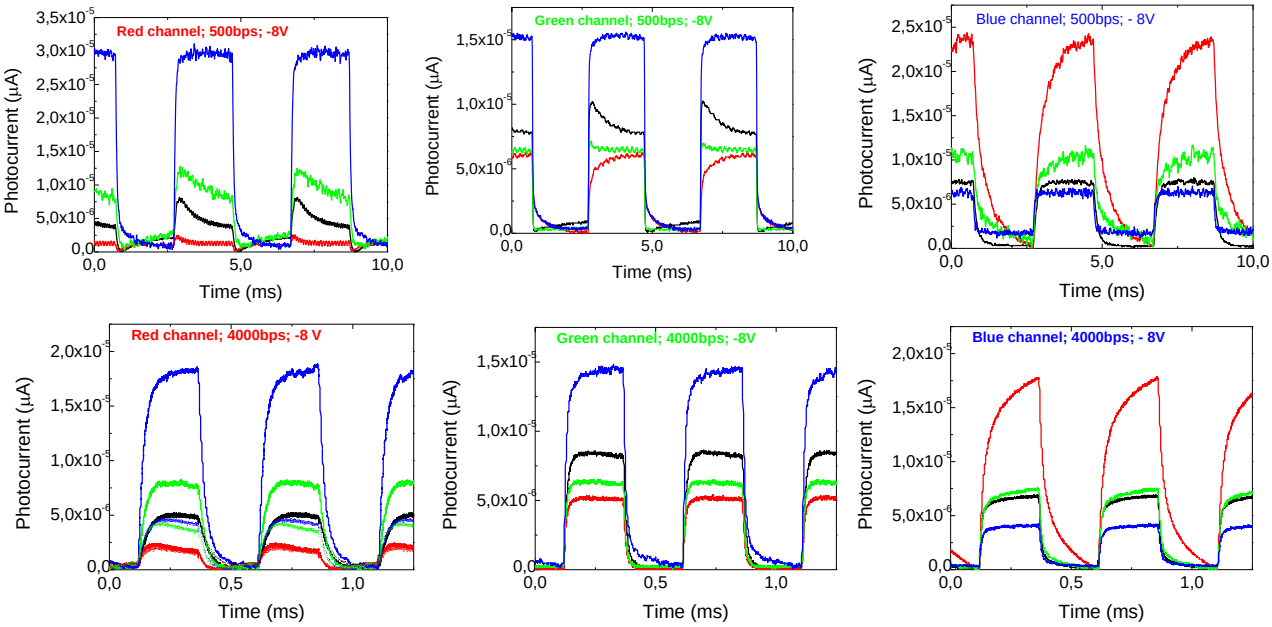

Figure 3.29 *(a) red (b) green and (c) blue channels under reverse and forward voltages without and with (λ_L) red, green and blue steady state bias at 250 Hz and 2000 Hz, on top and down part of the figure, respectively.*

7.3 Light filtering effect

Results from Figures 3.19 and 3.29 have shown that the red background enhances the light-to-dark sensitivity of the blue (α^R_B>1) and green (α^R_G>1) channels and quenches the red (α^R_R<1) acting, so, as a short pass filter. The blue bias has the opposite behavior; it reduces the ratio in the blue/green wavelength range and amplifies it in the red one, acting as a long pass filter. Under green irradiation the red and blue increases slightly and the green is reduced (α^G_G<1) by a factor that depends on the bit rate used for the transmission, acting as a band-stop filter.

A polychromatic combination of red, green and blue input channels in different color bit sequences was used to generate a multiplexed signal. In Figure 3.30, at 6000 bps and -8 V, the output with (RGB color lines) and without (φ=0, dark lines) background is displayed.

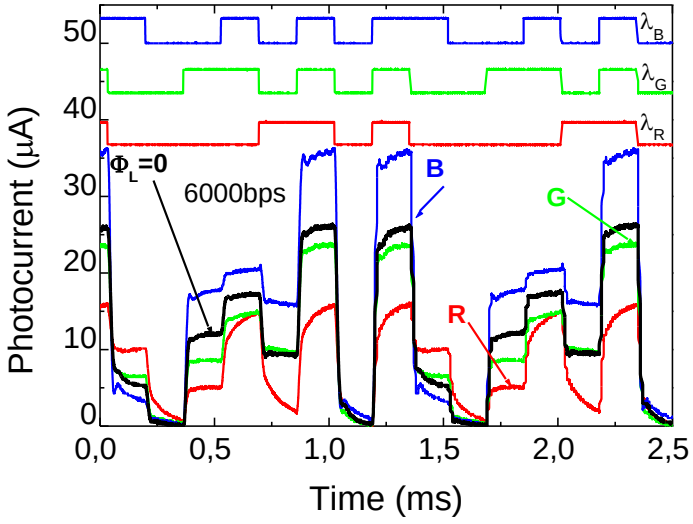

Figure 3.30 *Multiplexed signals with and without different backgrounds. On the top, the optical signal used to transmit the information.*

In Figure 3.31 the filtered signals under red, green and blue light control are displayed. The bit sequences used to transmit the information are shown at the top of the figures.

In Figure 3.31a the signal under red background is displayed. Here the quench of the electric field in the p-i-n back diode (Figure 3.4) cuts the red response and increases the spectral sensitivity of the front p-i'-n one in the blue-green range (Figure 3.14). Under red irradiation the red channel is rejected (short-pass filter), so the mixture of both blue and green is recovered. The filtered signal is a 4-level encoding (2^2, see thresholds in Figure 3.31a),

Under blue irradiation the optical bias effect is opposite (Figure 3.31b), the blue channel is rejected (long-pass filter) due to the quench of the electric field in the p-i´-n front diode. So, the change in the transmitted information (Bias ON-Bias OFF) is due exclusively to the presence of both red and green channels. The filtered signal becomes also a 4-level encoding (2^2).

Under green irradiation the devices acts as a stop-band filter (Figure 3.15) that drops the green channel. So, by subtracting the output signal under irradiation from the signal without it the green channel is decoded (Figure 3.31c). Here, the filtered information is a 2^1 level encoded data.

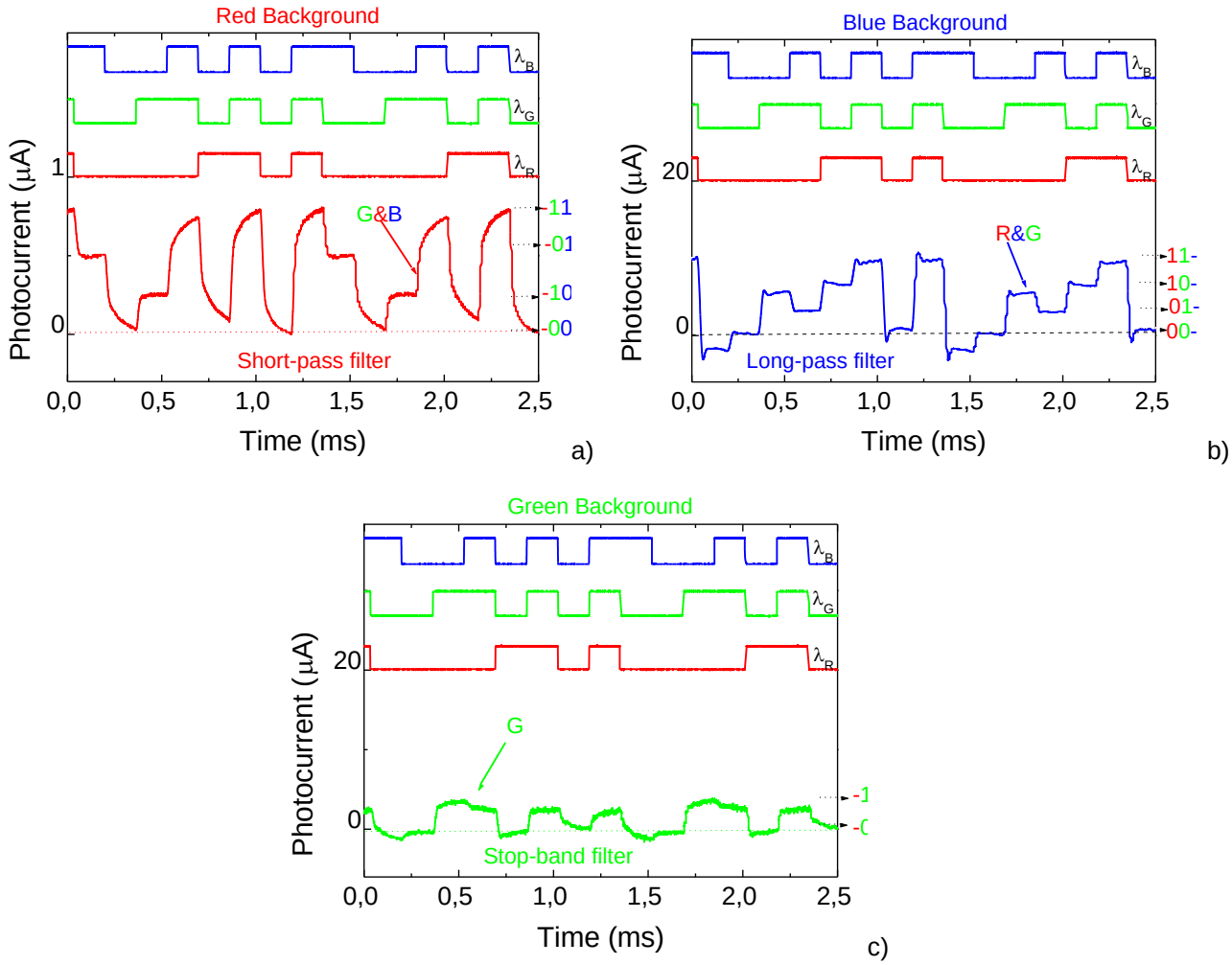

Figure 3.31 *Filtered output signals: a) red background. b) blue background c) green background. On the top, the optical signal used to transmit the information.*

8 Detection of change in fluorescence between reactive cyan and the yellow fluorophores using a-SiC:H multilayer transducers

8.1 Optical transducer configuration and operation

There is great interest in developing semiconductor devices able of sensing the distance between two molecular species in real time for medical and biological applications. One possible approach is to take advantage of the mechanism of Fluorescence Resonance Energy Transfer (FRET), by which the fluorescence wavelength of two labelled molecules is shifted when they are within close range. This technique has grown in popularity due to the emergence of various fluorescent mutants with shifted spectral properties (Chapter II, §7) .

The high degree of spectral overlap between the donor emission and acceptor absorption profiles that is required in FRET also generates a substantial level of background noise that can significantly interfere with the detection of FRET signals.

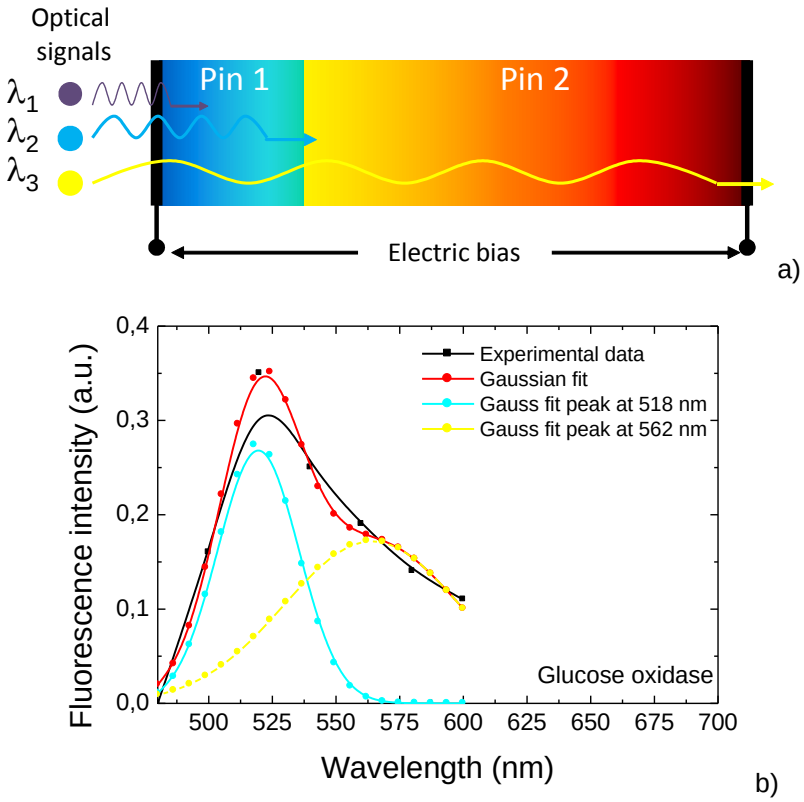

Figure 3.32 *a) Optical transducer configuration. b) Fluorescence emission of glucose oxidase.*

Here we extend the application of these devices to detect violet, cyan and yellow fluorophores. The optical transducer has to accomplish the detection of the transient fluorescent signals coming from the

different fluorescent proteins without losing any information about wavelength and intensity. The advantage of this type of sensor is that it does not rely on mechanical parts; it is compact and cost effective.

The transducer consists of a p-i'(a-SiC:H)-n/p-i(a-Si:H)-n heterostructures produced by PECVD and is optimized for the detection of the fluorescence resonance energy transfer between fluorophores with excitation in the violet (400 nm) and emissions in the cyan (470 nm) and yellow (588 nm) range of the spectrum. The thickness and the absorption coefficient of the i'- and i- layers were tailored for cyan and yellow optical confinement, respectively in the front and back photodiodes acting both as optical filters [23, 24] as dispicted in Figure 3.32 a). A wavelength of 450 nm was used as excitation source. The emission spectrum shows fluorescence in the range 480-600 nm with a peak located at 520 nm. The deconvolution of the experimental data Gaussian fit originates two peaks located at 518 nm and 562 nm, which corresponds respectively to the cyan and yellow emissions.

The device was operated within the visible range using as optical signals to simulate the excitation light and the emitted fluorescent signals (yellow and cyan) of glucose oxidase, the modulated light (external regulation of frequency and intensity) supplied by a violet (λ_1), a blue (λ_2) and a yellow (λ_3) LED with wavelengths of 400 nm, 470 nm and 588 nm, respectively.

To simulate the FRET pairs and the excitation light a chromatic time dependent combination of violet, cyan and yellow wavelengths was applied to the device. The generated photocurrent was measured under negative and positive bias to readout the combined spectra. The independent bit sequences (8 bit per wavelength channel) were chosen in order to sample all the possible chromatic mixtures for a pulse rate of 6000bps. Different wavelength backgrounds were also superimposed.

8.2 Spectral sensitivity

Figure 3.33 a) and b) displays the spectral photocurrent, measured along the visible spectrum, under reverse and forward bias without and with optical light bias of different wavelengths.

Results show that for wavelengths longer than 500 nm the use of short wavelengths (400 nm and 470 nm) for optical biasing the device enhances the photocurrent when compared to the absence of optical bias (Φ_L=0), while longer wavelengths of the optical bias (588 nm and 624 nm) cause a decrease of the signal. On the remaining part of the spectrum and opposite behavior is observed as the amplification effect occurs for longer light bias wavelengths and the reduction of the signal for shorter wavelengths.

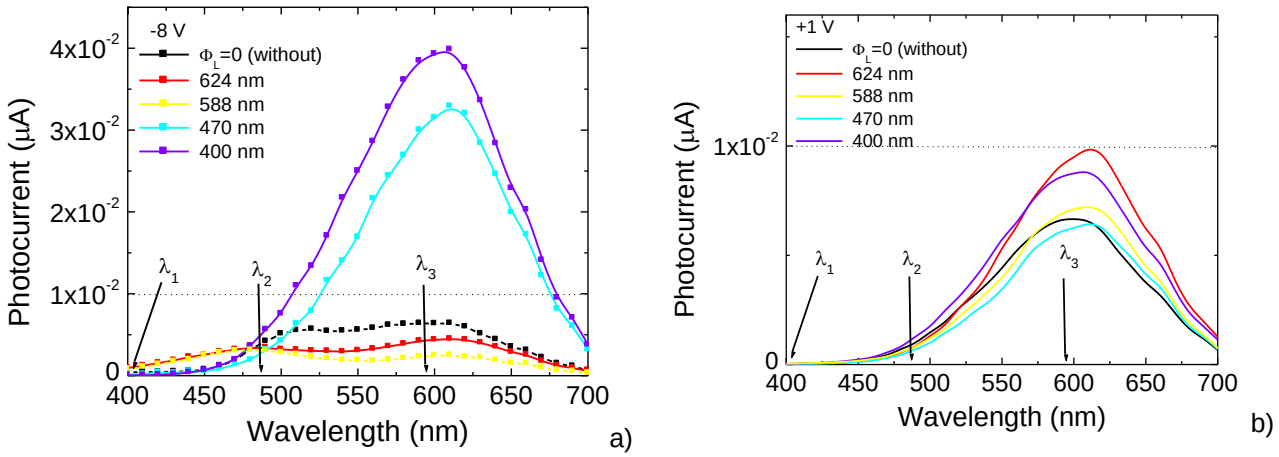

Figure 3.33 *Spectral photocurrent under: a) reverse (-8 V) and b) forward bias (+1 V).*

Thus, at reverse bias, the use of a 400 nm light source as optical bias amplifies both fluorescent signals (λ_2 and λ_3) and reduces the excitation signal (λ_1). This result is an effective method for tuning the device sensitivity in order to filter undesirable light prone to overlap with the fluorescent signals. From the comparison of data obtained results show that, without optical bias, in the long wavelengths range (> 600 nm) the spectral response is independent on the applied bias while in the short wavelength the collection strongly increases with the reverse bias. This means that under forward bias the violet excitation optical signal at 400 nm (λ_1) can be fully suppressed without changing the intensity of the fluorescent signal at 588 nm (λ_3). Under optical bias the variation of the electrical bias induces always a change of the photocurrent along the whole spectrum.

8.3 Transient photocurrent signals

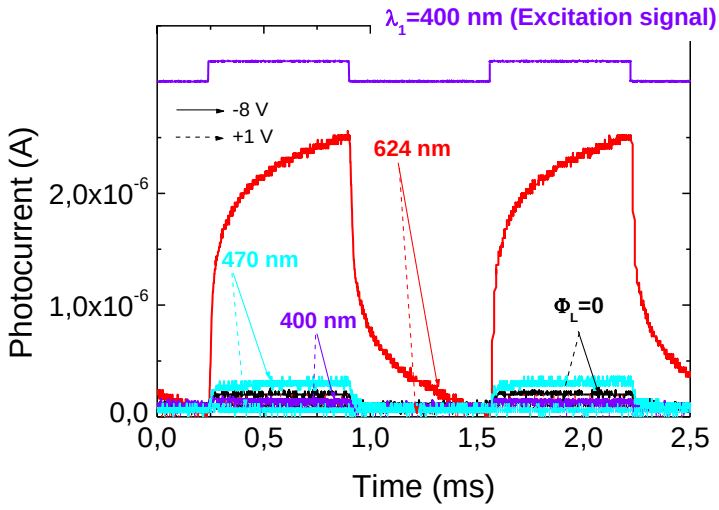

Figure 3.34 *Signal obtained with the excitation signal at -8 V/+1V without/with under background lights.*

The photocurrent signal obtained at reverse (-8 V, solid lines) and forward (+1 V, dash lines) electric bias with (dark lines) and without background light (400nm, 470 nm, 624 nm, color lines)) is displayed in Figure 3.34 and 3.35, respectively, for the excitation and fluorescent optical signals.

Results show that under red (624 nm) optical bias and at reverse bias the photocurrent waveform brought on by the excitation signal is highly amplified. The magnitude of the amplification factor is around 12. The other background lights (470 nm and 400 nm) do not change significantly the signal, inducing a slight decrease.

As already seen in Figure 3.33, this shrinkage of the output signal can be used to filter the effect of the excitation signal and improve the signal to noise ratio.

The amplification of the excitation signal can be used in the scope of this application, to check the state of the excitation source.

For the fluorescent signals, the photocurrent at -8 V is reduced when the wavelength of the optical bias is similar to the wavelength of the signal to be detected and amplified for complimentary wavelengths. In the cyan fluorescence signal the amplification under red (624 nm) bias has a magnitude factor around 2. The yellow signal is amplified under cyan and violet optical biases, with magnitude factors of 3 and 4, respectively.

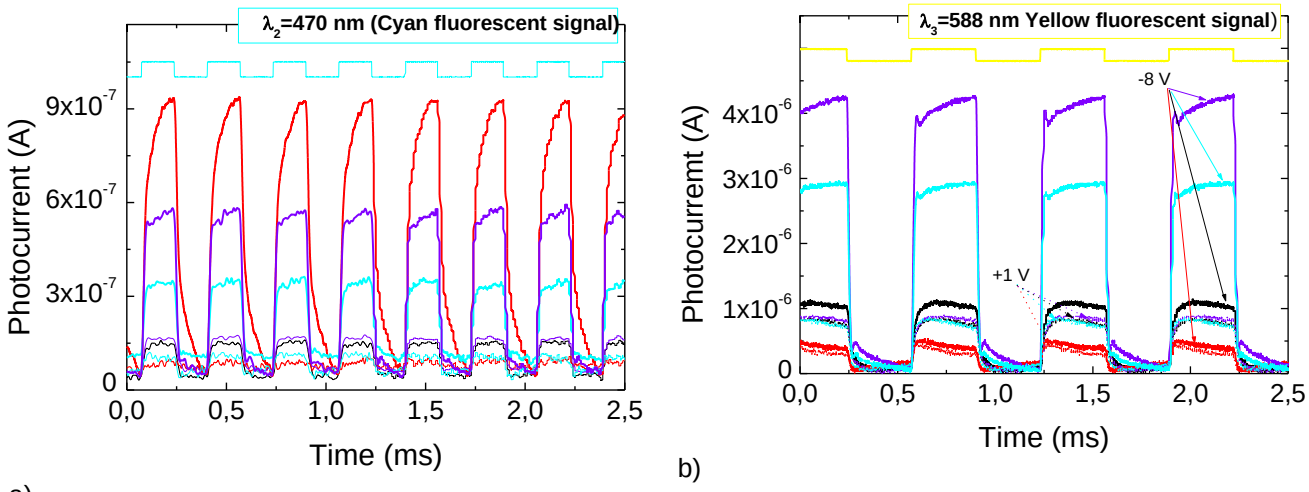

Figure 3.35 *Photocurrent signal obtained at reverse (-8 V, solid lines) and forward (+1 V, dash lines) bias without (dark lines) and with under different background lights (color lines) with the: a) cyan (470 nm) and b) yellow (588 nm) fluorescent signals.*

A chromatic time dependent wavelength combination (3000Hz) of λ_1 (400 nm), λ_2 (470 nm) and λ_3 (588 nm) pulsed input optical signals, was used to generate a multiplexed signal in the device. The output photocurrents, with (color lines) and without (dark lines) optical background light are displayed in Figure 3.36 a) and b) under forward and reverse voltages, respectively. The reference level was assumed to

be the signal when all the input optical signals channels OFF. At the top of the figure, the individual optical signals are displayed to guide the eyes in relation to the different ON-OFF states.

The independent bit sequences (8 bit per wavelength channel) were chosen in order to sample all the possible chromatic mixtures for a pulse rate of 3kHz (6000bps). Under forward bias (Figure 3.36a) the photocurrent signals with or without optical bias are similar and their waveform follows the yellow fluorescence signal, due to the lower sensitivity of the device to the cyan and violet (Figure 3.35) signals. This feature allows immediate decoding of the yellow fluorescence signal. Under reverse bias (Figure 3.36b) the photocurrent signal is more complex. Each waveform is 8-level encoding (2^3) due to the different combinations of the input optical signals.

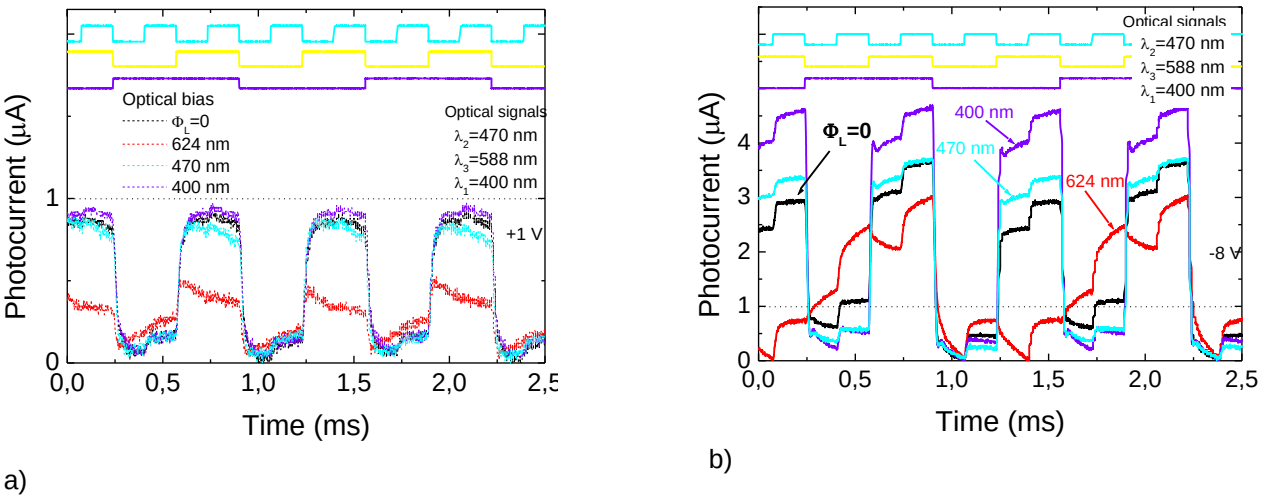

Figure 3.36 *Output photocurrent signals without (ΦL=0) and with optical bias (624 nm, 470 nm, 400 nm) at: a) forward bias (+1 V) and b) reverse bias (-8 V). The optical signals waveforms are shown at the top of the figure.*

Once the yellow signal is decoded by the use of forward bias, the other fluorescence signal can be obtained from the photocurrent signal at -8V taking into account the amplitude dependence on the applied bias (Figure 3.35). To recover the CFP and YFP emission intensities, red optical bias was used. Under red irradiation the yellow channel is quenched, the blue enhanced and the violet strongly amplified (Figure 3.35b and Figure 3.36a). So the highest four levels in the photocurrent signal under 624 nm (Figure 3.36b) corresponds to the presence of the excitation light (violet) and the lowest four levels to its absence. The yellow channel is decoded under forward bias (2-level encoding Figure 3.36 a). By subtracting the yellow coding to the signal under 624 nm (Figure 3.36 b) a 4-level encoding is obtained. Here the highest amplitude corresponds to the presence of both violet and cyan ´signals ON, the lowest to their absence and the two intermediated levels respectively to the presence of the violet or of the cyan signal. By using this simple algorithm the emission spectra of the CFP and YFP can be recovered, in real time, and its ratio can be correlated with the distance between the fluorophores.

8.4 FRET approach

Many proteins have benefited from the process of selective evolution to become very sensitive to specific molecular species such that in their presence conformational changes and binding events take place. One possible approach to detect such events is Fluorescence Resonance Energy Transfer (FRET), a mechanism by which the fluorescence wavelength changes if two labeled molecules come close enough [25]. To simulate the excitation light and the FRET pairs (CFP, YFP) three modulated (6000bps) monochromatic beams: Violet (V; λ_V =400nm); Cyan (C; λ_C =470nm); Yellow (Y; λ_Y =615 nm) with different bit rates and their polychromatic combinations illuminated separately the device from the glass side, and the photocurrent was measured without and with the red background under negative (-8V) and positive (+1V) voltages [26].

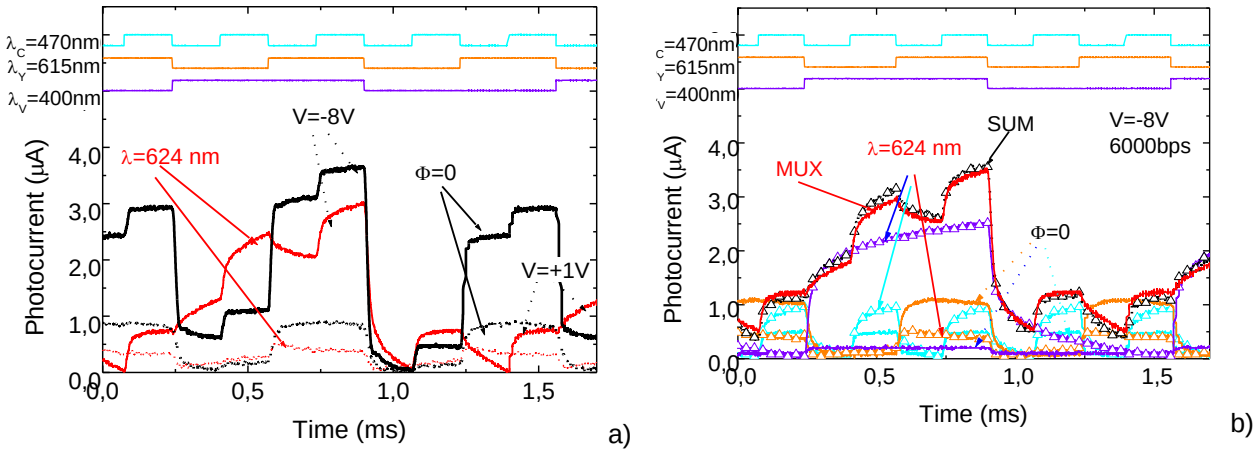

Figure 3.37 *a) Multiplexed signals with and without red background. b) Input channels with red irradiation and without it at -8V. On the top, the optical signal used to transmit the information.*

Figure 3.37 a displays the combined signals due to transmission of the three independent sequences, each one assigned to one color channel without (dark line) and under red background irradiation (color lines). The reference level was assumed to be the signal when all the input channels were OFF. At the top of the figure, the individual optical signals are displayed to guide the eyes in relation to different ON-OFF states. These independent bit sequences (8 bit per wavelength channel) were chosen in order to sample all the possible chromatic mixtures for a pulse rate of 6000bps. In Figure 3.37 b the input channels with red irradiation and without it are displayed at -8V. For comparison the sum of the individual channels at -8V (SUM) and the multiplexed signal (MUX), adjusted to their minimum values, are displayed. A good fit was obtained showing the independence of the three input channels. Results show that under negative voltage with and without optical bias the waveform of the output signals are always 8-level encoding (2^3). Under positive bias or red irradiation the levels are reduced to 2-level encoding (2^1) due to the lower sensitivity of the device to the cyan and violet allowing the immediate decoding of the yellow channel. Once the yellow channel is decoded the other two can be obtained from

the MUX signal at -8V taking into account their amplitude dependence with the applied bias (Figure 3.33). To recover the CFP and YFP emission intensities, red optical bias was used. Under red irradiation the yellow channel is quenched, the blue enhanced and the violet strongly amplified. So the highest four levels in the MUX signal (Figure 3.35b) corresponds to the presence of the excitation light (the violet) and the lowest four levels to its lack. The yellow channel is decoded under positive bias (2-level encoding). By subtracting the yellow coding to the MUX signal a 4 level encoding is obtained. Here the highest amplitude corresponds to the presence of both violet and cyan channels ON, the lowest to their lack and the two intermediated levels respectively to the presence of the violet or of the cyan ON. By using this simple algorithm the emission spectra of the CFP and YFP is recovered, in real time, and its ratio can be correlated with the distance between the fluorophores.

8.5 Summary

Results show that under negative bias the multiplexed signal presents eight separate levels each one assigned to the different polychromatic mixtures. If a blue background is superimposed the yellow channel is enhanced and the cyan suppressed while under red irradiation an opposite behavior occurs. So under appropriated steady state optical bias the sensor will detect separately the cyan and yellow fluorescence pairs. The ratio between both intensities is obtained without optical bias, which in turn can be correlated with the distance between the fluorophores.

9 Conclusions

A monolithic double pi'n/pin a-SiC:H is analyzed under different electrical and optical bias conditions at low and high excitation frequencies.

Results show that the transducer is bias wavelength current-controlled device that make use of changes in the wavelength of the background to control the power delivered to the load. Self optical bias amplification or quenching under uniform irradiation and transient conditions is achieved. The device acts as an optical amplifier whose gain depends on the background wavelength and frequency. An optoelectronic model supported by an electrical simulation explains the operation of the optical system.

There has been much research on semiconductor optical amplifiers. Here, a specific band or frequency need to be filtered from a wider range of mixed signals. Amorphous silicon carbon tandem structures, through an adequate engineering design of the multiple layers' thickness, absorption coefficient and dark conductivities can accomplish this function. Those devices have a nonlinear amplitude-dependent response to each incident light wave. Under controlled wavelength backgrounds can be enhanced the

light-to-dark sensitivity in a specific wavelength range and quenched in the others, tuning a specific band.

This chapter reports results on the use of a double pi'n/pin a-SiC:H Wavelength Division Multiplex (WDM) heterostructure as an active band-pass filter transfer function dependent on the frequence of the trigger light and on the electrical and optical applied bias.

The communication technology utilizes the visible light source as a signal transmitter, the air as a transmission medium, and the appropriate pi'n/pin a-SiC:H voltage and optical bias controlled device is presented as a signal receiving component.

An optoelectronic model explains the operation of the optical system. This smart system has the ability to sense, describes, and qualifies a given situation. It is able to predict, decide or help to decide through the integration of cognitive capabilities (transmitted sequence's algorithm to the data inputs prediction).

SiC pi'npin wavelength selective channel filters optimized for a fine tuning of different wavelengths are analyzed. The manipulation of amplitude is achieved by changing background wavelength. Transfer function characteristics are presented. A numerical simulation gives insight into the filter performances.

Results demonstrate that the device presents a nonlinear amplitude-dependent response to each wavelength. Depending on the wavelength of the external background it acts either as a short- or a long- pass or a band pass or as a notch optical filter. A device with the ability to memorize the previous value of the input light is potentially useful as a memory element. This nonlinearity provides the possibility for selectively removing or adding wavelengths and can be used to boost signal before demultiplexing.

A new RGB receiver based on multilayered a-SiC:H p-i-n structures is developed. The transducers are optimized for provide the high-sensitivity needed for low-light applications.

Many proteins have benefited from the process of selective evolution to become very sensitive to specific molecular species such that in their presence conformational changes and binding events take place. One possible approach to detect such events is Fluorescence Resonance Energy Transfer (FRET), a mechanism by which the fluorescence wavelength changes if two labeled molecules come close enough This chapter presents results on the optimization of multilayered a-SiC:H heterostructures that can be used as an optical transducer for fluorescent proteins detection. Different emission colors of fluorescent proteins were spectrally distinguished from their simultaneous emissions. Results show that the output waveform is balanced by the wavelength and frequency of each input fluorescent signal, keeping the memory of the wavelength and intensity of the incoming optical carriers. To selectively recover only one wavelength, a specific optical bias has to be applied.

By using a simple algorithm the emission spectra of the CFP and YFP is recovered, in real time, and its ratio can be correlated with the distance between the fluorophores.

The new light-activated photonic devices combines the simultaneous desmultiplexing operation with the photodetection and self amplification

Depending on the wavelength of the external background it acts either as a short- or a long- pass band filter or as a band-stop filter. This nonlinearity provides the possibility for selectively removing or adding wavelengths and can be used to boost signal before demultiplexing.
Optical switches are fundamental devices in optical network nodes and network access stations.

10 References

[1] Michael Bas, Fiber Optics Handbook, Fiber, Devices and Systems for Optical Communication, Chap, 13, Mc Graw-Hill, Inc. 2002.

[2] S. Randel, A.M.J. Koonen, S.C.J. Lee, F. Breyer, M. Garcia Larrode, J. Yang, A. Ng'Oma, G.J Rijckenberg, and H.P.A. Boom.. “Advanced modulation techniques for polymeroptical fiber transmission”. ECOC 07 (Th 4.1.4). (pp. 1-4). Berlin, Germany, 2007.

[3] Iguchi, Y.; Yamabayashi, N.; Kuhara, Y.; “Novel rear-illuminated 1.55μm –photodiode with high wavelength selectivity designed for bidirectional optical transceiver” Proc. 2th Int. Conf. On InP and Related Mater, 317 (2000), pp:317- 320.

[4] C. Petit, M. Blaser, “Photodiodes with Integrated Optical Filters for Passive Optical Network Applications” Workshop on Optical Components for Broadband Communication , edited by Pierre-Yves Fonjallaz, Thomas P. Pearsall, Proc. of SPIE Vol. 6350, 63500I, (2006).

[5] M. J. Connelly, “Semiconductor Optical Amplifiers”. Boston, MA: Springer-Verlag, 2002. ISBN 978-0-7923-7657-6.

[6] M. Vieira, A. Fantoni, M. Fernandes, P. Louro, G. Lavareda, C. N. Carvalho, “pinpín and pinpii’n multilayer devices with voltage controlled optical readout” Journal of Nanoscience and Nanotechnology, Vol. 9 , Number 7, July 2009 , pp. 4022-4027(6).

[7] M. A. Vieira, P. Louro, M. Vieira, A. Fantoni, A. S. Garção, “Light-activated amplification in Si-C tandem devices: A capacitive active filter model” IEEE Sensors Journal, accepted for publication in 2011).

[8] A. Fantoni, M. Vieira, R. Martins, "Simulation of hydrogenated amorphous and microcrystalline silicon optoelectronic devices" Mathematics and Computers in Simulation, Vol. 49. pp. 381-401 (1999).

[9] M. Vieira, A. Fantoni, P. Louro, M. Fernandes, R. Schwarz, G. Lavareda, and C. N. Carvalho, “Self-biasing effect in colour sensitive photodiodes based on double p-i-n a-SiC:H heterojunctions “Vacuum, Vol. 82, Issue 12, 8 August 2008, pp: 1512-1516.

[10] M. A. Vieira, A. Fantoni, P. Louro, A. S. Garção, and M.Vieira, “Photonic Active Filters Based on SiC Multilayer Structures: A Two Stage Active Circuit”, Technological Innovation for Value

Criation, IFIP Advances in Information and Communication Technology, 2012, Volume 372/2012, 511-518

[11] C. Casteleiro, R. Schwarz, U. Mardolcar, A. Maçarico, J. Martins, M. Vieira, F. Wuensch, M. Kunst, E. Morgado, P. Stallinga, H.L. Gomes, "Spatially-resolved photocapacitance measurements to study defects in a-Si:H based p–i–n particle detectors", Thin Solid Films, Volume 516, Issue 15, 2 June 2008, pp. 5118-5121 http://dx.doi.org/10.1016/j.tsf.2008.01.012

[12] M. Vieira, M. A. Vieira, P. Louro, J. Costa, M. Fernandes, A. Fantoni, and M. Barata "Multilayer Architectures Based on a-SiC:H Material: Tunable Wavelength Filters in Optical Processing Devices" Journal of Nanoscience and Nanotechnology, Volume 11, Number 6, June 2011 , pp. 5299-5304(6).

[13] M. Vieira, M. A. Vieira, A. Fantoni, P. Louro, M. Fernandes "Optical nonlinearity in SiC multilayer structures: self optical bias amplification" MPA Meeting Conference, Alvor, Algarve, Portugal, 27-29 Junho 2011 accepted for publication in Jornal of Nanosci. Nanotechnol (2012).

[14] M. Vieira, P. Louro, M. A. Vieira, J. Costa, M. Fernandes, "Direct Color Sensor, Optical Amplifier and Demux Device Integrated on a Single Monolithic SiC Photodetector" Procedia Engineering, Volume 5, 2010,Pages 232-235

[15] P. Louro, M. Vieira, M. Fernandes, M. A. Vieira, J. Costa, and A. Fantoni, "Semiconductor Device as Optical Demultiplexer for Short Range Optical Communications" Journal of Nanoscience and Nanotechnology, Volume 11, Number 6, June 2011 , pp. 5318-5322(5) DOI: 10.1166/jnn.2011.3779.

[16] P. Louro, M. Vieira, M. A. Vieira, J. Costa, M. Fernandes, "Optical Demultiplexer Device Operating in the Visible Spectrum", Available online 30 March 2011, Sensors & Actuators: A. Physical (2010).

[17] M. A. Vieira, M. Vieira, J. Costa, P. Louro, M. Fernandes, A. Fantoni, "Double pin Photodiodes with two Optical Gate Connections for Light Triggering: A capacitive two-phototransistor model" in Sensors & Transducers Journal Vol. 10, Special Issue, February 2011, pp.96-120. ISSN 1726-5479.

[18] Manuela Vieira, Paula Louro, M. A. Vieira, João Costa, Miguel Fernandes, Yury Vygranenko, Manuel Barata "Monolithic a-SiC:H Stack Architectures as Tunable Optical Filters for Spectral Analysis" in Silicon Carbide 2010 — Materials, Processing, and Devices, edited by S.E. Saddow, E. Sanchez, F. Zhao, M. Dudley (Mater. Res. Soc. Symp. Proc. Volume 1246, Warrendale, PA, 2010), B07-08.

[19] C. Petit, M. Blaser, "Photodiodes with Integrated Optical Filters for Passive Optical Network Applications", Workshop on Optical Components for Broadband Communication, edited by Pierre-Yves Fonjallaz, Thomas P. Pearsall, Proc. of SPIE Vol. 6350, 63500I, (2006).

[20] M. Vieira, P. Louro, M. Fernandes, M. A. Vieira, A. Fantoni and J. Costa (2011). "Three Transducers Embedded into One Single SiC Photodetector: LSP Direct Image Sensor, Optical Amplifier and Demux" Device, Advances in Photodiodes, Gian Franco Dalla Betta (Ed.), ISBN: 978-953-307-163-3, InTech, Chap.19, pp:403-425 (2011).

[21] P. Louro, M. Vieira, M. A. Vieira, M. Fernandes and J. Costa (2011). "Use of a-SiC:H Photodiodes in Optical Communications Applications", Advances in Photodiodes, Gian Franco Dalla Betta (Ed.), ISBN: 978-953-307-163-3, InTech, Chap.19, pp:377-402 (2011).

[22] M. Vieira, P. Louro, M. Fernandes, M. A. Vieira, J. Costa, "Optical transducers based on amorphous Si/SiC photodiodes", Technological Innovation for Sustainability IFIP Advances in Information and Communication Technology, 2011, Volume 349/2011, 604-611, DOI: 10.1007/978-3-642-19170-1_67.

[23] M. Vieira, P. Louro M. A. Vieira, J. Costa, M. Fernandes, and A. Fantoni, "Wavelength Selective a-SiC:H p-i-n/p-i-n Heterostructure for Fluorescent Proteins Detection", Sensor Letters, Vol. 8 (3), 413-418 (2010) ISSN 1546-198X. eISSN 1546-1971.

[24] M. Vieira, J, Costa, P. Louro, M A Vieira, M. Fernandes, A. Fantoni "Monolitic a-SiC:H heterostructures for proteins detection" MRS Symposium D: Compound Semiconductors for Energy Applications and Environmental Sustainability, Mater. Res. Soc. Symp. Proc. Vol. 132 © 2011 Materials Research Society pp. 137-142.

[25] Jovin, T.M. and Arndt-Jovin, D.J. "FRET microscopy: Digital imaging of fluorescence resonance energy transfer. Application in cell biology". In Cell Structure and Function by Microspectrofluometry, E. Kohen, J. G. Hirschberg and J. S. Ploem. London: Academic Press, 1989. pp. 99-117.

[26] M. Vieira, J. Costa, M. A Vieira, A. Fantoni, M. Fernandes, P. Louro "Detection of change in fluorescence between reactive cyan and the yellow fluorophores using a-SiC:H multilayer transducers" J. Nanosci. Nanotechnol. 11, 1–6, 2011.

CHAPTER IV

System simulator and computational methods for monolithic double p-i-n photodiode

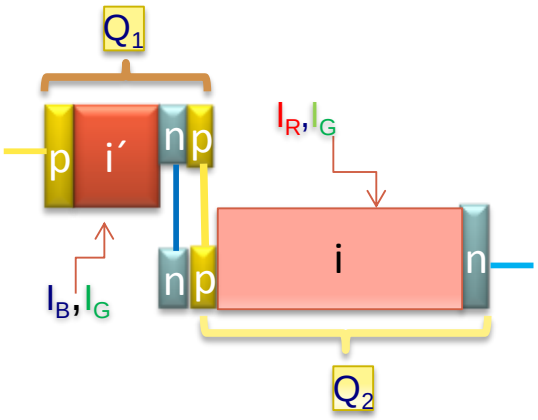

IV System simulator and computational methods for monolithic double p-i-n photodiode

1. Introduction

This chapter is an optoelectronic interface between SiC based photonic circuits and developed algorithms that take into accounts the voltage and the optical bias controlled sensitivities analyzed in chapters 2 and 3.

This work uses control theory to analyze, design, and optimize photonic circuits:

- To help improve our understanding of the output multiplexed signals
- To evaluate and design SiC based photonic circuits
- To control active photonic circuits for optimized performance
- To act either as a short- or a long- pass band filter or as a band-stop filter

Control theory provides a mathematically set of tools for system analysis, design, and control. Following the control theoretic methods we derive state-space representation and an equivalent circuit optoelectronic simulator. We validate each model and calibrate the spectral gain model by background–probe experiments. The input parameters are chosen in compliance with the experimental results and MATLAB used as the programming environment.

1.1 Hypothesis and approach

Based on the experimental results (Chapter II and Chapter III) and device configuration (Chapter I) in this chapter an optoelectronic model is developed and supported by an electrical simulation.

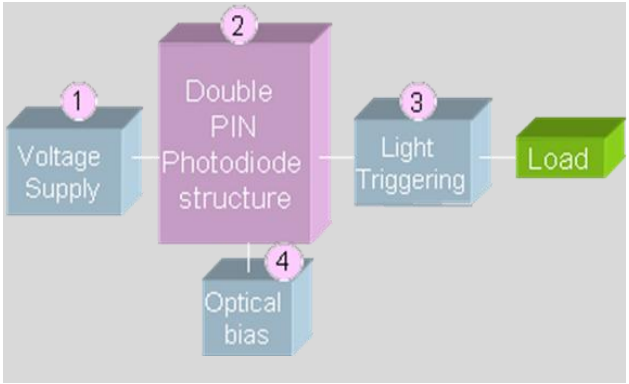

Figure 4.1 *Optoelectronic block diagram.*

The optoelectronic block diagram is presented in Figure 4.1 and consists of four essential elements: a double pin device for detection, a voltage supply of *dc* voltage bias; optical connections for light triggering and optical bias to *dc* light bias control. These four elements when connected together form the essential components of the optoelectronic WDM system.

The device is a double pi'n/pin a-SiC:H heterostructure with two optical gate connections for light triggering in different spectral regions. Multiple monochromatic pulsed communication channels are transmitted together, each one with a specific bit sequence. The combined optical signal is analyzed by reading out, under different applied voltages and optical bias, the generated photocurrent across the device.

An electrical model for the device operation is presented and used to compare output signals with experimental data.

To help to improve our understanding on the photonic integration and increased functionality, an electrical model for circuit simulation is presented. Several bias conditions were considered and the magnitude of leakage current for each case determined in order to extract the device parameters for simulation proposes.

The first step was to determine the dc biasing condition for each stage, followed by ac analysis using proper equivalent circuits. The ac circuit representation is supported by the complete dynamical large signal Ebers-Moll model with series resistances and capacities. The Kirchhoff's laws give the linear state model. The concept of a parallel current bucket connection inflow is established to give insight on the physics of the device.

The multiplexed signal is simulated by analyzing the simplified ac equivalent circuit and the four order Runge-Kutta method to solve the corresponding state equations. MATLAB was used as a programming environment and the input parameters chosen in compliance with the experimental results. The transfer characteristics effects due to changes in steady state light, dc control voltage or applied light pulses are presented.

Finally, experimental and simulated results will be compared to validate the use of multilayered structures based on amorphous silicon technology as a solution in WDM technique for information transmission and decoding in the visible range.

1.2 A conventional receiver based on standard photodiodes

In the structure of blocks of a conventional optical receiver for a direct detection system, the final block usually corresponds to a regenerator for a digital receiver or a demodulator for analog receivers. The regenerator includes a filter appropriate to the proper signal format, a circuit for recovering clock and a decision circuit. The circuit includes a comparator for a decision followed by a flip-flop synchronized by the clock signal produced by the clock recovery circuit. The structure of the analog demodulator depends on the type of modulation used.

A schematic conventional RGB receiver is shown in Figure 4.2.

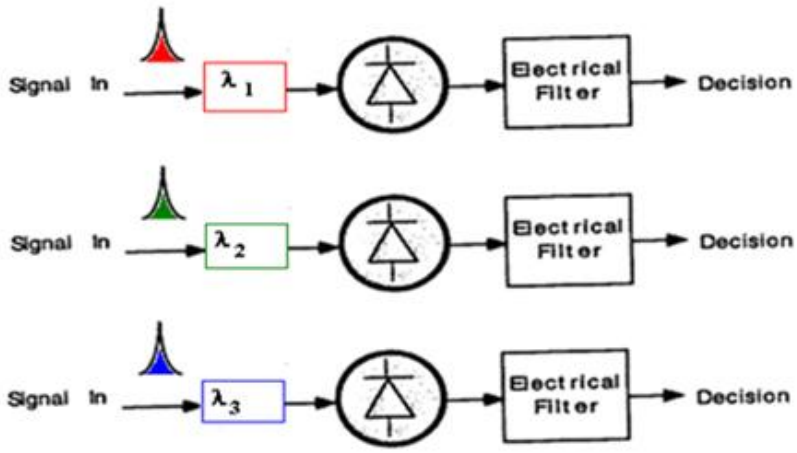

Figure 4.2 *A schematic conventional RGB receiver.*

To briefly summarize its functionality, the receiver consists of standard photodetectors (PIN or APD), which convert the optical (R or G or B) data into electrical pulses. The electrical pulses, after an optional preamplification stage, are passed through an electronic integrate-and-dump filter [1, 2. 3, 4, 5, 6, 7, 8. 9, 10, 11, 12].

In this chapter we propose a new approach for the RGB receiver based on multilayered a-SiC:H p-i-n structures. A schematic functionality of the proposed RGB receiver is shown in Figure 4.3.

In this figure and throughout this section, λ_s denotes the input signal wavelength, λ_c the converted wavelength and λ_B the background wavelength.

Here, the proposed device acts simultaneously as optical filter, photodetector and optical amplifier. The light-activated pi'n/pin a-SiC:H device combines the demultiplexing operation with the simultaneous photodetection and self amplification of an optical signal (Chapters II and III).

Multiple monochromatic pulsed communication channels are transmitted together under different electrical and optical bias conditions. As reported in Chapter III, the multiplexed output waveform presents a nonlinear amplitude-dependent response to the wavelengths of the input channels and of the optical bias, acting as an active filter. Depending on the wavelength of the external background it acts either as a short- or a long- pass band filter or as a band-stop filter. This nonlinearity provides the possibility for selectively removing or adding wavelengths and can be used to boost signal before demultiplexing.

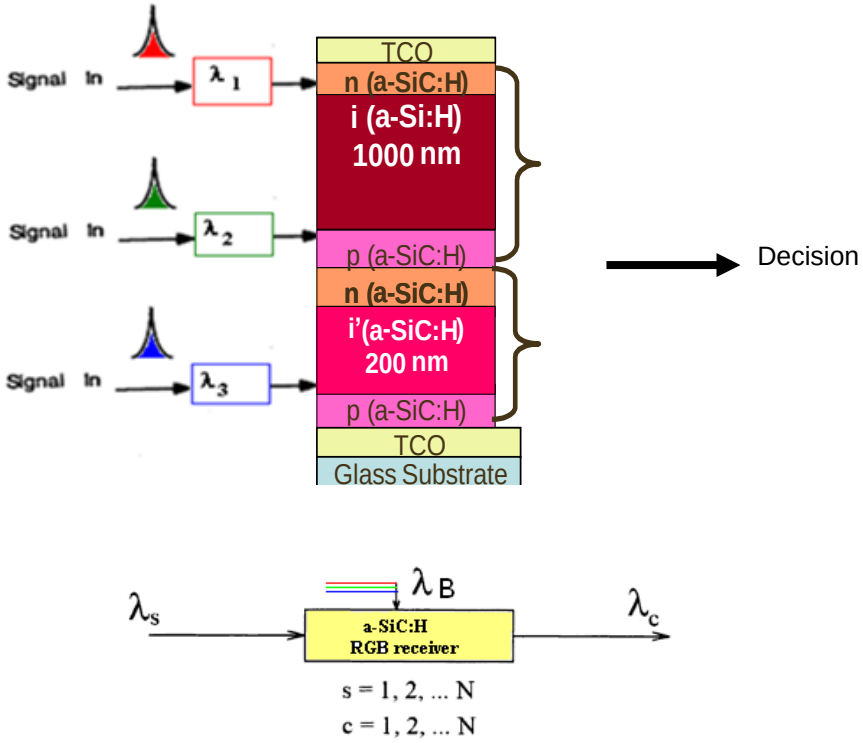

Figure 4.3 *A schematic functionality of a RGB receiver based on multilayered a-SiC:H p-i-n structures.*

1.3 *Working principle*

A chromatic time dependent wavelength combination of red (λ_R=650 nm), green (λ_G=550 nm) and blue (λ_B=450 nm) input channels with different transmission rates, were shining on the device. The generated photocurrent was measured under negative and positive bias to readout the combined spectra. In Figure 4.4 it is displayed the input RGB channels (lines) and the transient multiplexed signals (symbols) under negative (-10 V) and positive (+3 V) applied voltages. The highest frequency (red channel) was 3 KHz and the ratios among all of them always one half of each. The reference level was assumed to be the signal when all the input channels were OFF (dark level).

As explained in Chapters II and III, the multiplexed signal depends on the applied voltage and on the ON-OFF state of each channel. Under reverse bias, there are eight separate levels while under positive bias they were reduced to one half due to the blindness of the sensor to the blue component.

The highest level appears when all the channels are ON and the lowest when they are OFF.

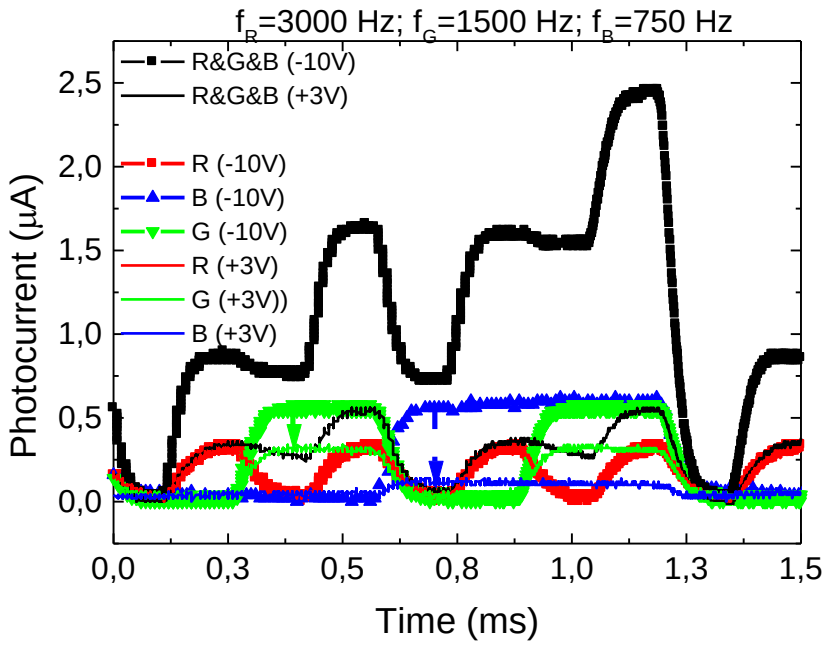

Figure 4.4 *Input channels (R, G, B) and multiplexed signals (R&G&B) under negative (symbols) and positive bias (lines) applied bias.*

When the voltage changes from negative to positive the input red signal remains constant while the blue and the green decrease (arrows in the figure). The lower decrease in the green channel when compared with the blue one can be ascribed to its red-like nature under positive bias. Also, the sum of the R, G and B input channels, under negative bias, is lower than the correspondent multiplexed signals suggesting capacitive effects due to its time-varying nature. Under positive bias this difference is negligible; the device becomes blind to the top photodiode, the blue component of the combined spectra falls into the dark level, allowing the recognition of both red and green input channels. Under negative bias, if the blue component is present (R&B; G&B, R&G&B), the eight levels are clearly observed. By comparing the signals under positive and negative bias and using a simple algorithm that takes into account the different sub-level behaviors under negative and positive bias it is possible to decode the RGB transmitted information (Chapter II §4).

2 Electrical model

2.1 Two connected transistor model

Based on the experimental results and device configuration an optoelectronic model was developed and published elsewhere [13, 14, 15 ,16. 17].

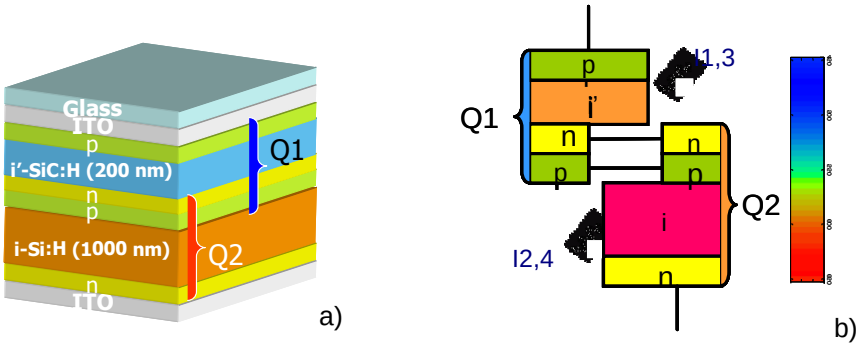

Figure 4.5 *Compound connected phototransistor equivalent model.*

The monolithic device (Figure 4.5a) is modeled by the two-transistor model (Q_1-Q_2) (Figure 4.5b). The two-phototransistor model is obtained by bisecting the two middle layers in two separate halves that can be considered to constitute *pinp* (Q_1) and *npin* (Q_2) phototransistors separately. In order to simulate the n-p internal junction, the collector and base of both transistors are shared.

The compound connected phototransistor model introduces a functional structure similar to the classic transistor. When the pi'npin device is reverse-biased, the base-emitter junction of both transistors are reverse biased and conceived as phototransistors, taking, so, advantage of the amplifier action of adjacent collector junctions which are forward biased.

We may take advantage of opposite polarity to design multi-stage cascading amplifiers in a direct–coupled way. Since there are no coupling components needed between stages, the direct coupled amplifier provides quite a simple circuit structure. If all stages use the same type of transistors in designing a direct-coupled amplifier, the dc biasing circuits will raise a problem. Alternatively, using pinp (Q_1) and npin (Q_2) is the most effective way to diminish the biasing problem and achieve all advantages of direct–coupling. Therefore, in solving these direct-coupled amplifier problems, the first step is to determine the dc biasing condition for each stage, followed by ac analysis using proper equivalent circuits.

2.2 Electric model validation and physics

An electrical model was developed [18, 19] and supported by a SPICE simulation. The simulated equivalent circuit is displayed in Figure 4.6a.

Time-varying versions of the linear circuit elements are the capacitors C_1 and C_2 used to simulate the transient capacitance due to the minority carriers trapped in both p-i-n junctions. A dc voltage source, V, was applied giving rise to an output signal, I (R_3). Two *ac* current sources, I_1 and I_2, are used to simulate the input blue and red channels. It is a two phase system since two separate pulses ($i_1(t)$ and $i_2(t)$), simulated through two square wave current sources applied to Q_1 (I_1) and Q_2 (I_2) bases, are needed to

provide the input signals. The frequencies are the same as the ones used in the experimental work (Chap II, Figure 2.10a).

In Figure 4.6b it is shown the input channels, I(I1), I(I2), the output signal, I(R3) and the current across the capacitors, I(IC1), I(IC2). Good agreement with the experimental data (Chap II, Figure 2.10a) is achieved. Results show that the internal junction (n-p) controls the current across the device. If the device is biased negatively (-5V), the p-n internal junction is forward-biased and the external voltage appears mainly across the front and back reverse-biased junctions. So, the current, I, depends not only on the balance between both blue and red photocurrents (I1, I2) but also on the end of each half-cycle of the modulated current frequency. Thus, the movement of charge carriers with an increase/decrease in the irradiation, results in a charging or a displacement current similar to the current (i=CdV/dt) that charges the capacitors.

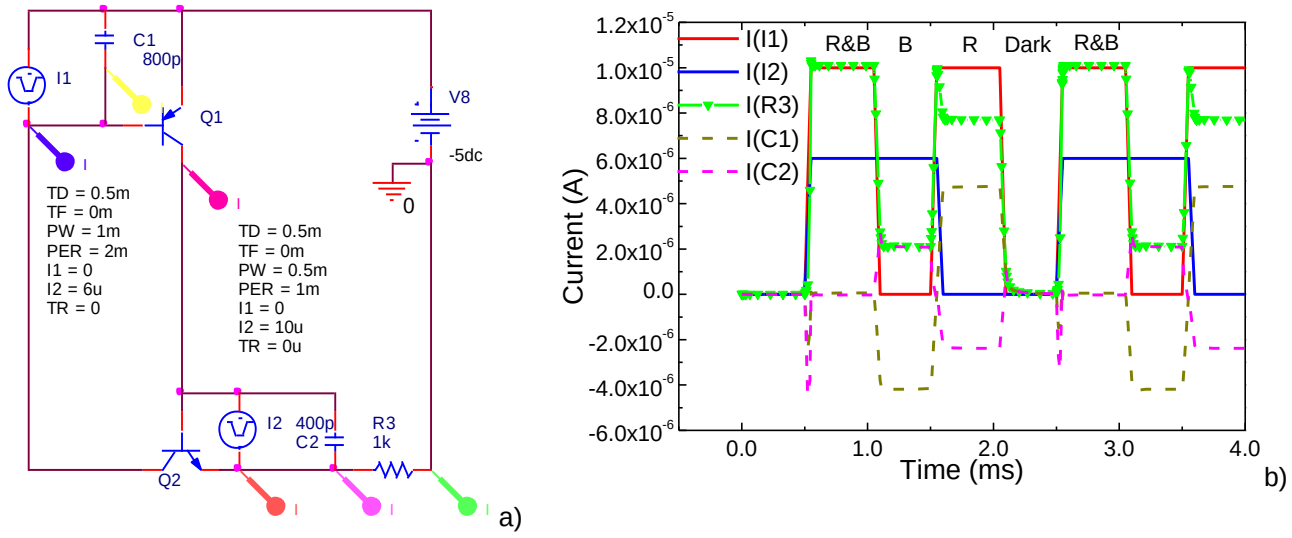

Figure 4.6 *a) Equivalent electrical circuit of the pinpin photodiode. b) Signals obtained using SPICE simulation when the red (I2) and the blue (I1) modulated lights are impinging the device.*

Under negative bias and in the beginning of the cycle (R&B), the carriers generated by the blue photons flow across Q_1 collector toward the base of Q_2 and together with the ones generated by the red photons recombine or are collected (R&B level). Under blue irradiation, I(I2)=0, only the carriers generated by the blue photons flow across the device (B level). C_1 charges positively and C_2 negatively as a reaction to the decrease in the red irradiation. The opposite occurs under red irradiation. When both red and blue lights are simultaneously off, the current is limited by the leakage current (dark level). So, once triggered, the device continues to conduct until the current through it drops below a certain threshold value, such as at the end of a half-cycle, keeping the information of the wavelength (R&B, R, B, Dark) and frequency of the impinging light. When a positive voltage is applied, the junction capacitance across the internal n-p junction is charged. The charging current flows through the emitter of the two

transistors. The device behaves essentially as a npn phototransistor with the pnp transistor acting like a emitter-follower with a very small gain. So, under lower positive voltages the only carriers collected come from the red channel and enables the demultiplexing of the previous multiplexed signal.

In Figure 4.7 the equivalent electrical circuit of the pinpin photodiode used in SPICE simulation when three input channels are present is displayed (Figure 4.7a) as well as the voltage drop (V_{BE}) across Q_1 and Q_2 obtained under red (I2=20uA), blue (I1=12uA) and green (I3=10uA, I4=8uA) pulsed lights and negative and positive applied voltages (Figure 4.7b). To allow independent blue, red and green channels transmission four square-wave current sources with different intensities are used; two of them, I1 and I2, with different frequencies to simulate the input blue and red channels and the other two, I3 and I4, with the same frequency but different intensities, to simulate the green channel due to its asymmetrical absorption across both front and back phototransistors.

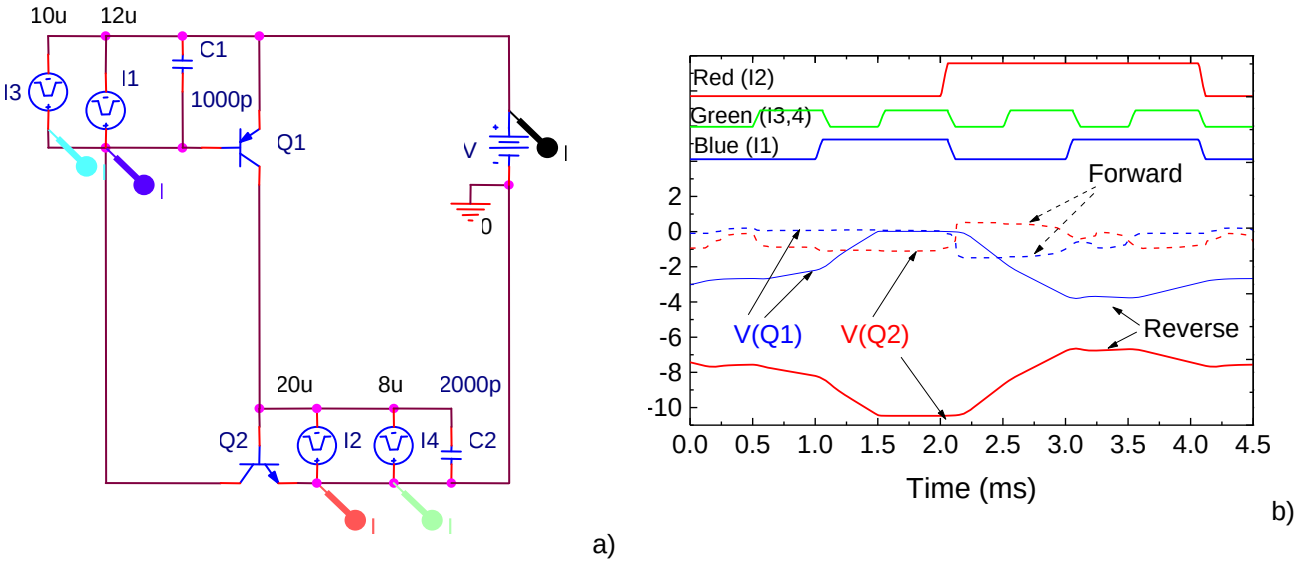

Figure 4.7 *a) Equivalent electric circuit of the pinpin photodiode used in SPICE simulation. b) Voltage drop (VBE) across Q_1 and Q_2 under red (I2=20uA), blue (I1=12uA) and green (I3=10uA, I4=8uA) pulsed lights and negative and positive applied voltages.*

In Figure 4.8, the output signals and the currents across the capacitors, I(IC1), I(IC2) are displayed. A good agreement between experimental (Figure 2.17, chapter II) and simulated results is achieved.

Results show that when the device is biased negatively, Q_1 and Q_2 are in their reverse active regions. The p-n internal junction is forward-biased and the external voltage drops across both front and back reverse-biased junctions, depending on the ON-OFF state of each channel. Under positive bias the internal junction is reverse-biased.

The device acts as a charge integrator, keeping the memory of the input channels. Under reverse bias, when all the channels are simultaneously ON I_1 and I_3 flow across Q_1 collector towards the base of Q_2 and together with I_2 and I_4 give rise to the highest signal. When all the channels are simultaneously OFF, the current is limited by the leakage current of both active junctions (dark level). If only the blue

channel is ON the carriers generated by the blue photons are injected into the base of Q_1. C_1 charges positively and C_2 negatively as a reaction to the decrease in the red and green irradiations. The opposite occurs if only the red channel is ON. Nevertheless, if the only channel ON is the green one, both front and back contribution must be considered and the photocurrent is a balance between the blue- and the red-like contributions. If only two input channels are ON (R&B, R&G, G&B) both front and back generations are taken into account. So, once triggered (R&B&G), the device continues to conduct until the current through it drops below a certain threshold value, such as at the end of a half-cycle, keeping the information of the wavelength (R, G, B) and transmission rate (frequency) of the impinging light.

When a positive voltage is applied to turn the internal junction from ON to OFF, the junction capacitance across the internal n-p junction is charged. The charging current flows through the emitter of the two transistors. The device behaves essentially as a *npn* phototransistor with the *pnp* transistor acting like a emitter-follower with a very small gain. So, under lower positive voltages, the only carriers collected come from the red and/or green channels enabling the demultiplexing of the previous multiplexed signal.

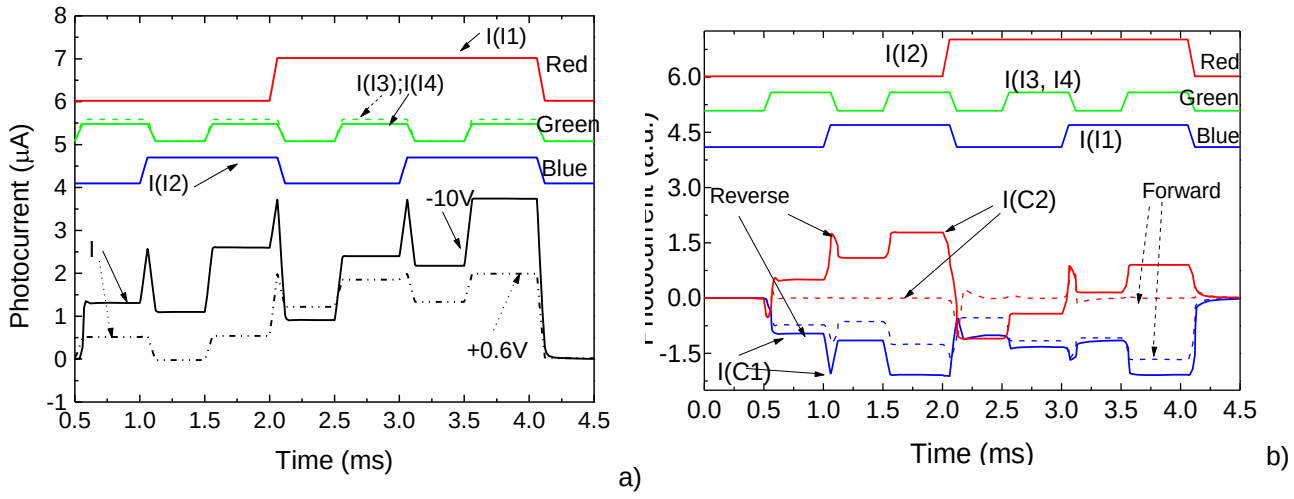

Figure 4.8 *Under red (I2=20uA), blue (I1=12uA) and green (I3=10uA, I4=8uA) pulsed lights and different applied voltages: a) Output signals. b) Current across the capacitors, I(IC1), I(IC2).*

As expected from Figure 4.4 the external current, I, depends on the balance between blue, green and red photocurrents (I_1; I_3, I_4; I_2) and on the end of each half-cycle of the modulated currents [20, 21, 22]. Comparing both experimental and simulated results it is observed that, under negative applied voltages, the multiplexed signal keeps the memory of the single input channels. By switching between forward and reverse bias the red, green and the blue channels can be recovered [23] (Chapter II, Figure 2.17). The pi´npin device is a two-input cascode circuit with a common source amplifier as input stage. This input stage drives a common base amplifier as output stage. The upper transistor (Q_1) acts as load of the input lower transistor (Q_2) and also uses it sources (I1, I3) as input node. So, Q_1 exhibits a low input resistance to Q_2, making the voltage gain of Q_2 very small. In Figure 4.9a the equivalent electric

circuit was redesign into the two-input cascode configuration. In Figure 4.9b the simulated voltage drop across Q_1 (symbols) and Q_2 (lines) is displayed.

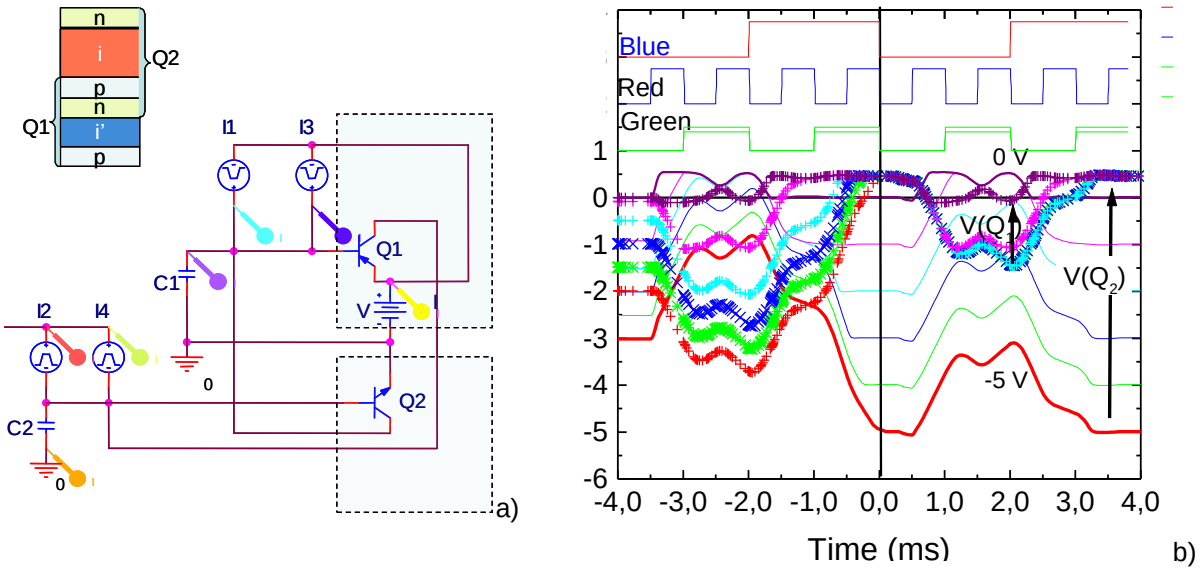

Figure 4.9 *a) Equivalent electrical circuit of the pi'npin device used for electrical simulation proposes. b) Voltage drop across Q_1(symbols) and Q2 (lines).*

The device is a transmission system able to store and to transport the minority carriers generated by the current pulses, through capacitors C_1 and C_2. It acts as a charge integrator, keeping memory of the input channels (color and frequency). The control strategy of this transmission system, using the two-input cascode configuration, improves input-output isolation (or reverse transmission) as there is no direct coupling from the output to input. Under negative bias, once the blue channel is *on*, the emiter-base of Q_1 becomes optically forward biased and C_2 is rapidly charged in inverse polarity of C_1 ($i_{C1}(t)C_2 = -i_{C2}(t)C_1$) with an input voltage in which a threshold value is inserted for clamping (arrows in Figure 4.9b) which results in a reinforcement of the reverse bias at Q_2. The current source keeps filling the capacitors for the duration of the pulse, Δt, of the input channel and the transferred charge between C_1 and C_2 will reach the output terminal as a capacitive charging current. The presence of the red channel changes, in the opposite way, the charge of both capacitors. If the green channel is *on* the current is the balance between the blue- and the red-like contributions. With several channels *on*, the packets of charge stored at C_1 (I1, I3) are sequentially transferred to C_2 and together with the minority carriers generated at the base of Q_2 (I2, I4) flow across the circuit. When all the channels are *off*, the current is limited by the leakage current of both active junctions (dark level). If a small positive voltage is applied, the junction capacitance across the internal n-p junction is charged and the only carriers collected come from the red-like channels (I2, I4) enabling the demultiplexing of the previous multiplexed signal by switching between positive and negative voltages.

The stacked multilayer device with the application of an optical bias to the gate i'-n (front diode) and/or p-i (back diode), converges to a common output current point of operation. The incident light crosses the p-i'-n-p-i-n sequence and is absorbed according to its wavelength (Chapter III). As both diodes are electrically in series, each one supplies the same current, I, and the applied voltage, V, is shared between both ($V=V_1+ V_2$). Any diode whose current is over the other would have to reduce its magnitude and consequently to self-bias (Chapter I §5.5). If the photocurrent, is higher than the net current the diode self forward biased ($V_{1,2}>0$), if not, it self reverse biases ($V_{1,2}<0$). The flow of carriers across the internal p-n junction is proportional to the difference between V_1 and V_2 [24]. So, if the device is biased negatively the n-p internal junction is forward-biased and, the external voltage drops across the external junctions. The current is limited by the leakage current of the less excited diode, the front under red and the back under blue irradiations. Under green light the limiting factor is the photocurrent of the less irradiated diode. Under positive bias the internal junction becomes always reverse-biased.

3 Optoelectronic model

3.1 *ac* equivalent electric circuit

The block diagram of the optoelectronic model [25] is displayed in Figure 4.1 and its working principle was described in § 1.1. The monolithic device is modeled by the two-transistor model (Q_1-Q_2) (Figure 4.5) that can be seen as a *pnp* (Q_1) and *npn* (Q_2) phototransistors separately.

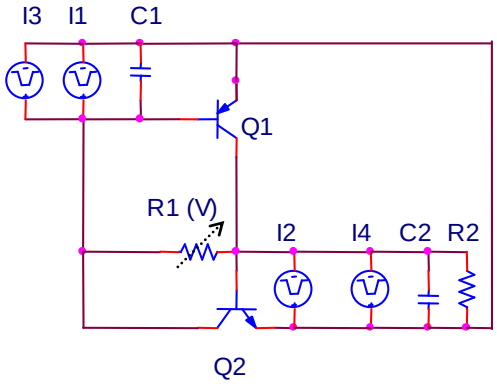

Figure 4.10 *ac equivalent circuit.*

The first step to establish the ac equivalent circuit was to determine the *dc* biasing condition for each stage (§2.1), followed by *ac* analysis using the proper equivalent circuits. Under negative bias, the p-n internal junction is forward-biased and the external voltage drops mainly across both front and back reverse-biased junctions, mainly at the front one due to its higher resistivity. Under positive bias the internal junction becomes reverse biased.

The *ac* circuit representation displayed in Figure 4.10 is supported by the complete dynamical large signal Ebers-Moll model with series resistances and capacities [26], [27].

As in section §2.2 the charge stored in the space-charge layers is modeled by the capacitor C_1 and C_2. R_1 and R_2 model the dynamical resistances of the internal and back junctions under different *dc* bias conditions. The operation is based upon the following strategic principle: the flow of current through the resistor connecting the two transistor bases is proportional to the difference in the voltages across both capacitors (charge storage buckets). The modified electrical model developed is the key of this strategic operation principle. The capacitors exhibit time-varying charge/voltage characteristics being the current across them the instantaneous rate of charge variation. If the device is biased negatively Q_1 and Q_2 are in their reverse active regions. Two optical gate connections ascribed to the different light penetration depths across the front (Q_1) and back (Q_2) phototransistors were considered to allow independent blue (I_1), red (I_2) and green (I_3, I_4) channels transmission. Four square-wave current sources with different intensities are used; two of them, I_1 and I_2, with different frequencies to simulate the input blue and red channels and the other two, I_3 and I_4, with the same frequency but different intensities, to simulate the green channel due to its asymmetrical absorption across both front and back phototransistors.

Once the *ac* sources are connected in the load loop an *ac* current flows through, establishing voltage modifications across the two capacitors. During the simultaneous transmission of the three independent bit sequences, the set-up in this capacitive circuit loop is constantly changing in magnitude and direction. This means that the voltage across one capacitor builds up until its maximum and the voltage across the other builds up to a minimum (see Figures 4.7 and 4.9). The system collapses and builds up in the opposite direction. It tends to saturate and then leave the saturation state because of the cyclic operation. This results in changes on the reactance of both capacitors. The use of separate capacitances on a single resistance R_1 results in a charging current gain proportional to the ratio between collector currents. The *dc* voltage, according to its strength, aids or opposes the *ac* currents. So, when the pi'npin device is reverse-biased, the base-emitter junction of both transistors are inversely polarized and conceived as phototransistors, taking, so, advantage of the amplifier action of adjacent collector junctions which are polarized directly. This results in a current gain proportional to the ratio between both collector currents. Under positive bias the internal junction becomes reverse-biased.

The external current depends not only on the balance between blue, green and red photocurrents (I_1, I_2, I_3, I_4) but also on the end of each half-cycle of each modulated current. Here, the movement of charge carriers with an increase/decrease in the irradiation, results in a charging or a displacement current similar to the current ($i=C\,dV/dt$) that charges the capacitors C_1 and C_2 in opposite ways.

Assuming that the frequency is low enough so that quasi-statics is maintained, the incremental capacitances are used to evaluate the total charge stored. So, the junction capacitance and diffusion capacitance would behave as if they have been kept in parallel. Because inherently they are leaky capacitors, C_1 and C_2, need to store higher charge that has also to be supplied. This charge will appear as a current component. The leaky capacitors can be represented as parallel combinations of ideal capacitors and resistances. The current would be the superposition of two components: one leakage

current that is in-phase with the voltage and one displacement-capacitive-current which is out of phase with the voltage.

3.2 Kirchhoff's laws for the simplified ac equivalent circuit

Taking into account the *ac* simplified equivalent circuit (Figure 4.10) the linear modified electrical model is based on one *ac* current source and dynamical resistances under different *dc* bias conditions includes time-varying versions of basic linear circuit elements:

$$i_{c1}(t) = C_1 \frac{dv_1(t)}{dt}$$

$$i_{c2}(t) = C_2 \frac{dv_2(t)}{dt} \qquad (1)$$

Following a standard procedure, we chose as state variables the voltage $v_1(t)$ across the capacitor C_1 and the voltage $v_2(t)$ across the capacitor C_2.
Then Kirchhoff's laws for the simplified ac equivalent circuit gives:

$$I_1(t) + I_3(t) = C_1 \frac{dv_1(t)}{dt} + \frac{v_1(t) - v_2(t)}{R_1} = i_1(t)$$

$$I_2(t) + I_4(t) = C_2 \frac{dv_2(t)}{dt} - \frac{v_1(t) - v_2(t)}{R_1} + \frac{v_2(t)}{R_2} = i_2(t) \qquad (2)$$

respectively at the nodes of the bases of Q_1 and Q_2. Those equations, in the present context, are written in the form:

$$\frac{dv_1}{dt} = -\frac{1}{R_1 C_1} v_1(t) + \frac{1}{R_1 C_1} v_2(t) + \frac{1}{C_1} i_1(t)$$

$$\frac{dv_2}{dt} = +\frac{1}{R_1 C_2} v_1(t) - \frac{1}{R_1 C_2} v_2(t) - \frac{1}{R_2 C_2} v_2(t) + \frac{1}{C_2} i_2(t) \qquad (3)$$

The two first-order equations are found for easily manipulating the system without having to use integral transforms**.** The output equation is:

$$i(t) = \frac{v_2(t)}{R_2} \qquad (4)$$

and are written as:

$$\frac{dv_{1,2}}{dt} = \begin{bmatrix} -\frac{1}{R_1 C_1} & \frac{1}{R_1 C_1} \\ \frac{1}{R_1 C_2} & -\frac{1}{R_1 C_2} - \frac{1}{R_2 C_2} \end{bmatrix} v_{1,2}(t) + \begin{bmatrix} \frac{1}{C_1} \\ \frac{1}{C_2} \end{bmatrix} i_{1,2}(t) \quad (5)$$

$$i(t) = \begin{bmatrix} 0 & \frac{1}{R_2} \end{bmatrix} v_{1,2}(t) \quad (6)$$

with $v_1(t)$ and $v_2(t)$ the emitter-base voltages of Q_1 and Q_2 transistors and $i(t)$ the generated photocurrent under transient conditions.

3.3 Simulation diagram of the system

When modeling a system using a state-space equation, we first need to define three vectors: the input variables with $i_{1,2}$, the output variables with i and the state variables with $v_{1,2}$. In an electric circuit, for instance, the node voltages or the mesh currents can be state variables.

In essence, we have the following relationship:

$$i(t) = f(\mathrm{v}_{1,2}, \mathrm{i}_{1,2}) \quad (7)$$

Where $f(\mathrm{v}_{1,2}, \mathrm{i}_{1,2})$ is the system. Also, the state variables can change with respect to the current state and the system input:

$$v'_{1,2} = g(\mathrm{v}_{1,2}, \mathrm{i}_{1,2}) \quad (8)$$

Where $v'_{1,2}$ is the rate of change of the state variables.

In the Laplace domain, if we want to account for systems with multiple inputs and multiple outputs, we are going to need to rely on the principle of superposition to create a system of simultaneous Laplace equations for each output and each input. The Laplace domain technique can be combined with the state-space techniques.

In a state-space system representation, we have a system of equations: equations for determining the state of the system, and another equation for determining the output of the system. We will use the variable i(t) as the output of the system, $v_{1,2}(t)$ as the state of the system, and $i_{1,2}(t)$ as the input of the system. We use the notation $v'_{1,2}(t)$ for the first derivative of the state vector of the system, as dependent on the current state of the system and the current input. Symbolically, we say that there are transforms *g* and *h* that display this relationship:

$$v'_{1,2}(t) = g(t_0, t, v_{1,2}(t), v_{1,2}(0), i_{1,2}(t)) \quad (9)$$

$$i(t) = h(t, v_{1,2}(t), i_{1,2}(t),] \quad (10)$$

If $v'_{1,2}(t)$ and $i(t)$ are not linear combinations of $v_{1,2}(t)$ and $i(t)$, the system is said to be nonlinear.

The first equation shows that the system state change is dependent on the previous system state, the initial state of the system, the time, and the system inputs. The second equation shows that the system output is dependent on the current system state, the system input, and the current time.

If we approximate the system state change $v'_{1,2}(t)$ and the system output $i(t)$ by linear state equation systems then we can say the systems are linear systems, and we can rewrite them in matrix form:

Input equation

$$v'_{1,2}(t) = \mathrm{A}(t)\ v_{1,2}(t) + \mathrm{B}(t)\ i_{1,2}(t) \quad (11)$$

Output equation

$$\mathrm{i}(t) = \mathrm{C}(t)\ v_{1,2}(t) + \mathrm{D}(t)\ i_{1,2}(t) \quad (12)$$

If the systems themselves are time-invariant, we can re-write the formulas as follows:

$$v'_{1,2}(t) = \mathrm{A}\, v_{1,2}(t) + \mathrm{B}\, i_{1,2}(t) \quad (13)$$

$$\mathrm{i}(t) = \mathrm{C}\, v_{1,2}(t) + \mathrm{D}\, i_{1,2}(t) \quad (14)$$

The state equations show the relationship between the system's current state and its input, and the future state of the system. The output equation shows the relationship between the system state and its input, and the output. These equations show that in a given system, the current output is dependent on the current input and the current state. The future state is also dependent on the current state and the current input.

It is important to note at this point that the state space equations of a particular system are not unique, and there are an infinite number of ways to represent these equations by manipulating the A, B, C and D matrices using row operations. There are a number of "standard forms" for these matrices, however, that make certain computations easier. Converting between these forms will require knowledge of linear algebra.

Any system that can be described by a finite number of n^{th} order differential equations or n^{th} order difference equations, or any system that can be approximated by them, can be described using state-space equations. The general solutions to the state-space equations, therefore, are solutions to all such sets of equations.

If these systems are time-invariant, we can simplify them by removing the time variables:

$$v'_{1,2}(t) = g\left(v_{1,2}(t), v_{1,2}(0), i_{1,2}(t)\right) \quad (15)$$

$$i(t) = h(v_{1,2}(t), i_{1,2}(t),] \quad (16)$$

The linearization is developed from the point of view of the application in the theoretical electrotecnic. Taylor's series expansion is used to linearize these systems [28, 29]. If we take the partial derivatives of these functions with respect to the input and the state vector at time t_0, we get the system matrices:

$$\text{A}= g_v \left[v_{1,2}(0), i_{1,2}(0)\right] \tag{17}$$

$$\text{B}= g_i [v_{1,2}(0), i_{1,2}(0)] \tag{18}$$

$$\text{C}= h_v [v_{1,2}(0), i_{1,2}(0)] \tag{19}$$

$$\text{D}= h_i [v_{1,2}(0), i_{1,2}(0)] \tag{20}$$

In the time-invariant state space equations, we write these matrices and their relationships as:

$$v'_{1,2}(t) = \text{A}\, v_{1,2}(t) + \text{B}\, i_{1,2}(t) \tag{21}$$

$$\text{i(t)} = \text{C}\, v_{1,2}(t) + \text{D}\, i_{1,2}(t) \tag{22}$$

We have four constant matrices: A, B, C, and D.

The Kirchhoff's laws for the simplified equivalent circuit give the linear state model. The time periodic linearized state equations are given by:

$$\frac{dv_{1,2}}{dt} = \text{A} \times v_{1,2}(t) + \text{B} \times i_{1,2}(t)$$

$$i(t) = C \times v_{1,2}(t) + D \times i_{1,2}(t) \tag{23}$$

Where A is the system matrix, and relates how the current state affects the state change $v'_{1,2}(t)$. B is the control matrix, and determines how the system input affects the state change. C is the output matrix, and determines the relationship between the system state and the system output. D is the feed-forward matrix, and allows for the system input affecting the system output directly. Here D matrix is considered the zero matrix.

$$\frac{dv_{1,2}}{dt} = \begin{bmatrix} -\frac{1}{R_1 C_1} & \frac{1}{R_1 C_1} \\ \frac{1}{R_1 C_2} & -\frac{1}{R_1 C_2} - \frac{1}{R_2 C_2} \end{bmatrix} v_{1,2}(t) + \begin{bmatrix} \frac{1}{C_1} \\ \frac{1}{C_2} \end{bmatrix} i_{1,2}(t) \tag{24}$$

$$i(t) = \begin{bmatrix} 0 & \frac{1}{R_2} \end{bmatrix} v_{1,2}(t) \tag{25}$$

with $v_1(t)$ and $v_2(t)$ the emitter-base voltages of Q_1 and Q_2 transistors and $i(t)$ the generated photocurrent under transient conditions.

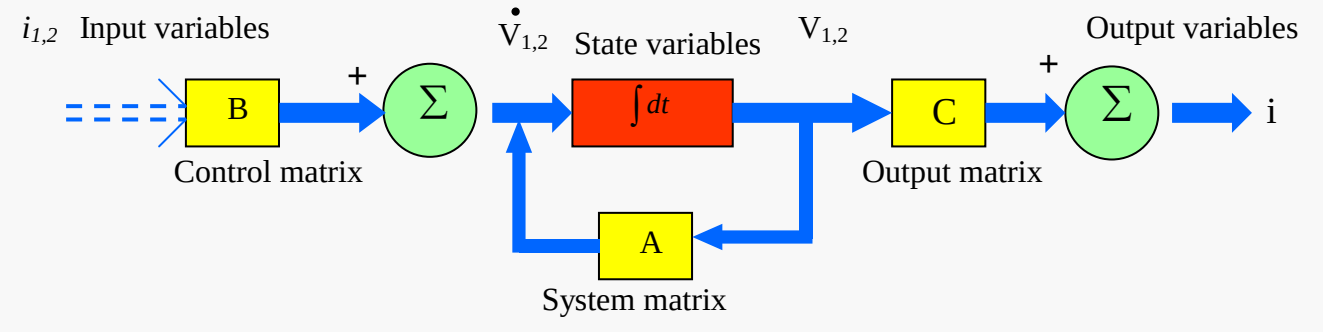

Figure 4.11 *Block diagram of the state model considered as a parallel current bucket connection inflow* $[i_1(t) // i_2(t)]$.

Figures 4.11 show simplified bloc diagram of the state model considered as a parallel current bucket connection inflow $[i_1(t) // i_2(t)]$.

Under optical bias the control matrix B takes into account the enhancement or quenching of the channels due to the steady state irradiation (Chapter III). It will be affected by α_1 and α_2 coefficients that determine how the system input affects the state change.

$$B=\begin{bmatrix} \frac{\alpha_1}{C_1} \\ \frac{\alpha_2}{C_2} \end{bmatrix} \tag{26}$$

The time periodic linearized state equations (equations 24 and 25) will then take the form:

$$\frac{dv_{1,2}}{dt}=\begin{bmatrix} -\frac{1}{R_1C_1} & \frac{1}{R_1C_1} \\ \frac{1}{R_1C_2} & -\frac{1}{R_1C_2}-\frac{1}{R_2C_2} \end{bmatrix} v_{1,2}(t)+\begin{bmatrix} \frac{\alpha_1}{C_1} \\ \frac{\alpha_2}{C_2} \end{bmatrix} i_{1,2}(t) \tag{27}$$

$$i(t)=\begin{bmatrix} 0 & \frac{1}{R_2} \end{bmatrix} v_{1,2}(t) \tag{28}$$

Where α_1 and α_2 coefficients determine how the background affects the state change. Based on Chapter III, Figures 3.15 and 3.17, under red background, α_1 >1 (α_B+ α_G >1) and α_2<1(α_R+ α_G <1). The opposite will occur under blue irradiation. Under green background both are balanced.

4 Capacitive active band pass filter model

4.1 *Two stage active circuit*

The optoelectronic model supported by the complete dynamical large signal Ebers-Moll model is displayed in Figure 4.12.

The model of the device looks fairly complex, but when broken down can be divided into two sections (Figure 12a): a short-pass filter (front phototransitor, Q_1) and a long-pass filter (back phototransistor, Q_2) sections. So, it can be made out of a short-pass and a long-pass filter when connected both active filter sections in parallel (Figure 4.12b).

To allow independent blue, red and green channels transmission four square-wave current sources with different intensities are used; two of them, $\alpha_1 I_1$ and $\alpha_2 I_2$, with different frequencies to simulate the input blue and red channels (Chapter III, Figure 3.2a) and the other two (Chapter III, Figure 2a) $\alpha_1 I_3$ and $\alpha_2 I_4$, with the same frequency but different intensities, to simulate the green channel due to its asymmetrical absorption across both front and back phototransistors (Chapter III, Figure 3.2b).

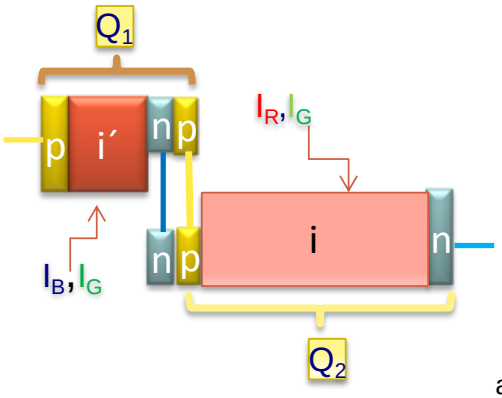

a)

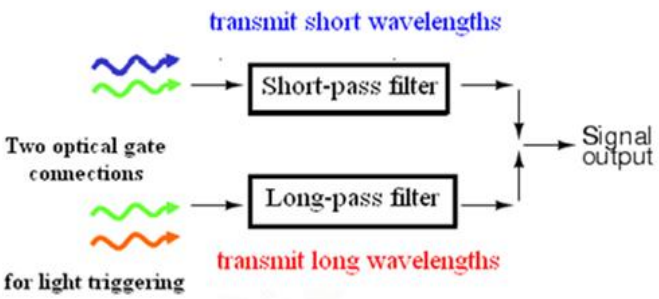

b)

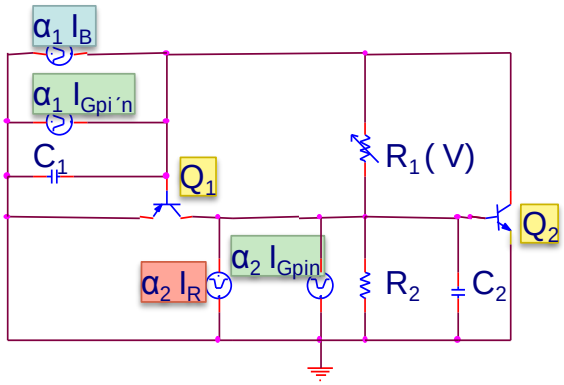

c)

Figure 4.12 *a) Two connected transistor model, b) Two active capacitive filter sections and c) ac equivalent circuit.*

Taking into account equations 25 and 26, in Figure 4.13 it is displayed the block diagram of the optoelectronic state model for a WDM pi´npin device under different electrical and optical bias conditions. λ_1, λ_2, λ_3 represent the color channels, R_1 and R_2 the dynamic internal and back resistances and α_1 and α_2 are the coefficients for the steady state irradiation.

The amplifying elements, α_1 and α_2, can provide gain if needed and attenuate unwanted wavelengths (<1) while amplifying (>1) desired ones. The values and the strategic placement of the resistors determine the basic shape of the output signals. Under negative bias the device has low ohmic resistance (low R_1) since the base emitter junction of both transistors are reverse polarized and conceived as phototransistors. This results in a charging current gain proportional to the ratio between both collector currents (α_2 C_1/ α_1 C_2). Taking into account Figure 3.15 in Chapter III, under red background, α_1 >1 and α_2<1. The opposite will occur under blue irradiation. Under green background both are balanced. Under positive bias the internal junction becomes reverse-biased and no amplification effect is observed.

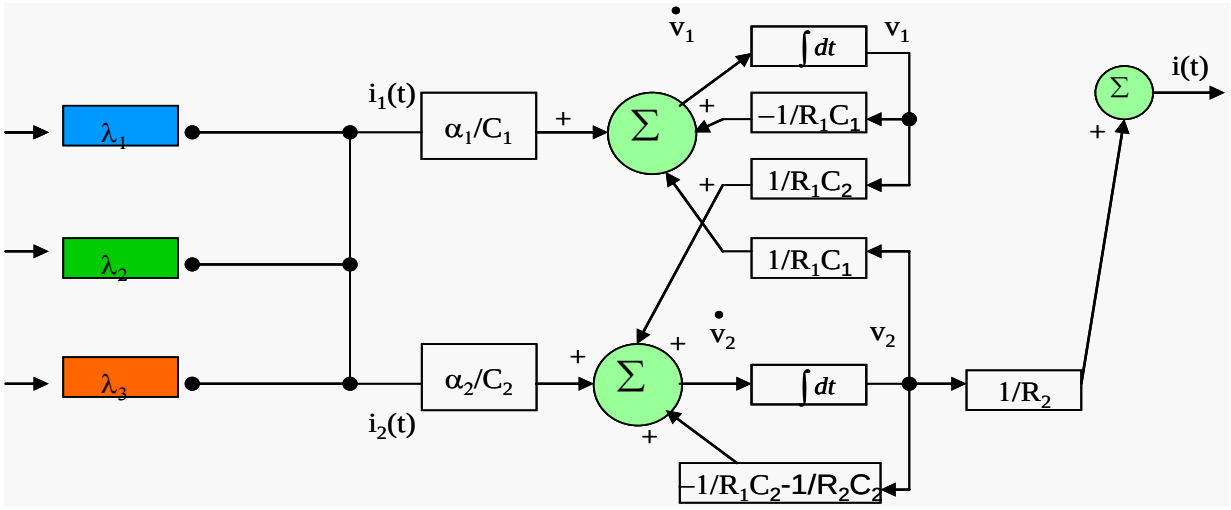

Figure 4.13 *Block diagram of the optoelectronic state model for a pi´n/pin device.*

4.2 Computational method

Research involving the use of computational methods is not more than one completion of investigation in theoretical and experimental, showing how main advantages validation and analysis of mathematical and physical models and support for experimental methods to identify those factors more complex to obtain experimentally.

Moreover, computational methods make it possible also to obtain results more quickly and lower cost compared with the experimental investigation, improve fundamental understanding of processes and design requirements; the technical focus of the simulator will involve the development of new methodologies and the next generation of technology for optical processing devices based on multilayered a-SiC:H p-i-n structures for short range optical communications.

Along this section, the multiplexed signals are simulated by applying the four order Runge-Kutta method [30] to solve the corresponding state equations. MATLAB can be used as a programming environment and the input parameters chosen in compliance with the experimental results. The multiplexed signal was simulated by applying the Kirchhoff's laws for the simplified ac equivalent circuit and the four order Runge-Kutta method to solve the corresponding state equations. MATLAB was used as a programming environment and the input parameters chosen in compliance with the experimental results.

4.3 Transfer characteristics

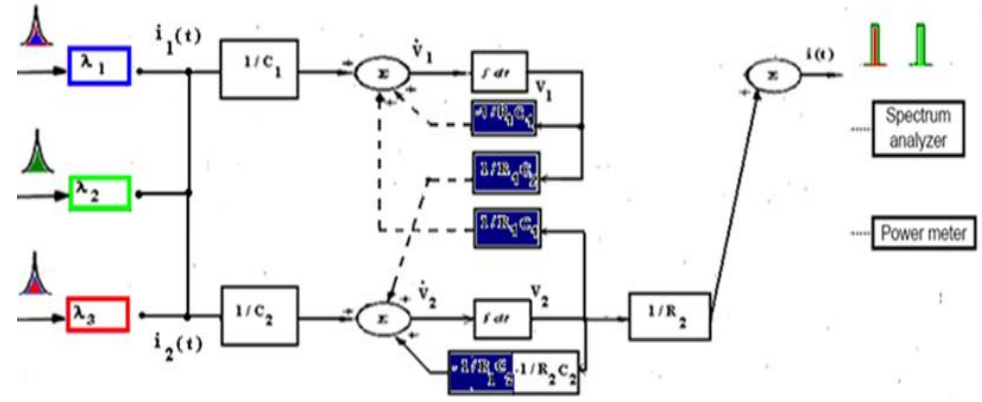

a)

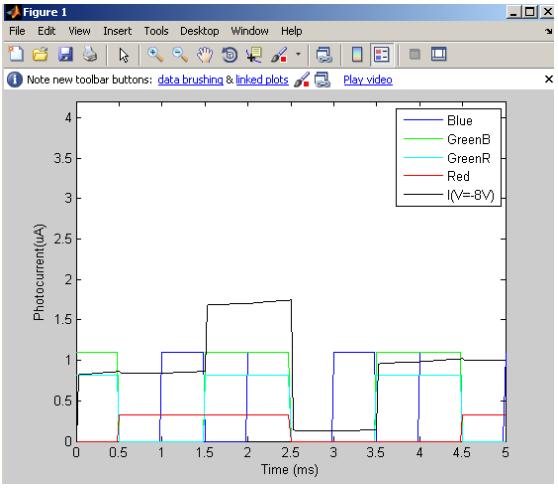

b)

Figure 4.14 *a) Schematic of the simulation under positive bias. b) Simulated multiplexed, current sources under positive dc bias (R1=1MΩ; +1V), without irradiation.*

To illustrate the transfer characteristics effects due to changes in steady state light, *dc* control voltage or applied light pulses the same bit sequence of Figure 3.24, Chapter III was used The following steps in the operation and control of the optoelectronic circuit are considered:

1 *Positive voltage bias control.* Only an *ac* current is flowing through the load capacitance C_2 (Figure 4.14a). The device has high ohmic resistance (high R_1) and remains in its non conducting state unless a light pulse (I_2 or I_2+I_4) is applied to the base of Q_2. This pulse causes Q_2 to conduct as the reversed biased n-p internal junction behaves like a capacitor inducing a charging current across R_2. No amplification effect was detected since Q_1 acts as a load and no charges are transferred between C_1 and C_2 (Figure 4.14b).

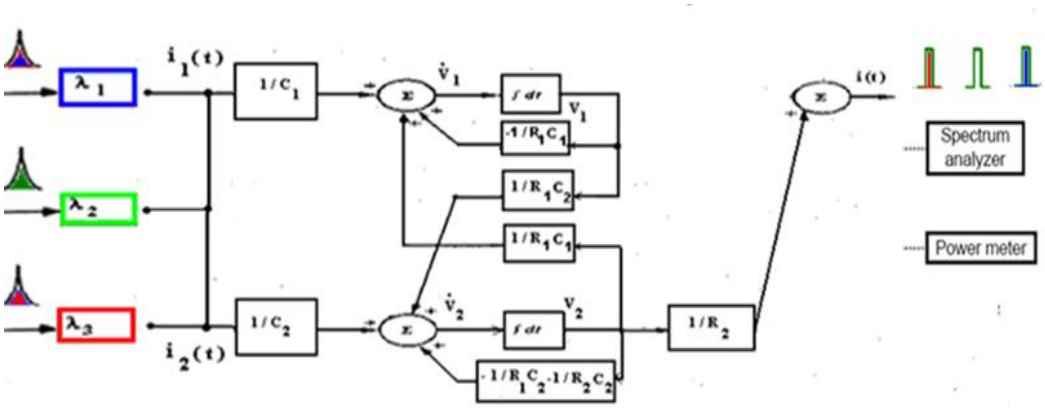

a)

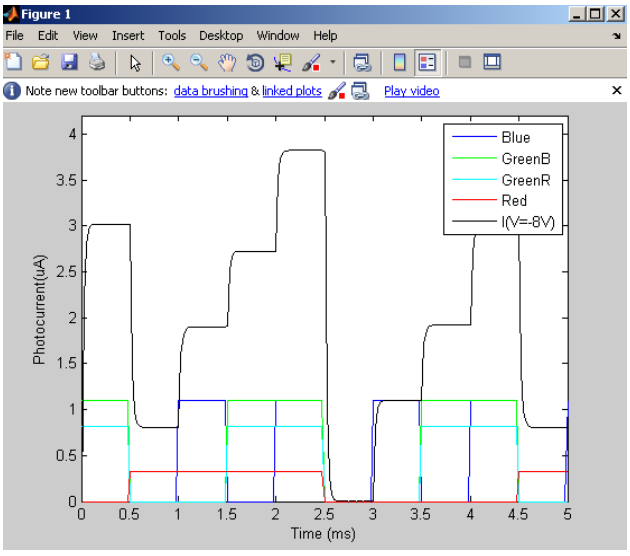

b)

Figure 4.15 *a) Schematic of the simulation under negative bias, b)Simulated multiplexed, current sources under negative (R1=1KΩ; -8V) dc bias, without irradiation.*

2 *Negative dc voltage bias control.* Under negative bias the device has low ohmic resistance (low R_1) the base emitter junction of both transistors are inversely polarized and conceived as

phototransistors, thus taking advantage of the amplifier action of neighboring collector junctions, which are polarized directly. This results in a charging current gain proportional to the ratio between both collector currents (C_1/C_2). The device behaves like an optoelectronic controlled transmission system that stores, amplifies and transports the minority carriers generated by the current pulses, through the capacitors C_1 and C_2. Here, the *dc* voltage control creates a voltage across one or both capacitors which, when superimposed with an *ac* pulse, collectively saturates the circuit. No additional change in the voltage across the capacitors occurs. This results in maximum power transfer to the load (Figure 4.15).

3 *Optical bias control.* Depending on it wavelength, the optical bias changes the amplitude of the $I_1(t)+I_3(t)$ and $I_2(t)+I_4(t)$ ac current sources by respectively α_1 and α_2 control factors. These control factors manages the way the system input affects the state change and so the voltages across one or both capacitors. Blue, red or green irradiations move asymmetrically the bases of Q_1, Q_2 or both toward (away) their emitter voltages, self-forward (reverse) effect, resulting, respectively in lower (higher) values of I_1, I_2, I_3 and I_4 when compared with no optical bias. The device is a wavelength current-controlled device that uses changing in the wavelength of the optical bias to control the power delivered to a load, acting as an optical amplifier.

Blue steady state irradiation (Figure 4.16a) ($\Phi \neq 0$) and negative bias moves asymmetrically Q_1 and Q_2 bases toward their emitter voltages (self-forward effect), resulting in lower values of I_1 and I_3 when compared without optical bias, To simulate the blue background, the current source intensities are multiplied by $\alpha_1 < 1$ and $\alpha_2 > 1$ (Figure 3.11, Chapter III).

The opposite occurs under red irradiation. So, to simulate the red background the intensities of the current sources are multiplied by $\alpha_1 > 1$ and $\alpha_2 < 1$ control factors.

As shown in Chapter III, §6, green steady state irradiation ($\Phi \neq 0$) and negative bias moves asymmetrically Q_1 and Q_2 bases toward their emitter voltages (self-forward effect), resulting in lower values of I_3 and I_4 when compared without optical bias. Opposite behavior occurs with I_1 and I_2 that slightly increase due to the self reverse effect of the less absorbing diode. The effect of the green bias is negligible if I_1 or I_2 are ON since Q_1 and Q_2 are triggered separately and the discharge of the capacitors independent. During the green pulse (I_3 and I_4 ON) only residual charges are transferred through R_1. So, only the charges generated in the base of Q_2 (I_4) are collected.

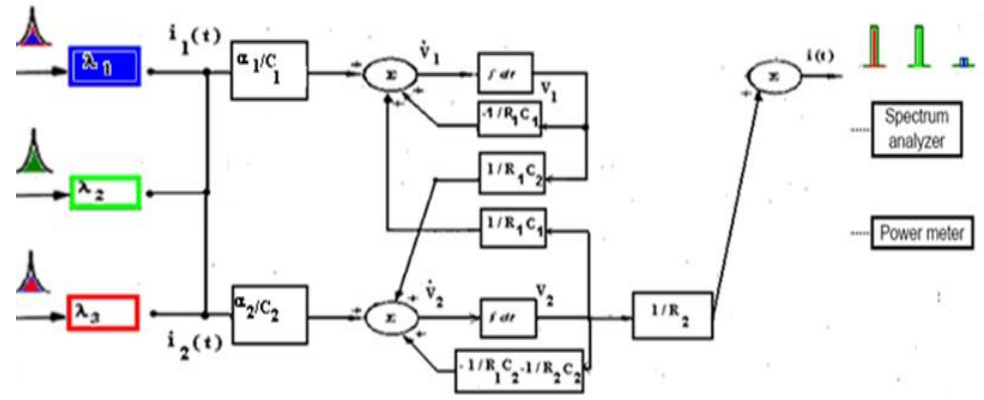

a)

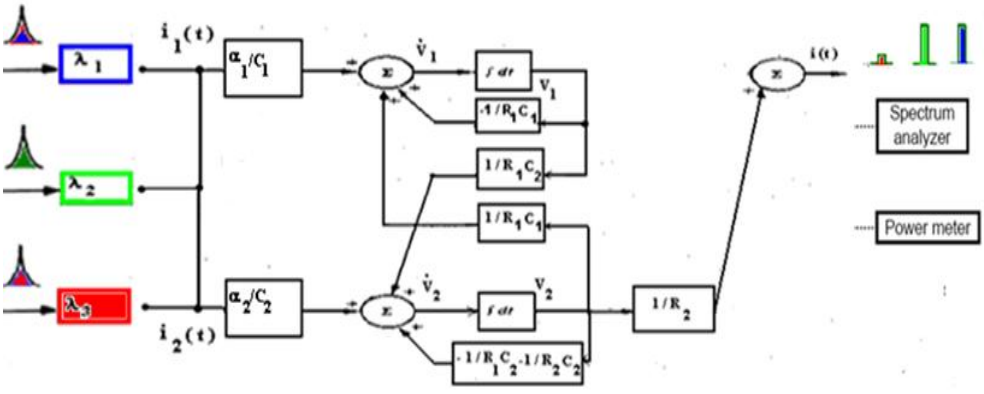

b)

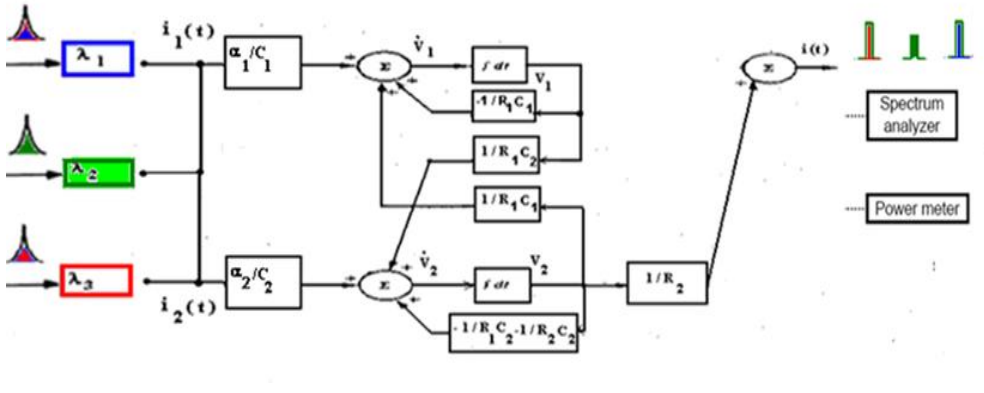

c)

Figure 4.16 *Schematic of the simulation under: a) blue; b) red, c) green steady state irradiation and negative bias.*

When an optical bias is applied it mainly enhances the field distribution within the less photo excited sub-cell: the back under blue irradiation and the front under red steady bias. Therefore, the reinforcement of the electric field under blue irradiation and negative bias increases the collection of

carriers generated by the red channel and decreases the blue one. Under red optical bias, the opposite behavior is observed. The green bias absorption is balanced in both front and back cells and the collection of carriers generated by the green channel is strongly reduced. Results show that the output signal has a strong nonlinear dependence on the light absorption profile due to the self biasing of the junctions under unbalanced light generation profiles. Self optical bias amplification under uniform irradiation and transient conditions is achieved. This optical nonlinearity effect, under transient conditions, is used to distinguish a wavelength, to read a color image, to amplify or to suppress a color channel add and drop an optical signal.

The use of a double pi'n/pin a-SiC:H WDM heterostructure as an active band-pass filter transfer function depends on the wavelength of the trigger lights and device bias. The dynamic response can range from a positive feedback (regeneration) under positive bias, to two different behaviors under negative bias. Under negative bias the device acts as an active multiple-feedback filter with or without transient gain, depending on the trigger lights. The expected optical amplification (Chapter III) is observed due to the effect of the active multiple-feedback filter when the back diode is light triggered

Results show that the two-transistor model explains the difference between the conduction mechanisms, under positive and negative bias, helping to understand the signal decoding algorithm. Under positive bias the red and green channels are immediately decoded. Under negative bias, different charging currents have to be considered. The balance between them depends on the presence of three, two or one channel ON. So, by comparing the different sublevels signals under positive and negative bias the input channels are recovered.

4.4 Dynamics of a parallel bucket connection

Branches of fluid dynamics include hydrodynamics, (where liquids in motion are studied). When the liquid settles, it balances out to the same level in all of the two containers regardless of the shape and volume of the containers [31]. This process occurs because gravity and pressure are constant in each vessel (hydrostatic pressure) Figure 4.17 a) and b). In Figure 4.17 c) it is modeled the red optical bias front placement within a WDM link. In Figure 4.17 d) it is modeled the red optical bias back placement within a WDM link. The analogy with a disruption of a high density cloud by a strong shock wave: a dynamic load balancing scheme is incorporated to improve the parallel efficiency.

The general approach, to construct communicating-vessels models of the parallel bucket connection containing a homogeneous fluid are displayed in Figure 4.17. Here, the distribution and output of fluid volume inside communicating-vessels system can visualize parallel bucket properties. Taking into account section §3 and §4, the area $A_{1,2}$ of the containers model the capacities of front and back diodes $C_{1,2}$ respectively. To the input variables $u_{1,2}(t)$ it corresponds the current sources $I_{1+3,2+4}$. (input

channels). To q_0 it is ascribed the current output *i(t)*, (multiplexed signal). The values of $h_{1,2}(t)$ signify the $v_{1,2}(t)$ state variables of the system (self voltage effect).

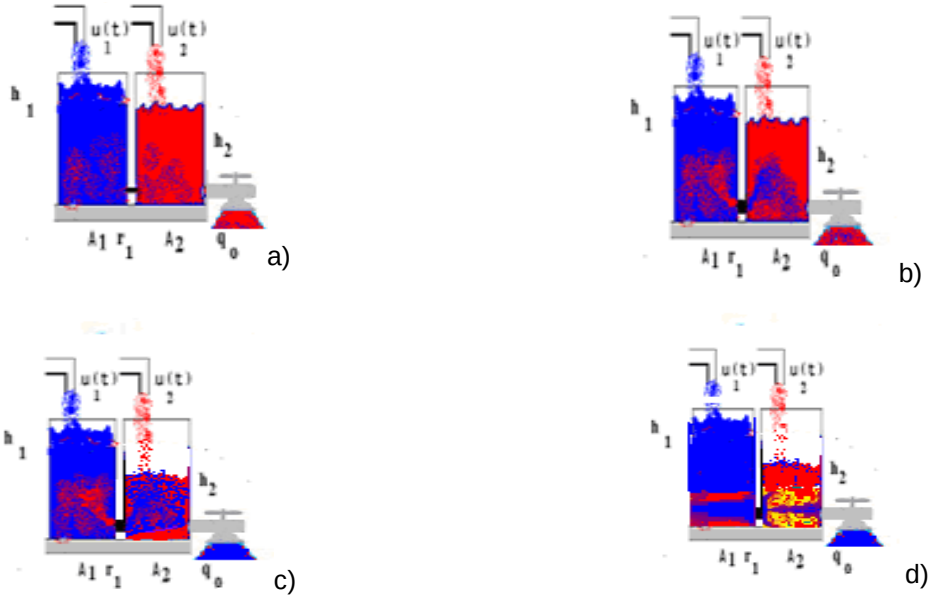

Figure 4.17 *The distribution and output of fluid volume inside communicating-vessels system visualize parallel bucket properties.a) positive voltage.b) negative voltage. c) front optical bias.d) back optical bias.*

Also, the distribution and output of fluid volume inside communicating-vessels system can visualize partitioning processes and parallel bucket properties that involve low or high hydrostatic resistance connecting communicating-vessels and conserved quantities between. In the analogical model R_1 represents the external applied voltage. It is high if the device is positively bias and low, under negative applied bias (Figure 4.12). The α_1 and α_2 control factors will affect $u_{1,2}(t)$ once they are related with the effect of the optical bias in the control matrix .

5 Model validation

5.1 Influence of the applied voltage

Based on the optoelectronic model, the multiplexed signal was simulated by applying the Kirchhoff's laws for the simplified *ac* equivalent circuit (Figure 4.12c). In Figure 4.18 the simulated currents (symbols) under negative and positive bias are compared. No steady state optical bias was added (α_1=α_2=1, Equation 28). To simulate the negative and positive electrical bias two values of R_1 were

used, a low one under negative bias since the internal junction is forward bias and a high value, under positive bias, due to its reverse state. The current sources are also displayed (dash lines). The same bit sequence of Figure 3.23, Chapter III was used [16]. To validate the model the experimental multiplexed signals are also shown.

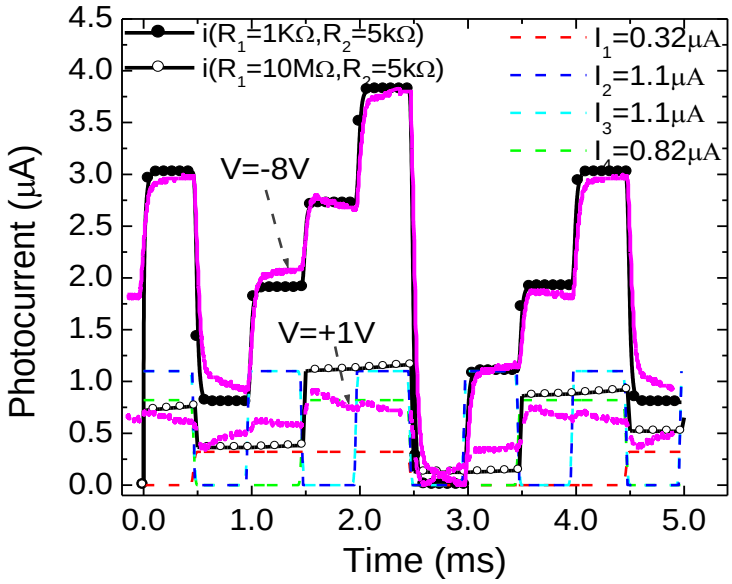

Figure 4.18 *Multiplexed simulated (symbols), current sources (dash lines) and experimental (solid lines) under negative (R_1=1KΩ; -8V) and positive (R_1=10MΩ; +1V) dc bias without any background.*

Figure 4.19a displays the current, i(t), under positive (open symbols) and negative (solid symbols) dc bias. The input transient current sources used to simulate the photons absorbed in the front (blue, I1), back (red, I_2), or across both (green, I_3 and I_4) photodiodes are also displayed (dash lines). We have used as input parameters the experimental values (Figure 4.19b). To validate the model the experimental multiplexed signal at -8V and +1V is also shown (lines) [32].Many proteins have benefited from the process of selective evolution to become very sensitive to specific molecular species such that in their presence conformational changes and binding events take place. One possible approach to detect such events is Fluorescence Resonance Energy Transfer (FRET), a mechanism by which the fluorescence wavelength changes if two labeled molecules come close enough [33].

To simulate the FRET pairs and the excitation light a chromatic time dependent combination of violet (λ_V =400nm), cyan (λ_C=470nm) and yellow (λ_Y=615 nm) wavelengths was applied to the device from the glass side (Chapter III, §8). The generated photocurrent was measured under negative (-8V, solid arrows) and positive (+1V, dot arrows) bias to readout the combined spectra

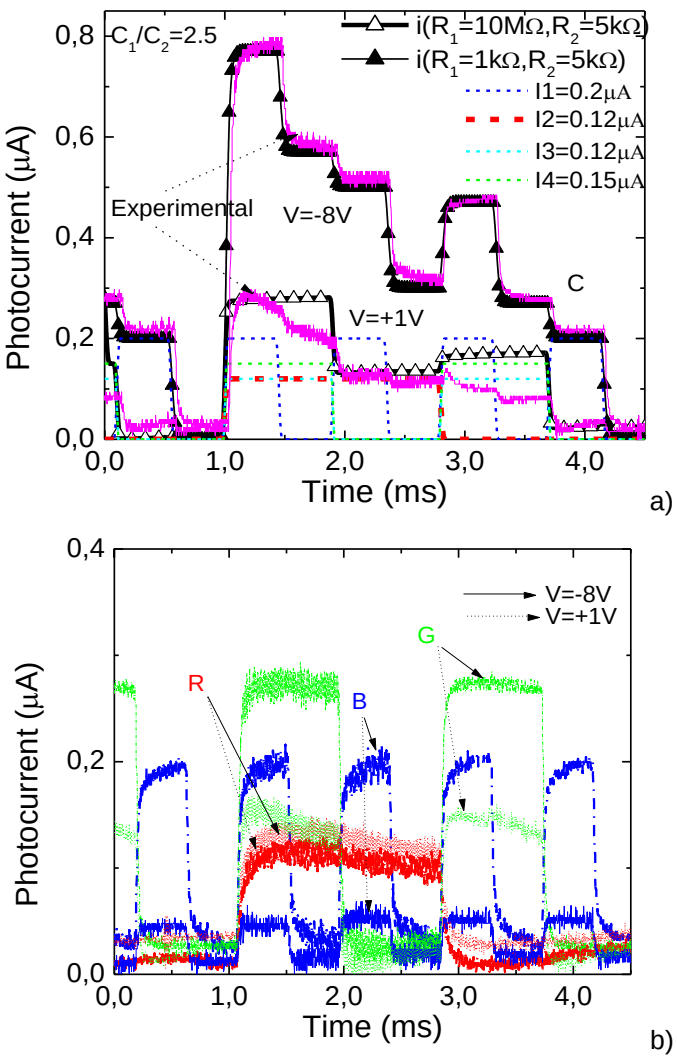

Figure 4.19 *Multiplexed simulated (symbols) and experimental (solid lines) results under positive and negative dc bias. b) Photocurrent signals measured with different input channels under reverse (-8 V, solid arrow) and forward (+1 V, dotted arrow) bias.*

Figure 20a displays the combined signals due to the individual (V, C, Y) and simultaneous (VCY) transmission of the three independent sequences, each one assigned to one color channel (λ_V , λ_C , λ_Y). The reference level was assumed to be the signal when all the input channels were OFF. At the top of the figure, the individual optical signals are displayed to guide the eyes in relation to the different ON-OFF states. The independent bit sequences (8 bit per wavelength channel) were chosen in order to sample all the possible chromatic mixtures for a pulse rate of 2000bps [34].

In Figure 4.20b the simulated (symbols) and experimental (lines) multiplexed signals (under positive (R1=10MΩ; +1V) and negative (R1=1kΩ; -8V) dc bias are displayed. The ac current sources used as input channels (I_1, I_2 , I_3 and I_4 dash lines) are also shown. We have used as input parameters the experimental values and the same bit sequence (V, C, Y, Figure 4.20a).

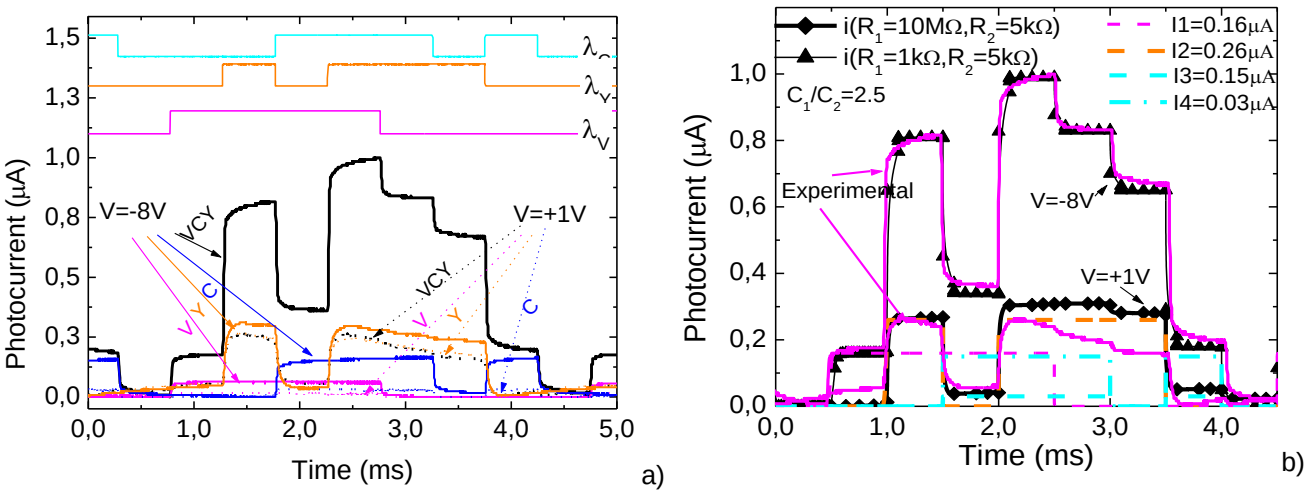

Figure 4.20 *a) Multiplexed signals under negative and positive bias. On the top, the optical signal used to transmit the information guide the eyes on the different ON-OFF states. b) Simulated (symbols) and experimental (lines) multiplexed signals (under positive (R_1=10MΩ; +1V) and negative (R_1=1kΩ; -8V) dc bias. The ac current sources used as input channels (dash lines) are displayed.*

Under negative bias it presents eight separate levels each one corresponding to the presence of three, two, one or no color channel ON. Under positive bias the levels are reduced due to the lower sensitivity of the device to the cyan and violet irradiation (Chapter III, §8). No optical amplification was detected. The output signal is mostly due to the collection of the yellow absorbed photons, thus allowing the instantaneous recognition of the yellow channel. By comparing the signals under positive and negative bias it is possible to decode both the cyan and yellow components. The device is a wavelength division multiplexer device (WDM). The combined effect of optical independent bit sequences is converted to an electrical signal, via the transducer, keeping the input information (color, intensity and pulse rate).

In Figure 4.21 the detection of only two fluorophores. (yellow and cyan channels) is attempted.

In Figure 21a the generated photocurrent (symbols) is measured under negative (-8V) and positive (+1V) bias to readout the combined spectra. The light modulation frequency of one channel was chosen to be double of the other to ensure a synchronous relation of ON-OFF states along each cycle. For each independent wavelength, the output optical powers were adjusted to give approximately the same signal amplitude at -8V (lines). The reference level was assumed to be the signal when all the input channels were OFF. In Figure 21b the multiplexed simulated (symbols) and experimental (solid lines) signals under positive (R_1=10MΩ; +1V) and negative (R_1=1kΩ; -8V) *dc* bias. The current sources used as input channels (I_1 and I_2) are displayed.

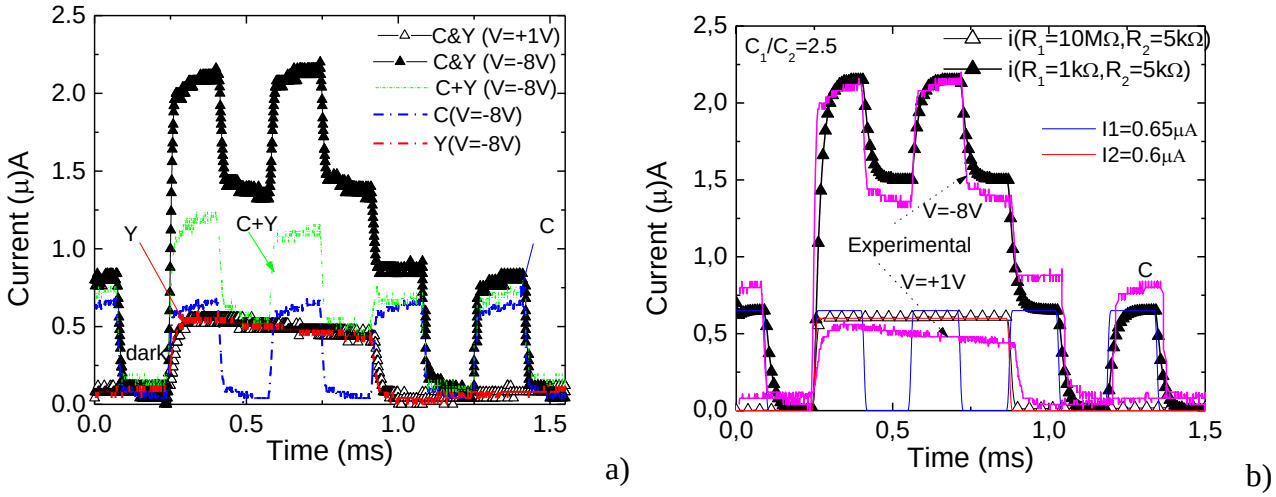

Figure 4.21 *a) Input channels (lines) and multiplexed signals (symbols) under negative and positive bias. b) Multiplexed simulated (symbols) and experimental (solid lines) signals under positive (R_1=10MΩ; +1V) and negative (R_1=1kΩ; -8V) dc bias. The current sources used as input channels (I_1 and I_2) are displayed.*

As expected (Chapter III) the absence of one input channels (the violet) reduces the number of separate levels. Under negative bias there are four separate levels while under positive bias, they were reduced to one half due to the blindness of the sensor to the cyan component. Also, under negative bias, the sum of the input channels is lower than the correspondent multiplexed signals (see arrows in the figure). This optical amplification, mainly on the ON-ON state is due to the self bias effect under negative applied bias. Under positive bias the device becomes blind to the top photodiode and the cyan component of the combined spectra falls into the dark level, allowing the recognition of the yellow input channel. By comparing the signals under positive and negative bias and using a simple algorithm that takes into account the different sub-level behaviors it is possible to decode the cyan and yellow components.

Good agreement between experimental and simulated data was observed. Under negative bias and if no optical bias is applied, the expected eight or four levels are detected, each one corresponding to the presence of three, two, one or no color channel. Under positive bias or steady state irradiation the levels are amplified or reduced depending on the external control. The expected optical amplification is observed due to the effect of the active multiple-feedback filter when the back diode is light triggered.

Under forward bias (high R_1) the device remains in its non conducting state unless a light pulse (I_2 or I_2+I_4) is applied to the base of Q_2. This pulse causes Q_2 to conduct because the reverse biased n-p internal junction behaves like a capacitor inducing a charging current (I_2+I_4) across both collector junctions. The collector of the conducting transistor pulls low, moving the Q_1 base toward its collector voltage, which causes Q_1 to conduct. The collector of the conducting Q_1 pulls high, moving the Q_2 base in the direction of its collector. This positive feedback (regeneration) reinforces the Q_2 already conducting state and a current I_2+I_4 will flow on the external circuit.

Results show also that the two-transistor model explains the difference between the conduction mechanisms, under positive and negative bias, helping to understand the signal decoding algorithm (section 5). Under positive bias the red and green channels are immediately decoded since the collected current is due exclusively to the generated carriers at the back diode. Under negative bias, depending on the ratio between C_1 and C_2, different charging currents across the reversed junctions have to be considered. The balance between them depends on the presence of three, two or one channel ON (Figure 4.2-3). So, by comparing the different sublevels signals under positive and negative bias it is possible to recover the blue, the green and the red input channels.

5.2 Influence of the optical bias

In Figure 4.22 the simulated current under green (a) and red (b) backgrounds are displayed under negative bias. The current sources are also displayed (dash lines). To simulate the red and the green backgrounds, current sources intensities were multiplied by the on/off ratio between the input channels with and without optical bias (Figure 3.11, Chapter III). The same bit sequence of Figure 4.18 was used. To validate the model the experimental multiplexed signals are also shown (solid lines).

Green irradiation (Figure 4.22b) moves asymmetrically the Q_1 and Q_2 bases toward their emitter voltages, resulting in lower values of I_3 and I_4 when compared without optical bias. I_1 and I_2 slightly increase due to the increased carrier generation on the less absorbing phototransistors. Under negative bias during the red and blue pulses (I_1 or I_2 ON), as well as without optical bias, the internal junction remains forward biased and the transferred charge between C_1 and C_2 reaches the output terminal as a capacitive charging current. During the green pulse (I_3 and I_4 ON) only residual charges are transferred between C_1 and C_2. So, only the charges generated in the base of Q_2 (I_4) reach the output terminal as can be confirmed by the good fitting between simulation and experimental results of both multiplexed signals with and without optical bias.

A chromatic time dependent wavelength combination of the same pulsed input channels but with different bit sequences was used to generate a multiplexed signal. The output waveforms are shown in Figure 4.23, under red steady state illumination (red line) and without it (dark line). The bit sequences to drive the channels are shown in the top of the figure to guide the eyes. The simulated current under negative bias with and without red background is shown. The current sources are also displayed (dash lines).

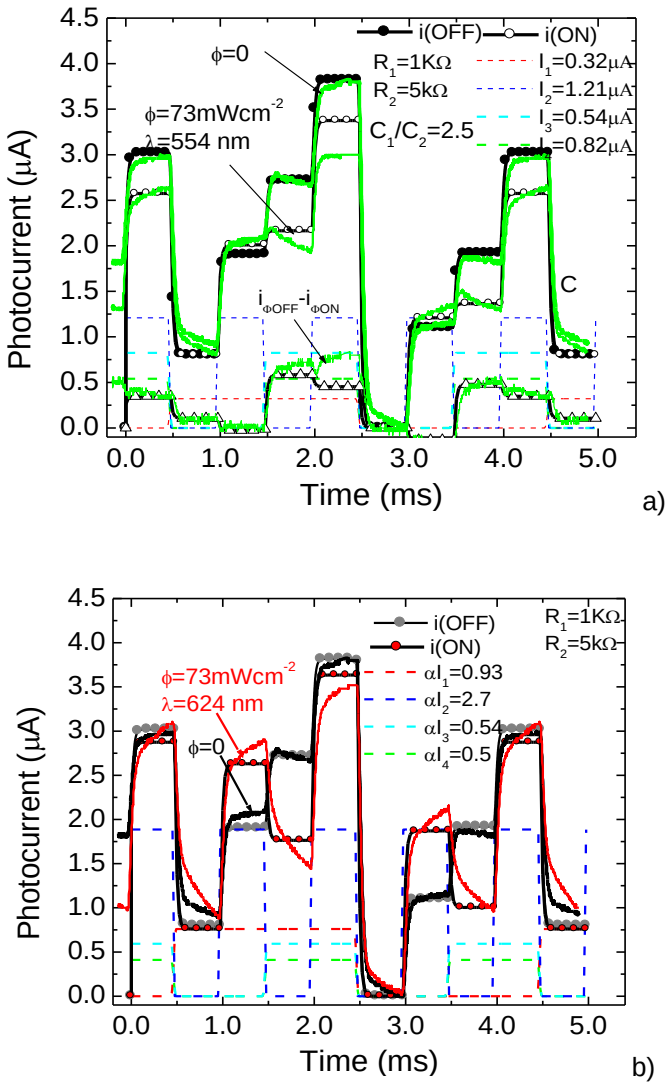

Figure 4.22 *Multiplexed simulated (symbols), current sources (dash lines) and experimental (solid lines): under negative (R1=1kΩ; -8V) dc bias and green (a) and red (b) backgrounds.*

A good agreement between experimental and simulated data was achieved. The device behaves like an optoelectronic controlled transmission system that stores, amplifies and transports the minority carriers generated by the current pulses, through the capacitors C_1 and C_2. Here, the *dc* voltage control creates a voltage across one or both capacitors which, when superimposed with an *ac* pulse, collectively saturates the circuit. No additional change in the voltage across the capacitors occurs. Under red background the expected optical amplification in the low wavelength range is observed due to the effect of the active multiple-feedback filter when the back diode is light triggered.

Therefore, depending on its wavelength, the optical bias changes the amplitude of the *ac* current sources by an α factor, and so the voltages across one or both capacitors. When compared with no optical bias, blue irradiations move asymmetrically the bases of Q_1 toward (self-forward effect) and Q_2 away (self-reverse effect) their emitter voltages, resulting, respectively in lower values of I_1, and higher

values of I_2. Red background promotes an opposite behavior while, under green irradiation the effect on I_3 and I_4 is balanced. The circuit can leave the saturation resulting in a wavelength controlled power transfer to the load that allows tuning an input channel or to optically demultiplex a polychromatic channel.

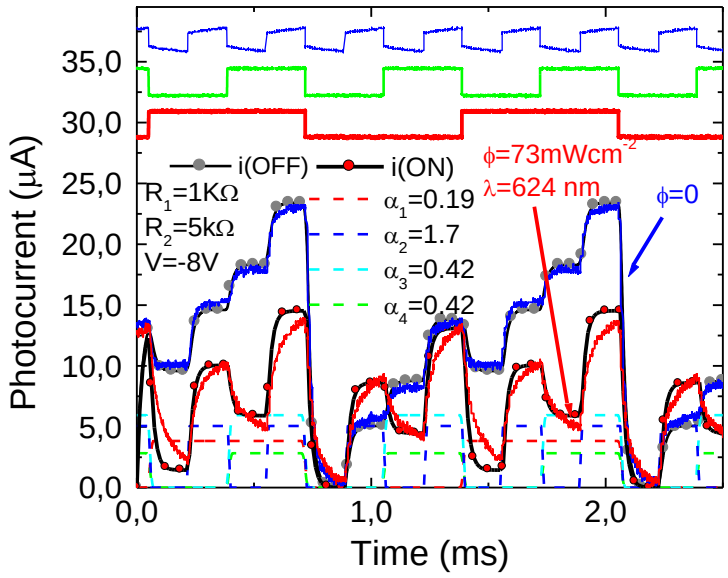

Figure 4.23 *Output simulated waveform (symbols), current sources (dash lines) and experimental signals (solid lines), under negative (R_1=1kΩ; -8V) without and with red background.*

Figure 4.24a displays the combined signals due to transmission of the three independent sequences, each one assigned to one color channel without (black line) and under red background irradiation (color lines). The reference level was assumed to be the signal when all the input channels were OFF. At the top of the figure, the individual optical signals are displayed to guide the eyes in relation to the different ON-OFF states. The independent bit sequences (8 bit per wavelength channel) were chosen in order to sample all the possible chromatic mixtures for a pulse rate of 6000bps.

In Figure 4.24b the simulated current without and under red backgrounds is displayed (symbols). The input channels (I_V, I_C , I_Y,) are also displayed (lines). To simulate the red background, current sources intensities (input channels) were multiplied by the on/off ratio between the input channels with and without red optical bias (α_C , α_Y, α_V,). The same bit sequence and bit rate of Figure 4.24a was used.

Good agreement between experimental and simulated data was observed. The eight expected levels, under reversed bias, and their reduction under red irradiation, are clearly seen. Under red background the expected optical amplification of the cyan channel and the quenching of the yellow one were observed due to the effect of the active multiple-feedback filter when the back diode is light triggered. Here the photocurrent rises as the front capacitor is charged up (self reverse effect), and falls as the capacitor discharges (self forward effect). Also when the red channel is on, with red background the back capacitor falls more than without red irradiation.

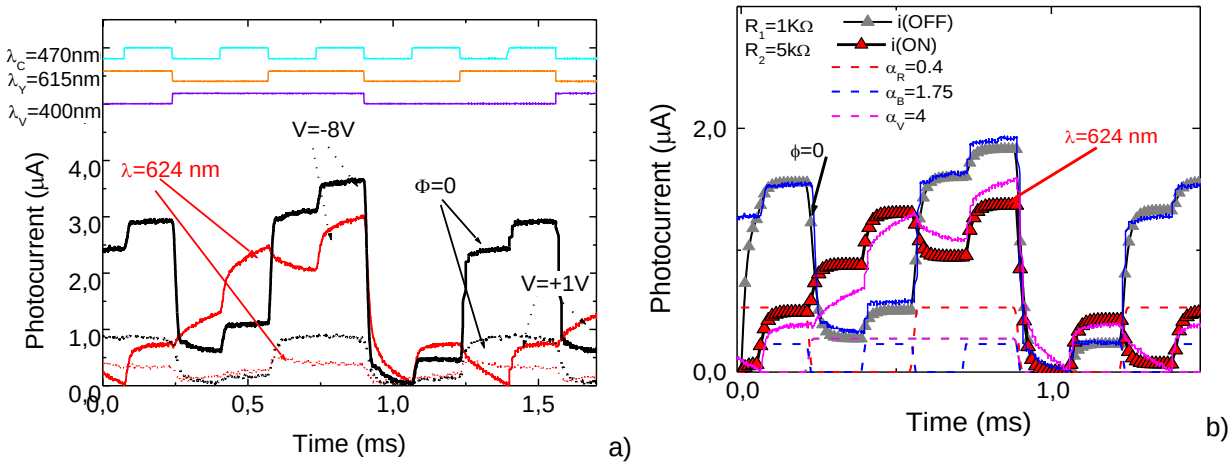

Figure 4.24 *a) Multiplexed signals with and without red background. b) Multiplexed simulated (symbols), input channels (dash lines) and experimental (solid lines): under negative dc bias and red background.*

A good fit between experimental and simulated results were achieved, mainly without background irradiation. Under red irradiation due to the high rise time of the violet channel the fit is not so good when the violet channel is on its ON state.

Experimental and simulated results show that the device acts as a charge transfer system. It filters, stores and transports the minority carriers generated by the current pulses, keeping memory of the input channels (color, intensity and modulated frequency). If this optical transducer is used in FRET analysis, under appropriated applied voltages, it can detect not only the cyan and yellow fluorescence pairs, but also the ratio between their intensities that correlates with the distance between the fluorophores.

6 Conclusions

A theoretical analysis, supported by numerical and electrical simulations, gives accurate description of the experimental results and help to understand the physics behind the circuit-switching solutions. Electrical models of the equivalent circuit are present to support the sensing methodologies.

MATLAB was used as a programming environment and the input parameters will be chosen in compliance with the experimental results. When a chromatic time dependent wavelength combination with different transmission rates are shinning on the device it operates as a tunable wavelength filter and can be used in wavelength division multiplexing systems for short range communications.

Based on the experimental results (Chapter 2 and 3), device configuration and combining the properties of active short-pass and long-pass filter sections, an optoelectronic model, is developed and supported by an electrical simulation. A demux algorithm is implemented.

The dc biasing condition for each stage, the ac circuit representation and linear state model are determined.

We have described the meaning of the physical parameters required to simulate photonic and electronic properties, and we have tried to find a connection between some of them in ways that can be considered intuitive for an end user. Further, we have found that the dependencies between the connected parameters work well with respect to applied voltage, and allow for various types optical bias.

The multiplexed signal is simulated by analyzing the simplified ac equivalent circuit and the four order Runge-Kutta method. The device, modeled by a simple circuit with variable capacitors and interconnected phototransistors through a resistor, is a current-control device. The introduction of two analogous RC networks in a block oriented simulation language like Matlab was used as a programming environment, establishing the link between a powerful modelling concept for dynamic systems and a simulation unit with good performance.

Interacting with the user-accessible Matlab subroutines, the transfer characteristics effects due to changes in steady state light, dc control voltage or applied light pulses are presented and have improved our understanding of the capabilities of the modeling approaches used to take into account the input parameters in compliance with the experimental results.

An increasing need for simulation tools exists, because simulation is recognized to be a very versatile and influential aid for analysis and design of a product, in the analysis of physical and technical systems.

The concept of a parallel current bucket connection inflow is established to give insight on the physics of the device.

This chapter reports results on the use of a pi'n/pin a-SiC:H heterostructure as an active band-pass filter transfer function whose operation depends on the wavelength of the trigger light, on the applied voltage and on the wavelength of the additional optical bias. We confirm that when a chromatic time dependent wavelength combination with different transmission rates are shinning on the device it operates as a tunable wavelength filter and can be used in wavelength division multiplexing systems for short range communications.

The model results for both applied voltage and optical bias are in good agreement with laboratory observations. Good fit experimental and simulated results were achieved concluding either applied voltage and optical bias influences either FRET analyses. As technology develops and we get more understanding, we can get better and better simulations. Experimental and simulated results have been compared and validated the use of multilayered structures based on amorphous silicon technology as a solution in WDM technique for information transmission and decoding in the visible range.

Simulated results show that the output signal has a strong nonlinear dependence on the light absorption profile, combining the demultiplexing process with the simultaneous photodetection and self amplification of the signal, improving our understanding of the multiplexed signal.

We conclude that computational photonic dynamics has enormous potential for future optoelectronic industry. It is a powerful tool for solving a wide variety of photonic industrial problems. Development

work on solver algorithms and user interface generation are ongoing, with the objectives of improving accuracy, reducing solution time and providing ready access throughout the enterprise. This would result in significant gains in productivity and profitability.

7 References

[1] COX III, C., Ackerman, E., Helkey, R. and Betts, G. E. – Technique and Performance of Intensity- Modulation Direct – Detection Analog Optical Links. IEEE Trans. Microwaves Theory Tech. 45(8):1375-1383, Aug., 1997

[2] Seeds, A. – Optical Transmission of Microwave . Ini STONE, W, Ed. – The Review of Radio Science. London, U.K.. pp. 325-360,1996

[3] G. Einarsson, " Principles of Lightwave Communications," John Wiley&Sons, 1996.

[4] Stallings, W. "Data and Computer Communications", Pearson Education, Inc., 2007. p.247-248

[5] Dagli, N. –Wide-Bandwidth Laser and Modulators for RF Photonics. IEEE Trans. Microwaves Theory Tech., 47(7) : 1151- 1171, Jul .,1999.

[6] G Nishihara, N. et all – Optical Integrated Circuits, New York, McGraw-Hill, 1989

[7] Ramo, S., Whinnery, J. R. and Van Duzer, T. –Fields and Waves in Communication Electronics, 3rd . Ed. Vew York, John Wiley, 1994

[8] Ackerman, E. et all – Input Impedance Conditions for Minimizing the noise Figure of an Analog Optical Link IEEE Trans. Microwaves Theory Tech.,46(12).2025-2031 Dec 1998

[9] G R.F. Wolffenbuttel, "Color filters integrated with he detector in silicon" IEEE electron device letters, Vol. EDL-8,No. 1 (1987) pp.13-15.

[10] COX III, C. H. – Broad Band Directely Modulated Analog Fiber Link with Passive Intrinsic Gain and Reduced Noise Figure. Proceedings of the International Optical Meeting on Microwaves Photonics, Princetown, pp. 12-14, Oct., 1998

[11] Daniel Nolan K. O. Hill et al "Fiber Optics Handbook iber, Devices, and Systems for Optical Communications" l, McGraw Hill 2002

[12] Daryoush, A. S. et all – Interface for High Speed Fiber Optic Links: Analysis and Experiment. IEEE Trans. Microwaves Theory Tech.,39 (12) :2031-2044, Dec 19991

[13] M. A. Vieira, M., Vieira, J. Costa, P. Louro, M. Fernandes, A. Fantoni, "Double pin Photodiodes with two Optical Gate Connections for Light Triggering: A capacitive two-phototransistor model" in Sensors & Transducers Journal, Vol 10, Sepecial Issue (2011), pp.96-120. ISSN 1726-5479, www.sensorsportal.com.

[14] M. A. Vieira, Manuela Vieira, João Costa, Paula Louro, Miguel Fernandes, Alessandro Fantoni "Light-triggered Silicon-carbon Pi'npin Devices for Optical Communications: Theoretical and Electrical Approaches" in Amorphous and Polycrystalline Thin-Film Silicon Science and

Technology — 2010, edited by Q. Wang, B. Yan, S. Higashi, C.C. Tsai, A. Flewitt (Mater. Res. Soc. Symp. Proc. Volume 1245, Warrendale, PA, 2010, -A18-06, DOI: 10.1557/PROC-1245-A18-06

[15] P. Louro, M. Vieira, M. A. Vieira, M. Fernandes, A. Fantoni, G. Lavareda, C. N. Carvalho "Optical Processing Devices for Optical Communications: Multilayered a-SiC:H Architectures Amorphous and Polycrystalline Thin-Film Silicon Science and Technology — 2009, MRS Proceedings Volume 1153, A19-01 http://dx.doi.org/10.1557/PROC-1153-A19-01

[16] M. A.Vieira, M. Vieira, P. Louro, J. Costa, A. Fantoni, M. Fernandes "Light-triggered silicon-carbon pi'npin devices with self optical gain" Phys. Status Solidi C 8, No. 3, 1083–1086 (2011) http://dx.doi.org /10.1002/pssc.201000184.

[17] M. Vieira, P. Louro, M. A. Vieira, M. Fernandes, J. Costa, A. Fantoni, M. Barata "Optical processing devices based on amorphous SiC multilayer architectures" Phys. Status Solidi C 7, No. 3–4, 1184– 187 (2010)/ http://dx.doi.org/10.1002/pssc.200982700.

[18] M. Vieira, M. Fernandes, A. Fantoni, M A Vieira, P. Louro, M. Barata, "Wavelength-division multiplexing/demultiplexing devices using a-SiC:H multilayer heterostuctures" Symposium K, S. Francisco, USA., 24 -29 March, 2008 in Materials and Devices for Laser Remote Sensing and Optical Communication, edited by F. Amzajerdian, A. Aksnes, N. Peyghambarian (Mater. Res. Soc. Symp. Proc. Volume 1076, Warrendale, PA, 2008), pp. 187-192, K09-02. DOI:10.1557/PROC-1076-K09-02).

[19] M. A. Vieira, M. Vieira, P. Louro, M. Fernandes, J. Costa and A. S. Garção (2011). "Self optical gain in multilayered silicon-carbon heterostructures: A capacitive active band-pass filter model." MRS Proceedings, 1321, mrss11-1321-a20-02 doi:10.1557/opl.2011.819

[20] Edward S. Yang, "Microlectronic devices", Cap. 5, Department of Electrical Engineering, Colombia University, Mc Graw-Hill, Inc. 1988.

[21] M. A. Vieira, M. Vieira, P. Lour0, M. Fernandes, A. S. Garção "Tunable capacitive active filters based on SiC multilayer structures" MPA Meeting Conference, Alvor, Algarve, Portugal, 27-29 Junho 2011 accepted for publication in Jornal of Nanosci. Nanotechnol (2012).

[22] M. A. Vieira, M. Vieira, J. Costa, P. Louro, M. Fernandes, A. Fantoni, "Double pin Photodiodes with two Optical Gate Connections for Light Triggering: A capacitive two-phototransistor model" in Sensors & Transducers Journal Vol. 10, Special Issue, February 2011, pp.96-120. ISSN 1726-5479.

[23] M. Vieira, M. Fernandes, P. Louro, A. Fantoni, M. Barata, M A Vieira, "Multilayered a-SiC:H device for Wavelength-Division (de)Multiplexing applications in the visible spectrum" Symposium A: S. Francisco, USA, 24 -29 March, 2008, in Amorphous and Polycrystalline Thin-Film Silicon Science and Technology, edited by A. Flewitt, J. Hou, S. Miyazaki, A. Nathan, and J. Yang (Mater. Res. Soc. Symp. Proc. Volume 1066, Warrendale, PA, 2008), pp.225-230 A08-01. DOI:10.1557/PROC-1066-A08-01.

[24] M. Vieira, A. Fantoni, M. Fernandes, P. Louro, G. Lavareda, C. N. Carvalho “pinpín and pinpii’n multilayer devices with voltage controlled optical readout” Journal of Nanoscience and Nanotechnology, Vol 9, Volume 9, Number 7, July 2009 , pp. 4022-4027(6). http://dx.doi.org/10.1166/jnn.2009.M05.

[25] P. Louro, M. Vieira , M. Fernandes, M. Barata, A. Fantoni, J. Costa,, J Caeiro M. A. Vieira “Optical demultiplexer based a-SiC:H voltage controlled device” ” Phys. Status Solidi C 7, No. 3–4, 1188– 1891 (2010) http://dx.doi.org/10.1002/pssc.200982702.

[26] M. A. Vieira, M. Vieira, M. Fernandes, A. Fantoni, P. Louro, M. Barata, “Voltage Controlled Amorphous Si/SiC Phototransistors and Photodiodes as Wavelength Selective Devices: Theoretical and Electrical Approaches”Amorphous and Polycrystalline Thin-Film Silicon Science and Technology — 2009, MRS Proceedings Volume 1153, A08-03.

[27] M. A. Vieira, M. Vieira, J. Costa, P. Louro, M. Fernandes, A. Fantoni, ”Double pin Photodiodes with two Optical Gate Connections for Light Triggering: A capacitive two-phototransistor model” in Sensors & Transducers Journal Vol. 9, Special Issue, December 2010, pp.96-120.

[28] Jordan, A. J., “Linearization of non linear state equations”, Bulletin of the Polish Academy of Sciences, Vol. 54, No. 1, 2006.

[29] Wilson J. Rugh, “Linear System Theory” (2nd Edition) Prentice-Hall Information and Systems Science Series, Serie E (1995).

[30] Dormand, J. R. and P. J. Prince, "A family of embedded Runge-Kutta formulae," J. Comp. Appl. Math., Vol. 6, 1980, pp 19-26.

[31] [M. J. Berger and P. Colella, Local adaptive mesh refinement for shock hydrodynamics, J. Comput. Phys.82 (1989), 64-84

[32] M. Vieira, J. Costa, M. A Vieira, A. Fantoni, M. Fernandes, P. Louro “Detection of change in fluorescence between reactive cyan and the yellow fluorophores using a-SiC:H multilayer transducers” J. Nanosci. Nanotechnol. 11, 1–6, 2011. http://dx.doi.org/10.1166/jnn.2011.3476.

[33] Jovin, T.M. and Arndt-Jovin, D.J. FRET microscopy: Digital imaging of fluorescence resonance energy transfer. Application in cell biology. In Cell Structure and Function by Microspectrofluometry, E. Kohen, J. G. Hirschberg and J. S. Ploem. London: Academic Press, 1989. pp. 99-117.

[34] P. Louro, M. Vieira, M A Vieira, M. Fernandes, A. Fantoni, C. Francisco, M. Barata “Optical multiplexer for short range application” Physica E, Low-dimentional Systems and Nanostructures, Vol. 41, Pages 1082-1085 (2009) http://dx.doi.org/10.1016/j.physe.2008.08.029

Chapter V

Opto-electronic conversion applications

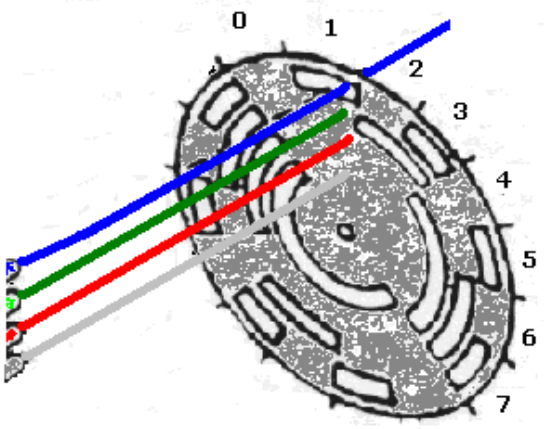

Encoder with generation of the binary code.

V Opto-electronic conversion applications

1 Using Switches

The transducers based on a- SiC:H multilayer architectures combine the simultaneous demultiplexing operation with the photodetection and self amplification. They are optimized in chapters II, III and IV for provide the high-sensitivity needed for MUX/DEMUX and FRET applications.

The purpose of this chapter is to present a new reconfigurable logic architecture that offers considerable improvements in sensing, measurement, manufacturing and opto-electronic conversion applications.

General principles of operation of optical switches are referred in Figure 5.1: a) Light emitting and sensor element (switch ON); b) interruption of the light beam (switch OFF) and c) reflection light beam with switch ON.

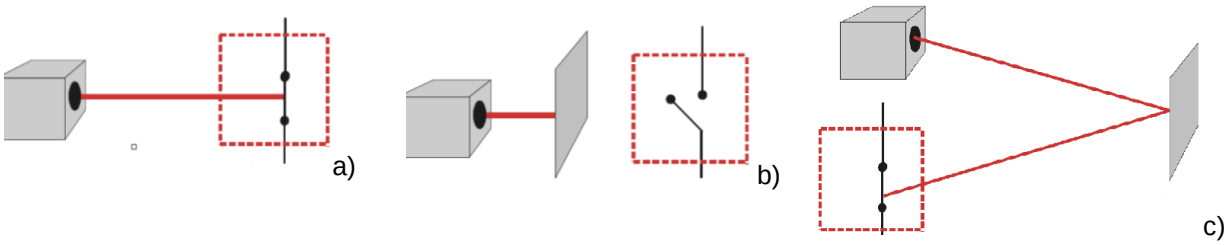

Figure 5. 1 *a)Light emitting and sensor element (switch ON) b) Interruption of the light beam (switch OFF) c) Reflection light beam (switch ON) .*

Commercial devices correspond to the more complex switches. We must use Boolean variables instead of mechanical motion to select a given input and introduce a variable to describe the position of the switch. Switches are referred to as being enabled or disabled. An enable (or strobe) switch, will act as a Boolean AND function.

Logic theory shows that all digital operations may be reduced to elementary logic functions [1]. The construction of most digital systems is a large task. Disciplined designers in any field will subdivide the original task into manageable subunits – building blocks – and will use the standard subunits wherever possible. In digital hardware, the building blocks have such names as adders, registers, and multiplexers. Logic theory shows that all digital operations may be reduced to elementary logic functions. We could regard a digital system as a huge collection of AND, OR, and NOT circuits, but the result would be unintelligible. We need to move up one level of abstraction from gates and consider some of the common operations that digital designers wish to perform.

We can perform all these operations with suitable arrangements of AND, OR, and NOT gates. Such an approach would be comparable to programming every software problem in binary machine language. Instead, we need to develop building blocks to perform standard digital system operations. The building blocks will allow us to suppress much irrelevant detail and design at a higher level. The procedure is analogous to giving the architect components such as doors, walls, and stairs instead of insisting that he designs only with boards, nails, and screws.
The purpose of this chapter is to present a new optical logic architecture that offers considerable improvements in reconfigurability [2].

2 SiC multilayer photonic structures with self optical bias amplification

Stacked layered pin a-SiC/a-Si devices based on a filter design are approached from a reconfigurable point of view. This section shows that a double SiC/Si pin photodiode can be de-composed into two photonic active filters changeable in function. Reconfiguration is provided by optical control signals to the optoelectronic front and back pin building blocks. Depending on the wavelength and irradiation side of the external optical bias the device acts either as a short- and a long- pass band filter or as a band-stop filter, amplifying or rejecting a specific wavelength range. Particular attention is given to the amplification coefficient weights, which allow taking into account the wavelength background effects. We illustrate these effects in detail and discuss the filters transfer function characteristics. We present examples of filters and we propose a reconfigurable device for directed optical logic. An algorithm to decode the information is presented. An optoelectronic model supports the optoelectronic logic architecture.

2.1 Introduction

Multilayered structures based on amorphous silicon technology are expected to become reconfigurable to perform WDM optoelectronic logic functions and provide photonic functions such as signal amplification and switching [2, 3]. They will be a solution in WDM technique for information transmission and decoding in the visible range [4]. The basic operating principle is the exploitation of the physical properties of a nonlinear element to perform a logic function, with the potential to be rapidly biasing tuned. Amplification and amplitude change are two key functionality properties outcome of a balanced interaction between frequency and wavelength of the optical signal and background

wavelength and placement within a WDM link. Any change in any of these factors will result in filter readjustments. Here, signal variations with and without front and back backgrounds move electric field action up and down in a known time frame. A numerical simulation support new optoelectronic logic architecture.

2.2 Device configuration and operation

The active device consists of a p-i'(a-SiC:H)-n/p-i(a-Si:H)-n heterostructure with low conductivity doped layers (Figure 5.2 and Figure 2.1). The thicknesses and optical gap of the front í'- (200 nm; 2.1 eV) and back i- (1000 nm; 1.8 eV) layers are optimized for light absorption in the blue and red ranges, respectively. Although the long wavelength photons are incident onto the front photodiode, they are not absorbed by a-SiC:H since the photon energy is less than the bandgap energy of a-SiC:H (E_g=2.1 eV). Photons pass through the a-SiC:H and become absorbed in the back photodiode (E_g=1.8 eV). On the other side, the short wavelength photons are only absorbed in the front structure due to the narrow dimensions (200 nm) of this photodiode. This selective spectral absorption of the light is responsible for the wavelength filtering properties of the device [5, 6].

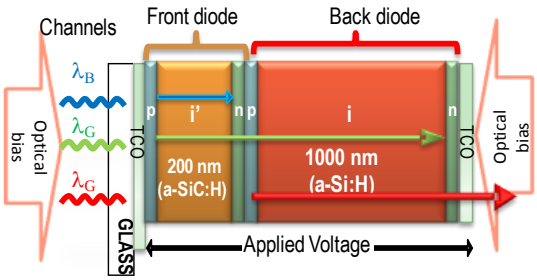

Figure 5. 2 *Device design and operation.*

Several monochromatic pulsed lights, separately ($\lambda_{R,G,B}$ input channels) or in a polychromatic mixture (multiplexed signal), at different bit rates illuminated the device from the glass side. Steady state optical bias with different wavelength are superimposed (400nm-800 nm) from the front or from the back sides and the generated photocurrent measured at -8 V.

The device operates within the visible range using as input color channels (data) the wave square modulated light (external regulation of frequency and intensity) supplied by a red (R: 626 nm; 51 μW/cm^2), a green (G: 524 nm; 73 μW/cm^2) and a blue (B: 470 nm; 115 μW/cm^2) LED. Additionally, steady state red, green, blue and violet (background) was superimposed by LEDS driven at a constant current value (R: 625 μW/cm^2, G: 515 μW/cm^2, B: 680 μW/cm^2, V: 2800 μW/cm^2).

2.3 Transfer function characteristics

The transfer function magnitude (or gain) allows determining the ability of the optical filter to distinguish between signals at different wavelengths. The spectral sensitivity was tested through spectral response measurements under different frequencies, with and without steady state optical bias applied either from the front or back side (Figure 5.3).

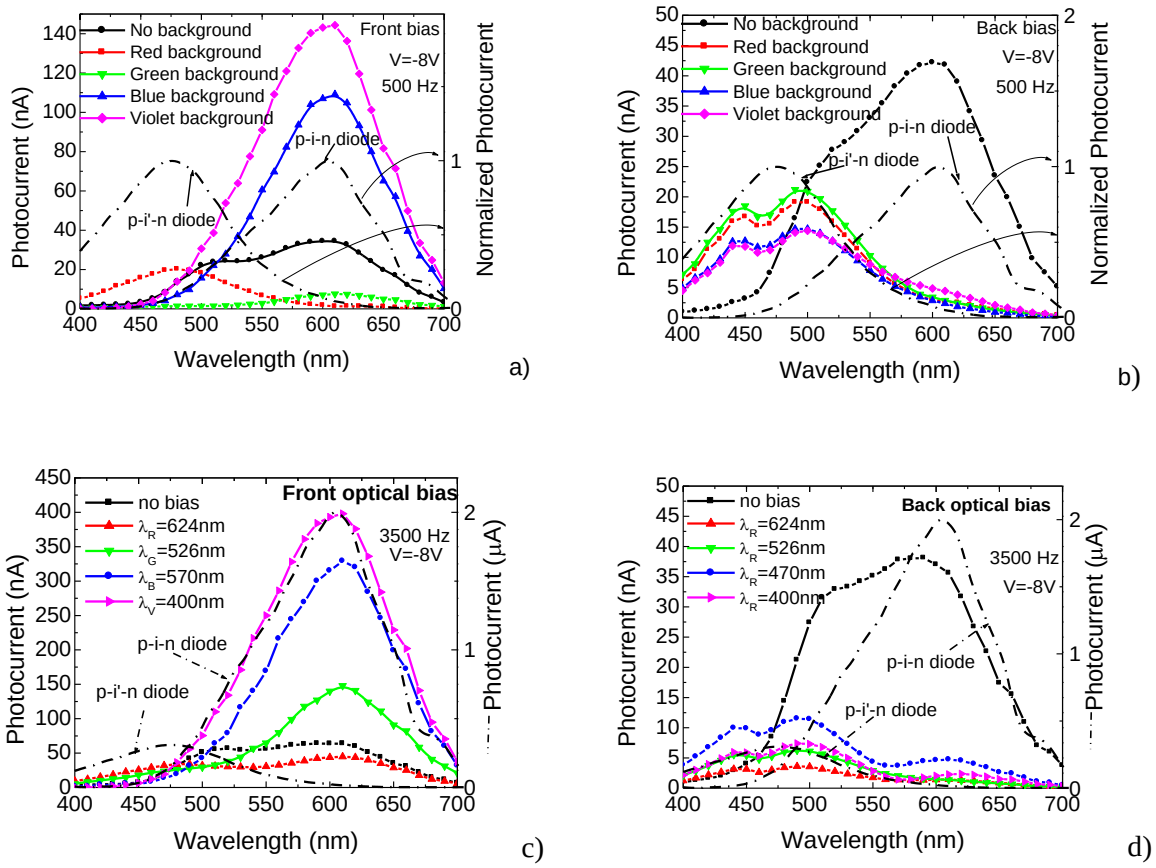

Figure 5. 3 *Photocurrent without and with front (a, c) and back (b, d) backgrounds.The current of the individual photodiodes are superimposed (dash lines).*

In Figure 5.3, at 500 Hz and 3500 Hz, the spectral photocurrent (symbols) is displayed under red, green, blue and violet background and without it. In Figure 5.3a (c) the steady state optical bias was applied from the front side and in Figure 5.3b (d) from the back side. For comparison the normalized spectral photocurrent for the front, p-i'-n, and the back, p-i-n, photodiodes (dash lines) are superimposed.

Data shows that the front and back building blocks, separately, presents the typical response of single p-i-n cells with intrinsic layers based on a-SiC:H or a-Si:H materials, respectively. The front diode cuts the wavelengths higher than 550 nm while the back one rejects the ones lower than 500 nm. The overall device presents an enlarged sensitivity when compared with the individual ones. Results show

that under front irradiation the sensitivity is much higher than under back irradiation. Under front irradiation (Figure 5. 3a, Figure 5.3c) the violet background amplifies the spectral sensitivity in the visible range while the blue optical bias only enhances the spectral sensitivity in the long wavelength range (>550 nm) and quenches it in the others. Under red bias, the photocurrent is strongly enhanced at short wavelengths and disappears for wavelengths higher than 550 nm. Under green the sensitivity is strongly reduced in all the visible spectra. In Figure 5.3b, and Figure 5.3d whatever the wavelength of the backgrounds, the back irradiation strongly quenches the sensitivity in the long wavelength range (>550nm) and enhances the short wavelength range. So, back irradiation, tunes the front diode while front irradiation, depending on the wavelength used, tunes the back one.

2.4 Optical bias amplification

In Figure 5.4 the spectral gain, defined as the ratio between the spectral photocurrents under red (α^R), green (α^G) blue (α^B) and Violet (α^V) illumination and without it is plotted at 500 Hz and 3500 Hz. The optical bias is applied from the front side, in Figure 5.4a and from the back side, in Figure 5.4b.

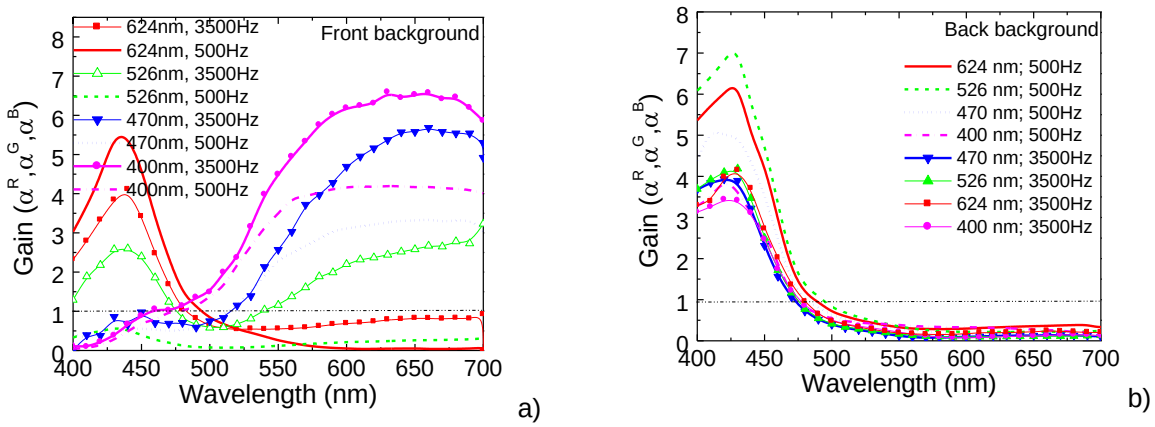

Figure 5. 4 *Spectral gain under red (α^R), green (α^G), and blue (α^B) optical bias, applied from the front (a) and the back (b) sides at different frequencies.*

Under front bias and red irradiation the gain is high at short wavelengths and strongly lowers for wavelengths higher than 550 nm, acting as a short-pass filter. Under green background and high frequencies, the device behaves as a band-stop filter that screens out the medium wavelength range (green) enhancing only the photocurrent for wavelengths outside of that range. Under blue and violet light the devices works as a long-pass filter for wavelengths higher than 550 nm, blocking the shorter wavelengths. Back light, whatever the frequency, leads to a short-pass filter performance. Results

show that by combining the background wavelengths and the irradiation side the short-, medium- and long- spectral region can be sequentially tuned.

In Figure 5.5 the front and back gains as a function of the frequency, at fixed wavelengths: 470 nm (blue channel), 526 nm (green channel) and as 624 nm (red channel) is plotted under 400 nm applied optical bias.

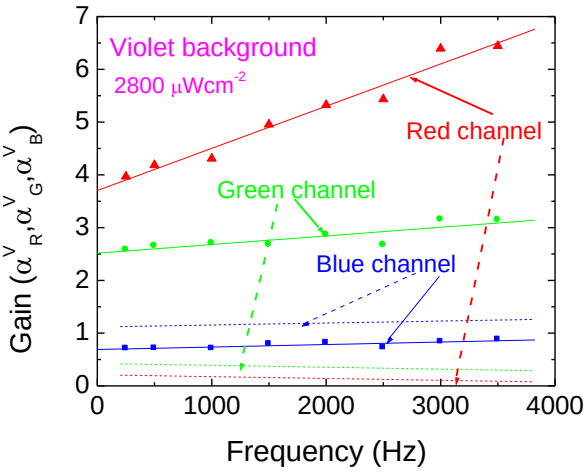

Figure 5. 5 *Input front (solid lines) and back (dot lines) channel gains (α_R, α_G, α_B), as a function of the frequency.*

Results show that, no matter what the irradiation side, the blue and green channel gain does not depend on the frequencies, while the red one increases under front illumination and is strongly reduced under back light.

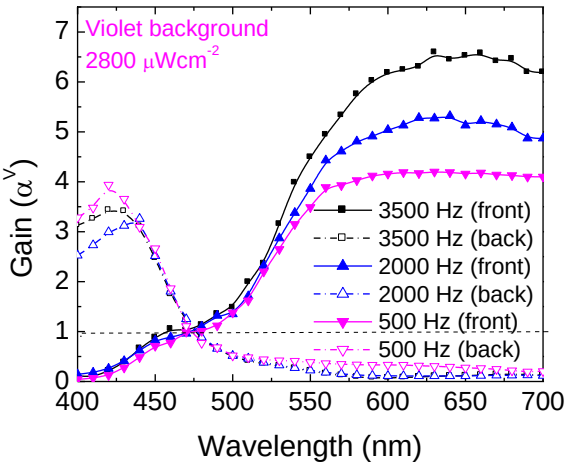

Figure 5. 6 *Spectral gain under violet optical bias (α^V) for different frequencies.*

In Figure 5.6 under front and back violet irradiation, it is displayed the spectral gain for three different frequencies. Results show that, whatever the frequency, the device acts as an active long-pass filter

under front irradiation and a low-pass filter under back irradiation. Under front bias the gain is higher than the unity for wavelengths above 500nm resulting in an amplification of the green and red spectral ranges. Back irradiation only amplifies the short wavelength range and extinguishes the others.

2.5 Encoder and decoder device

To analyze the device under information-modulated wave and uniform irradiation, three monochromatic pulsed lights separately (red, green and blue input channels, Figure 5.7a) or combined (multiplexed signal, Figure 5.7b) illuminated the device at 6000 bps. Steady state violet optical bias was superimposed separately from the front (solid lies, pin_1) and the back (dash lines, pin_2) sides and the photocurrent generated measured at -8 V. The transient signals were normalized to their values without background. In Figure 5.7b the multiplexed signal without and with background are displayed (solid lines). Here the input channels without optical bias (dash lines) are also superimposed. On the top of the figure the signals used to drive the input channels are shown to guide the eyes.

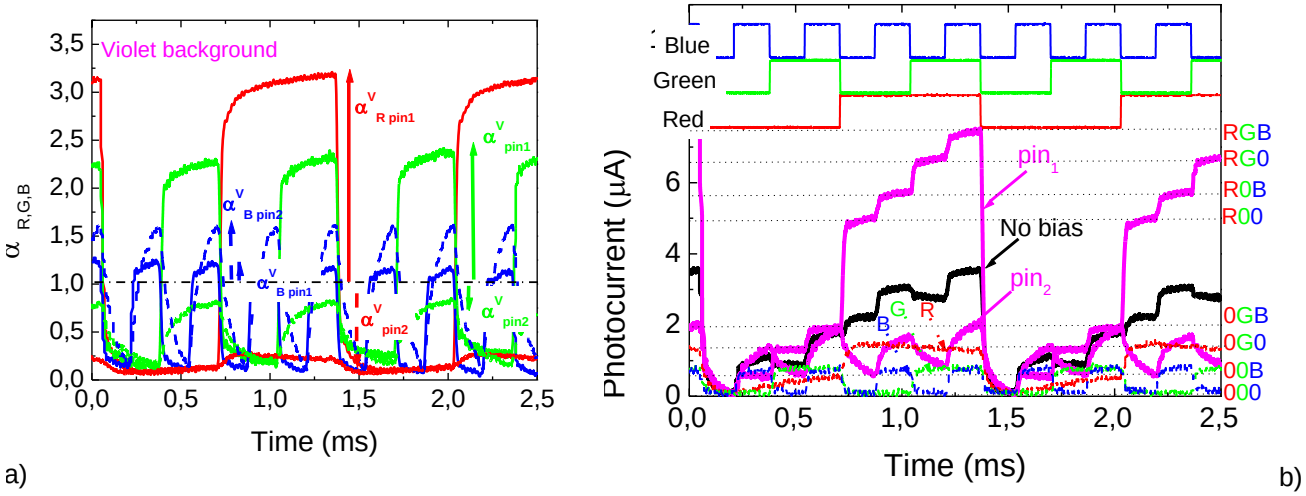

Figure 5. 7 *a) Normalized red, green and blue transient signals at -8V with violet (400 nm) steady state optical bias applied from the front side (α_{pin1}) and from the back side (α_{pin2}). b) Input R,G,B channels and multiplexed output without (no bias) and under front (pin_1) and back (pin_2) irradiation.*

Even under transient conditions, as in Figure 5.4, the front background presents the same nonlinear dependence on the wavelength. It enhances mainly the light-to-dark sensitivity in the medium-long wavelength ranges. Violet radiation is absorbed at the top of the front diode, increasing the electric field at the least absorbing cell [7], the back diode, where the red and part of the green channels generate optical carriers. So, the collection is strongly enhanced (α^V_{Gpin1}=2.2, α^V_{Rpin1}=3.1) while the blue collection stays near its dark value (α^V_{Bpin1}=1.1). Under back irradiation the small absorption depth of the violet photons across the back diode quenches the electric field and so, the red collection almost

disappears (α^{V}_{Rpin2}=0.2). Blue channel is absorbed across the front diode where the electric field is enhanced resulting in an increase collection of the blue channel (α^{V}_{Bpin1}=1.6). Since the green channel is absorbed across front and back diodes its collection is balanced by the increased collection in the front diode and its reduction at the back one (α^{V}_{Gpin2}=0.7).

Taking into account Chapter 3, Figure 3.23, the multiplexed signal without optical bias, presents eight separate levels. Here, the front violet irradiation increases the separation between them by weighting the magnitude of the input channels by different α^{V} factors (Figure 5.7a). So, under front irradiation the encoded multiplexed signal presents eight separate levels (2^3) each one related with an RGB bit sequence (right side of the Figure 5 7b). Those levels can be grouped into two main classes due to the high amplification of the red channel under front irradiation. The upper four levels are ascribed to the presence of the red channel ON and the lower four to its absence allowing the red channel decoder. Since under front irradiation the green channel is amplified, the two highest levels, in both classes, are ascribed to the presence of the green channel and the two lower ones to its lack.

Under back irradiation, the red channel is suppressed, the blue enhanced and the green reduced, so the encoded multiplexed signal presents only four main separate levels (2^2). The two higher levels correspond to the presence of the blue channel ON with or without the green ON respectively, and the other two to its absence. The blue channel is then decoded. The result is depicted in the right axis of Figure 5.7b.

As proof of concept a decoding algorithm was implemented in *Matlab* and tested. In order to make the decoding algorithm less dependent on sensor and LEDs positioning the pin_1 and pin_2 signals were normalized to the maximum intensity of the pin_1 signal.

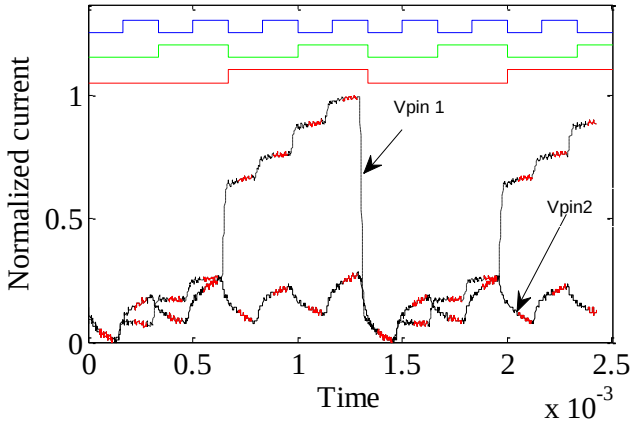

Figure 5. 8 *MUX/DEMUX signals under front and back irradiation. In the top, the RGB decoded information is shown.*

In the second step the intensity levels were determined by sampling and averaging in each time slot to minimize the effect of noise and interference from previous and subsequent time slots. At each time slot a two dimensional vector was defined having as one of the coordinates the sum of the intensity levels of pin_1 and pin_2 and their difference as the other coordinate. The rational for the choice of such

basis set is that one of the coordinates weighs the number of channels that are 'on' and the other weighs the red versus blue content of the measured signal. This approach allows a clear separation of all RGB vectors in the two dimensional space. The channels are then decoded using a simple Euclidean metric with pre-calculated vectors of all RGB combinations. The decoding is completed when the RGB combination of the closest pre-calculated vector is assigned to each time-slot.

In Figure 5.8, for the same bit sequences of Figure 5.7b, the multiplexed signal under front (V_{pin1})and back (V_{pin2}) violet irradiation as well as the RGB decode information are displayed. In all sequences tested the RGB signals were correctly decoded, as exemplified in Figure 5.9. Here, on the top the DEMUX signals obtained using the decoder algorithm are displayed as well as the correspondent binary bit sequences. An excellent fit was obtained in all the tested sequences.

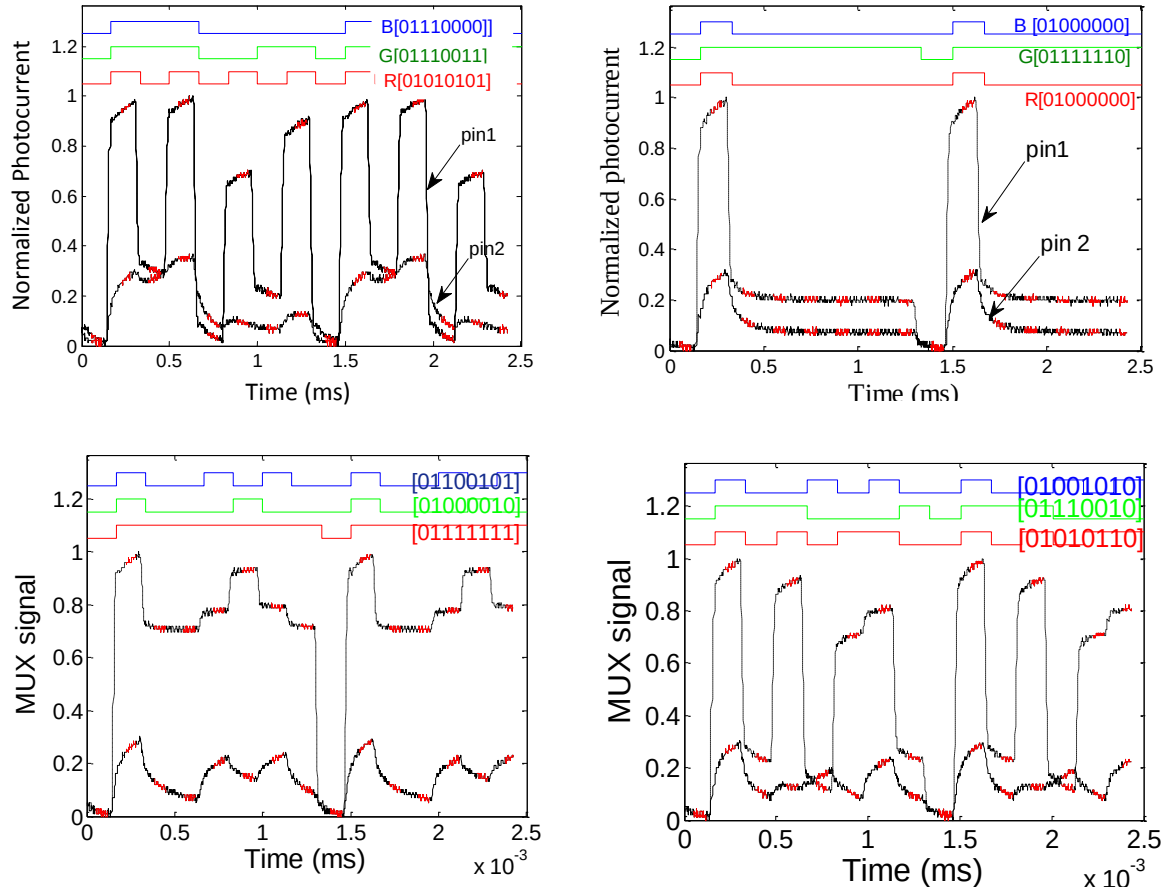

Figure 5. 9 *MUX signal under front and back irradiation. On the top the DEMUX signals obtained using the decoder algorithm is displayed as well as the binary bit sequences.*

Results show that the pinpi´n multilayered structure become reconfigurable under front and back irradiation. They perform WDM optoelectronic logic functions providing photonic functions such as signal amplification, filtering and switching. So, by means of optical control applied to the front or back

diodes, the photonic function is modified from a long- to a short-pass filter, giving a step reconfiguration of the device.

2.6 Optoelectronic model

Based on the experimental results and device configuration an optoelectronic model, made out of a short-pass and a long-pass filter (see Figure 5.5 and Figure 5.6) and supported by the complete dynamical large signal Ebers-Moll model, was developed [1, Chapter IV, §5].

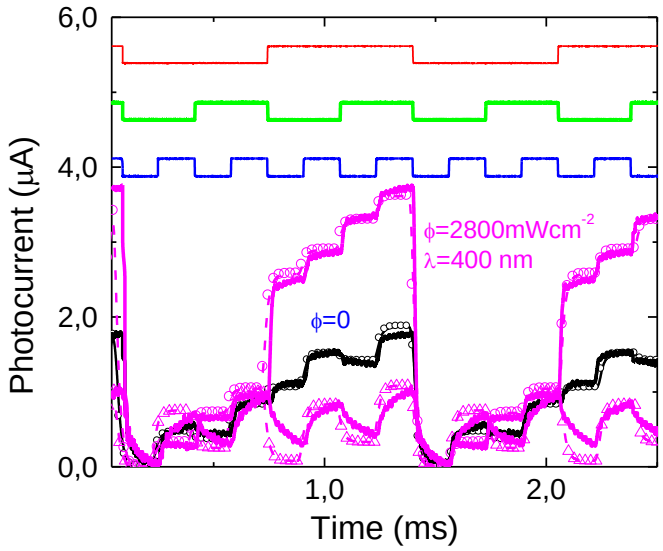

Figure 5. 10 *Simulated (symbols) and experimental (solid lines) multiplex signals under front and back violet background.*

To validate the model under front and back irradiation, in Figure 5.10, the experimental (solid lines) and the simulated (symbols) waveform under negative bias and violet front and back backgrounds is shown. The bit sequences to drive the channels are shown in the top of the figure to guide the eyes. To simulate the violet background, the current sources intensities that model the input channels (individual channels, Figure 5.7b) were multiplied by the on/off ratio between the input channels with and without optical bias ($\alpha^{V}_{R,G,B\ pin1,2}$, Figure 5.7a). A good agreement between experimental and simulated data was achieved.

The device is formed by two reconfigurable building-blocks (the front and the back diodes) interconnected both optical and electrically, each of which has a distinct function. Depending on the side and wavelength of the optical bias control, the magnitude of the *signals* are changed by an α factor, and so the voltages across the front and the back or both photodiodes. Under front irradiation the expected optical amplification in the short wavelength range and quenching in the long ones is observed due to the effect of the active multiple-feedback filter when the back diode is light triggered. The opposite occurs under back irradiation.

2.7 Summary

Combined tunable converters based on SiC multilayer photonics active filters are analyzed [8]. Results show that the light-activated pi'n/pin a-SiC:H devices combine the demultiplexing operation with the simultaneous photodetection and self amplification of an optical signal. The output waveform presents a nonlinear amplitude-dependent response to the wavelengths of the input channels. Depending on the wavelength of the external background it acts either as a short- or a long- pass band filter or as a band-stop filter. A two stage active circuit is presented and gives insight into the physics of the device.

3 Photonic active filters based on SiC multilayer structures

3.1 Introduction

Systems that transmit, receive, and/or process intelligence require some sort of modulation, which is the deliberate distortion of a carrier to impress intelligence (data) upon it that subsequently allows the information recovery. Data transmission can be improved using the wavelength division multiplexing-demultiplexing technique, WDM, [9]. In digital hardware, it corresponds to a building block named multiplexer (MUX). Logic theory shows that all digital operations may be reduced to elementary logic functions [1]. A digital system can be seen as a collection of AND, OR, and NOT circuits.
The purpose of this chapter is to present a new optical logic architecture that offers considerable improvements in reconfigurability [2]. The expression of a logic function can be mapped onto a parallel connection of p-i-n optical filter based on a-Si:H and a-SiC:H double structures.

3.2 Photonic active filters

The device operates within the visible range using as input color channels (data) the wave square modulated light (external regulation of frequency and intensity) supplied by a red (λ_R=624 nm), a green (λ_G=526 nm) and a blue (λ_B=470 nm) LED. Steady state violet (λ_{Vback}=400 nm), red (λ_{Rback}=624 nm), green (λ_{Gback}=524 nm) and blue (λ_{Bback}=470nm) illumination (background) with different intensities was superimposed from the front (pin_1) and back (pin_2) sides and the photocurrent measured at -8V.
In Figure 5.11, at 2000Hz, the spectral photocurrent under different background intensities is displayed under red (a), green (b), blue (c) and violet (d) backgrounds and without it. The steady state optical bias

was applied from the front (pin_1, solid symbols) and back side (pin_2, open symbols) sides. The values were normalized to the maximum value without background.

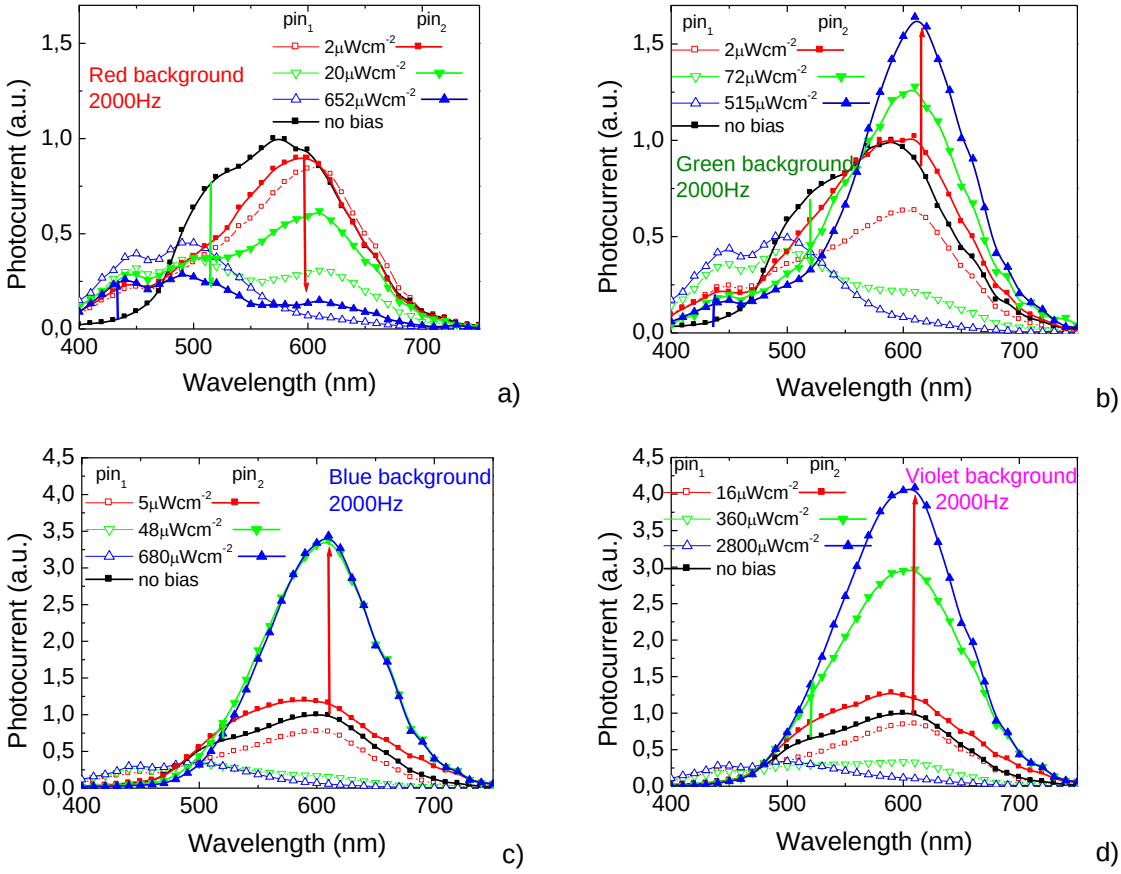

Figure 5. 11 *Spectral photocurrent without and under different background intensities and wavelengths: red (a), green (b), blue (c) and violet (d) backgrounds. The optical bias is applied from the front (solid symbols) and from the back (open symbols) sides.*

Results show that the sensitivity is much higher under front than under back irradiation. Under front violet or blue, when compared with the response without optical bias (see arrows in figures), the sensitivity increases with the decrease of the background wavelength and increases with its intensity. Under red irradiation an opposite behaviour is detected. So, under low wavelength backgrounds (violet or blue) the device acts as a long-pass filter for wavelengths higher than 500 nm and under red irradiation as an active short-pass filter for the same wavelength. Under front green background the device is a band-rejection filter that works to screen out wavelengths that are within the medium range (475nm-550nm), giving easy passage at all wavelengths below and above. The back irradiation, whatever the background wavelength, strongly quenches the sensitivity in the long wavelengths (> 550 nm) and enhances it at the short wavelengths acting as a short-pass filter with a gain that increases with the intensity

In Figure 5.12, the spectral photocurrent, normalized to its value without background is displayed, under front (a) and back (b) violet irradiations, and different intensities. A peak fit adjustment to the data was performed (lines) with peaks centred around 630 nm (solid), 520 nm (dash) and 430 nm (dot). Results show that under violet irradiation, as the background intensity increases, the peak centered at 630 nm (red range) strongly increases while under back light an opposite behavior is observed and the red peak is strongly reduced (see arrows). Under front and back side irradiation, the peak at 520 nm (green range) increases slightly with the intensity. Under back irradiation, a new peak centered at 430 nm appears and increases with the background intensity. So, under front illumination the reddish part of the spectrum is strongly enhanced with the intensity while under back illumination the main enhancement occurs at the blue region.

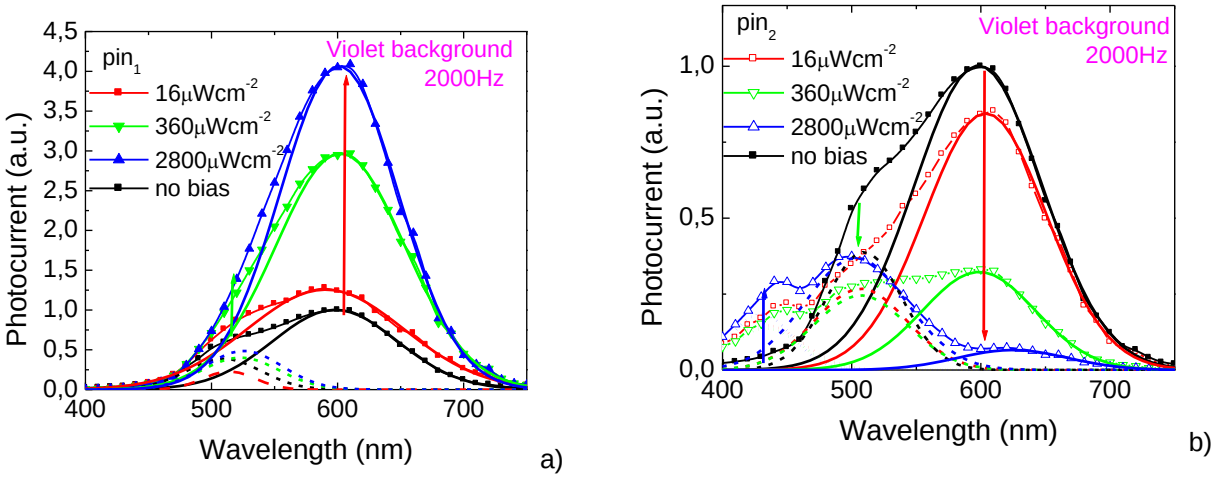

Figure 5. 12 *Normalized spectral photocurrent under front (a) and back (b) violet irradiations with different intensities.*

To analyze the device under information-modulated wave and uniform irradiation, three monochromatic pulsed lights separately (red, green and blue input channels) or their combination (MUX signal) illuminated the device. Steady state red (652μWcm^{-2}), green (515μWcm^{-2}), blue (680μWcm^{-2}) and violet (2800μWcm^{-2}) optical bias was superimposed separately from the front (pin_1) and the back (pin_2) sides and the photocurrent measured at -8 V. In Figure 5.13 the transient results for the input channels are displayed. In Table 5.1 the gains (α), defined as the ratio between photocurrents under irradiation and without it, for the red, green, and blue input channels are presented. Here, the superscripts are related to the background wavelength (R, G, B) and the subscripts ($Rpin_{1,2}$,$Gpin_{1,2}$ $Bpin_{1,2}$) to the channel colour and irradiation side.

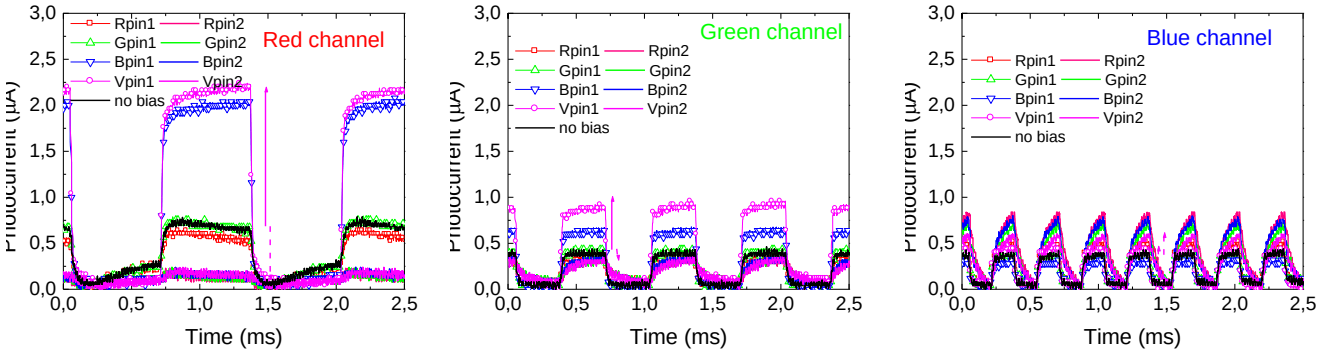

Figure 5. 13 *Input red, green and blue transient signals at -8V without (no bias) and with: red (R), green (G), blue (B) and violet (V) optical bias from the front (pin1) and back (pin2) sides.*

Even under transient conditions the effect of the background wavelength and impinging side leads to the same nonlinear dependence. In the device the morphology of filter results from the interaction of the electric field under applied optical bias (red, green, blue, violet) and the transient electric field induced by the input channels (red, green and blue). This interaction results in electric field lines that guides the photocarrriers generated by the input channels. The flow rate of the carriers through those field lines towards the output depends on the *on/off* state of the channels. Violet and blue radiations, absorbed at the top or across the front diode, increase the electric field at the least absorbing cell [10], the back diode, where the red and part of the green channels generate the carriers. So the red and the green collections are enhanced while the blue one stays near its dark value or slightly decreases.

Table 5.1 *Gains ($\alpha^{R,\ G,B,V}{}_{R,G.B,pin1,2}$) at the input red, green, and blue channels wavelengths.*

Channels	α^R	α^G	α^B	α^V
$\alpha_{R,pin1}$	0,83	1,01	2,84	3,09
$\alpha_{R,pin2}$	0,14	0,19	0,19	0,19
$\alpha_{G,pin1}$	0,92	1,03	1,64	2,21
$\alpha_{G,pin2}$	0,79	0,77	0,82	0,74
$\alpha_{B,pin1}$	1,39	1,00	0,81	1,11
$\alpha_{B,pin2}$	2,22	1,94	1,97	1,64

Under back irradiation the small absorption depth of the violet photons across the back diode quenches the electric field on it and so, the red collection almost disappears and the blue is enhanced. The green channel is absorbed across both front and back diodes and the collection is balanced by its increase in the front and its reduction at the back.

3.3 Opto-electronic conversion

For an optoelectronic digital capture system, opto-electronic conversion is the relationship between the optical input levels and the corresponding digital output levels. Figure 5.13 displays the normalized MUX signals due to the combination of the input channels of Figure 5.11, under front (a) and back (b) violet irradiations. On the top the signals used to drive the input channels are displayed showing the presence of all the possible 2^3 *on/off* states. The truth tables of both encoders, that perform 8-to-1 MUX function, are also shown. In the inputs (x_0….x_7), the index of each bit is related to the first (highest) nonzero logic input. Here, the MUX device selects, through the violet background, one of the eight input logic signals and sends it to the output ($y=x_S$). The output is a three-bit [$S_2S_1S_0$] binary RGB number that may identify one of eight possible inputs. To understand this mapping, in Figure 5.13a and Figure 5.13b, for the input x_7 and output S_2, the first nonzero logic input is 7 ($2^2+2^1+2^0$), which corresponds an output [111]. Those OR gates are expressed, respectively, as: $S_2=x_7+x_6+x_5+x_4$ and $S_2=x_7+x_3+x_5+x_1$.

Any combinational logic function can be written in a sum-of-products format. Each product is an AND function of the input logic signals, where each input signal appears only once in either its inverted or noninverted form. The sum is the result of an OR function of all the products. The sum-of-products expression of a logic function can be mapped onto a two-stage directed-logic circuit.

While the OR function is hard to implement directly, we can take advantage of this relationship between OR and NAND functions:

$$x_A + x_B = \overline{\overline{x_A} \cdot \overline{x_B}} \tag{1}$$

Equation (1) shows that the inversion of the sum is a product that can be calculated in the same way as discussed above. To take advantage of this, we express the inversion of the target function in the sum-of-products form. Then the target function can be obtained by calculating the product of the inverted products. In the next subsections, we will use examples to illustrate this process.

The inverted output functions $\overline{S}_0$, $\overline{S}_1$ and $\overline{S}_2$ expressed in the sum of the products form is:

$$\overline{S}_0 = \overline{x_7}x_6 + \overline{x_7x_6x_5}x_4 + \overline{x_7x_6\,x_5x_4x_3}x_2x_0 \tag{2}$$

$$\overline{S}_1 = \overline{x_7x_6}x_5 + \overline{x_7x_6x_5}x_4 + \overline{x_7x_6\,x_5x_4x_3}x_2x_1 + \overline{x_7x_6\,x_5x_4x_3x_2}x_1x_0 \tag{3}$$

$$\overline{S}_2 = \overline{x_7x_6x_5x_4}x_3 + \overline{x_7x_6x_5x_4x_3}x_2 + \overline{x_7x_6\,x_5x_4x_3x_2}x_1 + \overline{x_7x_6\,x_5x_4x_3x_2x_1}x_0 \tag{4}$$

then, the output can be written as a product of the inverted products:

$$S_0 = \overline{\overline{x_7}x_6} \cdot \overline{\overline{x_7x_6\,x_5}x_4} \cdot \overline{\overline{x_7x_6\,x_5x_4x_3}x_2} \cdot \overline{\overline{x_7x_6\,x_5x_4x_3x_2}x_0} \tag{5}$$

$$S_1 = \overline{\overline{x_7 x_6 x_5}} \cdot \overline{\overline{x_7 x_6 x_5 x_4}} \cdot \overline{\overline{x_7 x_6\ x_5 x_4 x_3 x_2 x_1}} \cdot \overline{\overline{x_7 x_6\ x_5 x_4 x_3 x_2 x_1 x_0}} \quad (6)$$

$$S_2 = \overline{\overline{x_7 x_6 x_5 x_4 x_3}} \cdot \overline{\overline{x_7 x_6 x_5 x_4 x_3 x_2}} \cdot \overline{\overline{x_7 x_6\ x_5 x_4 x_3 x_2 x_1}} \cdot \overline{\overline{x_7 x_6\ x_5 x_4 x_3 x_2 x_1 x_0}} \quad (7)$$

Violet irradiation is applied from the front (pin$_1$; α^V_{Rpin1}>>1, α^V_{Gpin1}>1 and α^V_{Bpin}~1) and back (pin$_2$; α^V_{Rpin2}<<1, α^V_{Gpin2}<1 and α^V_{Bpin2}>1) sides (see Table 5.1). Under front irradiation (Figure 5.14a) the 2^3 levels can be grouped into two main classes due to the high amplification of the red channel. The upper four levels are ascribed to the presence of the red channel ON, and the lower four to its absence, allowing the red channel decoder (4-to-1 multiplexer; long-pass filter function).

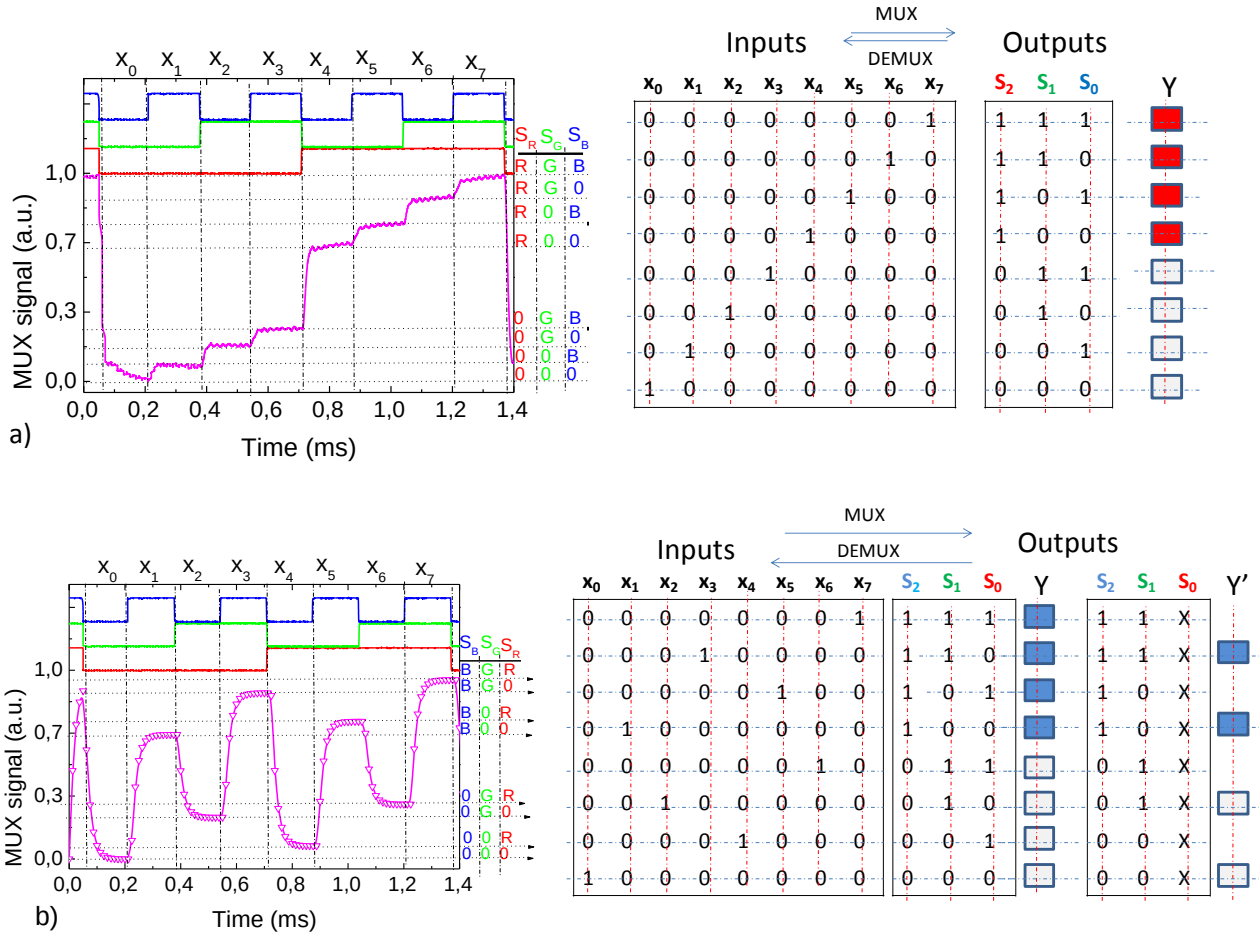

Figure 5. 14 *MUX signal outputs and truth tables of the encoders that perform 8-to-1 multiplexer (MUX) function, under front (a) and back (b) violet irradiations (x means " not significant").*

Since under front irradiation the green channel is amplified the two highest levels, in both classes, are ascribed to the presence of the green channel and the two lower ones to its lack. So, the correspondence between the outputs S_2, S_1, S_0, and the on/off state of the input channels, S_R, S_G, S_B, is clear.

Under back irradiation (Figure 5.14b), the blue channel is enhanced; the green reduced the red almost suppressed. The encoded multiplexed signal is grouped in two main classes, the uppers four where the blue channel is ON and the others where it is OFF (S_B) (4-to-1 multiplexer; short-pass filter function). In each class the four sublevels are grouped in two main levels, with and without the channel green ON (S_G). Each of those levels splits into two near sublevels, attributed to the presence or absence of the red channel (S_R). If we consider this output bit "not significant" only four separate levels (2^2) are considered and the logic MUX function is converted into a logic filter function. The blue channel is then decoded.

Like regular binary numbers, the binary RGB code is an arithmetic code and so, it is weighted, *i. e.* there is specific weights assigned to each bit position. Under front violet irradiation, the most significant digit, *the left most bit*, in the RGB code is the *red* (α^V_{Rpin1}>>1). Going from the left to right, the next is the *green* (α^V_{Gpin1}>1) and the last is the *blue* (α^V_{Bpin1}~1). Under back violet irradiation, the left most bit is the *blue.* Going from the left to right, the next is the *green* and last the *red*. So, the correspondence between the outputs S_2, S_1, S_0, in Fig, 10 and the on/off state of the input channels, S_R, S_G, S_B in Figure 5.14 are obvious.

As explain before, the multiplexer is a device for selecting one of several possible input signals and presenting that signal to an output terminal. It is analogous to a mechanical switch, such as the selector switch presented in Figure 5.15. It is a two-position switch with inputs "Front violet" (a) and "Back violet" (b) and output Y.

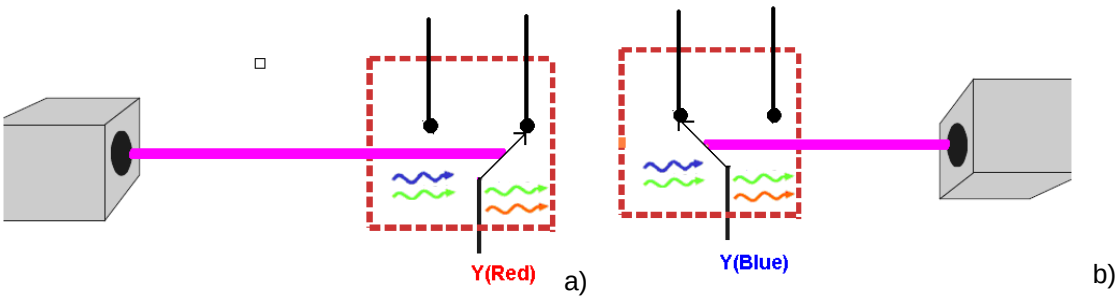

Figure 5. 15 *A two-position opto-mechanical switch: a) Front violet background (Red ON, Blue OFF) b) Back violet background (Blue ON, red OFF).*

3.4 Summary

WDM converters based on amorphous SiC multilayer filters were analyzed [11]. Results show that the background wavelength and irradiation side control the output signal. Depending on the wavelength of the external background and irradiation side, it acts either as a short- or a long- pass band filter or as a band-stop filter. MUX signals that perform 8-to-1 MUX function and truth tables lookup are compared. A decoding algorithm was implemented and tested.

4 Light filtering effects

4.1 Numerical simulation

In the pi'n/pin device the morphology of filter system results from the interaction of the electric field under applied optical bias (red, green, blue, violet) and the transient electric field induced by the input channels. This interaction results in electric field lines that guides the photocarrriers generated by the input channels. The flow rate of the optical carriers through those field lines towards the output depends on the on/off state of the colour channels, acting as a Boolean AND function (enable switch analogy).

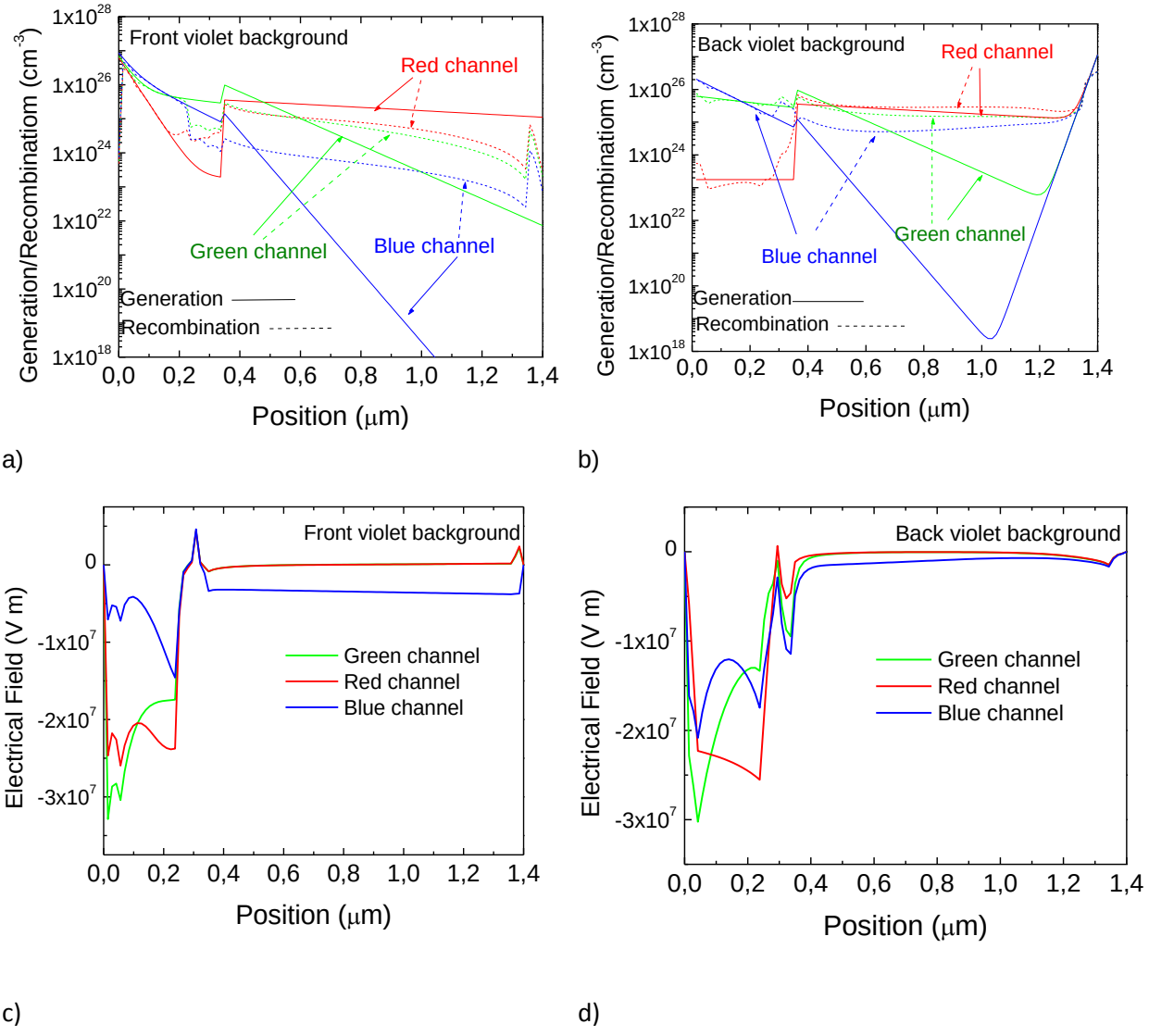

Figure 5. 16 *ASCA simulated recombination and generation profiles under front (a) and back (b)violet irradiation.Simulated electrical field profiles under front (c) and back (d)violet irradiation.*

In order to understand the light filtering properties of the device, under different wavelength and side optical bias conditions we used a device simulation program ASCA-2D (see Chappter III) to analyze the generation rate profiles in the device under violet front and back backgrounds. The generation rate is calculated following a Urbach-Tauc-Lorentz model [12] for the absorption coefficient.
In Figure 5.16 the simulated recombination and generation profiles under front and back violet irradiation as well as the electrical field profiles under the same conditions are shown confirming that the light penetration depth across the device controls the optical gain of the input channels.
The depth of light penetration within the device depends on the wavelength. If the light in the background is a short wavelength radiation, the photogeneration profile is strongly influenced by the choice of the device side for light incidence. Under back irradiation the generation in the back photodiode and so the electrical field increase for short/medium wavelengths due to the light penetration depth of the violet light across the bottom of the a-Si:H intrinsic layer.

4.2 Short-pass, long-pass and reject band filters

Three monochromatic pulsed lights (input channels): red (R_{Ch}), green (G_{Ch}) and blue (B_{Ch}) illuminate the device. Steady state red, green, blue and violet optical bias was superimposed separately from the front and the back sides (see Figure 5.2), and the generated photocurrent measured at -8V. The LEDs used for the background illumination were driven at different currents in order to produce different levels of optical intensity (0.1 mA: 2 mW/cm^2 for all wavelengths except the violet at 16 mW/cm^2; 1 mA: 50 mW/cm^2 for all wavelengths except the violet at 360 mW/cm^2, 10 mA: 500 mW/cm^2 for all wavelengths except the violet at 2800 mW/cm^2).
In Figure 5.17a, the transient signals under front and back violet irradiations are plotted. In Figure 5.17b the signals are displayed under red and blue front backgrounds. As expected, even under transient condition, the device acts as an active bias controlled optical filter. Under front short wavelength irradiation (blue or violet) the magnitude of the red and green channels are amplified and the blue reduced (see solid arrows). Under red optical bias (dash arrows in Figure 5.17b) an opposite behaviour is achieved. The green and red channels are amplified and the blue quenched. Violet back irradiation (dash arrows in Figure 5.17a) cuts the red channel and slightly influences the magnitude of the green and blue ones.

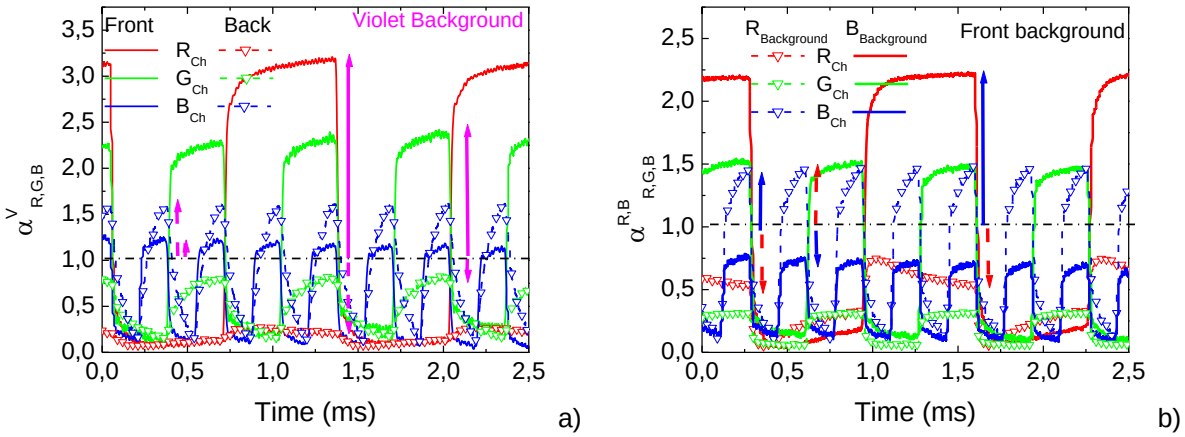

Figure 5. 17 *Red (R_{Ch}), green (G_{Ch}) and blue (B_{Ch}) channel signals under: a) violet background from the front and back sides; b) front red and blue irradiations.*

A polychromatic combination of red, green and blue input channels, in different bit sequences, was used to generate a multiplexed (MUX) signal. In Figure 5.18 the filtered signals under red, green blue and violet light control are displayed. The signals were normalized to the maximum intensity under violet (Figure 5.18a) and red (Figure 5.18b) front irradiations to suppress the dependence on sensor and LEDs positioning. The bit sequences used to transmit the information are shown at the top of the figures.

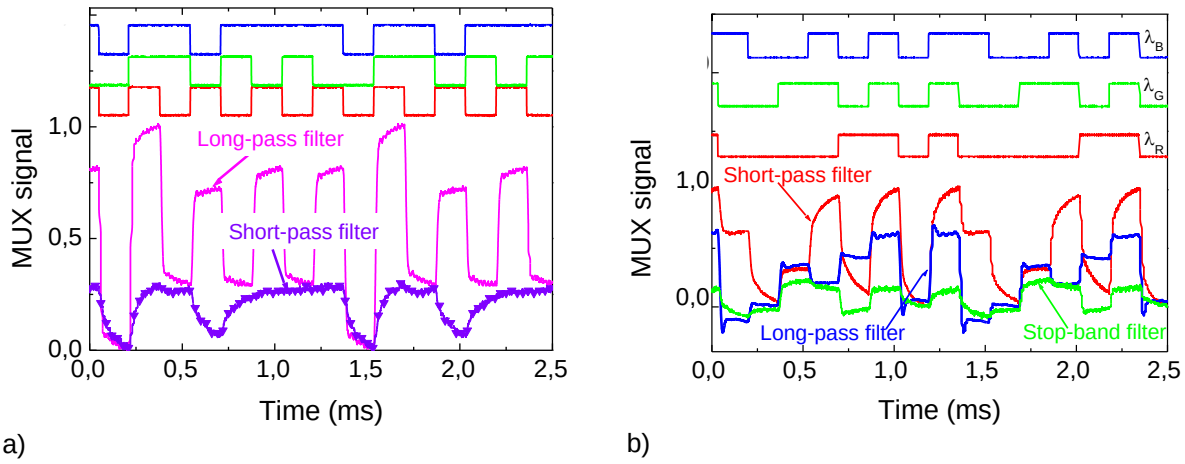

Figure 5. 18 Filtered output signals: a) front (lines) and back (symbols) violet irradiation. b) Front red, green and blue background. On the top, the optical signal used to transmit the information guide the eyes.

Results show that the optical bias enhances the electric field in the less absorbing diode, i.e. the front, under back or front long wavelengths irradiation and, the back, under short wavelength optical bias [6]. Taking into account Figure 5.3 and Figure 5.4, the front violet background (Figure 5.17a, lines) is absorbed at the surface of the front diode, increasing the electric field at the back diode (Figure 5.16),

where the red and part of the green channels generate optical carriers. The collection is strongly enhanced (α^{V}_{R}>>1, α^{V}_{G}>1) while the blue collection stays near its dark value (α^{V}_{B}~1). Under back irradiation (Figure 5.17a, symbols) the small absorption depth of the violet photons across the back diode quenches the electric field there and so, the red collection almost disappears (α^{V}_{R}<<1). Blue channel is absorbed across the front diode where the electric field was enhanced resulting in an increase collection of the blue channel (α^{V}_{B}>1). Since the green channel is absorbed across front and back diodes its collection is balanced by the increase collection in the front diode and its reduction at the back (α^{V}_{G}~1).

Different gains for the RGB channels were obtained. Due to this wavelength non-linearity under front violet background, the encode multiplexed signal presents as many levels as the possible RGB combinations, in a maximum of 2^3 (eight-level encode).Those levels can be grouped into two main classes due to the high amplification of the red channel. The upper levels are ascribed to the presence of the red channel and the lower to its absence allowing the red channel decoder. Since under front irradiation the green channel is amplified, the highest levels, in both classes, are ascribed to the presence of the green channel and the lower ones to its lack. Under back irradiation (short-pass filter), the red channel is suppressed, the blue enhanced and the green reduced, so the encoded multiplexed signal presents a maximum of four separate levels (2^2). The highest levels correspond to the presence of the blue channel ON with or without the green ON respectively, and the other to its absence. The blue channel is then decoded using this simple algorithm.

In Figure 5.18b, under red front background, the red channel response is reduced (α^{R}_{R}<1) and the blue (α^{R}_{B}>1) and green (α^{R}_{G}>1) ones increased. The red channel is rejected (short-pass filter), so the mixture of both blue and green is recovered. The filtered signal is a 4-level encoding (2^2). Under blue irradiation the optical bias effect is opposite, the blue channel is rejected (long-pass filter) due to the quench of the electric field in the p-i´-n front diode. So, the change in the transmitted information is due exclusively to the presence of both red and green channels. The filtered signal becomes a 4-level encoding (2^2). Under green irradiation the devices acts as a stop-band filter that drops the green channel. By subtracting the output signal under irradiation from the signal without it the green channel is decoded. Here, the filtered information is, mainly, a 2^1 level encoded data. It is interesting to notice that when the green channel is alone, whatever the side or background wavelength, the signal magnitude is the same. So, as stated before, under green irradiation, the device behaves as a band-stop filter made of the interception of a long- and a short- pass filter.

4.3 Summary

Tandem a-SiC:H pi'n/pin active filters are analyzed under different back and front optical bias wavelengths [13, 14]. Results show that the devices have a nonlinear amplitude-dependent response

to each incident light wave. Under controlled wavelength backgrounds the light-to-dark sensitivity can be enhanced in a specific wavelength range and quenched in the others, tuning a specific band.

5 Characterization of a monolithic device for detection of FRET signals

As described in Chapters II, III and IV, Fluorescence Resonance Energy Transfer (FRET) is a standard technique used in many medical and biological applications [15, 16]. It involves the detections of transient fluorescent signals coming from the different fluorescent proteins that work in the visible range of the spectrum. Common fluorescent emissions come from the cyan/yellow fluorophores that emit respectively, at 470 nm and 588 nm. Here we use optical filters based on multilayered a-SiC:H heterostructures to detect optical signals at these wavelengths [17]. The transducer consists of two heterostructures based on a-SiC:H/a-Si:H optimized for the detection of the fluorescence emissions at wavelengths 470 nm (cyan) and 588 nm (yellow). Both front and back structures were designed to optimize the detection of these wavelengths.

5.1 Transfer function of each fluorescent optical signal

We as used the same pinpin device (Figure 5.2). To simulate the FRET pairs and the excitation light a chromatic time dependent combination of cyan (470 nm) and yellow (588 nm) wavelengths was applied to the device. In Figure 5.19 the simplified schematic diagram of the structure of the device is displayed as well as the light penetration depths of the violet, blue, green, yellow and red impinging lights.

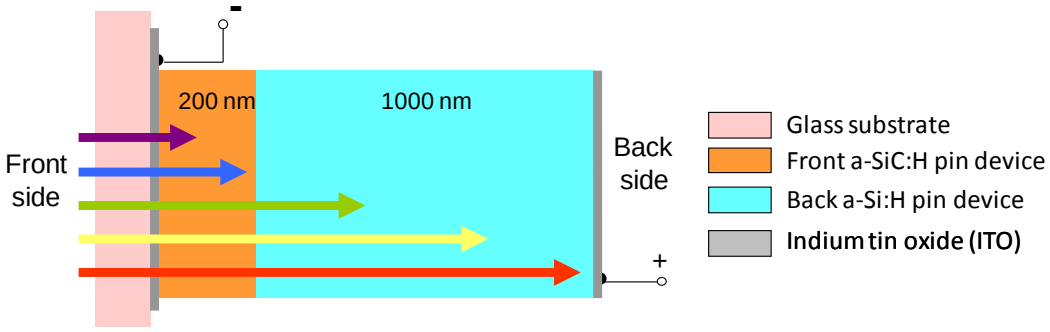

Figure 5. 19 Simplified schematic diagram of the structure of the device.

The photocurrent signal obtained at reverse electric bias (-8 V) with (dark lines) and without background light (violet at 400 nm from the front side and cyan at 470 nm from the back side, violet and cyan colored lines, respectively) is displayed in Figure 5.20 for simulated fluorescent optical signals (cyan and yellow emissions, respectively, at 470 nm and 588 nm).

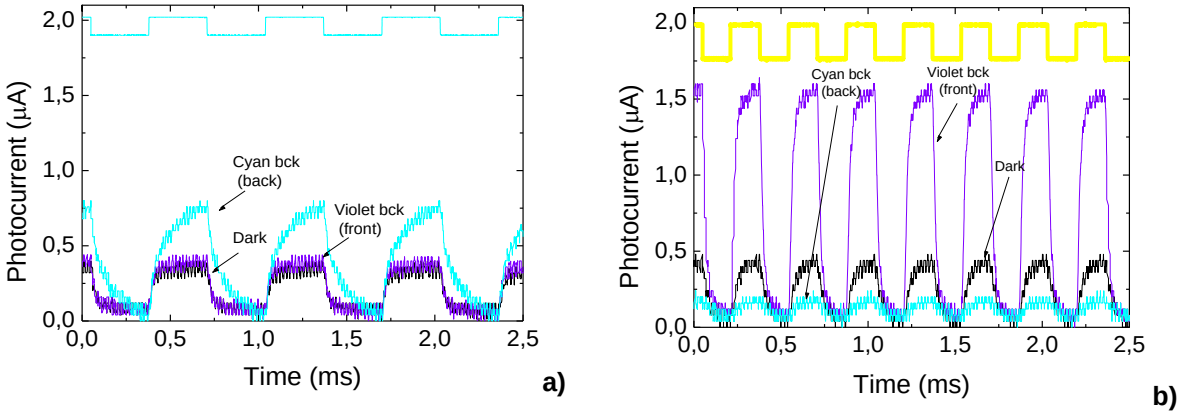

Figure 5. 20 Photocurrent signal obtained at reverse bias without (dark lines) and under different background lights (color lines) with the: a) cyan (470 nm) and b) yellow (588 nm) signals.

As expected, the cyan signal at 470 nm is amplified when background light of the same wavelength is focusing on the device back side. The use of violet light from the front side has a negligible effect on this signal. For the yellow emission at 588 nm the effect of the background light is opposite. The violet steady state light from the front side causes a large amplification of the photocurrent (amplification factor around 4 times) and at the same time the cyan light from the back side cuts the signal by half. These amplification mechanism is useful for the determination of the each fluorescent signal contribution to the whole output signal. With cyan background light from the back side the cyan fluorescent signal will be enhanced and the yellow one reduced. On the other hand violet background from the front side will increase the photocurrent component due to the yellow signal.

5.2 Transfer function of a FRET optical signal

Different chromatic time dependent wavelength combination both fluorescent pulsed input optical signals (at 470 nm and 588 nm) was used to generate a multiplexed signal in the device. The output photocurrents, with (color lines) and without (dark lines) optical background light are displayed in Figure 5.21. The reference level was assumed to be the signal when all the input optical signals channels are OFF. At the top of the figure, the individual optical signals are displayed to guide the eyes in relation to the different ON-OFF states.

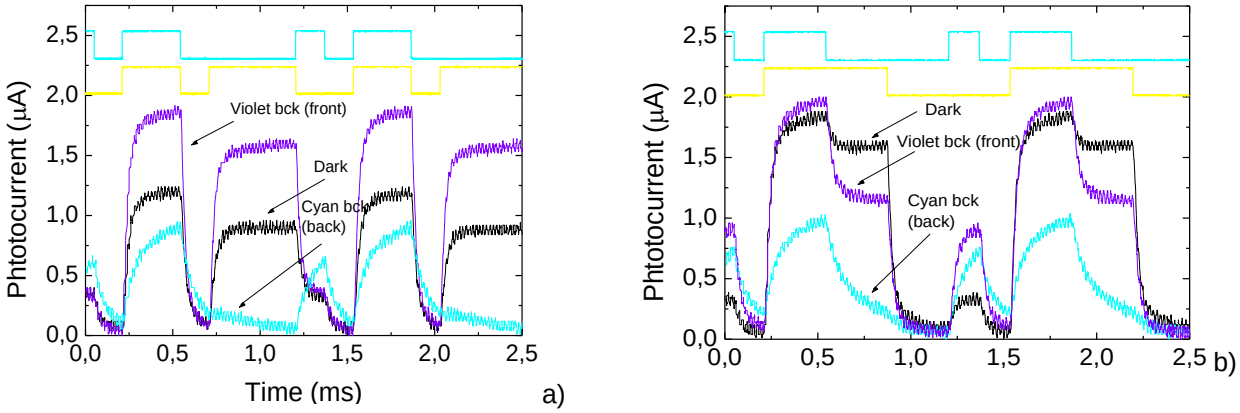

Figure 5. 21 Output photocurrent signals without (ΦL=0) and with optical bias (violet light at 400 nm from the front side, and cyan light at 400 nm from the back side) of two different optical signals waveforms (shown at the top of the figure).

In both chromatic sequences it is clearly observed that the shape of the photocurrent signal measured under dark (black line) exhibits four threshold levels, each assigned to the correspondent optical conditions of the input signals. The ON-ON state corresponds to the maximum intensity of light bias, while the ON-OFF and OFF-ON to a lower intensity and the OFF-OFF to the dark conditions. However, when the device is optically biased the output photocurrent changes enhancing the presence of each input fluorescent optical signal. In both sequences of Figure 5.21 the shape of the photocurrent, measured by soaking the device with violet light by the front side, follows the shape of the yellow fluorescent signal (violet lines). Whenever the yellow optical signal is ON, the measured photocurrent is higher than its correspondent without optical bias. On the other hand, the use of cyan optical bias by the device back side results in an output signal that follows the cyan fluorescent emission, which allows the recognition of the presence of this fluorescent signal. Thus, the proper optical bias of the device through the choice of light wavelength and the device soaking light side results in the correct tune of each fluorescence signal. These features allow immediate decoding of both yellow and cyan emitted signals.

5.3 Recovery of the input fluorescent signals

A similar decoding algorithm was implemented in Matlab and tested. The photocurrent intensity levels were determined by sampling and averaging in each time slot to minimize the effect of noise and interference from previous and subsequent time slots. At each time slot a two dimensional vector was defined having as one of the coordinates the sum of the intensity levels of the photocurrent signals measured under violet and cyan optical backgrounds and their difference as the other coordinate. The rational for the choice of such basis set is that one of the coordinates weighs the number of optical signals that are ‘ON’ and the other weighs the yellow versus cyan content of the measured signal. The

channels are then decoded using a simple Euclidean metric with pre-calculated vectors of all cyan and yellow combinations. The decoding is completed when the yellow-cyan combination of the closest pre-calculated vector is assigned to each time-slot. In all cases tested the transmitted sequence was correctly decoded. In Figure 5.22 we present an example of the output obtained for the different sequences of Fig. 5.21. Both were found to be in exact agreement with the original sequences of optical signals that were used.

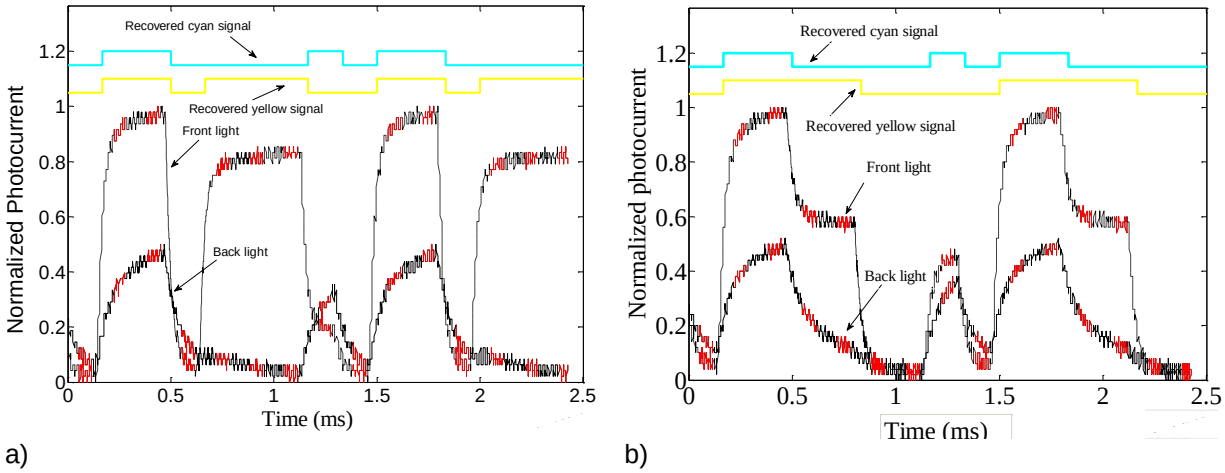

Figure 5. 22 A snapshot of the output from the MatLab routine used to identify the transmitted chromatic sequences of Figure 5.21. The sequence of the input fluorescent signals (shown at the top) was derived from the measured currents.

5.4 Influence of the fluorescent light intensity

In the FRET technique the ratio between the intensities of each fluorescence emission wavelengths can be correlated with the distance between the fluorophores. Thus it is important to identify the contribution of each wavelength to the photocurrent signal, and to determine the relative intensity of each one. In order to simulate different proximity conditions of the fluorophores, and their inherent fluorescence level of emission we used optical signals of different intensities. In Figure 5.23 it is displayed the photocurrent measured for each emission signal using different optical intensities.

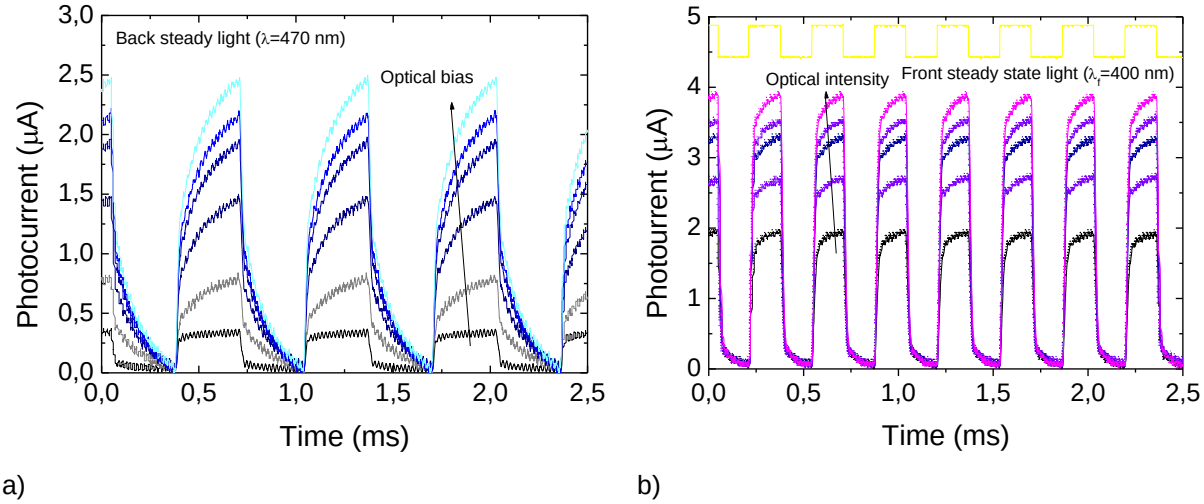

a) b)

Figure 5. 23 Output photocurrent with increasing optical intensities of the emission signals: a) cyan emission under back cyan background; b) yellow emission under front violet background.

For both emission signals the device is sensitive to the optical intensity. The output photocurrent increases with the optical intensity of the optical signal. The sensitivity is stronger for the cyan signal. In Figure 5.24 it is displayed the output photocurrent measured under different optical intensities of the yellow/cyan emission signals.

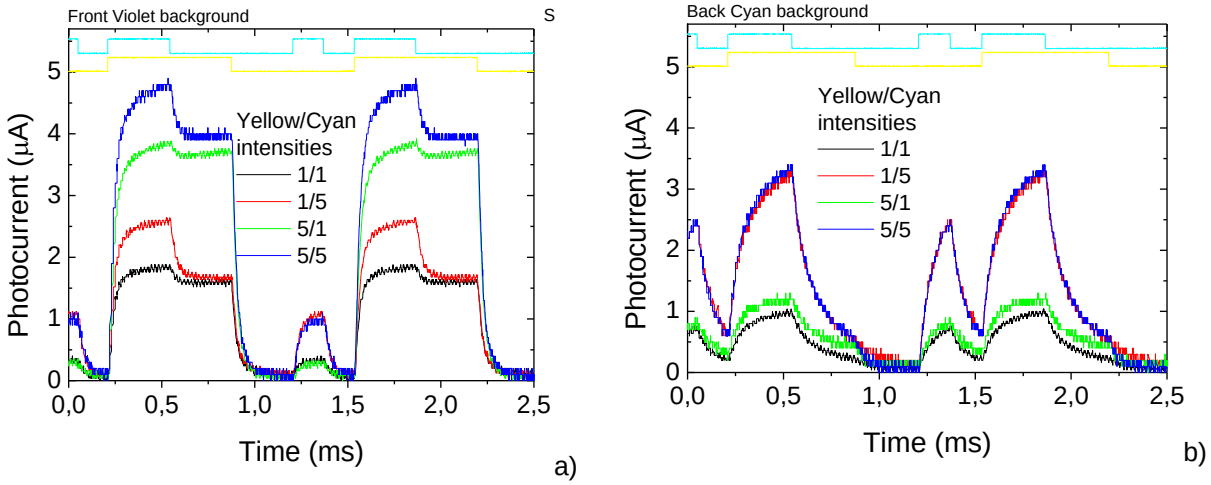

a) b)

Figure 5. 24 Output photocurrent signals with different optical intensities of the yellow/cyan emission signals: a) cyan emission under back optical bias of cyan background; b) yellow emission under front optical bias of violet background.

When the device is violet front biased the yellow emission signal is strongly. Thus in Fig. 5.24a it is observed an increase of the output signal whenever the yellow emission signal is ON with high intensity (green and blue lines). Under back cyan background the cyan signal is enhanced and thus the resulting

photocurrent is at high values when the cyan emission signal is ON with high intensity (Fig. 5.24b, red and blue lines).

5.5 Summary

We have use the double pin device for the detection of optical signals near the cyan and yellow regions of the visible spectrum, which can be used for the detection of the emission signals used in the FRET technique. Two different modulated optical signals were used to simulate the emission signals of the fluorophores. The output emission spectrum was analyzed by reading out the photocurrent generated by the device under reverse bias and using different wavelengths of background light to soak the device from the front and back side. The influence of the fluorescent emission optical signals on the output photocurrent was also analyzed. Future work comprises the use of lower power intensities for the simulated emission signals in order to reach the same range of the ones produced during the FRET phenomenon. In a further stage tests with emission fluorescence signals from different samples must also be done.

6 Conclusions

Tandem a-SiC:H pi'n/pin active filters are analyzed under different back and front optical bias wavelengths. Results show that the devices have a nonlinear amplitude-dependent response to each incident light wave. Under controlled wavelength backgrounds the light-to-dark sensitivity can be enhanced in a specific wavelength range and quenched in the others, tuning a specific band.

WDM converters based on amorphous SiC multilayer filters were analyzed. Results show that the background wavelength and irradiation side control the output signal. Depending on the wavelength of the external background and irradiation side, it acts either as a short- or a long- pass band filter or as a band-stop filter. MUX signals that perform 8-to-1 MUX function and truth tables lookup are compared. A decoding algorithm was implemented and tested.

We have use the double pin device for the detection of optical signals near the cyan and yellow regions of the visible spectrum. The influence of the fluorescent emission optical signals on the output photocurrent was studied.

7 References

[1] R. A. Soref, “Towards Silicon-based Longwave Integrated Optoelectronics (LIO)” invited paper 6898-5, SPIE Proceedings, vol. 6898 (SPIE Photonics West, Silicon Photonics III Conference), San Jose, CA, 21 Jan 2008.

[2] S. Ibrahim, L. W. Luo, S. S. Djordjevic, C. B. Poitras, I. Zhou, N. K. Fontaine, B. Guan, Z. Ding, K. Okamoto, M. Lipson, and S. J. B. Yoo, “Fully reconfigurable silicon photonic lattice filters with four cascaded unit cells”paper OWJ5. Optical Fiber Communications Conference, OSA/OFC/NFOEC, San Diego, 21 Mar 2010.

[3] C. Petit, M. Blaser, “Photodiodes with integrated optical filters for passive optical network applications”Workshop on Optical Components for Broadband Communication , ed. by Pierre-Yves Fonjallaz, Thomas P. Pearsall, Proc. of SPIE Vol. 6350, 63500I, (2006).

[4] S. Randel, A.M.J. Koonen, S.C.J. Lee, F. Breyer, M. Garcia Larrode, J. Yang, A. Ng'Oma, G.J Rijckenberg, and H.P.A. Boom.. “Advanced modulation techniques for polymer optical fiber transmission”, ECOC 07 (Th 4.1.4). (pp. 1-4). Berlin, Germany, 2007.

[5] M. Vieira, P. Louro, M. A. Vieira, M. Fernandes, J. Costa, A. Fantoni, and M. A. Barata, “Optical processing devices based on a-SiC:H multilayer architectures” Phys. Status Solidi C 7, No. 3–4, 1184– 1187 (2010) / DOI: 10.1002/pssc.200982700.

[6] P. Louro, M. A. Vieira, M. Vieira, J. Costa, M. Fernandes, “Optical Processing Devices Based on Multilayered a-SiC:H p-i-n Structures for Short Range Optical Communications” Sensor Dev. Techn. Appl. (SENSORDEVICES), 2010 First Int. Conf., vol., no., pp.146-150, 18-25 July 2010

[7] M. Vieira, A. Fantoni, P. Louro, M. Fernandes, R. Schwarz, G. Lavareda, and C. N. Carvalho, “Self-biasing effect in colour sensitive photodiodes based on double p-i-n a-SiC:H heterojunctions” Vacuum, 82, Issue 12, 8 August 2008, pp: 1512-1516.

[8] M. Vieira, M. A. Vieira, P. Louro. A. Fantoni, V. Silva, M. Barata, “SiC multilayer photonic structures with self optical bias amplification”, to be published in MRS 2012 spring meeting proceedings, symposium A.

[9] Iguchi, Y.; Yamabayashi, N.; “Novel rear-illuminated 1.55 μm-photodiode with high wavelength selectivity designed for bi-directional optical transceiver” Proc. 2th Int. Conf. On InP and Related Mater, 317 (2000), pp:317- 320.

[10] M. A. Vieira, M. Vieira, J. Costa, P. Louro, M. Fernandes, A. Fantoni, Sensors & Transducers Journal Vol. 10, ”Double pin Photodiodes with two Optical Gate Connections for Light Triggering: A capacitive two-phototransistor model” Special Issue, February 2011, pp.96-120. ISSN 1726-5479.

[11] M. A. Vieira, M. Vieira, P. Louro. V. Silva, J. Costa, M. Barata, “Photonic active filters based on SiC multilayer structures”, MRS Proceedings, 1438 , mrss12-1438-m06-03 doi:10.1557/opl.2012.1276

[12] A.S. Ferlauto , G.M. Ferreira , J.M. Pearce, C.R. Wronski, R.W. Collins, X. Deng, G. Ganguly, "Evaluation of Compositional Depth Profiles in Mixed Phase (Amorphous + Crystalline) Silicon Films from Real Time Spectroscopic Ellipsometry" Thin Solid Films 455–456 , 388 (2004)

[13] M. A. Vieira, M. Vieira, P. Louro, V. Silva, A. S. Garção, "Optical filter design using background wavelength processing techniques" to be published in MRS 2012 spring meeting conference proceedings, symposium M.

[14] P. Louro, M. Vieira, M. A. Vieira, V. Silva, A. Fantoni, "Novel device for implementation of WDM in the visible spectrum" MRS Proceedings, Volume1438, 2012 DOI: http://dx.doi.org/10.1557/opl.2012.1474

[15] D.A LaVan, Terry McGuire, Robert Langer, Small Scale Systems for Drug Delivery Nat. Biotechnol. 21 (10), 2003, 1184–1191.

[16] D. Grace, Medical Product Manufacturing News, 12, 2008, 22–23.

[17] P. Louro, M. Vieira, M. A. Vieira, V. Silva, J. Costa, "Characterization of a monolithic device for detection of FRET signals" MRS Proceedings, Volume1426 2012 DOI: http://dx.doi.org/10.1557/opl.2012.1261

Chapter VI

Optical communications strategies evaluation, conclusions and future research directions

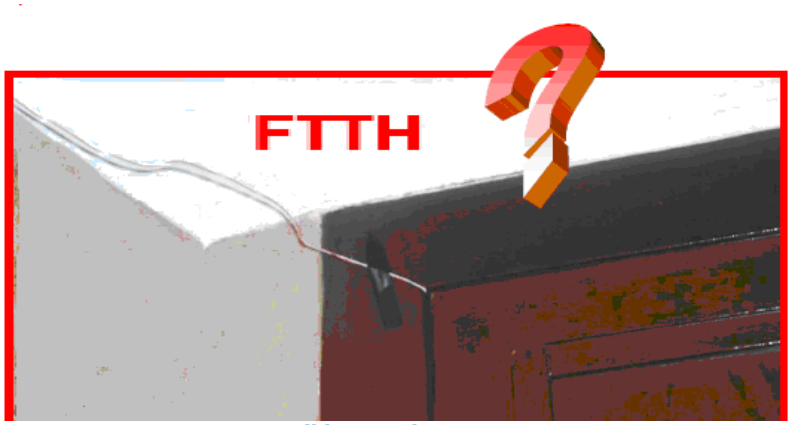

Fibber To The Home

VI Optical communications strategies evaluation, conclusions and future research directions

1 Optical technologies strategies evaluation

This chapter presents a photonic vision building which defines the thesis and guides our arguments and studies. It demands innovative approaches to the exploration of problems and gaps to achieving the vision, involves a new methodology and a new conceptual approach. Detailed remote and afterward states of art are presented.

An extended look at the future of transmission, switching and control is presented and multi-disciplinary resources and associated efforts are focused.

In order to enhance the transmission capacity and the application flexibility of optical communication and sensor systems in visible spectrum, different tasks have to be considered, namely: -The fundamentals of Wavelength Division Multiplexing (WDM) amorphous technology when different optical signals are encoded in the same short range optical transmission path. -The design of reconfigurable logic active filter gates by “bridging the gaps” and combining the optical filters properties.

1.1 Introduction

In this chapter, first, a brief overview is given about future priorities for optical technology support for innovation and knowledge [1, 2].

Technological advancement often brings not just new concepts and products but opportunities to change the foundations of an individual, business, organization, or entire sector. Optical network is no exception.

The fundamental problem of communications is a design problem. The combination of transmitter, transmission medium and receiver is termed the communication link. Because of the limitation placed on the information to be a sequence of bits, this combination is generally referred to as a data link. The trouble launched into the transmission medium by the transmitter is usually referred to as the input data signal. The resulting disturbance at the receiver is termed the output data signal. In the context of our discussion the fundamental problem of communications is to design a data link appropriate for connecting a given source-user pair.

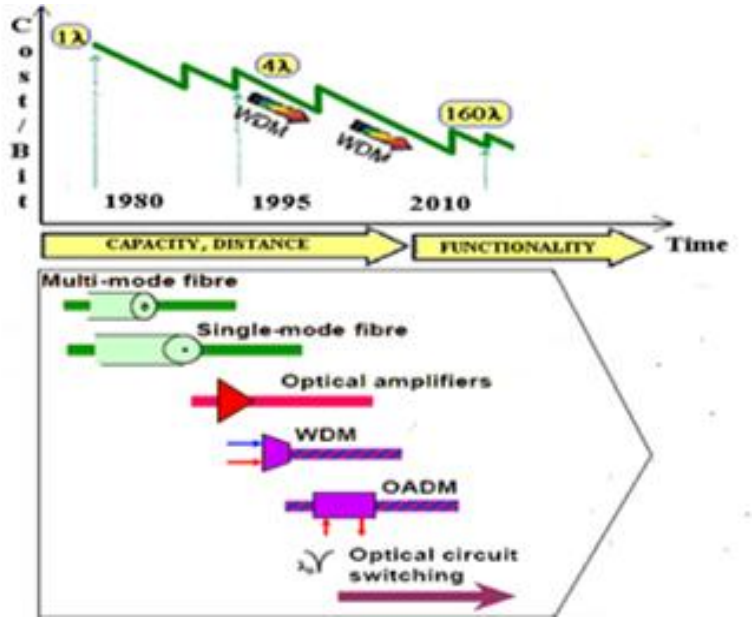

Figure 6. 1 *Multi-disciplinary technologies for infrared telecommunication systems, capacity, distance and functionality versus the cost per bit rate.*

Several innovations are being introduced in these optical network switching nodes, with various degrees of development. Every transmission medium has constraints on its operation, on its performance. It is these constraints that really decide which transmission medium will be employed for the data link design.

Multi-disciplinary technologies for telecommunication systems have evolved from material systems for LEDs and lasers sources, to optical fiber technology and photo detection materials. Newly developed technologies, for infrared telecommunication systems, allowed increase of capacity, distance and functionality as shown in Figure 6.1 [3 , 4].

An extended look at the future of transmission, switching and control as fields of inquiry to focus their multi-disciplinary resources and associated efforts and a scan of communication literature and communication organizations reveals a variety of strategies and strategy development processes.

In this roadmap process, before setting out a plan to where we want to go, we must clearly understand where we are.

1.2 Where are we today?

Techniques such as semaphore lines, ship flags, and smoke signals were the earliest form of technological optical communication. Paul Revere, who successfully defended the New England coast of America from a massive British invasion, used a flare signal from an observation post on Beacon Hill, signaling “one if by land, two if by sea.” One flare meant invasion through land; two flares meant

invasion through Boston harbor. Modern communication theory would describe Revere's warning light as being amplitude modulated by the baseband signal of one pulse meaning by land, and two pulses meaning by sea. Aircraft use the landing lights at airports to land safely, especially at night.

Initial systems introduced from 1980 used multimode fiber at 850 nm wavelength. The initial driver for optical fiber technology was the opportunity to reduce costs: fiber was made from silica, which was a much cheaper material than copper, fiber cable was lighter, easier and therefore cheaper to handle. Besides, buried repeaters could be either eliminated or dramatically reduced in number and system capacities could be increased substantially compared to copper cables. The choice of wavelengths was dictated by:

Ability to manufacture and joint fiber with a small core;

A 'low loss' fiber window located at 850nm;

The ability to produce semiconductor sources and detectors at this wavelength, and to couple the light into the fiber.

Material systems for LED sources at this wavelength were reasonably well understood as they were close to visible wavelengths and LEDs and Fabry-Perot lasers were produced. Si and Ge materials were suitable for photo detection.

By the time the first multimode systems were introduced, scientists had recognized the improved capability offered by single mode operation at longer wavelengths and research interest turned to methods of manufacturing and handling single mode fiber and the material systems that would be needed, first at around 1300 nm, where it was possible to manufacture fiber with zero dispersion, and later around 1550 nm where additional techniques would be needed to overcome the effects of dispersion. High performance operation demanded improved device architectures and new systems techniques. Specialist fibers were designed with 'negative dispersion' properties and methods to compensate for dispersion were developed, enabling a further increase in bit rate and distance to be achieved.

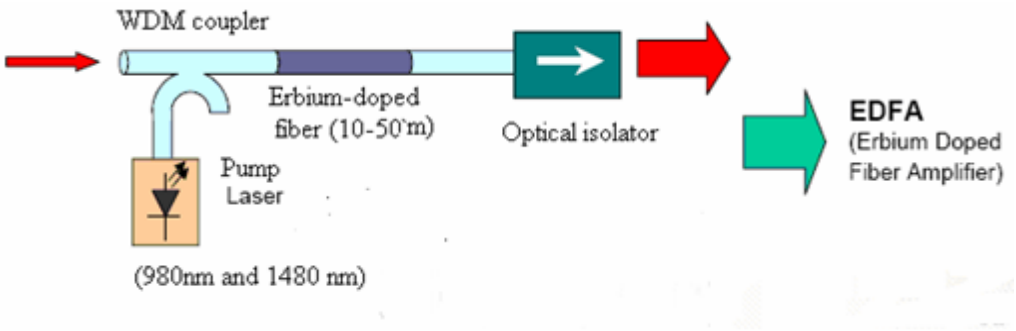

Figure 6. 2 *Erbium-Doped Fiber Amplifier Design*

As capacities increased operators needed more flexible and more manageable transport systems and Synchronous Digital Hierarchy (SDH) systems were introduced from 1990. The plesiochronous systems continued to be used for many years in parallel with SDH but, by now, most administrations have replaced them. Although increased system speeds could be achieved, as speeds increased the available power budget limited the system range. The invention of Erbium-Doped Fiber Amplifiers (EDFAs) gave the solution, allowing the digital signals to be amplified (Figure 6.2).

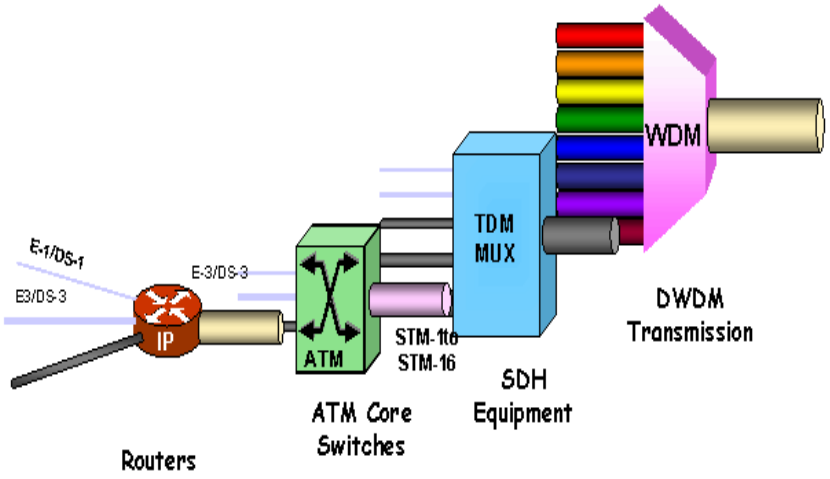

Figure 6. 3 *WDM Transmission System.*

The demand for higher speed systems continued to increase progressively. However technical difficulties associated with higher speed operation slowed down the rate of development. By 1995 the US was faced with the prospect of installing new fiber cables in its long distance networks. Up to this point systems had operated at a single wavelength. The following year saw the first WDM systems introduced into Europe (Figure 6.3).

Early WDM began in the late 1980s using the two widely spaced wavelengths in the 1310 nm and 1550 nm (or 850 nm and 1310 nm) regions, sometimes called wideband WDM (Figure 6.3). The early 1990s saw a second generation of WDM, sometimes called narrowband WDM, in which two to eight channels were used. WDM involves a small number of physical-layer functions.

The emergence of WDM is one of the most important phenomena in the development of fiber optic transmission technology. Transmission of light in optical fiber presents several challenges that must be dealt with. These fall into the following three research categories:

Attenuation— loss of light power, as the signal propagates through the fiber;

Chromatic dispersion—spreading of light pulses as they travel along the fiber ;

Nonlinearities—cumulative effects from the interaction of light with the material through which it travels, resulting in changes in the lightwave and interactions between lightwaves.

Each of these effects has several causes, not all of which affect WDM. The adaptation of EDFAs was critical to the success of WDM systems. Initially designed for single wavelength channel operation, they were soon adapted to multiwavelength working when WDM systems were needed. Modified designs included mid-stage access which allowed performance enhancing components to be inserted such as wavelength flattening filters and dispersion compensating fiber. Up to this point the main driver for improved systems was the demand for higher capacity to meet requirements first for voice networks, and later for private circuits.

Among the years 2000-2006 the volume of generated data grew from 3 billion to 160 billion Gigabytes and 93% of all data was born digitally [5, 6]. This heralded the start of a huge wave of data which is still growing as many traditional services and industries move from analogue to digital platforms (for example, TV broadcasting and movie making) and as e-services spread across public services and industry. In the face of this the traditional telecommunications network must be transformed and optimized for data.

1.3 Out comings from the thesis

The main out comings are recapitulated here in short; for more detailed conclusions the reader is referred to the corresponding chapters.

In this review *Chapter I* single and stack pin heterojunctions based on a-SiC:H alloys are compared under different optical and electrical bias conditions and different readout techniques. Several applications are presented. A theoretical model gives insight on the physics of the device. Results show that when a pinpin device is used as color and image transducer it uses self- field induced depletion layers for light detection and a modulated laser beam for sequential readout. By sampling, at appropriated voltages, it is possible to extract separately the RGB integrated information with good rejection ratio allowing continuous and fast color recognition and image detection. Scans speeds up to 10^4 lines per second can be achieved without degradation in the resolution.

In *Chapter II* results are present on the optimization of multilayered a-SiC:H heterostructures for wavelength-division (de) multiplexing voltage control technique. The single or the multiple modulated wavelength channels are passed through the device, and absorbed accordingly to its wavelength, giving rise to a time dependent wavelength electrical field modulation across it. The effect of single or multiple input signals is converted in an electrical signal to regain the information (wavelength, intensity and frequency) of the incoming carriers. Here, the (de) multiplexing channels are accomplished electronically, not optically. This approach has advantages in terms of cost since several channels share the same optical components; and the electrical components are typically less expensive than optical ones. An electrical model gives insight into the device operation. Results show that by switching between positive and negative voltages the input channels can be recovered or removed. So, this optical device allows to add and drop one or several channels in a WDM optical network (OADMS) and

can be used in optical communications. A physical model supported by an electrical and a numerical simulation gives insight into the device operation. An application as optical transducer for fluorescent proteins detection is presented.

Chapter III reports on the use of a double pi'n/pin a-SiC:H Wavelength Division Multiplex (WDM) heterostructure as an active filter transfer function dependent on the frequency of the trigger light and on the electrical and optical applied bias. The communication technology utilizes the visible light source as a signal transmitter, the air as a transmission medium, and the appropriate pi'n/pin a-SiC:H voltage and optical bias controlled device is presented as a signal receiving component. The manipulation of amplitude is achieved by changing background wavelength. Transfer function characteristics are presented. A numerical simulation gives insight into the filter performance. This smart system has the ability to sense. It is able to predict, decide or help to decide through the integration of cognitive capabilities (transmitted sequence's algorithm to the data inputs prediction). Different emission colors of fluorescent proteins are spectrally distinguished from their simultaneous emissions.

In *Chapter IV* a theoretical analysis, supported by numerical and electrical simulations, gives accurate description of the experimental results and help to understand the physics behind the circuit-switching solutions. Electrical models of the equivalent circuit are present to support the sensing methodologies. When a chromatic time dependent wavelength combination with different transmission rates are shinning on the device it operates as a tunable wavelength filter and can be used in wavelength division multiplexing systems for short range communications. An optoelectronic model combining the properties of active short-pass and long-pass filter sections is developed. The concept of a parallel current bucket connection inflow is established to give insight on the physics of the device. A demux algorithm is implemented. Finally we describe the meaning of the physical parameters required to simulate photonic and electronic properties, and tried to find a connection between some of them in ways that can be considered intuitive for an end user. Further, it was found that the dependencies between the connected parameters work well with respect to applied voltage, and allow for various types optical bias.

2 An optoelectronic product innovation strategy

2.1 Motivation

The past several decades brought continual advances in the underlying technologies of optical communication. Researchers and practitioners continue to develop and deploy advanced technology concepts, products, and services. Despite technological gains, many of the organizations responsible for optical communication have not yet realized the full, strategic value of advanced optical

communication technologies. The potential exists to improve the performance of optical communication systems by fundamentally changing underlying approaches to the development strategy, such as planning, which is currently the predominant approach.

Ensuring the proper awareness towards the motivation of developing the new kind of device based on amorphous silicon-carbon technology and the justification behind producing the results is the main step. It offers insight on what the thesis is about, who would benefit from it and how. Thus, one main goal of these thesis was to instantiate and to demonstrate the possibility to develop a new kind of device based on the amorphous Si/C technology both to the research and academic environment as well as to the industry, aiming at higher penetration and ultimately exploitation of the underlying concepts and technologies.

2.2 Dissemination strategy

The various steps of strategy development were described, from best-practice ways to define innovation goals and objectives through to the selection of strategic areas of focus for new product development sharing similar or complementary goals (see Figure 6.4). Focus is the key to an effective product innovation strategy. Our product innovation strategy specifies where you'll attack, or perhaps more importantly, where you won't attack. Thus, the concept of strategic arenas—the markets, industry sectors, applications, product types, or technologies on which your business will focus its new product efforts—is at the heart of a new product strategy. The potential dissemination target groups of this thesis were identified as being the FCT and EC – ICT communities, the scientific community and the industrial community.

Figure 6. 4 *Dissemination Strategy*

Along this thesis a dissemination strategy has been be used, for acquiring a complete picture of the most important activities undertaken or scheduled on the future route to full dissemination of the knowledge acquired during this research. Although the decision makers and researchers working together do not know the results of the research until it is complete, working through an initial dissemination strategy can help ISEL/UNINOVA I&D research team to focus current projects and to identify key audiences.

The main objective guiding the dissemination activities is the provision of appropriate and reliable information to the scientific community about the development of a new RGB receiver for optical communications. The device combines the simultaneous desmultiplexing operation, photodetection and self amplification. By switching between positive and negative voltages or by applying an appropriate optical bias wavelength the input wavelength channels are identified and can be recovered or removed.

In Figure 6.4 it is shown the dissemination strategy of the research group and the main conference where the results of this thesis have been presented around the world.

2.3 Research

At present, the research on visible light communication was focused on laboratory applications. The communication technology utilized the visible light source as a signal transmitter, the air as a transmission medium, and the appropriate pi'n/pin a-SiC:H voltage and optical bias controlled device is presented as a signal receiving component. In Figure 5.5 a schematic diagram of the transducers essays is displayed.

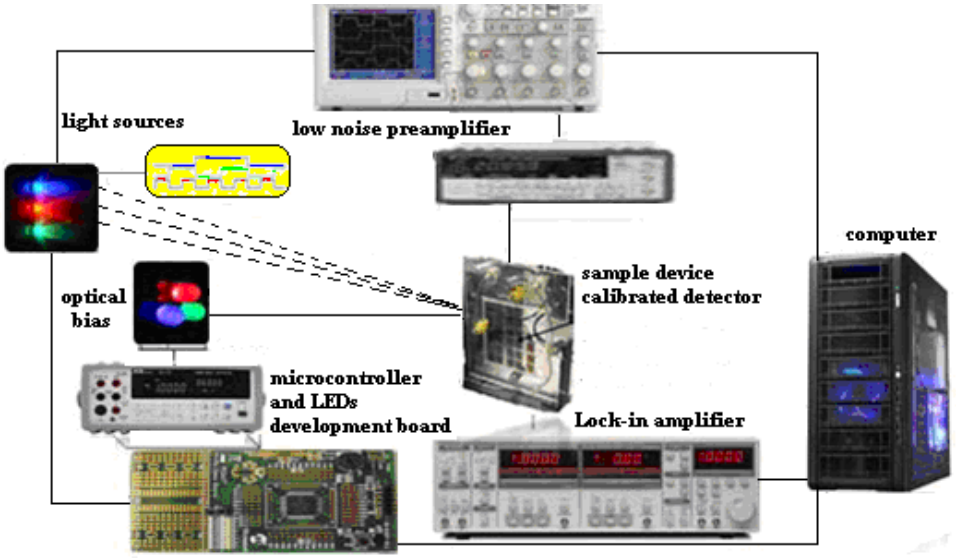

Figure 6. 5 *Schematic diagram of the transducers essays. An indoor, line-of-sight visible light communication link.*

The emergence of WDM is one of the most important phenomena in the development of fiber optical transmission technology. Transmission of light in optical fiber presents several challenges that must be dealt with.

For WDM two key-elements are indispensable, a multiplexer and a demultiplexer. The multiplexer is placed before the POF to integrate every wavelength to a single waveguide. The second element, the demultiplexer, is placed behind the fiber to regain every discrete wavelength. Therefore the polychromatic light must be split in its monochromatic parts to regain the information. These two components are well known for infrared telecom systems, but must be developed completely new, because of the different transmission windows.

In order to enhance the transmission capacity and the application flexibility of optical communication and sensor systems in the visible range, different tasks have to be considered, namely:

The use of Wavelength Division Multiplexing (WDM) devices when different optical signals are encoded in the same optical transmission path.

This will involve a small number of physical-layer functions:

- *Construction of a multiplexing transmitter, generating and combining the signals*—the source, must provide stable light within a specific, narrow bandwidth that carries the digital data, modulated as an analog signal. WDM system employ pi'n/pin a-SiC:H multiplexers to combine the signals. There is some inherent loss associated with multiplexing and demultiplexing. This loss is dependent upon the number of channels but can be mitigated with pi'n/pin a-SiC:H d optical amplifiers, which boost all the wavelengths.

- *Transmitting the signals*—the effects of crosstalk and optical signal degradation or loss must be reckoned with in fiber optic transmission. These effects can be minimized by controlling variables such as channel spacing's, wavelength tolerance, and source power levels. Over a transmission link, using a system test module, the signal may need to be optically amplified.

- *Separating the received signals and receiving the signals* —At the receiving end, implementing a video capture data flow pipeline with a code extraction module the multiplexed signals must be separated out, demultiplexed and received by a pi'n/pin a-SiC:H photodetector.

Several technical solutions for those problems are available, but none of them can be efficiently utilized for any mass production in the POF application scenario described here. All these schemes introduce a significant increase in complexity with respect to the basic concept especially when required different hardware blocks, relational algorithms, routing and wavelength conversion, congestion avoidance, control and physical security and synchronization between transmitter and receiver.

The design of reconfigurable logic active filter gates integrates the properties of short-pass, notch, long-pass and band-pass optical filters.

Components are therefore required to be wavelength selective in the visible range, allowing for the transmission, recovery, or routing of specific wavelengths.

Results have shown that the input channels could be recovered or removed by using an optical bias control. So, this optical device allows to add and drop one or several channels in a WDM optical network (OADMS).

It was introduced the basic principle of the emerging technologies of photonic switching under visible range. So, the device can be used as a bistable optical gate and act either as a short- or a long- pass band filter or as a band-stop filter depending on the wavelength of the external background. A device with this ability to memorize the previous value of the input light is potentially useful as a memory element of a “light computer” (Figure 6.6).

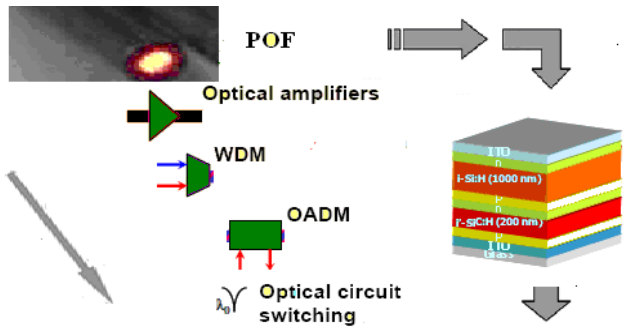

Figure 6. 6 *POF and pi’n/pin a-SiC:H device: a memory element of a “light computer”.*

2.4 Photonic vision building

Information and communication technologies ensure that progress is rapidly transformed into benefits for European citizens, businesses and industry. This section summarize scientific and technical quality, relevant to the topics addressed for technological development and demonstration activities guidelines that can be drawn from the research theme. Information and communication technologies are at the very core of the knowledge-based society. Activities will continue to support European scientific and technological basis base and ensure its global leadership in information and communication technologies.

The main constrains to reach the industrialization are:

The technology development *is rather expensive*, because it requires research in several areas, including (expensive) integrated circuit design. Moreover, it suffers from a lack of appeal due to its conceptual complexity. This hampers the acquisition of funds for doing research on the implementation of applications, although it is an excellent topic for doing multidisciplinary academic research, which might result in huge cost savings in case of visible light communication, visible light sources and plastic based fiber optic cable and competitive attenuation in short distance communication.

An *economic feasibility* study can only be done after further technological research. Priority was given to innovative approaches rather than incremental developments. Research actions should be driven by device requirements and include validation of results for the targeted applications. Extending the state-

of-the art for application fields, including notably application-specific photonic components and sub-systems for a given set of application fields, (such as transmitters and receivers, multiplexers, detectors and sensors according to their suitability of adoption in optical cross connects OXCs, switches and routers). The priorities for technological development and the criteria that will be used for evaluating the demonstration activities responding to these technological developments, reflect the input received from European technology platforms in information and communication technologies and other preparatory activities including workshops involving the main stakeholders.

2.5 Future research directions

More research is required in order to optimize the design of the corresponding transmitters and receivers, realize them as integrated microwave circuits and compare these with existing equipment. Some directions for further research will be suggested. These include also improvements for the simulation tool, optical source design and integrated optics technology, optical receiver design, visible range-like techniques and plastic based fiber optic cable transmission, relational algorithms, routing and wavelength conversion and an extension of the system level research that has been described in this thesis, possible improvements for the simulation tool that has been described in Chapter IV, and research in related areas, namely:

Optical source *design,* integrated optics technology, optical receiver design and network-related topics.

Application-specific *photonic components* and *subsystems* cover optical data communications for optical amplifier and demux device applications, biophotonics for early, fast and reliable medical diagnosis and imaging and sensing equipment (color sensor).

The *integration of new functionalities* for the next generation of application-specific components and smart systems will be done through the convergence of optoelectronic, biochemistry, measurement, information and communication technologies.

The *further development of core and photonic technologies* (photodetectors, optical amplifiers, modulators, transmitters and receivers, multiplexers, cross-connects, and sensors), will be fundamental in strategic applications such as medicine, communications, lighting, sensing and measurement, and manufacturing.

Micro-Nano Bio Systems are smart systems combining microsensing and nano-materials, molecular biology, biochemistry, measurement information and communication technologies. Within this objective, a high level of industry participation is expected and demonstration aspects will be encouraged.

At present, the *research on visible light* communication and directed, line-of-sight link was focused on laboratory applications. The multiplexed indoor application is expected to be developed in a near future. When multiplexed networks are realized for application, they will either have to be combined with existing transmission and/or networking standards or new standards might have to be defined a

collection of system requirements and definition of reference architectures, an identification of technical challenges and research directions for enhancing current systems with cognition capabilities, an elaboration on business paths and technology roadmaps for fully exploiting cognition and a specification of criteria and experiments (architectures, platforms, models, results and feedback from proof-of-concept activities).

In the filter representations, all inputs, outputs or states are function of a single variable, which is time in most cases. We call these types of filters one-dimensional (1-D) filters. There are other types of filters in which the inputs, outputs and states are the function of more than one variable. One example is the filter used in image processing. Therein, the inputs and outputs values are the function of two variables, i.e., horizontal and vertical coordination. The filters used in this case are two-dimensional (2-D) filters. Since images are defined over two dimensions (perhaps more) digital image processing may be modeled in the form of multidimensional systems [7].

Apart from the optical nonlinearity, light-to-dark sensitivity, color recognition, selective optical and electrical output and amplification schemes that were considered in this thesis alternative formats like implementing a video capture data flow pipeline, using different hardware blocks, software thread, relational algorithms, routing and wavelength conversion, rate adaptation, congestion avoidance and control and physical security could be studied. All these schemes introduce a significant increase in complexity with respect to the basic concept (especially when required synchronization between transmitter and receiver).

A technological topic that has not been considered in much detail is optical sources. Instead of using commercially available sources, the production and installation costs might be reduced by designing dedicated sources for application in WDM systems, eventually integrated together with the optical encoding circuit on a single transmitter chip. Two types of semiconductor lasers are widely used, monolithic Fabry-Perot lasers, and distributed feedback (DFB) lasers. The latter type will be particularly well suited for WDM applications in visible range.

Light emitters and light detectors are active devices at opposite ends of an optical transmission system. Light sources, or light emitters, are transmit-side devices that convert electrical signals to light pulses. The process of this conversion, or modulation, can be accomplished by externally modulating a continuous wave of light or by using a device that can generate modulated light directly. Light detectors perform the opposite function of light emitters. They are receive-side opto-electronic devices that convert light pulses into electrical signals.

First of all it is critical that the source is able to couple enough optical power into the encoding circuit, which puts requirements on the total amount of emitted power and the coupling efficiency, distance between an LED and a detector's surface and high-brightness LEDs for communication applications.

3 Running projects

It was proved that the conception of new devices based on new materials for signal (de)multiplexing in the visible spectrum includes the ability to memorize the previous value of the input light. So, new optoelectronic WDM system in the visible range, being able to transmit, receive and process intelligence, is, an original idea.

As referred in Chapters II, III and IV, the developed system consist of four essential elements: the heart of the matter (a double pi'n/pin a-SiC:H heterostructure), a voltage supply to dc voltage bias; optical connections for light triggering and optical bias to dc light bias control. This photonic vision is seen as part of a larger project or line of inquiry: "optical communications industry", of a clearly articulated and well-communicated product innovation and technology strategy.

Strategy becomes real when we start spending money. Any good product innovation strategy must deal with how much to spend on product innovation, and it should indicate the relative emphasis, or strategic priorities, accorded each arena of strategic focus. Thus, an important aspect of a product innovation strategy is resource commitment and allocation. Earmarking resources (funds or person-days targeted at different strategic arenas, project types, or major development initiatives) helps to ensure the strategic alignment of product development with business goals.

Each new project that use the concept of this new device, will cover its own goals, attack plans and resource allocation, but no project can succeed alone. Every project contributes to the overall objectives of the network of the future, and the synergies between groups of projects working on similar topics are vital to the overall success of the research. This will be achieved by stimulating the development of an European Research Area in the domain of amorphous Si/SiC multilayer optoelectronic components, within the execution of the framework programme's photonic thematic priority.

With the aim to raise awareness regarding the proposal objectives and results and to trigger collaborations which will enable proposal to exploit synergies with projects sharing similar or complementary goals, three projects that use the concept of this new device were already accepted by the FCT and are currently:

3.1 Optical biosensor systems

The first project (PTDC/EEA-ELC/111854/2009 "Optical Biosensor based on FRET (OBIOS)"

aims to develop a compact remote control optical biosensor system to detect, in-vivo, biomolecular reactions, at low production costs. The biosensors will consist of a nanoelectronics-based transducer with an interface chemistry which makes the connection to the clinical sample to be analyzed.

The detection mechanism is based on real time Fluorescence Resonance Energy Transfer (FRET). Such compact devices are of great interest in medicine and agriculture for monitoring several physiological parameters, such as glucose levels. The goal is to build a prototype with a level of performance comparable with classical remote sensing FRET techniques. The sensor unit comprises a fluorophores sample holder (nanosensor where the pair of fluorescent proteins interacts when excited by incident light), coupled with the a-SiC:H p-i-n-p-i-n wavelength sensitive transducer to monitor their fluorescence.

Optical transduction is based on FRET between Cyan Fluorescent Protein (CFP) and Yellow Fluorescent Protein (YFP). Excitation of the FRET pair requires blue light, in the spectral window between 400 and 440 nm, provided by a blue laser diode. The excitation light is injected into a hydrogel immobilization matrix containing a fusion protein (e.g. Glucose Binding Protein and both the CFP and YFP). Upon binding the analyte (e.g. glucose) the protein performs a conformational motion which changes the donor-acceptor distance thus affecting the level of acceptor fluorescence. The ratio between both fluorescence pairs correlates with the analyte levels, thus allowing near-real time detection of the concentration of a given analyte. A low power battery will supply the light source, the semiconductor transducer and the control and communication electronics.

The energy source will be complemented by specially developed electronics and a wireless transceiver to transmit the measured receptor level. The novelty of the project lies within the integration of the optical transducer module with the nanosensor, containing living cells or proteins, and its compactness with optics and microelectronics for continuously measuring analyte levels and provide users with online data. The data will be automatically collected, stored and processed resulting in a “complete integrated system” able to be used as a prototype and with a future goal to perform it as an end product. Such device could be also easily integrated in a closed loop system.

Using the existing synergies among the partners, two conception routes to reach the main objective are proposed. The first joins the experience of the partner on biochemistry/molecular biology and microelectronics and consists on the integration and optimization of the biosensor with the wavelength sensitive photodetector allowing high-sensitive low-noise wavelength-to-voltage conversion. The second route brings together the experience of the partners in the field of hardware and software to carry out an intelligent network, for remote or local process control, using as a basis the sensor unit produced. Research will be carried out in order to develop special hardware able to acquire, digitalize and process the analog signal produced by the sensors.

The project plans to use the existing know-how distributed into six tasks. The first one deals with the project specification and requirements. The next two are dedicated to the biosensor and transducer technology, research and development. Here the development of laboratory prototypes constitutes the main research points. Different biological systems and transducer architectures will be proposed and tested taking into account the requirements for FRET-based measurements and the spectral sensitivity of the optical transducer. Task four is dedicated to sensor and transducer integration and redefinition of the specifications. Task five deals with the development of the signal acquisition sub-system. Finally

task six combines the expertise of the partners in relevant areas (biochemistry, molecular biophysics, optical microscopy, sensors, numerical and electrical simulation) in order to simulate, validate and test a FRET based prototype to detect fluorescence of the excited fluorophores when glucose is present, allowing to monitor its level in a mammalian cell line.

As demonstrators of the proposed technology the following set of films, devices and systems will be produced:

Genetically encoded biosensors for glucose binding taking into account the best possible mutant proteins. Stable silicon based thin films with the required optoelectronic properties. Sample holder suitable for FRET measurements compatible with the optical transducer. Process of deposition of films;

Free and immobilized protein biosensors for in vitro characterization. Colour sensitive p-i-n-p-i-n a-SiC:H photodiodes optimized for fluorimetric detection;

Analog sensor readout and signal conditioning. Analog-to-digital (A/D) conversion, to provide a digital output signal. Calibration of the sensor transfer curve, digitally programmable.

Devices and systems for communication and remote control of the sensor.

3.2 X-Ray flat-panel detector for Medical Applications

This project (PTDC/EEA-ELC/115577/2009 X-Ray flat-panel detector for Medical Applications (MARx) intends to build a large area X- ray flat detector with optical readout and additional capability of real time digital radiography having a level of performance far above the classic film-screen. Furthermore, high frame rate at very low dose for fluoroscopy will also be addressed giving a new realm of possibilities in medical imaging such as: improved image quality; easier and faster data transmission, processing and archiving; reduced running costs; potentially lower dose. This technology also will help industries see defect easier, establish better quality control, and facilitates the storage and transmission of images. The detector to be developed comprises a converter layer, a large area a-Si panel and connections to external electronics and readout.

Essentially two concepts have to be implemented: intermediate conversion of the X-rays image into an optical image by a scintillator and the conversion of the optical image into an electric one by a large area a-Si:H-based image sensor with optical readout.

To overcome problems associated with CCDs (use of long focal length optics leading to bulk packages and linear distortions at the image edges) and flat-panel arrays (special photolithography techniques for patterning and complex design) the use of Laser Scanned Photodiode (LSP) sensor is proposed.

The stumbling blocks in this development are large size and high signal-to-noise ratio at low dose. Dynamic imaging higher than 30 frames/s is our goal. The technical challenges at the level of the a-Si image sensors are the light-to-dark sensitivity of the LSP, the memory effects associated with traps in a-Si:H. Of course, long-term reliability and stability are major concerns for medical components.

The project plans to use the existing know-how distributed into seven tasks. The first one deals with the project specification and requirements. The next two are dedicated to transducer technology research and developments. Different configurations and readout architectures will be proposed and tested taking into account the imaging requirements. Task four is dedicated to the development and implementation of a suitable optical readout system. The task five deals with the development of the signal acquisition sub-system. Task six combines the expertise of the partners in allied areas (sensors and transducers, numerical and electrical simulation and remote control) in order to develop large area X-ray imaging prototype to be used in remote static and dynamic medical imaging applications (radiography, fluoroscopy and non destructive material inspection). Finally, the detector prototype will be tested to evaluate image quality using the methods described in task seven.

As demonstrators of the proposed technology the following set of films, devices and systems will be produced:

Stable intrinsic and doped silicon thin films for device applications.

Stacked p i-n image sensors and flat X-ray detectors with optical readout.

Analogue readout electronics and A/D signal processing unit.

Integration of the data acquisition sub-system with a standard network to enable image processing, storage and remote control.

3.3 Wavelength Division Multiplexing System for short range optical communications (WDM)

Finally the project (PTDC/EEA-ELC/120539/2010) aims to develop a WDM-based optical communication system for short-range communication spectral window. The proposal outlines an effort of building a complete system in which the novelty is mainly on the a-Si ba multiplexing device and its integration with plastic optical fiber. The goal is ambitious (demonstrating a complete system) a well thought out and nicely integrated. The optimization goals and deliverables for resulting devices and systems are clear successful, the resulting system has commercial applications in several digital city industry segments including auto industry, aerospace, medical sector and in-house communication.

As stated along this thesis, WDM is a standard technique used in communication systems to enlarge the bandwidth of the transmission channel. It consists on integrating different wavelengths into a waveguide using a multiplexer device and on separating, at the receiving end, the different wavelengths in order to recover the original input signals, using a demultiplexing device. This demux device is usually based on interference filters or diffraction gratings.

The novelty of the project lies mainly on the demultiplexing device used, which is a multilayered semiconductor structure based on a-SiC:H, that behaves as an optical filter, exhibiting a spectral sensitivity that can be tuned by the applied voltage, and also on the subsequent integration of the

optical demultiplexing device with POF. The integration of these different technologies allows the realization of a low cost short range communication system, which has potential applications in domestic networks, in the automotive industry, etc.. The additional integration of the electronics acquisition on-chip represents an important contribution for the project as it can anticipate a preliminary prototype of an integrated communication system.

The system comprises four main modules: the optical signal generator, the transmission medium of the optical system, the photodetector for the demultiplexing operation, and the electronics acquisition integrated circuit and signal processor.

Each data channel is implemented as a monochromatic light source assembled with a light modulating system. The transmission medium is a POF as this type of fiber is more appropriate in the visible spectral range than the traditional optical fiber, due to a lower attenuation. The photodetector is a multilayered device based on a-SiC:H that works as a selective wavelength filter tuned by the external applied bias.

Using the existing synergies among the partners, two conception routes to reach the main objective are proposed. The first joins the experience of the partners on fiber optics communications and on microelectronics and consists on the integration and optimization of the optical signal transmitted by the POF with the wavelength sensitive photodetector allowing high-sensitive low-noise wavelength-to-voltage conversion. The second route brings together the experience of the partners in the field of hardware and software to integrate the electronics acquisition control with the transducer. Research will be carried out in order to develop special hardware able to process the analog signal produced by the photodetector, using modern digital signal processing techniques and processors.

The project plans to use the existing know-how distributed into seven tasks. The first one deals with the project specification and requirements. Task 2 is dedicated to the light source and to the optical fiber. Task 3 deals with the photodetector technology, research and development. Task 4 involves numerical, electrical and optical modelling for analytical characterisation of devices and sub-systems. Task 5 is dedicated to the development of the WDM unit integrating the sub-system light source coupled to the POF and to the photodetector. Here the development of laboratory prototypes constitutes the main research points. Different optical signals will be proposed and tested taking into account the requirements of the spectral sensitivity of the photodetector and the attenuation along the POF. Task 6 deals with the development of the signal acquisition sub-system. Finally task 7 combines the expertise of the partners in allied areas in order to simulate, validate and test a prototype able to demultiplex different optical signals.

As demonstrators of the proposed technology the following set of films, devices and systems will be produced:

Optical system for optical light source couplig with the POF;

Stable silicon thin films, suitable for optical device applications;

Colour sensitive p-i-n and p-i-n-p-i-n phototransducers based on a-SiC:H;

Analog sensor readout and signal conditioning. A/D conversion, to provide a digital output signal. Calibration of the sensor transfer curve, digitally programmable.

This project will ensure appropriate transfer of technology to other research sectors such as semiconductors, optoelectronics, telecommunications and electronics/optics engineering.

4 The digital city of tomorrow

4.1 Urban traffic control

Urban Traffic Control (UTC) is a term used to describe the technique of co-coordinating traffic signals, normally through a centrally located computer.

A standard traffic control system (Figure 6.7) depends on good traffic data for successful operation. Inductive loops are most common, though other types of detector can be used. For best results, detectors are required on each link.

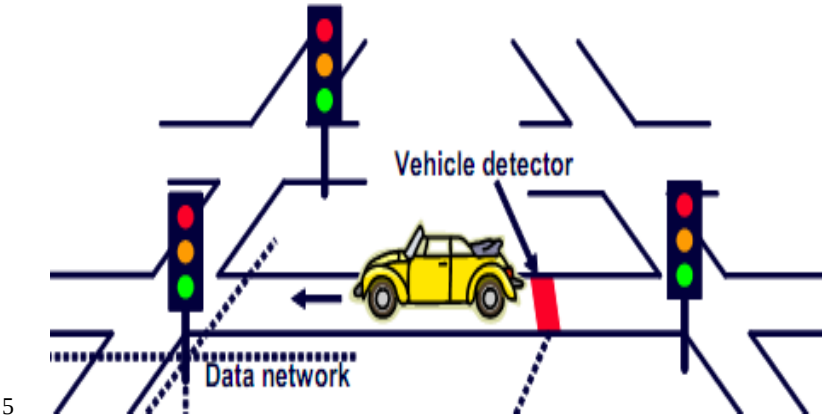

Figure 6. 7 *Ilustration of a standard traffic control system*

The visible light communication system consists of transmitters and receivers, which are physically separated. This communication paradigm has drawn interest from both research and industrial communities (Telematics).

The transmitters modulate the intensities of lighting sources, e.g., LEDs, at such high frequencies that human eyes cannot perceive any difference in lighting compared to that when there is no modulation. Solid-state light sources are rapidly replacing conventional ones in signaling, illumination and display infrastructures. It thus becomes possible to carry communication data on such light sources. As a

result, transmitters can be used for lighting, background irradiation and data communication simultaneously.

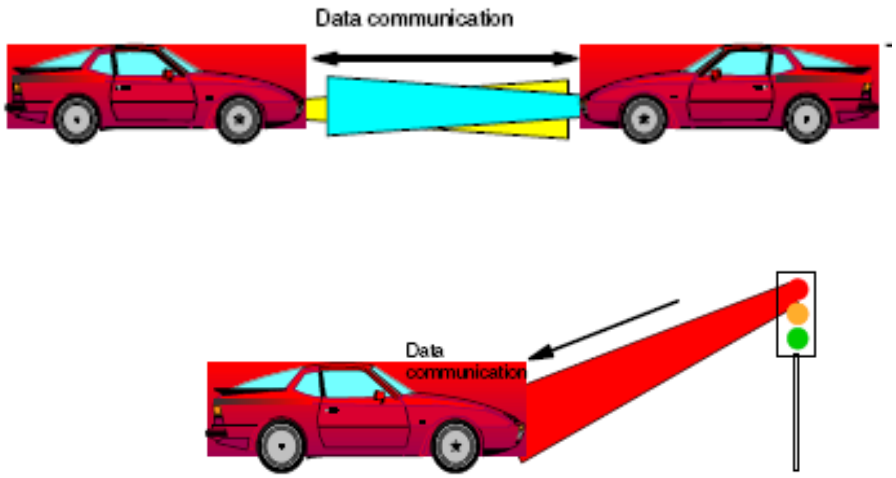

Figure 6. 8 *Lighting sources can be used for background irradiation, data communication and infrastructure lightings simultaneously*

The receivers consist of photodiodes either as stand-alone elements or in the form of image sensors to receive information from varying lighting intensities, considering the constraints imposed by outdoor environments and vehicular traffic.

As stated in the last chapters, amorphous SiC tandem heterostructures can be used to filter a specific band, in the visible range. Experimental and simulated results have shown that the use of SiC multilayered structures in applications where gain compensation is needed or to attenuate unwanted wavelengths is possible. The transducers combine the simultaneous demultiplexing operation with the photodetection and self amplification. They were optimized in chapters II, III and IV for provide the high-sensitivity needed for MUX/DEMUX. As explain before, the device is a two-position switch with inputs “front side background irradiation” and “back side background irradiation” (Chapter V). It selects one of several possible input signals and transfer the signal to an output terminal. Potential applications include:

- point-to-point communication
- indoor location based service
- point-to-multipoint communication
- information broadcast
- intelligent transportation system

A vehicular applications network will provide economic opportunities to equipment manufacturers, component suppliers, service providers, and infrastructure operators [8,9,10,11,12]. It will consist of infrastructure lighting sources as fixed gateways and vehicles as mobile nodes. Both the mobile nodes

and infrastructure lightings, such as street lamps, traffic lights, in-vehicle illumination, outdoor applications, can be equipped with multiple transmitters and receivers which can operate simultaneously. As an example of the placement of transmitters and receivers, the headlights and brake lights of a vehicle can serve as transmitters, and multiple receivers can be mounted around the vehicle.

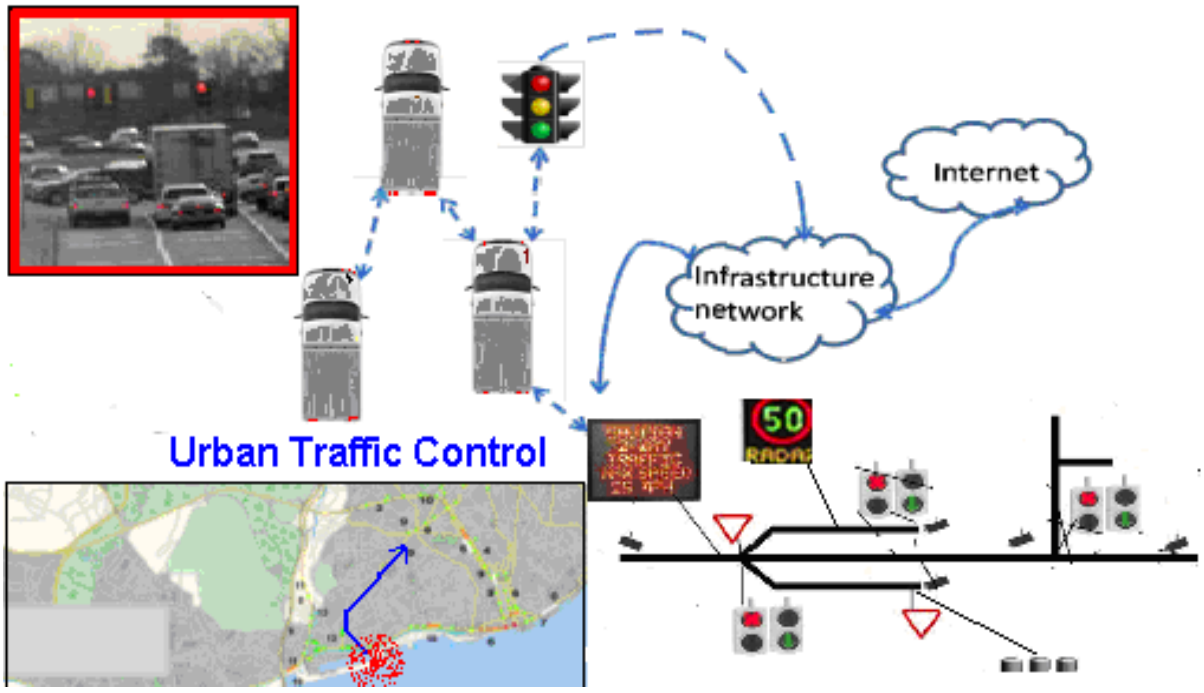

Figure 6. 9 *An illustration of traffic control system of tomorrow*

Figure 6.9 illustrates the traffic control system of tomorrow, in which vehicles can either directly communicate with the gateway infrastructure lightings or reach the gateways using other vehicles as relays. The gateways are connected by an infrastructure network, which is further connected to the internet. The information related to the vehicle safety applications is contained within the infrastructure network and vehicles. Depending on the nature of the application, it may involve none, one, or more gateways.

Traffic signal violation warning, curve speed warning, left turn assistant, stop sign movement assistant, lane change warning, cooperative forward collision warning, pre-crash sensing, and emergency electronic brake lights are high-priority vehicular applications.

The lighting will be also very convenient to inform an exact location, for guidance systems, optical navigation or emergency use. Optical navigation starts where the Global Positioning System (GPS) has its limits: for instance inside public parking buildings, tunnels, undergrounds or in overcrowded areas. Here, GPS is not available or too inaccurate. Optical navigation can provide an alternative solution to this problem.

Due to the increasing market penetration of long-life, energy-efficient light emitting diodes (LEDs) as means of lighting, the development of future optical navigation systems can simultaneously solve the usage of LEDs for illumination applications. In consequence, optical navigation offers the opportunity to provide new and additional services – not only to improve operative production processes even to enhance citizens' quality of life.

4.2 Polymer Optical Fibers in automotive networks

The Polymer Optical Fibers (POF) was a niche technology as shown in Figure 6.10, only a few years ago, [4, 13, 14].

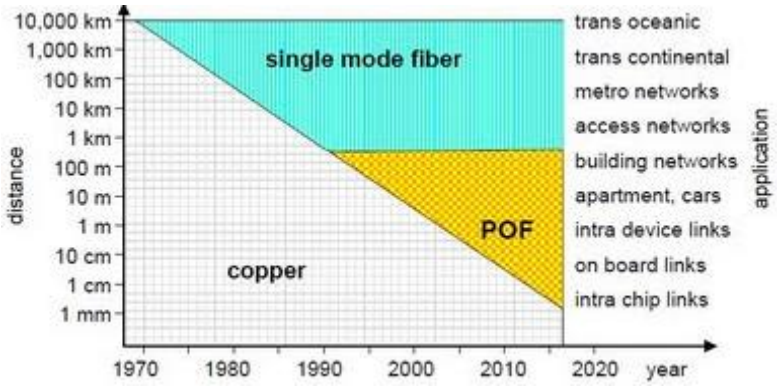

Figure 6. 10 *Competing communication technologies, distance and applications.*

Plastic Optical Fiber (POF), with different attenuation behavior (Figure 5.8), has emerged as a low-cost alternative to traditional copper cabling in office, home and automotive networks.

Plastic optical Fiber was invented as a cheaper substitute of Glass Optical Fiber. But by time it has proven, not only it is cheap it is also better in various manner. Plastic Optical Fibred offers many benefits to the user, such as lightweight, robust, and easy installation. As Plastic Optical Fiber is an excellent medium of transmission, it is massively used for short distance communication.

The dominant use of POF in automobiles is connected to the media oriented system transport standard, which was developed as a POF-based system connecting audio devices including telephone systems, head units, DVD changers, and navigation units in a single-fiber unidirectional optical ring. This architecture uses less fiber and transceivers than a two-fiber bidirectional structure and is thus much more cost-effective

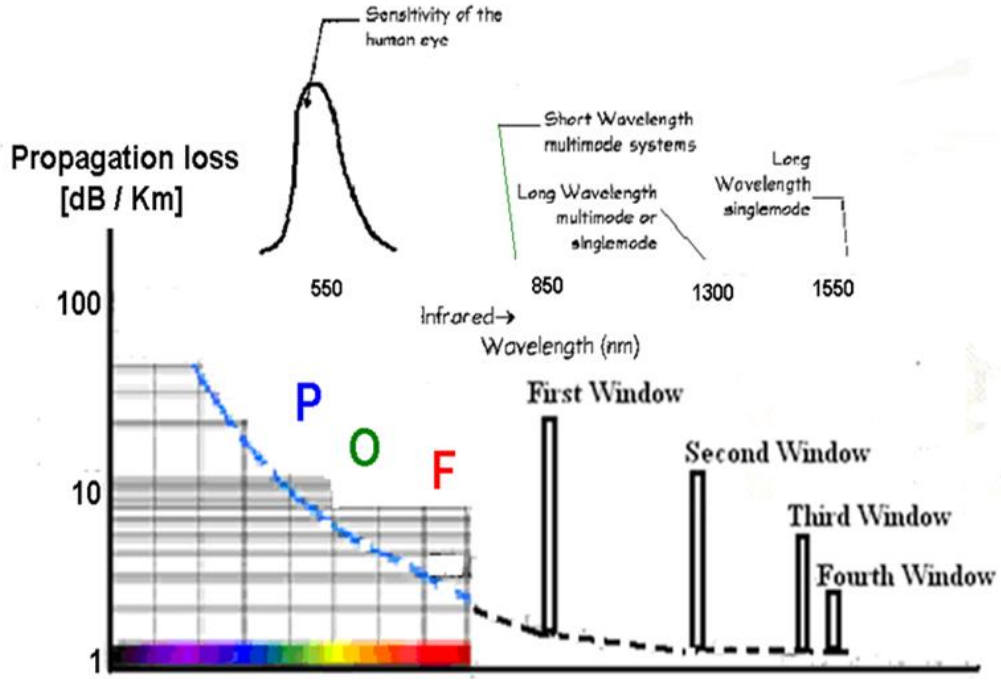

Figure 6. 11 *Loss spectrum of optical fibers.*

The automotive industry is constantly looking for new ways to make their cars safer, more reliable and more efficient. The industry is also looking at a shift toward hybrid and fully electric vehicles, and provides a low-cost solution to many aspects of automotive vision control operation, sensor interface, power control and safety. Since 1989 with CEC DRIVE PROGRAMME, European cities have been involved in several projects aimed at achieving the interconnection and interoperability of local and regional networks and access to these networks [15, 16].

Since 1998, European car manufacturers adopted optical fibers networks as displayed in Figure 6.9 The emergence of Wavelength-Division Multiplexing (WDM) was one of the most important developments in the field of fiber optic transmission technology. There is an increasing amount of information, for short range communications, that must be transmitted at low costs and high transmission rates. Data transmission can be improved using WDM technique. Vehicles will use this network to share vehicle speed information among all Electronic Engine Control systems, and the On-Board Unit, responsible for the wireless communication with roadside stations.

The modular design of In-vehicle units and the high capacity secure bidirectional communications link to the roadside will open the way to all kinds of information services. Beyond speed, the network will also share GPS positioning and routing information, leaving a large bandwidth available for future services.

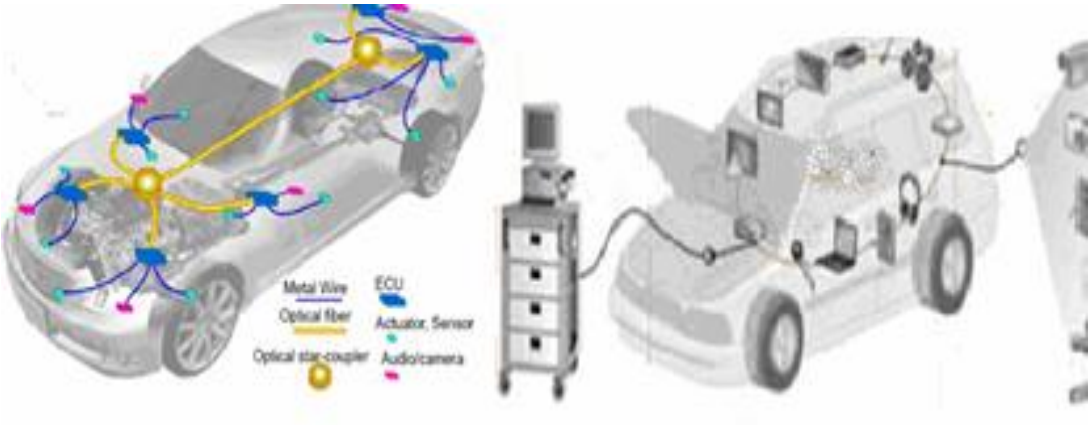

Figure 6. 12 *Future Automotive Networks with POF and repair shop infrastructure*

The first step will be the definition and implementation of a general interface data bus to allow the connection of different peripheral devices to the On-Board Unit. New traffic control systems will depend on good traffic data for successful operation.

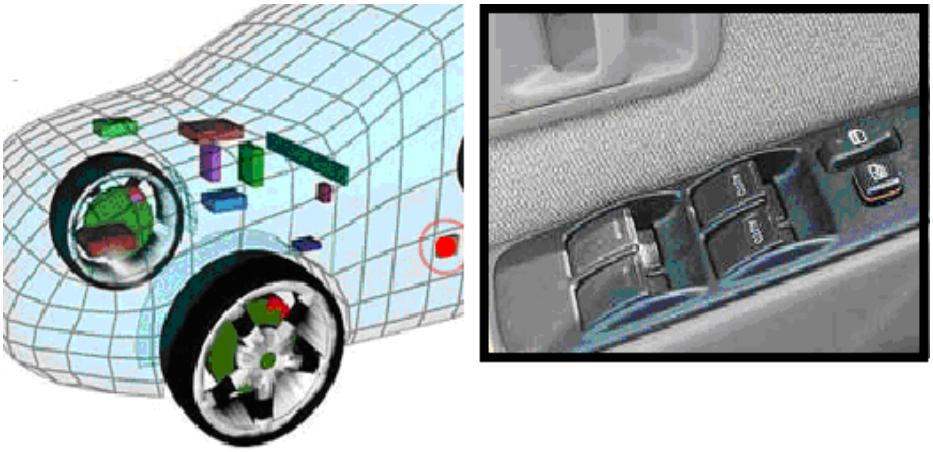

Figure 6. 13 *Driver's door module with various switches.*

Multiplex technology opens up new possibilities in the electrical systems. It breaks new ground with its design and function and offers substantial advantages over a conventional system. In the multiplexed system, a module containing at least one processor centralizes inputs and outputs to an area of the car. Figure 6.13 presents driver's door module with various switches to control electric windows, electric mirrors, power locks and power seats even at the door. It would be impractical to install a thick bundle of wires for a system like this from a door. Instead, the driver's door module monitors all commands.

4.3 Optical Fibers in house communications

Due to the rapidly growth of the number of private broadband access lines and the increase in the available bit rate at the same time, mainly driven by IP TV Internet Protocol Television") applications, optical communications will be used in home networks more and more for different scenarios Figure 6.14a (FTTx solutions) and in Figure 6.14b (FTT Cab "Fiber to the Cabinet" scenario).

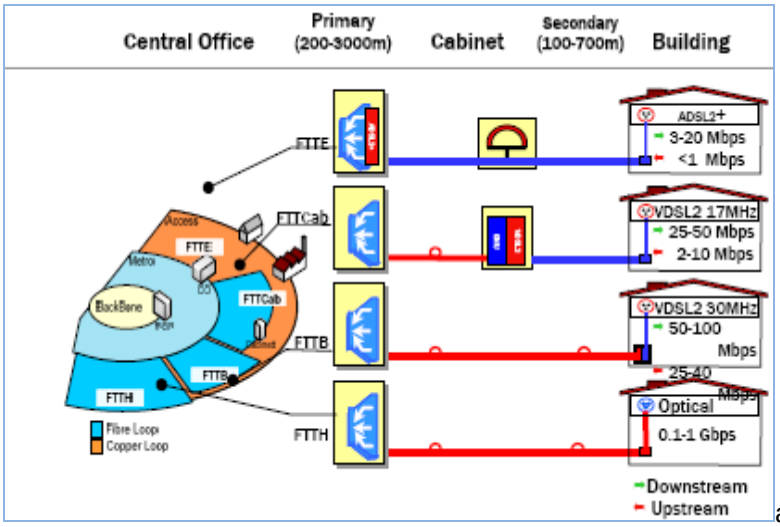

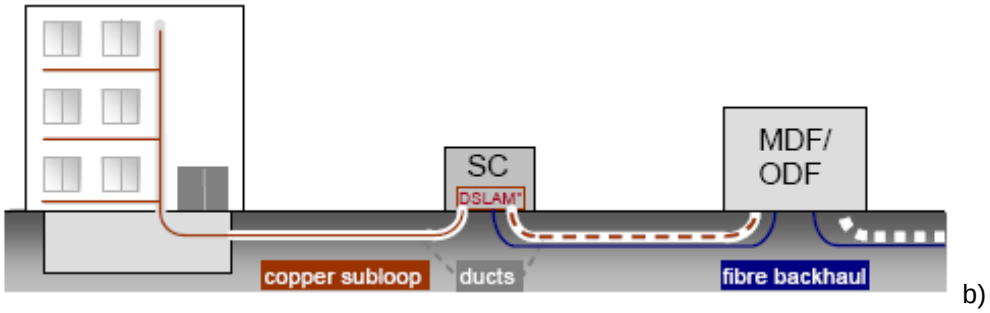

Figure 6. 14 *Conceptual illustration In House Communication: a) FTTx* solutions; *b) FTTCab "Fiber to the Cabinet" scenario,*

The ACCORDANCE project investigates on a new paradigm for the access network. The research leading to project results has received funding from the European Community's Seventh Framework Programme (FP7/2007-2013) [17]. The main objectives of ACCORDANCE are:

Define a novel Access Network Architecture achieving convergence among heterogeneous technologies (optical, wireless, copper);

Propose low-cost, low-complexity concepts to achieve ultra-high data rates in the access network (even up to 100Gb/s);

Introduce a flexible bandwidth allocation concept.

So, those scenarios cannot be definitive or mutually exclusive. Figure 6.15 shows glass optical fiber networking to reach the building and then use plastic optical fiber to reach home or office equipment. The Fiber to the Desk (FTTD) propose an intermediate solution for integration of Internet, telecommunications and IPTV networks. This solution can be adopted in schools, hospitals, museums and so on.

There are a lot of technologies available to deploy for residential, commercial and industrial networking. We believe that Plastic Optical Fiber (POF) cables and Ethernet over Plastic Optical Fiber (EoPOF) solutions are the right choice for builders, installers, designers and architects challenged to deliver broadband services in the frame of the last one-hundred meter optical networking. Plastic optical fiber is the only technology that is quick and easy to install, even customer installable, as well as inexpensive and self-powered, and that provides whole house coverage, works in an unlimited number of outlets, is immune to electro-magnetic interference and is highly reliable.

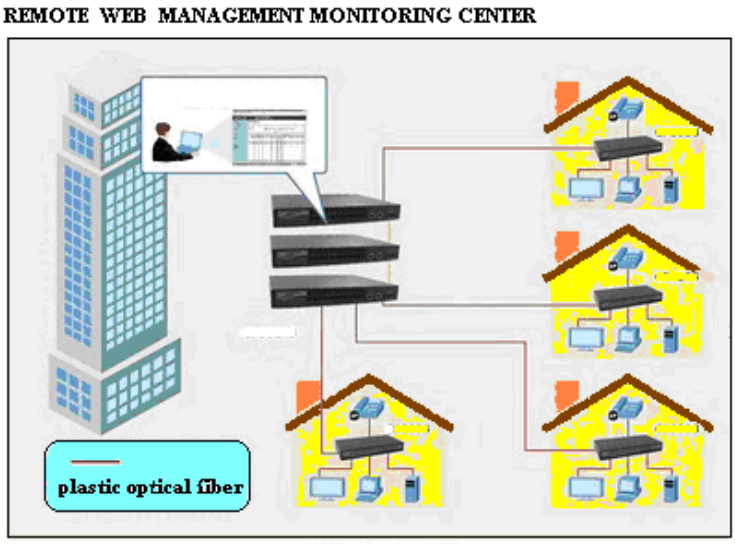

Figure 6. 15 *Conceptual illustration In House Communication FTTH_ Fiber to the Desk (FTTD) using plastic optical fiber to reach office equipment.*

POF is also far less expensive to deploy than other competing technologies, which makes it the ideal choice for many customers.

The fiber is only one element of a POF network; the ruggedness of the individual fibers must also be matched by the network's sending and receiving elements in combination with state-of-the-art driver integrated circuits.

4.4 Conceptual Communication technologies

Strategic priority for the cities, in the electronic communications sector, promoting investment in Next Generation Networks will play a stronger role contributing to the goals of sustainable development. The environment war will be won or lost in digital cities.

With the traditional cellular network, it is very difficult for operators to provide high quality services and cell coverage to indoor users. The Global System for Mobile communications (GSM) that was developed in Europe in the late 1980s was initially designed to support, narrowband speech telephony with bitrates between 5 and 15 Kbit/s, but with the passage of time, the focus of GSM technology has been shifted from voice to data services. The further development of the Universal Mobile Telecommunications Systems network is based on an `All IP' solution. This concept also introduces the IP traffic handling in the UMTS core network (CN). The IP-based Multimedia Services architecture in the CN opens the door for the creation of new mobile-based multimedia applications (Figure 6.16).

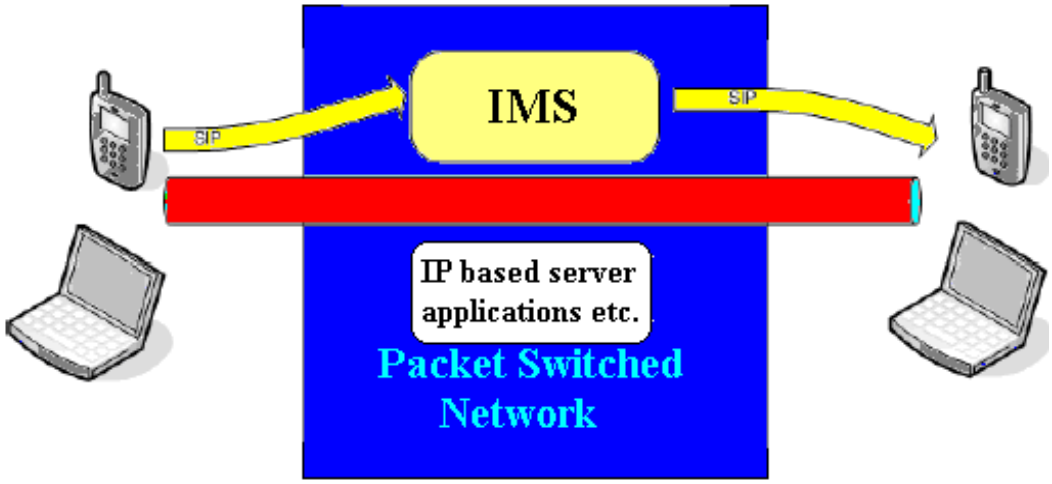

Figure 6. 16 *The IP-based Multimedia Services architecture opens the door for the creation of new optical cell phone applications.*

The IMS enables the UMTS network to provide rich content delivery service simultaneously to the users. The IMS establishes an IP-based end-to-end multimedia session, and is used to provide transparent communication over different networks. Moreover, the IMS enables applications in the UE to establish peer-to-peer connections, something which were not possible before.

The optical wireless communication is a general term for explaining wireless communication with optical technology. Usually, optical wireless communication includes infrared communication. Data transmission can be improved using the well known wavelength division multiplexing-demultiplexing technique for infrared telecommunication systems. Multi-stage architectures help to overcome some limitations of single-stage optical cross-connects which require either a large number of space switching elements or tunable wavelength converters that are tuned over a large number of wavelength channels.
Optical computing has a long and diverse history. In our opinion, the future of optical computing resides in four areas: digital optical logic, quantum computing, analog-and-digital optical signal processing, and photonic reservoir computing that involves nonlinear elements, neural networks and training sets.
Usually, each wavelength selector consists of Mux/Demuxes (or any device with equivalent functionality) separated by an array of optical devices that are able to operate as an on/off gate [18,19,20,21,22]. Optical switches blocks using wavelength selective channel filters are also used for infrared telecommunication systems [23,24,25,26,27].
The visible light communication denotes a communication technology which uses visible light as optical carrier for data transmission. This communication technology makes use of the visible light source as a signal transmitter, the air as a transmission medium, and the appropriate controlled device is presented as a signal receiving component.
We may be able to find the ideal transmission medium relative to attenuation, interference and bandwidth. But, we still may not be able to select it as part of the solution to the data link design problem. Why? It simply costs too much. The expense that it presents is beyond the budget allowed for the source-user communications. Money doesn't drive the world. But, it sure has a tremendous influence on the ultimate choice of solution to any problem based in technology. To be absolutely clear, it is the pure glass- silica based fiber optic cable that has the low attenuation properties. Glass fiber optic cable has the lowest attenuation and comes at the highest cost. The plastic based fiber optic cable has much higher attenuation. But, it does have some attractive features.

4.5 Moving towards Next-Generation Networks

Next-Generation Network (NGN) is the term given to describe a telecommunications packet-based network that handles multiple types of traffic (such as voice, data, and multimedia). It is the convergence of service provider networks that includes the public switched telephone network, the data network (the Internet), and, in some instances, the wireless network as well.
The first step will be the definition and implementation of a general interface data bus to allow the connection of different peripheral devices to the On-Board Unit. New traffic control systems will depend on good traffic data for successful operation.
Although NGN development enables the telecommunication companies to gain new resources, but there isn’t a unique and complete solution for establishing and developing a NGN deployment.

Resolution of the Council of Ministers No. 120/2008 of 30 of July 30, promoted investment in next generation networks. Decree-Law No. 123/2009 of 21 May, has established a set of obligations for the State, the Autonomous Regions, local authorities, public companies [28].

Next generation networks will not switch on overnight. Neither will customers be migrated from old to new services in an instant. The pattern emerging at carriers where transformations are underway indicates operators will have to manage legacy and next generation platforms in parallel for sustained period of time, with resulting challenges in managing customer services across old and new. This uncertainty over how the transition will be managed has led to delays in undertaking the transition.

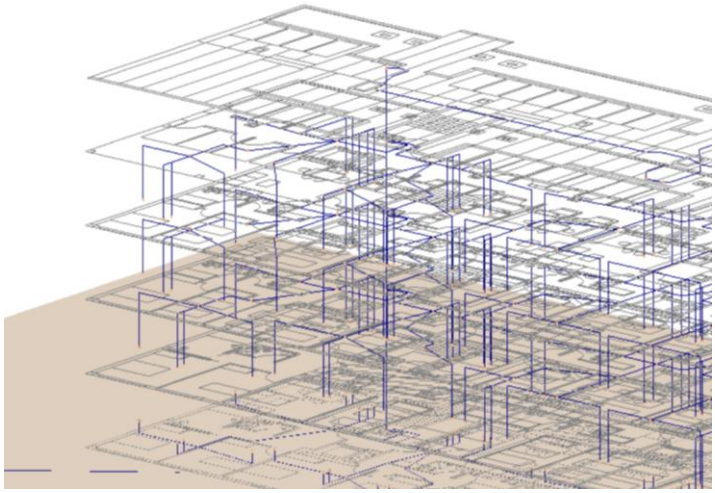

Figure 6. 17 *A building telecomunication project using plastic optical fiber to reach office equipments.*

The migration to next generation packet based networks can be much easier and smoother than previously thought, using the emerging a-Si solutions and its integration with plastic optical fiber (Figure 6.17). It will push the limits of functionality, cost/performance and integration level.

4.6 Innovation strategy framework

Many of the people who will shape this process — national policy makers, mayors, corporate strategists, and managers of sovereign and private wealth — now see the city as a fundamental unit of social analysis. To use an analogy from software, cities are the modules of the modern world. Externally, they connect via such standardized interfaces as the shipping container, the airplane, the Internet. Internally, they can be diverse, experimental, and innovative. As they respond to technological and environmental change, new and restructured cities will be our most important source of social progress.

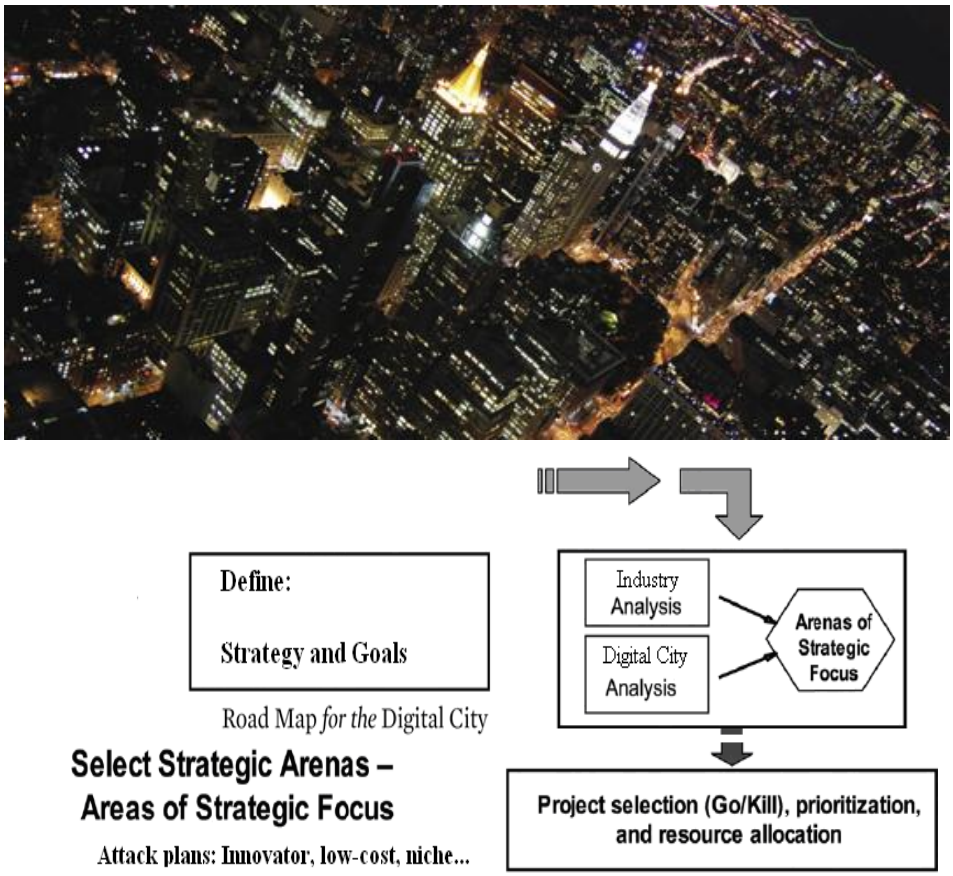

Figure 6. 18 *The world's top-ranked digital city as the place for innovation strategies framework .*

Today, cities remain the leaders in many major industries - from finance to media. As technology lowers barriers to entry, emerging cities are making significant investments in their economy, and, the competitive landscape is being remade on an almost daily basis. In order to compete internationally, therefore, we must adapt. They are so focused on supporting city businesses to help them compete in a world in which the only certainty is change. In so doing, we believe that we are positioning digital city as the place for innovation strategies framework (Figure 6.18). It begins with product innovation goals at the top and moves through to tactical project selection decisions at the bottom.

An innovation strategy is an essential tool for product development and continued growth even in difficult times. So, we are dedicated to understanding the anatomy of the digital city of tomorrow, the urban centralized brain processing millions of megabytes of information over arterial WDM networks and monitoring each movement in the video surveillance systems.

Road Map for the digital city outlines a path to build on New York City's successes and establish it as the world's top-ranked Digital City, based on indices of Internet access and digital industry growth [29].

Across the globe, cities face unique challenges and opportunities. But we all share the common goal of serving our citizens with the goal of creating a unified, integrated system for providing services and

information. An innovation strategy is an essential tool for product development and continued growth even in difficult times.

Moving to such an all pervasive networked society however puts increased demands on network reliability and security. The telecommunications industry is part of a nation's critical infrastructure and all critical national infrastructures depends on reliable and secure telecommunications. The network must therefore be always available and have the ability and flexibility to interface and integrate multiple technologies and service requirements.

Over the past decade there has been an explosion in the deployment of pervasive systems such as cell phone networks and user-generated content aggregators on the Internet that produce massive amounts of data as a by-product of their interaction with users. This data is related to the actions of people and thereby to the overall dynamics of cities, including how they function and evolve over time, that today allow researchers to better understand how people flow through urban space, and could ultimately help those who manage and live in urban areas to configure more livable, sustainable, and efficient cities [30].

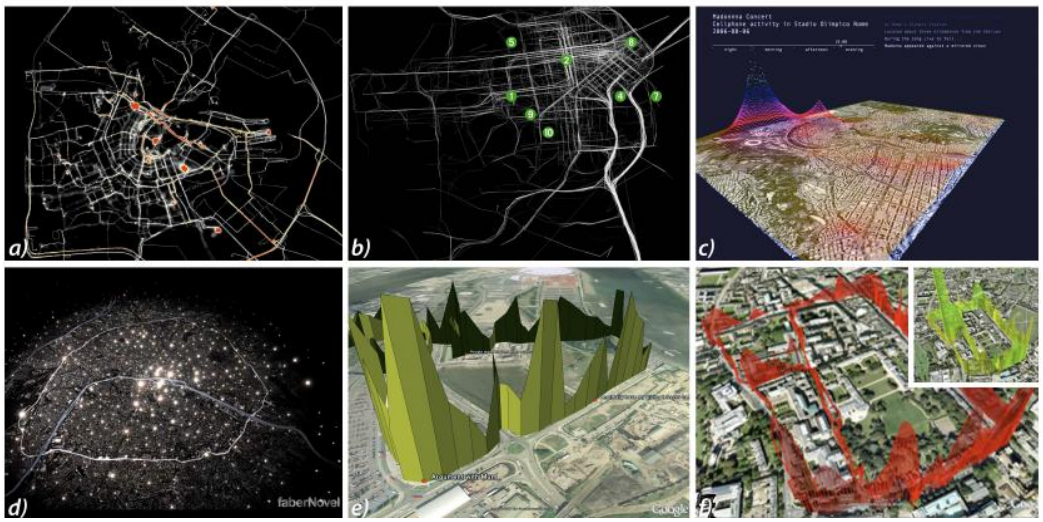

Figure 6. 19 *Examples of visualizations of urban dynamics in digital city of tomorrow*

Figure 6.19a focused on visualizing the connection between the structure of the city and the movements of inhabitants; in Figure 6.19b the visualization employs information flows to reveal the geographic space of the city, highlighting thoroughfares of movement but leaving out buildings and public spaces; in Figure 6.19c and Figure 6.19d real time city took aggregated data from cell phones and mapped these calls onto the geography of the city during two special event and provide a sense of the collective emotions of a city; Figure 6.19e measuring and mapping people's emotional responses to the built environment itself is the goal of biomapping; finally in Figure 6.19f, using sensors mounted on pedestrians and cyclists, monitors pollution in the city and relays the collected data to a website in real time. Depending on the objective of the visualization, some perspectives are in 2D (Figures 6.19a,

6.19b) as in the representation of traffic flows, and others are in 3D to present concepts like the volume of activity in urban space [31,32].

The figure presents a low-cost distributed sensor model where people themselves collect data that can be visualized to better understand the environmental impacts of urban functions such as transportation. This in turn can help those who manage urban regions to make more informed decisions. These systems present the possibility of extracting and inserting real-time information about social dynamics into the built environment. This dynamic feedback loop of information about how a city functions has the potential to influence many aspects of urban management by assisting local authorities, service providers, enterprises, and even citizens themselves to make more accurate, informed decisions and as a result to create a more efficient urban environment. In order for this to happen, we contend that it is necessary to first educate the public in understanding how individual choices build up to form emerging urban processes that affect the city and its inhabitants as a whole. So, we are dedicated to understanding the anatomy of the digital city of tomorrow, the urban centralized brain, monitoring each movement in the video surveillance systems, and processing millions of megabytes of information over arterial WDM networks.

We are living in the age of cities: estimations suggest that by the year 2050 over 70% of the world's population will be living in cities. There are many open issues and research questions related to this development, from urban development, transportation and economic development to social services, healthcare, energy, public safety, education and more. Tomorrows cities are seen as innovative places with efficient, effective and sustainable services where people can enjoy a high quality of life, cities anatomy that is characterized by their connectivity, intelligent services and digital heartbeat that benefit their population [33]:

The urban centralized brain, with video surveillance systems, monitors each movement, processing millions of megabytes of information over arterial WDM networks

Driven by rapidly changing mobility needs, traffic control systems and applications are undergoing a paradigm shift: inductive loops information will be replaced by smart urban mobility sensors and senseable control strategies.

The performance of public transports could be highly increased through a feed-back real time cooperative control. The improvement of current high bandwidth secure communications link between the public transport vehicle location systems and centralised traffic lights system open the way to more effective forms of bus priority traffic control.

The bidirectional communication infrastructure will be used as a platform to implement additional services to supply real-time traffic information to the commuters, avoiding congestions and increasing traffic speed.

Medical and housing sectors will in addition quickly accelerate the expansion of capillary short distance communication systems and clearly demonstrates their relevance to society. The buildings will act as kidneys, to filter the water and making their reuse.

These innovative tools, services and methods for demand management will bring a large improvement to urban transport efficiency. The multi-modal urban mobility concept will be a key element for the efficiency of urban traffic and sustainable development policy. It will ensure greater fluidity, reducing energy consumption, accidents, jams and resulting nuisances (noise and CO_2 pollution).
The increase of speed in public transportation is an important factor for city attractiveness and quality of life.

5 References

[1] Kirk, B. 2009. “Creating an Environment for Effective Innovation”. Presentation given at the Stage-Gate Innovation Summit, 2009, Clearwater Beach, FL, February.

[2] Cooper, R. G., Edgett, S. J., and Kleinschmidt, E. J., “Benchmarking Best NPD Practices—2: Strategy, Resources and Portfolio Management Practices”. Research-Technology Management, 2004, 47(3), pp. 50–60

[3] Stallings, W. "Data and Computer Communications", Pearson Education, Inc., 2007. p.247-248

[4] Mark G. Kuzyk, “Polimer Fiber Optics, Materials Physics and Applications”, Taylor and Francis Group, LLC; 2007.

[5] Daniel Nolan K. O. Hill et all “Fiber Optics Handbook Fiber, Devices, and Systems for Optical Communications”, McGraw Hill 2002

[6] S. Randel, A.M.J. Koonen, S.C.J. Lee, F. Breyer, M. Garcia Larrode, J. Yang, A. Ng'Oma, G.J Rijckenberg, H.P.A. Boom. “1 Gbit/s Transmission with 6.3 bit/s/HzSpectral Efficiency in a 100 m Standard 1 mm Step-Index Plastic Optical Fibre Link Using Adaptive Multiple Sub-Carrier Modulation” ECOC 07 (Th 4.1.4). (pp. 1-4). Berlin, Germany, 2007.Telephone Traffic, Academic Press, New York, 1965.

[7] Wang, D. “Identification and Approximation of 1-D and 2-D Digital, Filters”, Ph.D Dissertation, Florida Atlantic University, Boca Raton, FL, May, 1998.

[8] A. Ashok, M. Gruteser, N. Mandayam, J. Silva, M. Varga, and K. Dana. Challenge: “Mobile Optical Networks Through Visual MIMO”. In ACM MobiCom, 2010

[9] K. Bilstrup, E. Uhlemann, E. Strom, and U. Bilstrup. “On theAbility of the 802.11p MAC Method and STDMA to Support Real-Time Vehicle-to-Vehicle Communication”. In EURASIP Journal on Wireless Communication and Networking, Vol. 2009, 2008.

[10] S. Eichler. “Performance Evaluation of the IEEE 802.11p WAVE Communication Standard”. In IEEE Vehicular Technology Conference, 2007.

[11] M. Fiore, and J. Harri. “The Networking Shape of Vehicular Mobility. In ACM MobiHoc”, 2008.

[12] S. Okada, T. Yendo, T. Yamazato, T. Fujii, M. Tanimoto, and Y. Kimura. “On-vehicle Receiver for Distant Visible Light Road-to-vehicle Communication”. In IEEE Intelligent Vehicle Symposium, 2009.

[13] Manabu Kagami. “Optical Technologies for Car Applications Innovation of the optical waveguide device fabrication”. Optical communications - perspectives on next generation Technologies”, October 23-25, 2007 in Tokyo, Japan.

[14] O. Ziemann, J. Krauser, P.E. Zamzow, W. Daum, POF Handbook, “Optical Short Range Transmission Systems”, Springer, 2nd Ed., 2008.

[15] CEC DRIVE PROGRAMME: PAMELA CONSORTIUM Project Reference Nº 6412(CEE/DRIVE I- 1989-1991).

[16] CEC DRIVE PROGRAMME ADEPT CONSORTIUM Project V2026(CEE/DRIVE II- 1991-1994).

[17] http://cordis.europa.eu/fp7/home_en.html

[18] S.L. Danielsen, P.B. Hansen, K.E. Stubkjaer, “Wavelength conversion in optical packet switching, Journal of Lightwave Technology” 16 (9) (1998) 2095–2108.

[19] A. Stavdas, H. Avramopoulos, E. Protonotarios, J.E. Midwinter, “A novel architecture for a wavelength crossconnect node”, Photonic Network Communications 1 (1) (1999) 77–88.

[20] L. Dittmann et al, “The European IST project DAVID: a viable approach toward optical packet switching”, IEEE Journal on Selected Areas in Communications 21 (7) (2003) 1026–1040.

[21] C. Raffaelli, M. Savi, A. Stavdas, “Sharing wavelength converters in multistage optical packet switches”, in: Proceedings of HPSR 2006, Poznan, Poland, 7 9 June, 2006, pp. 203–208.

[22] G. Maier, L. Savastano, A. Pattavina, S. Bregni, M. Martinelli, “Optical switch Benes architecture based on 2-D MEMS”, in: Proceedings of the IEEE 2006 Workshop on High Performance Switching and Routing (HPSR 2006), Poznan, Poland, 7–9 June, 2006.

[23] H.N. Poulsen, D. Wolfson, S. Rangarajan, D.J. Blumenthal, “Burst mode 10G optical header recovery and lookup processing for asynchronous variable length 40G optical packet switching”, in: Proceedings of the OFC06, Anaheim, CA, USA, March 2006, Paper OFJ2.

[24] F. Xue, Z. Pan, H. Yang, J. Yang, J. Cao, K. Okamoto, S. Kamei, V. Akella, S.J.B. Yoo, “Design and experimental demonstration of a variablelength optical packet routing system with unified contention resolution”, IEEE Journal of Lightwave Technology 22 (11) (2004) 2570–2581.

[25] Dimitra Simeonidou, Reza Nejabati, Georgios Zervas, Dimtrios Klonidis, Anna Tzanakaki, Mike J. O'Mahony, "Dynamic optical network architectures and technologies for existing and emerging grid services", Journal of Lightwave Technology Member 23 (10) (2005) 3347–3357.

[26] A. Pattavina, "Switching Theory: Architectures and Performance in Broadband ATM Networks", first ed., John Wiley and Sons, Baffin Lane, Chichester, West Sussex, England, 1998.

[27] J. Aracil, N. Akar, S. Bjornstad, M. Casoni, K. Christodoulopoulos, D. Careglio, J. Fdez-Palacios, C. Gauger, O. Gonzalez de Dios, G. Hu, E. Karasan, M. Klinkowski, D. Morato, R. Nejabati, H. Overby, C. Raffaelli, D. Simeonidou, N. Stol, G. Tosi-Beleffi, K. Vlachos, "OBS task force, Research in optical burst switching within the e-Photon/ ONe network of excellence", Optical Switching and Networking, Elsevier, 2006.

[28] MOPTC – Decreto-Lei n.º 123/2009 de 21 de Maio. [Consult. 19 Nov. 2010]. avaiable in WWW: <URL: http://www.anacom.pt/render.jsp?contentId=952960>.

[29] NYC DIGITAL Road Map for the Digital City Achieving New York City´s Digital Future Spring 2011

[30] Andrienko G, Andrienko N, Wrobel S. "Visual analytics tools for analysis of movement data". ACM SIGKDD Explorations 2007; 9:38–46.

[31] Azizyan, M., I. Constandache, and R. R. Choudhury. "Surroundsense: Mobile phone localization via ambience " MobiCom'09, September 20–25, 2009, Beijing, China.

[32] Vieira P., Vieira M.A., Queluz M.P., Rodrigues A., "Validation of a Novel Vehicular Mobility Model for Wireless Networks", Proceedings of 9th International Symposium of Wireless Personal Multimedia Communications 2006, San Diego, EUA, 17-21 september 2006.

[33] Vieira, M.A.,"Melhoria da Velocidade dos Transportes Públicos de Superfície em Lisboa por Regulação da Admissão de Trânsito" MSc. Thesis, Instituto Superior Técnico, Janeiro 2004.